

1

2

3

4

5

Simultaneous Measurement of Oscillation Parameters in Beam and Atmospheric Neutrino Data from Tokai-to-Kamioka and Super-Kamiokande Experiments

6

Daniel Robert Clement Barrow

7

8

Magdalen College,
Oxford University

9

Version 1.2

10

A Dissertation Submitted to Oxford University
11 for the Degree of Doctor of Philosophy

13 **Simultaneous Measurement of**

14 **Oscillation Parameters in Beam and**

15 **Atmospheric Neutrino Data from**

16 **Tokai-to-Kamioka and**

17 **Super-Kamiokande Experiments**

18 *Abstract*

19 Lorem ipsum dolor sit amet, consectetur adipiscing elit, sed do eiusmod tempor incididunt ut labore et dolore magna aliqua. Nulla aliquet porttitor lacus luctus accumsan tortor posuere. Pulvinar neque laoreet suspendisse interdum. Sem viverra aliquet eget sit. Nunc sed velit dignissim sodales ut eu sem integer vitae. At erat pellentesque adipiscing commodo elit at imperdiet dui accumsan. Fames ac turpis egestas integer eget aliquet nibh. Scelerisque eu ultrices vitae auctor eu augue. Purus non enim praesent elementum facilisis leo vel. Sollicitudin nibh sit amet commodo. Vitae auctor eu augue ut. Vel quam elementum pulvinar etiam. A condimentum vitae sapien pellentesque habitant morbi tristique senectus. Viverra accumsan in nisl nisi scelerisque eu ultrices. Sed viverra ipsum nunc aliquet bibendum enim.

32 Declaration

33 This dissertation is the result of my own work, except where ex-
34 plicit reference is made to the work of others, and has not been sub-
35 mitted for another qualification to this or any other university. This
36 dissertation does not exceed the word limit for the respective Degree
37 Committee.

38 Daniel Robert Clement Barrow

39 ©The copyright of this thesis rests with the author and is made available under a Creative
40 Commons Attribution Non-Commercial No Derivatives licence. Researchers are free to copy,
41 distribute or transmit the thesis on the condition that they attribute it, that they do not use
42 it for commercial purposes and that they do not alter, transform or build upon it. For any
43 reuse or redistribution, researchers must make clear to others the licence terms of this work.

44

Acknowledgements

45 at pretium nibh ipsum. Eget nunc scelerisque viverra mauris in aliquam. Arcu vitae
46 elementum curabitur vitae nunc sed velit dignissim. Sed arcu non odio euismod lacinia
47 at quis risus sed. Vitae tempus quam pellentesque nec nam aliquam sem et tortor.
48 Viverra aliquet eget sit amet tellus cras adipiscing. Purus sit amet luctus venenatis
49 lectus magna. In aliquam sem fringilla ut morbi tincidunt augue. Fermentum dui
50 faucibus in ornare. Aliquam malesuada bibendum arcu vitae elementum curabitur
51 vitae nunc sed.

52 Ultricies leo integer malesuada nunc vel risus commodo. Tellus cras adipiscing
53 enim eu turpis egestas pretium. Dictumst quisque sagittis purus sit amet volutpat
54 consequat mauris nunc. Vitae congue mauris rhoncus aenean vel elit scelerisque
55 mauris pellentesque. Vel facilisis volutpat est velit egestas dui id ornare. Suscipit
56 adipiscing bibendum est ultricies. At in tellus integer feugiat scelerisque varius
57 morbi enim. Cras semper auctor neque vitae tempus. Commodo sed egestas egestas
58 fringilla phasellus faucibus. Cras pulvinar mattis nunc sed blandit. Pretium viverra
59 suspendisse potenti nullam ac tortor vitae. Purus sit amet volutpat consequat. Orci
60 sagittis eu volutpat odio facilisis mauris. Sit amet massa vitae tortor condimentum
61 lacinia quis. Commodo sed egestas egestas fringilla phasellus. Sed libero enim sed
62 faucibus turpis. Vitae tempus quam pellentesque nec.

63 Blandit massa enim nec dui. Viverra tellus in hac habitasse platea dictumst vestibulu-
64 lum. Bibendum enim facilisis gravida neque convallis. Sagittis nisl rhoncus mattis
65 rhoncus urna neque. Nisl rhoncus mattis rhoncus urna neque. Ac tortor vitae purus
66 faucibus ornare. Aenean sed adipiscing diam donec adipiscing tristique risus. Sapien
67 nec sagittis aliquam malesuada bibendum. Et leo duis ut diam quam nulla. Tellus
68 rutrum tellus pellentesque eu tincidunt tortor aliquam nulla facilisi.

Contents

| | | |
|----------|---|-----------|
| 1 | Introduction | 1 |
| 2 | Neutrino Oscillation Physics | 2 |
| 2.1 | Discovery of Neutrinos | 2 |
| 2.2 | Theory of Neutrino Oscillation | 4 |
| 2.2.1 | Three Flavour Oscillations | 4 |
| 2.2.2 | The MSW Effect | 8 |
| 2.3 | Neutrino Oscillation Measurements | 9 |
| 2.3.1 | Solar Neutrinos | 11 |
| 2.3.2 | Atmospheric Neutrinos | 13 |
| 2.3.3 | Accelerator Neutrinos | 16 |
| 2.3.4 | Reactor Neutrinos | 18 |
| 2.4 | Summary | 20 |
| 3 | T2K and SK Experiment Overview | 23 |
| 3.1 | The Super-Kamiokande Experiment | 23 |
| 3.1.1 | The SK Detector | 24 |
| 3.1.2 | Calibration | 28 |
| 3.1.3 | Data Acquisition and Triggering | 31 |
| 3.1.4 | Cherenkov Radiation | 33 |
| 3.2 | The Tokai to Kamioka Experiment | 35 |
| 3.2.1 | The Neutrino Beam | 37 |
| 3.2.2 | The Near Detector at 280m | 40 |
| 3.2.2.1 | Fine Grained Detectors | 43 |
| 3.2.2.2 | Time Projection Chambers | 44 |

| | | | |
|-----|----------|--|-----|
| 93 | 3.2.2.3 | π^0 Detector | 46 |
| 94 | 3.2.2.4 | Electromagnetic Calorimeter | 46 |
| 95 | 3.2.2.5 | Side Muon Range Detector | 48 |
| 96 | 3.2.3 | The Interactive Neutrino GRID | 48 |
| 97 | 4 | Bayesian Statistics and Markov Chain Monte Carlo Techniques | 50 |
| 98 | 4.1 | Bayesian Statistics | 51 |
| 99 | 4.2 | Monte Carlo Simulation | 52 |
| 100 | 4.2.1 | Markov Chain Monte Carlo | 53 |
| 101 | 4.2.2 | Metropolis-Hastings Algorithm | 56 |
| 102 | 4.2.3 | MCMC Optimisation | 58 |
| 103 | 4.3 | Understanding the MCMC Results | 61 |
| 104 | 4.3.1 | Marginalisation | 62 |
| 105 | 4.3.2 | Parameter Estimation and Credible Intervals | 63 |
| 106 | 4.3.3 | Bayesian Model Comparisons | 65 |
| 107 | 4.3.4 | Comparison of MCMC Output to Expectation | 66 |
| 108 | 5 | Simulation, Reconstruction, and Event Reduction | 68 |
| 109 | 5.1 | Simulation | 68 |
| 110 | 5.2 | Event Reconstruction at SK | 73 |
| 111 | 5.2.1 | Validation of Reconstruction in SK-V | 82 |
| 112 | 5.3 | Event Reduction at SK | 86 |
| 113 | 6 | Sample Selections and Systematics | 92 |
| 114 | 6.1 | Atmospheric Samples | 94 |
| 115 | 6.2 | Near Detector Beam Samples | 101 |
| 116 | 6.3 | Far Detector Beam Samples | 104 |
| 117 | 6.4 | Systematic Uncertainties | 109 |
| 118 | 6.4.1 | Beam Flux | 109 |

| | | |
|-----|--|------------|
| 119 | 6.4.2 Atmospheric Flux | 111 |
| 120 | 6.4.3 Neutrino Interaction | 112 |
| 121 | 6.4.4 Near Detector | 118 |
| 122 | 6.4.5 Far Detector | 120 |
| 123 | 6.4.5.1 Beam Samples | 120 |
| 124 | 6.4.5.2 Atmospheric Samples | 123 |
| 125 | 6.4.5.3 Correlated Detector Model | 124 |
| 126 | 7 Oscillation Probability Calculation | 132 |
| 127 | 7.1 Overview | 133 |
| 128 | 7.2 Treatment of Fast Oscillations | 141 |
| 129 | 7.3 Calculation Engine | 147 |
| 130 | 7.4 Matter Density Profile | 150 |
| 131 | 7.5 Production Height Averaging | 156 |
| 132 | 8 Oscillation Analysis | 160 |
| 133 | 8.1 Likelihood Calculation | 160 |
| 134 | 8.1.1 Likelihood Scans | 162 |
| 135 | Bibliography | 165 |
| 136 | List of Figures | 178 |
| 137 | List of Tables | 189 |

¹³⁹ **Chapter 1**

¹⁴⁰ **Introduction**

¹⁴¹ **Chapter 2**

¹⁴² **Neutrino Oscillation Physics**

¹⁴³ When first proposed, neutrinos were expected to be massless fermions that only in-
¹⁴⁴ teract through weak and gravitational forces. This meant they were very difficult to
¹⁴⁵ detect as they can pass through significant amounts of matter without interacting. De-
¹⁴⁶ spite this, experimental neutrino physics has developed with many different detection
¹⁴⁷ techniques and neutrino sources being used today. In direct tension with standard
¹⁴⁸ model physics, neutrinos have been determined to oscillate between different lepton
¹⁴⁹ flavours, requiring them to have mass.

¹⁵⁰ The observation techniques which lead to the discovery of the neutrino are doc-
¹⁵¹ umented in section 2.1. The theory underpinning neutrino oscillation is described
¹⁵² in section 2.2 and includes the approximations which can be made to simplify the
¹⁵³ understanding of neutrino oscillation in the two-flavour approximation. Past, current,
¹⁵⁴ and future neutrino experiments are detailed in section 2.3, including the reactor,
¹⁵⁵ atmospheric, and long-baseline accelerator neutrino sources that have been used to
¹⁵⁶ successfully constrain oscillation parameters. Finally, the current state of oscillation
¹⁵⁷ parameter measurements are summarised in section 2.4.

¹⁵⁸ **2.1 Discovery of Neutrinos**

¹⁵⁹ At the start of the 20th century, the electrons emitted from the β -decay of the nucleus
¹⁶⁰ were found to have a continuous energy spectrum [1,2]. This observation seemingly
¹⁶¹ broke the energy conservation invoked within that period's nuclear models. Postulated

¹⁶² in 1930 by Pauli as the solution to this problem, the neutrino (originally termed
¹⁶³ “neutron”) was theorized to be an electrically neutral spin-1/2 fermion with a mass of
¹⁶⁴ the same order of magnitude as the electron [3]. This neutrino was to be emitted with
¹⁶⁵ the electron in β -decay to alleviate the apparent breaking of energy conservation. As a
¹⁶⁶ predecessor of today’s weak interaction model, Fermi’s theory of β -decay developed
¹⁶⁷ the understanding by coupling the four constituent particles; electron, proton, neutron,
¹⁶⁸ and neutrino, into a consistent model [4].

¹⁶⁹ Whilst Pauli was not convinced of the ability to detect neutrinos, the first observa-
¹⁷⁰ tions of the particle were made in the mid-1950s when neutrinos from a reactor were
¹⁷¹ observed via the inverse β -decay (IBD) process, $\bar{\nu}_e + p \rightarrow n + e^+$ [5, 6]. The detector
¹⁷² consisted of two parts: a neutrino interaction medium and a liquid scintillator. The
¹⁷³ interaction medium was built from two water tanks. These were loaded with cadmium
¹⁷⁴ chloride to allow increased efficiency of neutron capture. The positron emitted from
¹⁷⁵ IBD annihilates, $e^+ + e^- \rightarrow 2\gamma$, generating a prompt signal and the neutron is captured
¹⁷⁶ on the cadmium via $n + {}^{108}Cd \rightarrow {}^{109*}Cd \rightarrow {}^{109}Cd + \gamma$, producing a delayed signal. An
¹⁷⁷ increase in the coincidence rate was observed when the reactor was operating which
¹⁷⁸ was interpreted as interactions from neutrinos generated in the reactor.

¹⁷⁹ After the discovery of the ν_e , the natural question of how many flavours of neutrino
¹⁸⁰ exist was asked. In 1962, a measurement of the ν_μ was conducted at the Brookhaven
¹⁸¹ National Laboratory [7]. A proton beam was directed at a beryllium target, generating
¹⁸² a π -dominated beam which then decayed via $\pi^\pm \rightarrow \mu^\pm + (\nu_\mu, \bar{\nu}_\mu)$, and the subsequent
¹⁸³ interactions of the ν_μ were observed. As the subsequent interaction of the neutrino
¹⁸⁴ generates muons rather than electrons, it was determined the ν_μ was fundamentally
¹⁸⁵ different from ν_e . The final observation to be made was that of the ν_τ from the DONUT
¹⁸⁶ experiment [8]. Three neutrinos seem the obvious solution as it mirrors the known
¹⁸⁷ number of charged lepton (as they form weak isospin doublets) but there could be

¹⁸⁸ evidence of more. Several neutrino experiments have found anomalous results [9, 10]
¹⁸⁹ which could be attributed to sterile neutrinos. However, cosmological observations
¹⁹⁰ indicate the number of neutrino species $N_{eff} = 2.99 \pm 0.17$ [11], as measured from
¹⁹¹ the cosmic microwave background power spectrum, and LEP measured the number
¹⁹² of active neutrino flavours to be $N_\nu 2.9840 \pm 0.0082$ [12] from measurements of the
¹⁹³ Z -decay width.

¹⁹⁴ 2.2 Theory of Neutrino Oscillation

¹⁹⁵ As direct evidence of beyond Standard Model physics, a neutrino generated with
¹⁹⁶ lepton flavour α can change into a different lepton flavour β after propagating some
¹⁹⁷ distance. This phenomenon is called neutrino oscillation and requires that neutrinos
¹⁹⁸ must have a non-zero mass (as seen in subsection 2.2.1). This observation is direct
¹⁹⁹ evidence of beyond standard model physics. This behaviour has been characterised
²⁰⁰ by the Pontecorvo-Maki-Nakagawa-Sakata (PMNS) [13–15] mixing matrix which
²⁰¹ describes how the flavour and mass of neutrinos are associated. This is analogous to
²⁰² the Cabibbo-Kobayashi-Maskawa (CKM) [16] matrix measured in quark physics.

²⁰³ 2.2.1 Three Flavour Oscillations

²⁰⁴ The PMNS parameterisation defines three flavour eigenstates, ν_e , ν_μ and ν_τ (indexed
²⁰⁵ ν_α), which are eigenstates of the weak interaction and three mass eigenstates, ν_1 , ν_2 and
²⁰⁶ ν_3 (indexed ν_i). Each mass eigenstate is the superposition of all three flavour states,

$$|\nu_i\rangle = \sum_\alpha U_{\alpha i} |\nu_\alpha\rangle. \quad (2.1)$$

207 Where U is the PMNS matrix which is unitary and connects the mass and flavour

208 eigenstates.

209 The weak interaction couples to flavour eigenstates so neutrinos interact with
210 leptons of the same flavour. The propagation of a neutrino flavour eigenstate, in a
211 vacuum, can be re-written as a plane-wave solution to the time-dependent Schrödinger
212 equation,

$$|\nu_\alpha(t)\rangle = \sum_i U_{\alpha i}^* |\nu_i\rangle e^{-i\phi_i}. \quad (2.2)$$

213 The probability of observing a neutrino of flavour eigenstate β from one which
214 originated as flavour α can be calculated as,

$$P(\nu_\alpha \rightarrow \nu_\beta) = |\langle \nu_\beta | \nu_\alpha(t) \rangle|^2 = \sum_{i,j} U_{\alpha i}^* U_{\beta i} U_{\alpha j} U_{\beta j}^* e^{-i(\phi_j - \phi_i)} \quad (2.3)$$

215 The ϕ_i term can be expressed in terms of the energy, E_i , and magnitude of the
216 three momenta, p_i , of the neutrino, $\phi_i = E_i t - p_i x$ (t and x being time and position
217 coordinates). Therefore,

$$\phi_j - \phi_i = E_j t - E_i t - p_j x + p_i x. \quad (2.4)$$

218 For a relativistic particle, $E_i \gg m_i$,

$$p_i = \sqrt{E_i^2 - m_i^2} \approx E_i - \frac{m_i^2}{2E_i}. \quad (2.5)$$

219 Making the approximations that neutrinos are relativistic, the mass eigenstates
220 were created with the same energy and that $x = L$, where L is the distance traveled by
221 the neutrino, Equation 2.4 then becomes

$$\phi_j - \phi_i = \frac{\Delta m_{ij}^2 L}{2E}, \quad (2.6)$$

222 where $\Delta m_{ij}^2 = m_j^2 - m_i^2$. This, combined with further use of unitarity relations
223 results in Equation 2.3 becoming

$$P(\nu_\alpha \rightarrow \nu_\beta) = \delta_{\alpha\beta} - 4 \sum_{i>j} \Re \left(U_{\alpha i}^* U_{\beta i} U_{\alpha j} U_{\beta j}^* \right) \sin^2 \left(\frac{\Delta m_{ij}^2 L}{4E} \right) + (-) 2 \sum_{i>j} \Im \left(U_{\alpha i}^* U_{\beta i} U_{\alpha j} U_{\beta j}^* \right) \sin \left(\frac{\Delta m_{ij}^2 L}{2E} \right). \quad (2.7)$$

224 Where $\delta_{\alpha\beta}$ is the Kronecker delta function and the negative sign on the last term is
225 included for the oscillation probability of antineutrinos.

226 Typically, the PMNS matrix is parameterised into three mixing angles, a charge
227 parity (CP) violating phase δ_{CP} , and two Majorana phases $\alpha_{1,2}$,

$$U = \underbrace{\begin{pmatrix} 1 & 0 & 0 \\ 0 & c_{23} & s_{23} \\ 0 & -s_{23} & c_{23} \end{pmatrix}}_{\text{Atmospheric, Accelerator}} \underbrace{\begin{pmatrix} c_{13} & 0 & s_{13}e^{-i\delta_{CP}} \\ 0 & 1 & 0 \\ -s_{13}e^{-i\delta_{CP}} & 0 & c_{13} \end{pmatrix}}_{\text{Reactor, Accelerator}} \underbrace{\begin{pmatrix} c_{12} & s_{12} & 0 \\ -s_{12} & c_{12} & 0 \\ 0 & 0 & 1 \end{pmatrix}}_{\text{Reactor, Solar}} \underbrace{\begin{pmatrix} e^{i\alpha_1/2} & 0 & 0 \\ 0 & e^{i\alpha_2/2} & 0 \\ 0 & 0 & 1 \end{pmatrix}}_{\text{Majorana}}. \quad (2.8)$$

²²⁸ Where $s_{ij} = \sin(\theta_{ij})$ and $c_{ij} = \cos(\theta_{ij})$. The oscillation parameters are often
²²⁹ grouped; (1,2) as “solar”, (2,3) as “atmospheric” and (1,3) as “reactor”. Many
²³⁰ neutrino experiments aim to measure the PMNS parameters from a wide array of
²³¹ origins, as is the purpose of this thesis.

²³² The Majorana phase, $\alpha_{1,2}$, included within the fourth matrix in Equation 2.8 is only
²³³ included for completeness. For an oscillation analysis experiment, any terms contain-
²³⁴ ing this phase disappear due to taking the expectation value of the PMNS matrix.
²³⁵ Measurements of these phases are typically performed by experiments searching for
²³⁶ neutrino-less double β -decay [17].

²³⁷ A two flavour approximation can be obtained when one assumes the third mass
²³⁸ eigenstate is degenerate with another. As discussed in section 2.3, it is found that
²³⁹ $\Delta m_{21}^2 \ll |\Delta m_{31}^2|$. This results in the two flavour approximation being reasonable for
²⁴⁰ understanding the features of the oscillation. In this two flavour case, the mixing
²⁴¹ matrix becomes,

$$U_{2 \text{ Flav.}} = \begin{pmatrix} \cos(\theta) & \sin(\theta) \\ -\sin(\theta) & \cos(\theta) \end{pmatrix}. \quad (2.9)$$

²⁴² This culminates in the oscillation probability,

$$\begin{aligned} P(\nu_\alpha \rightarrow \nu_\alpha) &= 1 - \sin^2(2\theta) \sin^2\left(\frac{\Delta m^2 L}{4E}\right), \\ P(\nu_\alpha \rightarrow \nu_\beta) &= \sin^2(2\theta) \sin^2\left(\frac{\Delta m^2 L}{4E}\right). \end{aligned} \tag{2.10}$$

²⁴³ Where $\alpha \neq \beta$. For a fixed neutrino energy, the oscillation probability is a sinusoidal
²⁴⁴ function depending upon the distance over which the neutrino propagates. The
²⁴⁵ frequency and amplitude of oscillation are dependent upon $\Delta m^2/4E$ and $\sin^2 2\theta$,
²⁴⁶ respectively. The oscillation probabilities presented thus far assume $c = 1$, where
²⁴⁷ c is the speed of light in vacuum. In more familiar units, the maximum oscillation
²⁴⁸ probability for a fixed value of θ is given at $L[km]/E[GeV] \sim 1.27/\Delta m^2$. It is this
²⁴⁹ calculation that determines the best L/E value for a given experiment to be designed
²⁵⁰ around for measurements of a specific value of Δm^2 .

²⁵¹ 2.2.2 The MSW Effect

²⁵² The theory of neutrino oscillation in a vacuum has been described in subsection 2.2.1.
²⁵³ However, the beam neutrinos and atmospheric neutrinos originating from below the
²⁵⁴ horizon propagate through matter in the Earth. The coherent scattering of neutrinos
²⁵⁵ from a material target modifies the Hamiltonian of the system. This results in a change
²⁵⁶ in the oscillation probability. Notably, charged current scattering ($\nu_e + e^- \rightarrow \nu_e + e^-$,
²⁵⁷ propagated by a W boson) only affects electron neutrinos whereas the neutral current
²⁵⁸ scattering ($\nu_l + l^- \rightarrow \nu_l + l^-$, propagated by a Z^0 boson) interacts through all neutrino
²⁵⁹ flavours equally. In the two-flavour approximation, the effective mixing parameter
²⁶⁰ becomes

$$\sin^2(2\theta) \rightarrow \sin^2(2\theta_m) = \frac{\sin^2(2\theta)}{(A/\Delta m^2 - \cos(2\theta))^2 + \sin^2(2\theta)}, \quad (2.11)$$

261 where $A = 2\sqrt{2}G_F N_e E$, N_e is the electron density of the medium and G_F is Fermi's
262 constant. It is clear to see that there exists a value of $A = \Delta m^2 \cos(2\theta)$ for $\Delta m^2 > 0$
263 which results in a divergent mixing parameter. This resonance is termed the Mikheyev-
264 Smirnov-Wolfenstein (MSW) effect (or more colloquially, the matter resonance) which
265 regenerates the electron neutrino component of the neutrino flux [18–20]. The density
266 at which the resonance occurs is given by

$$N_e = \frac{\Delta m^2 \cos(2\theta)}{2\sqrt{2}G_F E}. \quad (2.12)$$

267 At densities lower than this critical value, the oscillation probability will be much
268 closer to that of vacuum oscillation. For antineutrinos, $N_e \rightarrow -N_e$ [21]. The resonance
269 occurring from the MSW effect depends on the sign of Δm^2 . Therefore, any neutrino
270 oscillation experiment which observes neutrinos and antineutrinos which have propa-
271 gated through matter can have some sensitivity to the ordering of the neutrino mass
272 eigenstates.

273 2.3 Neutrino Oscillation Measurements

274 As evidence of beyond standard model physics, the 2015 Nobel Prize in Physics was
275 awarded to the Super-Kamiokande (SK) [22] and Sudbury Neutrino Observatory
276 (SNO) [23] collaborations for the first definitive observation of solar and atmospheric

²⁷⁷ neutrino oscillation [24]. Since then, the field has seen a wide array of oscillation
²⁷⁸ measurements from a variety of neutrino sources. As seen in subsection 2.2.1, the
²⁷⁹ neutrino oscillation probability is dependent on the ratio of the propagation baseline, L ,
²⁸⁰ to the neutrino energy, E . It is this ratio that determines the type of neutrino oscillation
²⁸¹ a particular experiment is sensitive to.

²⁸² As illustrated in Figure 2.1, there are many neutrino sources that span a wide
²⁸³ range of energies. The least energetic neutrinos are from diffuse supernovae and
²⁸⁴ terrestrial neutrinos at $O(1)$ MeV whereas the most energetic neutrinos originate from
²⁸⁵ atmospheric and galactic neutrinos of $> O(1)$ TeV.

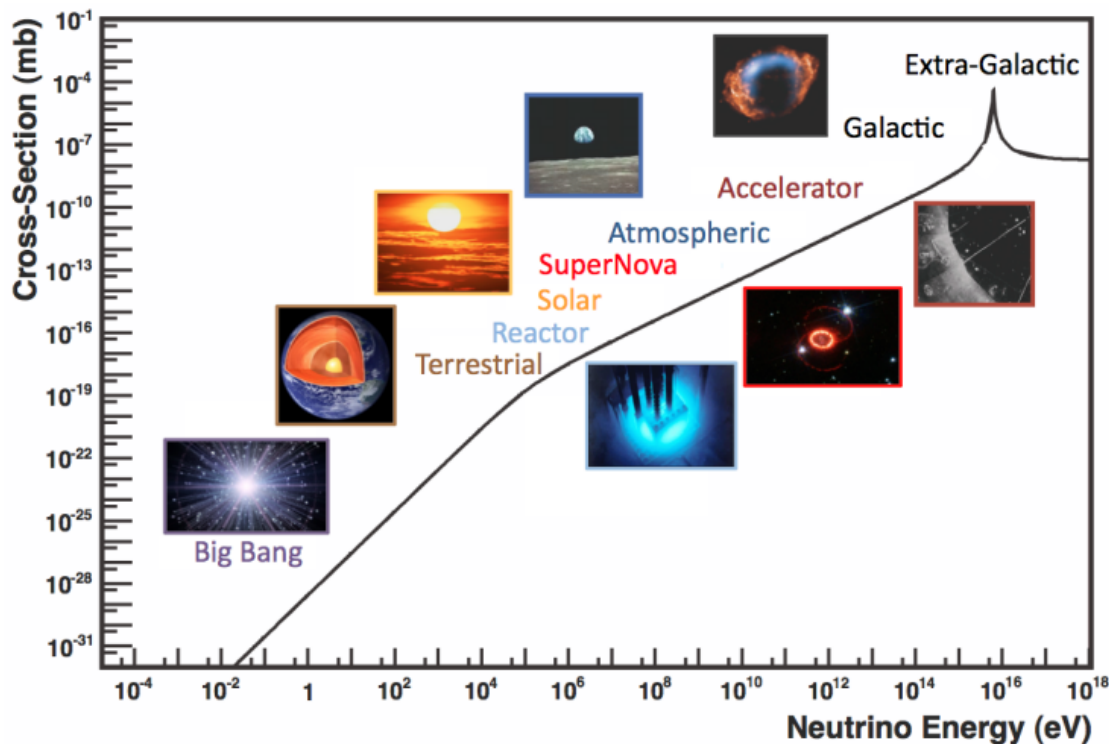


Figure 2.1: The cross-section of neutrinos from various natural and man-made sources as a function of neutrino energy. Taken from [25]

²⁸⁶ 2.3.1 Solar Neutrinos

²⁸⁷ Solar neutrinos are emitted from fusion reaction chains at the center of the Sun. The
²⁸⁸ solar neutrino flux, given as a function of neutrino energy for different fusion and
²⁸⁹ decay chains, is illustrated in Figure 2.2. Whilst proton-proton fusion generates the
²⁹⁰ largest flux of neutrinos, the neutrinos are of low energy and are difficult to reconstruct
²⁹¹ due to the IBD interaction threshold of 1.8MeV. Consequently, most experiments focus
²⁹² on the neutrinos from the decay of 8B (via $^8B \rightarrow ^8Be^* + e^+ + \nu_e$), which are higher
²⁹³ energy.

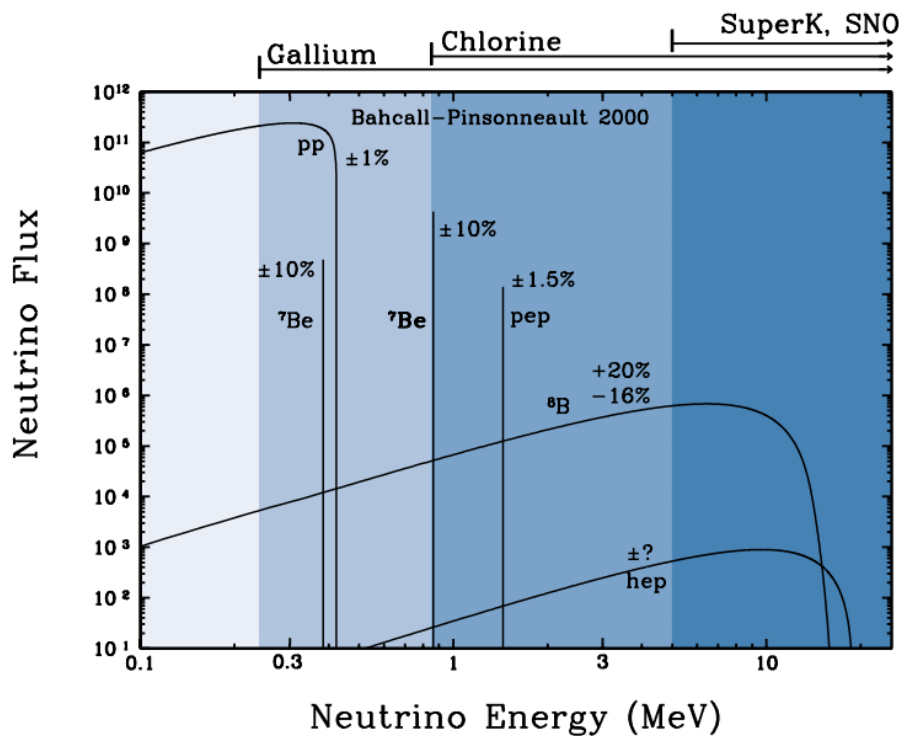
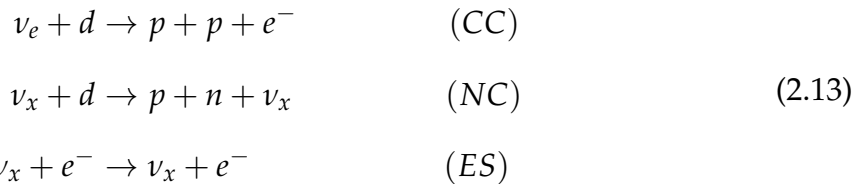


Figure 2.2: The solar neutrino flux as a function of neutrino energy for various fusion reactions and decay chains as predicted by the Standard Solar Model. Taken from [26].

²⁹⁴ The first measurements of solar neutrinos observed a significant reduction in the
²⁹⁵ event rate compared to predictions from the Standard Solar Model [27, 28]. The
²⁹⁶ proposed solution to this “solar neutrino problem” was $\nu_e \leftrightarrow \nu_\mu$ oscillations in a

²⁹⁷ precursory version of the PMNS model [29]. The Kamiokande [30], Gallex [31] and
²⁹⁸ Sage [32] experiments confirmed the ~ 0.5 factor deficit of solar neutrinos.

²⁹⁹ The conclusive solution to this problem was determined by the SNO collaboration
³⁰⁰ [33]. Using a deuterium water target to observe 8B neutrinos, the event rate of charged
³⁰¹ current (CC), neutral current (NC), and elastic scattering (ES) interactions (Given in
³⁰² Equation 2.13) was simultaneously measured. CC events can only occur for electron
³⁰³ neutrinos, whereas the NC channel is agnostic to neutrino flavour, and the ES reaction
³⁰⁴ has a slight excess sensitivity to electron neutrino interactions. This meant that there
³⁰⁵ were direct measurements of the ν_e and ν_x neutrino flux. It was concluded that the
³⁰⁶ CC and ES interaction rates were consistent with the deficit previously observed.
³⁰⁷ Most importantly, the NC reaction rate was only consistent with the others under the
³⁰⁸ hypothesis of flavour transformation.



³⁰⁹ Many experiments have since measured the neutrino flux of different interaction
³¹⁰ chains within the sun [34–36]. The most recent measurement was that of CNO neutrinos
³¹¹ which were recently observed with 5σ significance by the Borexino collaboration.
³¹² Future neutrino experiments aim to further these spectroscopic measurements of
³¹³ different fusion chains within the Sun [37–39]. Solar neutrinos act as an irreducible
³¹⁴ background for dark matter experiments like DARWIN but oscillation parameter
³¹⁵ measurements can be made [40].

³¹⁶ 2.3.2 Atmospheric Neutrinos

- ³¹⁷ The interactions of primary cosmic ray protons in Earth's upper atmosphere generate
³¹⁸ showers of energetic hadrons. These are mostly pions and kaons which when they
³¹⁹ decay produce a natural source of neutrinos spanning energies of MeV to TeV [41].
³²⁰ The main decay is via

$$\begin{aligned} \pi^\pm &\rightarrow \mu^\pm + (\nu_\mu, \bar{\nu}_\mu) \\ \mu^\pm &\rightarrow e^\pm + (\nu_e, \bar{\nu}_e) + (\nu_\mu, \bar{\nu}_\mu) \end{aligned} \tag{2.14}$$

³²¹ such that for a single pion decay, three neutrinos are typically produced. The
³²² atmospheric neutrino flux energy spectra as predicted by the Bartol [42], Honda
³²³ [43–45], and FLUKA [46] models are illustrated in Figure 2.3. The flux distribution
³²⁴ peaks at an energy of $O(10)\text{GeV}$. The uncertainties associated with these models
³²⁵ are dominated by the hadronic production of kaon and pions as well as the primary
³²⁶ cosmic flux.

³²⁷ Unlike long-baseline experiments which have a fixed baseline, the distance at-
³²⁸ mospheric neutrinos propagate is dependent upon the zenith angle at which they
³²⁹ interact. This is illustrated in Figure 2.4. Neutrinos that are generated directly above
³³⁰ the detector ($\cos(\theta) = 1.0$) have a baseline equivalent to the height of the atmosphere
³³¹ whereas neutrinos that interact directly below the detector ($\cos(\theta) = -1.0$) have to
³³² travel a length equal to the diameter of the Earth. This means atmospheric neutrinos
³³³ have a baseline that varies from $O(20)\text{km}$ to $O(6 \times 10^3)\text{km}$. Any neutrino generated
³³⁴ at or below the horizon will be subject to matter effects as they propagate through the
³³⁵ Earth.

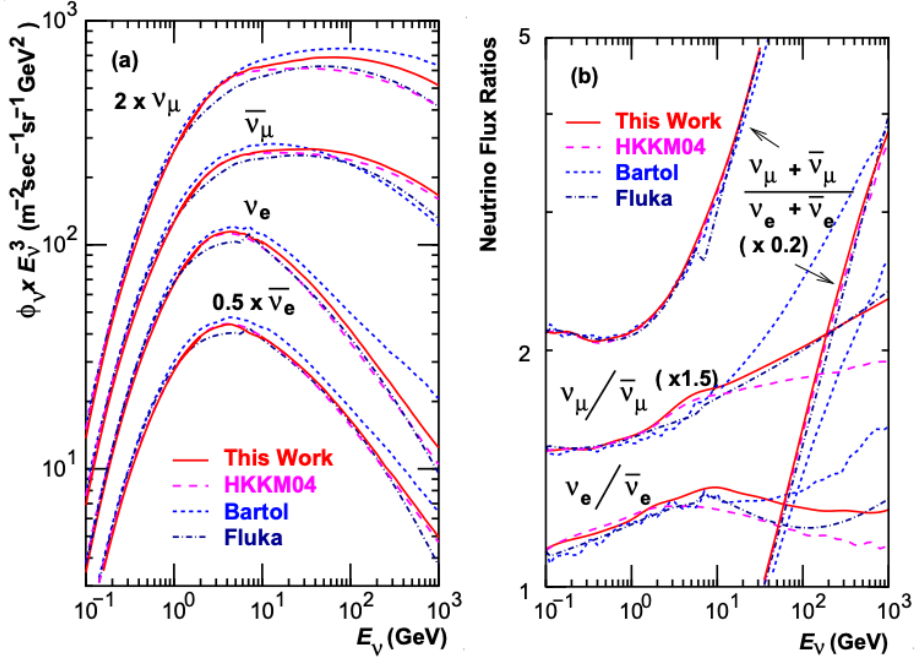


Figure 2.3: Left panel: The atmospheric neutrino flux for different neutrino flavours as a function of neutrino energy as predicted by the 2007 Honda model (“This work”) [43], the 2004 Honda model (“HKKM04”) [44], the Bartol model [42] and the FLUKA model [46]. Right panel: The ratio of the muon to electron neutrino flux as predicted by all the quoted models. Both figures taken from [43].

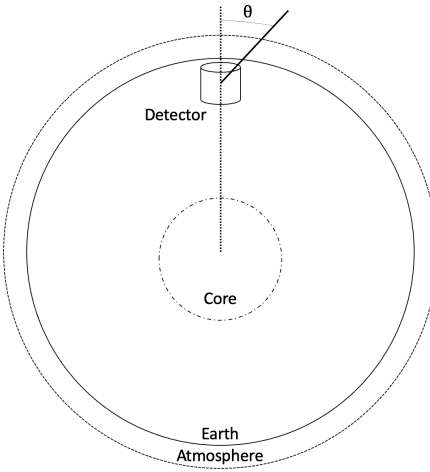


Figure 2.4: A diagram illustrating the definition of zenith angle as used in the Super Kamiokande experiment [47].

Figure 2.5 highlights the neutrino flux as a function of the zenith angle for different

slices of neutrino energy. For medium to high-energy neutrinos (and to a lesser degree for low-energy neutrinos), the flux is approximately symmetric around $\cos(\theta) = 0$.

³³⁶ Figure 2.5 highlights the neutrino flux as a function of the zenith angle for different
³³⁷ slices of neutrino energy. For medium to high-energy neutrinos (and to a lesser degree
³³⁸ for low-energy neutrinos), the flux is approximately symmetric around $\cos(\theta) = 0$.

To the accuracy of this approximation, the systematic uncertainties associated with atmospheric flux for comparing upward-going and down-going neutrino cancels. This allows the down-going events, which are mostly insensitive to oscillation probabilities, to act as an unoscillated prediction (similar to a near detector in an accelerator neutrino experiment).

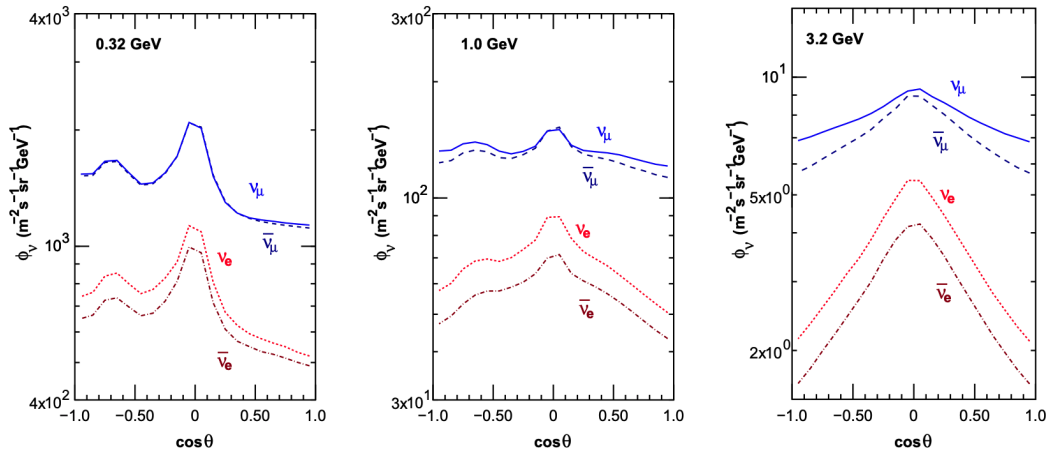


Figure 2.5: Prediction of $\nu_e, \bar{\nu}_e, \nu_\mu, \bar{\nu}_\mu$ fluxes as a function of zenith angle as calculated by the HKKM model [45]. The left, middle and right panels represent three values of neutrino energy, 0.32GeV, 1.0GeV and 3.2GeV respectively. Predictions for other models including Bartol [42], Honda [43] and FLUKA [46] are given in [47].

Precursory hints of atmospheric neutrinos were observed in the mid-1960s searching for $\nu_\mu + X \xrightarrow{(-)} X^* + \mu^\pm$ [48], although it was called an anomaly at the time of measurement. This was succeeded with the IMB-3 [49] and Kamiokande [50] experiments which measured the ratio of muon neutrinos compared to electron neutrinos $R(\nu_\mu/\nu_e)$. Both experiments were found to have a consistent deficit of muon neutrinos, with $R(\nu_\mu/\nu_e) = 0.67 \pm 0.17$ and $R(\nu_\mu/\nu_e) = 0.60^{+0.07}_{-0.06} \pm 0.05$. Super-Kamiokande (SK) [47] extended this analysis by fitting oscillation parameters in $P(\nu_\mu \rightarrow \nu_\tau)$ which found best fit parameters $\sin^2(2\theta) > 0.92$ and $1.5 \times 10^{-3} < \Delta m^2 < 3.4 \times 10^{-3}$ eV 2 .

Since then, atmospheric neutrino experiments have been making precision measurements of the $\sin^2(\theta_{23})$ and Δm^2_{32} oscillation parameters. Atmospheric neutrino oscillation is dominated by $P(\nu_\mu \rightarrow \nu_\tau)$, where SK observed a 4.6σ discovery of ν_τ

³⁵⁵ appearance [51]. Figure 2.6 illustrates the current estimates on the atmospheric mixing
³⁵⁶ parameters from a wide range of atmospheric and accelerator neutrino observatories.

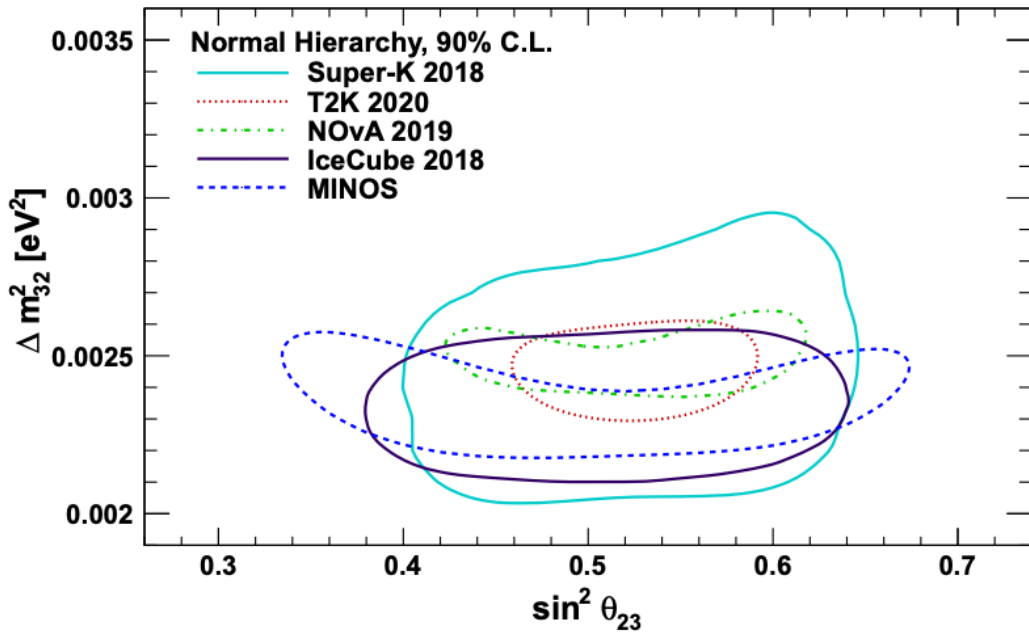


Figure 2.6: Constraints on the atmospheric oscillation parameters, $\sin^2(\theta_{23})$ and Δm_{32}^2 , from atmospheric and long baseline experiments: SK [52], T2K [53], NOvA [54], IceCube [55] and MINOS [56]. Figure taken from [57].

³⁵⁷ 2.3.3 Accelerator Neutrinos

³⁵⁸ The concept of using a man-made “neutrino beam” was first realised in 1962 [58].
³⁵⁹ Since then, many experiments have followed which all use the same fundamental
³⁶⁰ concepts. Typically, a proton beam is aimed at a target producing charged mesons that
³⁶¹ decay to neutrinos. The mesons can be sign-selected by the use of magnetic focusing
³⁶² horns to generate a neutrino or antineutrino beam. Pions are the primary meson that
³⁶³ decay and depending on the orientation of the magnetic field, a muon (anti-)neutrino
³⁶⁴ beam is generated via $\pi^+ \rightarrow \mu^+ + \nu_\mu$ or $\pi^- \rightarrow \mu^- + \bar{\nu}_\mu$. The decay of muons and
³⁶⁵ kaons does result in an irreducible intrinsic electron neutrino background. In T2K,
³⁶⁶ this background contamination is $O(< 1\%)$ [59]. There is also an approximately $\sim 5\%$

³⁶⁷ “wrong-sign” neutrino background of $\bar{\nu}_\mu$ generated via the same decays. As the beam is
³⁶⁸ generated by proton interactions (rather than anti-proton interactions), the wrong-sign
³⁶⁹ component in the antineutrino beam is larger when operating in neutrino mode.

³⁷⁰ Tuning the proton energy in the beam and using beam focusing techniques allows
³⁷¹ the neutrino energy to be set to a value that maximises the disappearance oscillation
³⁷² probability in the L/E term in Equation 2.10. This means that accelerator experiments
³⁷³ are typically more sensitive to the mixing parameters as compared to a natural neutrino
³⁷⁴ source. However, the disadvantage compared to atmospheric neutrino experiments is
³⁷⁵ that the baseline has to be shorter due to the lower flux. Consequently, there is typically
³⁷⁶ less sensitivity to matter effects and the ordering of the neutrino mass eigenstates.

³⁷⁷ A neutrino experiment measures

$$R(\vec{x}) = \Phi(E_\nu) \times \sigma(E_\nu) \times \epsilon(\vec{x}) \times P(\nu_\alpha \rightarrow \nu_\beta), \quad (2.15)$$

³⁷⁸ where $R(\vec{x})$ is the event rate of neutrinos at position \vec{x} , $\Phi(E_\nu)$ is the flux of neutrinos
³⁷⁹ with energy E_ν , $\sigma(E_\nu)$ is the cross-section of the neutrino interaction and $\epsilon(\vec{x})$ is the
³⁸⁰ efficiency and resolution of the detector. In order to leverage the most out of an
³⁸¹ accelerator neutrino experiment, the flux and cross-section systematics need to be
³⁸² constrained. This is typically done via the use of a “near detector”, situated at a baseline
³⁸³ of $O(1)$ km. This detector observes the unoscillated neutrino flux and constrains the
³⁸⁴ parameters used within the flux and cross-section model.

³⁸⁵ The first accelerator experiments to precisely measure oscillation parameters were
³⁸⁶ MINOS [60] and K2K [61]. These experiments confirmed the ν_μ disappearance seen in
³⁸⁷ atmospheric neutrino experiments by finding consistent parameter values for $\sin^2(\theta_{23})$
³⁸⁸ and Δm_{23}^2 . The current generation of accelerator neutrino experiments, T2K and NO ν A

389 extended this field by observing $\bar{\nu}_\mu \rightarrow \bar{\nu}_e$ and lead the sensitivity to atmospheric mix-
 390 ing parameters as seen in Figure 2.6 [62]. The two experiments differ in their peak
 391 neutrino energy, baseline, and detection technique. The NO ν A experiment is situated
 392 at a baseline of 810km from the NuMI beamline which delivers 2GeV neutrinos. The
 393 T2K neutrino beam is peaked around 0.6GeV and propagates 295km. The NO ν A
 394 experiment also uses functionally identical detectors (near and far) which allow the
 395 approximate cancellation of detector systematics whereas T2K uses a plastic scintil-
 396 lator technique at the near detector and a water Cherenkov far detector. The future
 397 generation experiments DUNE [63] and Hyper-Kamiokande [64] will succeed these
 398 experiments as the high-precision era of neutrino oscillation parameter measurements
 399 develops.

400 Several anomalous results have been observed in the LSND [9] and MiniBooNE [10]
 401 detectors which were designed with purposefully short baselines. Parts of the neu-
 402 trino community attributed these results to oscillations induced by a fourth “sterile”
 403 neutrino [65] but several searches in other experiments, MicroBooNE [66] and KAR-
 404 MEN [67], found no hints of additional neutrino species. The solution to the anomalous
 405 results is still being determined.

406 2.3.4 Reactor Neutrinos

407 As illustrated in the first discovery of neutrinos (section 2.1), nuclear reactors are a very
 408 useful man-made source of electron antineutrinos. For reactors that use low-enriched
 409 uranium ^{235}U as fuel, the antineutrino flux is dominated by the β -decay fission of ^{235}U ,
 410 ^{238}U , ^{239}Pu and ^{241}Pu [68] as illustrated in Figure 2.7.

411 Due to their low energy, reactor electron antineutrinos predominantly interact
 412 via the inverse β -decay (IBD) interaction. The typical signature contains two signals

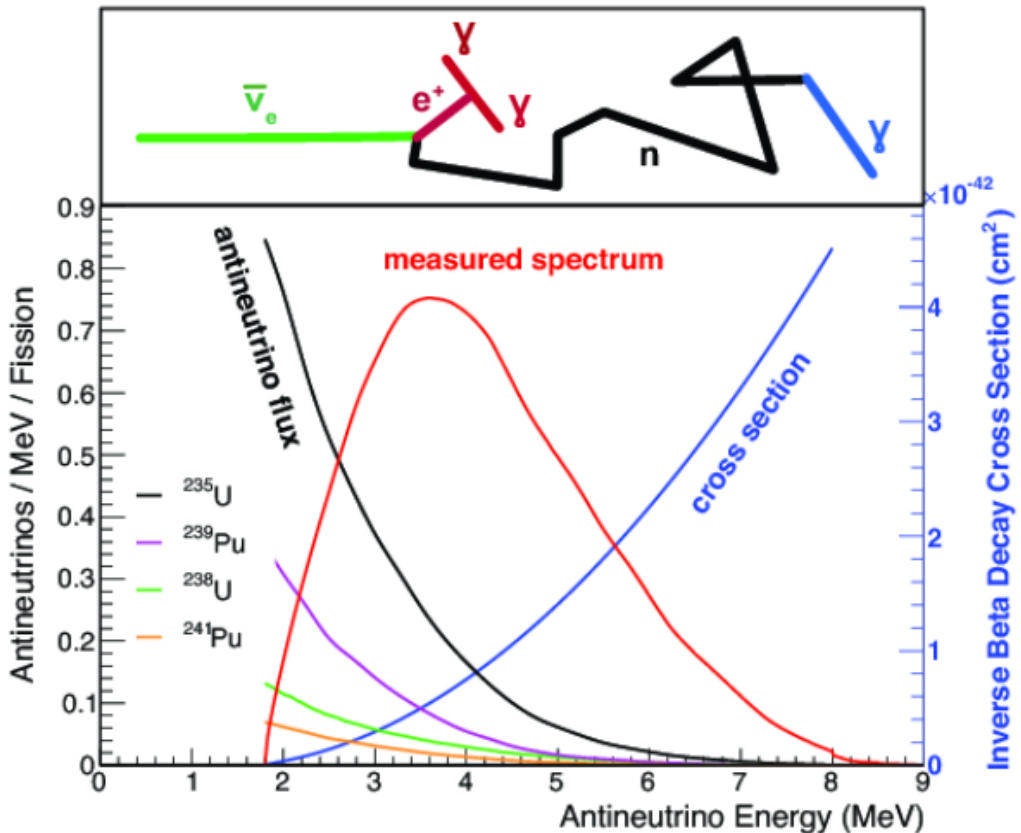


Figure 2.7: Reactor electron antineutrino fluxes for ^{235}U (Black), ^{238}U (Green), ^{239}Pu (Purple), and ^{241}Pu (Orange) isotopes. The inverse β -decay cross-section (Blue) and corresponding measurable neutrino spectrum (Red) are also given. Top panel: Schematic of Inverse β -decay interaction including the eventual capture of the emitted neutron. This capture emits a γ -ray which provides a second signal of the event. Taken from [69].

delayed by $O(200)\mu\text{s}$; firstly the prompt photons from positron annihilation, and secondly the photons emitted ($E_{tot}^\gamma = 2.2\text{MeV}$) from de-excitation after neutron capture on hydrogen. Searching for both signals improves the detector's ability to distinguish between background and signal events [70]. Recently, SK included gadolinium dopants into the ultra-pure water to increase the energy released from the photon cascade to $\sim 8\text{MeV}$ and reduce the time of the delayed signal to $\sim 28\mu\text{s}$.

There are many short baseline experiments ($L \sim O(1)\text{km}$) that have measured the $\sin^2(\theta_{13})$ and Δm_{23}^2 oscillation parameters. Daya Bay [71], RENO [72] and Double Chooz [73] have all provided precise measurements, with the first discovery of a

422 non-zero θ_{13} made by Daya Bay and RENO (and complemented by T2K [73]). The
423 constraints on $\sin^2(\theta_{13})$ by the reactor experiments lead the field and are often used as
424 external inputs to accelerator neutrino experiments to improve their sensitivity to δ_{CP}
425 and mass hierarchy determination. JUNO-TAO [74], a small collaboration within the
426 larger JUNO experiment, is a next-generation reactor experiment that aims to precisely
427 measure the isotopic antineutrino yields from the different fission chains. Alongside
428 this, it aims to explain the ‘5MeV excess’ [75–77] by conducting a search for sterile
429 neutrinos with a mass scale of around 1eV.

430 Kamland [78] is the only experiment to have observed reactor neutrinos using a
431 long baseline (flux weighted averaged baseline of $L \sim 180\text{km}$) which allows it to have
432 sensitivity to Δm_{12}^2 . Combined with the SK solar neutrino experiment, the combined
433 analysis puts the most stringent constraint on Δm_{12}^2 [79].

434 2.4 Summary

435 Since observing the first evidence of neutrino oscillations in the late 1990’s, numerous
436 measurements of the mixing parameters have been made. Many experiments use
437 neutrinos as a tool for discovery of new physics (diffuse supernova background,
438 neutrinoless double beta decay and others) so the PMNS parameters are summarised
439 in the Particle Data Group (PDG) review tables. The analysis presented in this thesis
440 focuses on the 2020 T2K oscillation analysis presented in [80] where the 2018 PDG
441 constraints [81] were used. These constraints are outlined in Table 2.1.

442 The $\sin^2(\theta_{13})$ measurement stems from the electron antineutrino disappearance,
443 $P(\bar{\nu}_e \rightarrow \bar{\nu}_e)$, and is take as the average best-fit from the combination of Daya Bay,
444 Reno and Double Chooz. It is often used as a prior uncertainty within other neu-
445 trino oscillation experiments, typically termed the reactor constraint. The $\sin^2(\theta_{12})$

| Parameter | 2018 Constraint |
|----------------------------------|--|
| $\sin^2(\theta_{12})$ | 0.307 ± 0.013 |
| Δm_{21}^2 | $(7.53 \pm 0.18) \times 10^{-5} \text{ eV}^2$ |
| $\sin^2(\theta_{13})$ | $(2.12 \pm 0.08) \times 10^{-2}$ |
| $\sin^2(\theta_{23})$ (I.H., Q1) | $0.421^{+0.033}_{-0.025}$ |
| $\sin^2(\theta_{23})$ (I.H., Q2) | $0.592^{+0.023}_{-0.030}$ |
| $\sin^2(\theta_{23})$ (N.H., Q1) | $0.417^{+0.025}_{-0.028}$ |
| $\sin^2(\theta_{23})$ (N.H., Q2) | $0.597^{+0.024}_{-0.030}$ |
| Δm_{32}^2 (I.H.) | $(-2.56 \pm 0.04) \times 10^{-3} \text{ eV}^2$ |
| Δm_{32}^2 (N.H.) | $(2.51 \pm 0.05) \times 10^{-3} \text{ eV}^2$ |

Table 2.1: The 2018 Particle Data Group constraints of the oscillation parameters taken from [81]. The value of Δm_{23}^2 is given for both normal hierarchy (N.H.) and inverted hierarchy (I.H.) and $\sin^2(\theta_{23})$ is broken down by whether its value is below (Q1) or above (Q2) 0.5.

parameter is predominantly measured through electron neutrino disappearance, $P(\nu_e \rightarrow \nu_{\mu,\tau})$, in solar neutrino experiments. The long-baseline reactor neutrino experiment Kamland also has sensitivity to this parameter and is used in a joint fit to solar data from SNO and SK, using the reactor constraint. Measurements of $\sin^2(\theta_{23})$ are made by long-baseline and atmospheric neutrino experiments. The PDG value is a joint fit of T2K, NOvA, MINOS and IceCube DeepCore experiments. The latest T2K-only measurement, provided at Neutrino2020 and is the basis of this thesis, is given as $\sin^2(\theta_{23}) = 0.546^{+0.024}_{-0.046}$ [80]. The PDG constraint on Δm_{12}^2 is provided by the KamLAND experiment using solar and geoneutrino data. This measurement utilised a $\sin^2(\theta_{13})$ constraint from accelerator (T2K, MINOS) and reactor neutrino (Daya Bay, RENO, Double Chooz) experiments. Accelerator measurements make some of the most stringent constraints on Δm_{23}^2 although atmospheric experiments have more sensitivity to the mass hierarchy determination. The PDG performs a joint fit of accelerator and atmospheric data, in both normal and inverted hierarchy separately. The latest T2K-only result is $\Delta m_{32}^2 = 2.49^{+0.058}_{-0.082} \times 10^{-3} \text{ eV}^2$ favouring normal hierarchy [80]. The value of δ_{CP} is largely undetermined. CP-conserving values of 0 and π were

⁴⁶² rejected with $\sim 2\sigma$ intervals, as published in Nature, although more recent analysis
⁴⁶³ have reduced the rejection intervals to 90%. Since the 2018 PDG publication, there has
⁴⁶⁴ been a new measurement of $\sin^2(\theta_{13}) = (2.20 \pm 0.07) \times 10^{-2}$ [82], alongside updated
⁴⁶⁵ Δm_{23}^2 and $\sin^2(\theta_{23})$ measurements.

⁴⁶⁶ Throughout this thesis, several sample spectra predictions and contours are pre-
⁴⁶⁷ sented which require oscillation parameters to be assumed. Table 2.2 defines two sets
⁴⁶⁸ of oscillation parameters, with “Asimov A” set being close to the preferred values
⁴⁶⁹ from a previous T2K-only fit [83] and “Asimov B” being CP-conserving and further
⁴⁷⁰ from maximal θ_{23} mixing.

| Parameter | Asimov A | Asimov B |
|-----------------------|-------------------------------------|----------|
| Δm_{12}^2 | $7.53 \times 10^{-5} \text{ eV}^2$ | |
| Δm_{32}^2 | $2.509 \times 10^{-3} \text{ eV}^2$ | |
| $\sin^2(\theta_{12})$ | 0.304 | |
| $\sin^2(\theta_{13})$ | 0.0219 | |
| $\sin^2(\theta_{23})$ | 0.528 | 0.45 |
| δ_{CP} | -1.601 | 0.0 |

Table 2.2: Reference values of the neutrino oscillation parameters for two different oscillation parameter sets.

⁴⁷¹ **Chapter 3**

⁴⁷² **T2K and SK Experiment Overview**

⁴⁷³ As the successor of the Kamiokande experiment, the Super-Kamiokande (SK) collaboration has been leading atmospheric neutrino oscillation analyses for over two decades.
⁴⁷⁴ The detector has provided some of the strongest constraints on proton decay and the
⁴⁷⁵ first precise measurements of the Δm_{23}^2 and $\sin^2(\theta_{23})$ neutrino oscillation parameters.
⁴⁷⁶ The ability of the detector to low-energy neutrino events has been significantly im-
⁴⁷⁷ proved with the recent gadolinium doping of the ultra-pure water target. The history,
⁴⁷⁸ detection technique, and operation of the SK detector is described in section 3.1.

⁴⁸⁰ The Tokai-to-Kamioka (T2K) experiment was one of the first long-baseline ex-
⁴⁸¹ periments to use both neutrino and antineutrino beams to precisely measure the
⁴⁸² charge parity violation within the neutrino sector. With the SK detector observing
⁴⁸³ the oscillated neutrino flux, the T2K experiment observed the first hints of a non-zero
⁴⁸⁴ $\sin^2(\theta_{13})$ measurement and continues to lead the field with the constraints it provides
⁴⁸⁵ on $\sin^2(\theta_{13})$, $\sin^2(\theta_{23})$, Δm_{23}^2 and δ_{CP} . The techniques which T2K uses in gener-
⁴⁸⁶ ating its neutrino beam as well as the near-detector used to constrain the flux and
⁴⁸⁷ cross-section parameters used in this analysis are documented in section 3.2.

⁴⁸⁸ **3.1 The Super-Kamiokande Experiment**

⁴⁸⁹ The SK experiment began taking data in 1996 [84] and has had many modifications
⁴⁹⁰ throughout its lifespan. There have been seven defined periods of data taking as
⁴⁹¹ noted in Table 3.1. Data taking began in SK-I which ran for five years. Between the

492 SK-I and SK-II periods, a significant proportion of the PMTs were damaged during
 493 maintenance. Those that survived were equally distributed throughout the detector
 494 in the SK-II era, which resulted in a reduced photo-coverage. From SK-III onwards,
 495 repairs to the detector meant the full suite of PMTs was operational. Before the
 496 start of SK-IV, the data acquisition and electronic systems were upgraded. Between
 497 SK-IV and SK-V, a significant effort was placed into tank open maintenance and
 498 repair/replacement of defective PMTs, a task for which the author of this thesis was
 499 required. Consequently, the detector conditions were significantly different between
 500 the two operational periods. SK-VI saw the start of the 0.01% gadolinium doped water.
 501 SK-VII, which started during the writing of this thesis, has increased the gadolinium
 502 concentration to 0.03% for continued operation [85].

| Period | Start Date | End Date | Live-time (days) |
|--------|----------------|----------------|------------------|
| I | April 1996 | July 2001 | 1489.19 |
| II | October 2002 | October 2005 | 798.59 |
| III | July 2006 | September 2008 | 518.08 |
| IV | September 2008 | May 2018 | 3244.4 |
| V | January 2019 | July 2020 | 461.02 |
| VI | July 2020 | May 2022 | 583.3 |
| VII | May 2022 | Ongoing | N/A |

Table 3.1: The various SK periods and respective live-time. The SK-VI live-time is calculated until 1st April 2022. SK-VII started during the writing of this thesis.

503 3.1.1 The SK Detector

504 The basic structure of the Super-Kamiokande (SK) detector is a cylindrical tank with a
 505 diameter 39.3m and height 41.1m filled with ultrapure water [86]. A diagram of the
 506 significant components of the SK detector is given in Figure 3.1. The SK detector is
 507 situated in the Kamioka mine in Gifu, Japan. The mine is underground with roughly
 508 1km rock overburden (2.7km water equivalent overburden) [87]. At this depth, the

509 rate of cosmic ray muons is significantly decreased to a value of $\sim 2\text{Hz}$. The top of
 510 the tank is covered with stainless steel which is designed as a working platform for
 511 maintenance, calibration, and location for high voltage and data acquisition electronics.

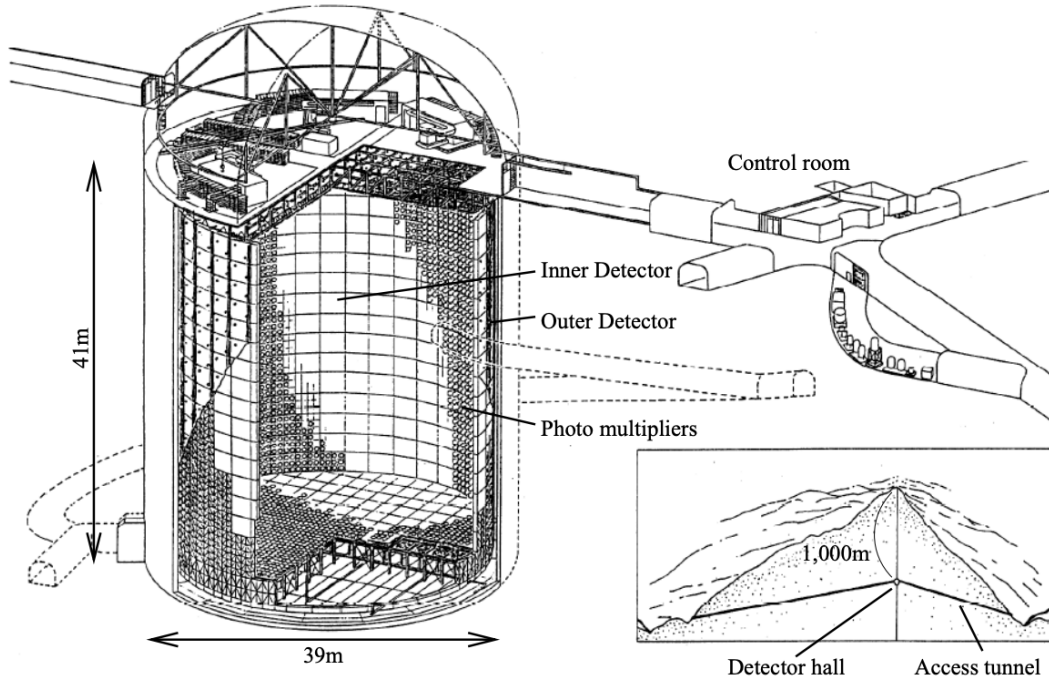


Figure 3.1: A schematic diagram of the Super-Kamiokande Detector. Taken from [88].

512 A smaller cylindrical structure (36.2m diameter, 33.8m height) is situated inside the
 513 tank, with an approximate 2m gap between this structure and the outer tank wall. The
 514 purpose of this structure is to support the photomultiplier tubes (PMTs). The volume
 515 inside and outside the support structure is referred to as the inner detector (ID) and
 516 outer detector (OD), respectively. In the SK-IV era, the ID and OD are instrumented
 517 by 11,129 50cm and 1,885 20cm PMTs respectively [86]. The ID contains a 32kton
 518 mass of water. Many analyses performed at SK use a “fiducial volume” defined by the
 519 volume of water inside the ID excluding some distance to the ID wall. This reduces the
 520 volume of the detector which is sensitive to neutrino events but reduces radioactive
 521 backgrounds and allows for better reconstruction performance. The nominal fiducial

volume is defined as the area contained inside 2m from the ID wall for a total of 22.5kton water [89].

The two regions of the detector (ID and OD) are optically separated with opaque black plastic. The purpose of this is to determine whether a track entered or exited the ID. This allows cosmic ray muons and partially contained events to be tagged and separated from neutrino events entirely contained within the ID. This black plastic is also used to cover the area between the ID PMTs to reduce photon reflection from the ID walls. Opposite to this, the OD is lined with a reflective material to allow photons to reflect around inside the OD until collected by one of the PMTs. Furthermore, each OD PMT is backed with $50 \times 50\text{cm}$ plates of wavelength shifting acrylic which increases the efficiency of light collection [87].

In the SK-IV data-taking period, the photocathode coverage of the detector, or the fraction of the ID wall instrumented with PMTs, is $\sim 40\%$ [87]. The PMTs have a quantum efficiency (the ratio of detected electrons to incident photons) of $\sim 21\%$ for photons with wavelengths of $360\text{nm} < \lambda < 390\text{nm}$. The proportion of photoelectrons that produce a signal in the dynode of a PMT, termed the collection efficiency, is $> 70\%$ [87]. The PMTs used within SK are most sensitive to photons with wavelength $300\text{nm} \leq \lambda \leq 600\text{nm}$ [87]. One disadvantage of using PMTs as the detection media is that the Earth's geomagnetic field can modify its response. Therefore, a set of compensation coils is built around the inner surface of the detector to mitigate this effect [90].

As mentioned, the SK detector is filled with ultrapure water, which in a perfect world would contain no impurities. However, bacteria and organic compounds can significantly degrade the water quality. This decreases the attenuation length, which reduces the total number of photons that hit a PMT. To combat this, a sophisticated water treatment system has been developed [87, 91]. UV lights, mechanical filters,

548 and membrane degasifiers are used to reduce the bacteria, suspended particulates,
549 and radioactive materials from the water. The flow of water within the tank is also
550 critical as it can remove stagnant bacterial growth or build-up of dust on the surfaces
551 within the tank. Gravity drifts impurities in the water towards the bottom of the
552 tank which, if left uncontrolled, can create asymmetric water conditions between
553 the top and bottom of the tank. Typically, the water entering the tank is cooled
554 below the ambient temperature of the tank to control convection and inhibit bacteria
555 growth. Furthermore, the rate of dark noise hits within PMTs is sensitive to the PMT
556 temperature [92] so controlling the temperature gradients within the tank is beneficial
557 for stable measurements.

558 SK-VI is the first phase of the SK experiment to use gadolinium dopants within
559 the ultrapure water [85]. As such, the SK water system had to be replaced to avoid
560 removing the gadolinium concentrate from the ultrapure water [93]. For an inverse
561 β -decay (IBD) interaction in a water target, the emitted neutron is thermally captured
562 on hydrogen. This process releases 2.2MeV γ rays which are difficult to detect as
563 the resulting Compton scattered electrons are very close to the Cherenkov threshold,
564 limiting the number of photons produced. Thermal capture of neutrons on gadolin-
565 ium generates γ rays with higher energy (8MeV [70]) meaning they are more easily
566 detected. SK-VI has 0.01% Gd loading (0.02% gadolinium sulphate by mass) which
567 causes \approx 50% of neutrons emitted by IBD to be captured on gadolinium [94, 95].
568 Whilst predominantly useful for low energy analyses, Gd loading allows better $\nu/\bar{\nu}$
569 separation for atmospheric neutrino event selections [96]. Efforts are currently in place
570 to increase the gadolinium concentrate to 0.03% for \approx 75% neutron capture efficiency
571 on gadolinium [97]. The final stage of loading targets 0.1% concentrate.

⁵⁷² 3.1.2 Calibration

⁵⁷³ The calibration of the SK detector is documented in [86] and summarised below. The
⁵⁷⁴ analysis presented within this thesis is dependent upon ‘high energy events’ (Charged
⁵⁷⁵ particles with $O(> 100)\text{MeV}$ momenta). These are events that are expected to generate
⁵⁷⁶ a larger number of photons such that each PMT will be hit with multiple photons.
⁵⁷⁷ The reconstruction of these events depends upon the charge deposited within each
⁵⁷⁸ PMT and the timing response of each individual PMT. Therefore, the most relevant
⁵⁷⁹ calibration techniques to this thesis are outlined.

⁵⁸⁰ Before installation, 420 PMTs were calibrated to have identical charge responses
⁵⁸¹ and then distributed throughout the tank in a cross-shape pattern (As illustrated by
⁵⁸² Figure 3.2). These are used as a standardised measure for the rest of the PMTs installed
⁵⁸³ at similar geometric positions within SK to be calibrated against. To perform this
⁵⁸⁴ calibration, a xenon lamp is located at the center of the SK tank which flashes uniform
⁵⁸⁵ light at 1Hz. This allows for geometrical effects, water quality variation, and timing
⁵⁸⁶ effects to be measured in-situ throughout normal data-taking periods.

⁵⁸⁷ When specifically performing calibration of the detector (in out-of-data taking
⁵⁸⁸ mode), the water in the tank was circulated to avoid top/bottom asymmetric water
⁵⁸⁹ quality. Any non-uniformity within the tank significantly affects the PMT hit proba-
⁵⁹⁰ bility through scattering or absorption. This becomes a dominant effect for the very
⁵⁹¹ low-intensity light sources discussed later which are designed such that only one
⁵⁹² photon is incident upon a given PMT.

⁵⁹³ The “gain” of a PMT is defined as the ratio of the total charge of the signal produced
⁵⁹⁴ compared to the charge of photoelectrons emitted by the photocathodes within the
⁵⁹⁵ PMT. To calibrate the signal of each PMT, the “relative” and “absolute” gain values are

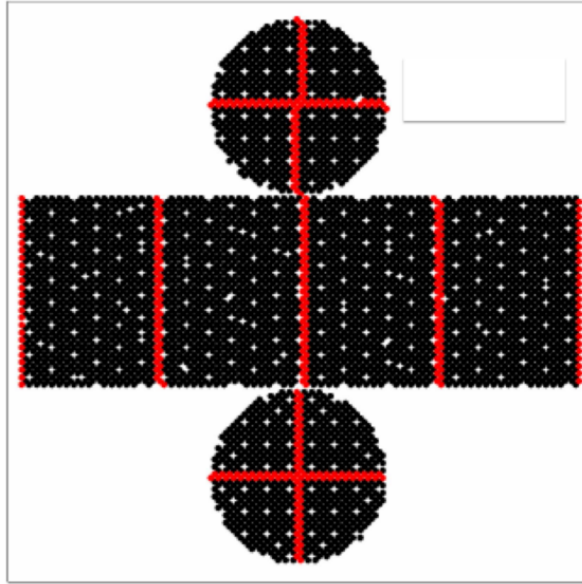


Figure 3.2: The location of “standard PMTs” (red) inside the SK detector. Taken from [86].

596 measured. The relative gain is the variation of gain among each of the PMTs whereas
 597 the absolute gain is the average gain of all PMTs.

598 The relative gain is calibrated as follows. A laser is used to generate two measure-
 599 ments: a high-intensity flash that illuminates every PMT with a sufficient number of
 600 photons, and a low-intensity flash in which only a small number of PMTs collect light.
 601 The first measurement creates an average charge, $Q_{obs}(i)$ on PMT i , whereas the second
 602 measurement ensures that each hit PMT only generates a single photoelectron. For the
 603 low-intensity measurement, the number of times each PMT records a charge larger
 604 than 1/4 photoelectrons, $N_{obs}(i)$, is counted. The values measured can be expressed as

$$\begin{aligned} Q_{obs}(i) &\propto I_H \times f(i) \times \epsilon(i) \times G(i), \\ N_{obs}(i) &\propto I_L \times f(i) \times \epsilon(i), \end{aligned} \tag{3.1}$$

605 Where I_H and I_L is the intensity of the high and low flashes, $f(i)$ is the acceptance
 606 efficiency of the i^{th} PMT, $\epsilon(i)$ is the product of the quantum and collection efficiency

607 of the i^{th} PMT and $G(i)$ is the gain of the i^{th} PMT. The relative gain for each PMT can
608 determined by taking the ratio of these quantities.

609 The absolute gain calibration is performed by observing fixed energy γ -rays of
610 $E_{\gamma} \sim 9\text{MeV}$ emitted isotropically from neutron capture on a NiCf source situated at
611 the center of the detector. This generates a photon yield of about 0.004 photoelec-
612 trons/PMT/event, meaning that $> 99\%$ of PMT signals are generated from single
613 photoelectrons. A charge distribution is generated by performing this calibration over
614 all PMTs, and the average value of this distribution is taken to be the absolute gain
615 value.

616 As mentioned in subsection 3.1.1, the average quantum and collection efficiency
617 for the SK detector is $\sim 21\%$ and $> 70\%$ respectively. However, these values do differ
618 between each PMT and need to be calibrated accordingly. Consequently, the NiCf
619 source is also used to calibrate the “quantum \times collection” efficiency (denoted “QE”)
620 value of each PMT. The NiCf low-intensity source is used as the PMT hit probability
621 is proportional to the QE ($N_{\text{obs}}(i) \propto \epsilon(i)$ in Equation 3.1). A Monte Carlo prediction
622 which includes photon absorption, scattering, and reflection is made to estimate the
623 number of photons incident on each PMT and the ratio of the number of predicted
624 to observed hits is calculated. The difference is attributed to the QE efficiency of that
625 PMT. This technique is extended to calculate the relative QE efficiency by normalizing
626 the average of all PMTs which removes the dependence on the light intensity.

627 Due to differing cable lengths and readout electronics, the timing response between
628 a photon hitting the PMT and the signal being captured by the data acquisition can be
629 different between each PMT. Due to threshold triggers (Described in subsection 3.1.3),
630 the time at which a pulse reaches a threshold is dependent upon the size of the pulse.
631 This is known as the ‘time-walk’ effect and also needs to be accounted for in each PMT.
632 To calibrate the timing response, a pulse of light with width 0.2ns is emitted into the

633 detector through a diffuser. Two-dimensional distributions of time and pulse height
634 (or charge) are made for each PMT and are used to calibrate the timing response. This
635 is performed in-situ during data taking with the light source pulsing at 0.03Hz.

636 The top/bottom water quality asymmetry is measured using the NiCf calibration
637 data and cross-referencing these results to the “standard PMTs”. The water attenuation
638 length is continuously measured by the rate of vertically-downgoing cosmic-ray
639 muons which enter via the top of the tank.

640 Dark noise is the phenomenon where a PMT registers a pulse that is consistent
641 with a single photoelectron emitted from photon detection despite the PMT being in
642 complete darkness. This is predominately caused by two processes. Firstly there is
643 intrinsic dark noise which is where photoelectrons gain enough thermal energy to be
644 emitted from the photocathode, and secondly, the radioactive decay of contaminants
645 inside the structure of the PMT. Typical dark noise rate for PMTs used within SK are
646 $O(3)$ kHz [87]. This is lower than the expected number of photons generated for a ‘high
647 energy event’ (As described in subsection 3.1.4) but instability in this value can cause
648 biases in reconstruction. Dark noise is related to the gain of a PMT and is calibrated
649 using hits inside a time window recorded before an event trigger [98].

650 3.1.3 Data Acquisition and Triggering

651 The analysis presented in this thesis only uses the SK-IV period of the SK experiment
652 so this subsection focuses on the relevant points of the data acquisition and triggering
653 systems to that SK period. The earlier data acquisition and triggering systems are
654 documented in [99, 100].

655 Before the SK-IV period started, the existing front-end electronics were replaced
656 with “QTC-Based Electrons with Ethernet, QBEE” systems [101]. When the QBEE

observes a signal above a 1/4 photoelectron threshold, the charge-to-time (QTC) converter generates a rectangular pulse. The start of the rectangular pulse indicates the time at which the analog photoelectron signal was received and the width of the pulse indicates the total charge integrated throughout the signal. This is then digitized by time-to-digital converters and sent to the “front-end” PCs. The digitized signal from every QBEE is then chronologically ordered and sent to the “merger” PCs. It is the merger PCs that apply the software trigger. Any triggered events are passed to the “organizer” PC. This sorts the data stream of multiple merger PCs into chronologically ordered events which are then saved to disk. The schematic of data flow from PMTs to disk is illustrated in Figure 3.3.

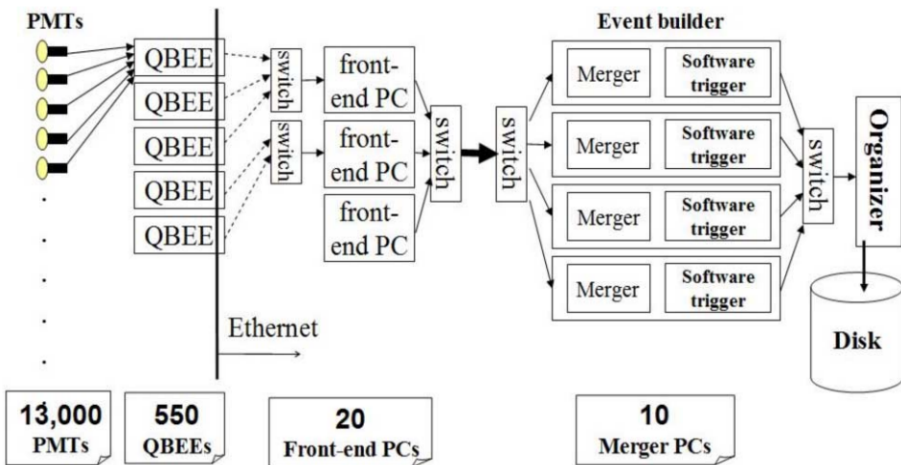


Figure 3.3: Schematic view of the data flow through the data acquisition and online system. Taken from [102].

The software trigger (described in [103]) operates by determining the number of PMT hits within a 200ns sliding window, N_{200} . This window coincides with the maximum time that a Cherenkov photon would take to traverse the length of the SK tank [100]. For lower energy events that generate fewer photons, this technique is useful for eliminating background processes like dark noise and radioactive decay which would be expected to separate in time. When the value of N_{200} exceeds some threshold, a software trigger is issued. There are several trigger thresholds used within

the SK-IV period which are detailed in Table 3.2. If one of these thresholds is met, the PMT hits within an extended time window are also read out and saved to disk. In the special case of an event that exceeds the SHE trigger but does not exceed the OD trigger, the AFT trigger looks for delayed coincidences of 2.2MeV gamma rays emitted from neutron capture in a $535\mu\text{s}$ window after the SHE trigger. A similar but more complex “Wideband Intelligent Trigger (WIT)” has been deployed and is described in [104].

| Trigger | Acronym | Condition | Extended time window (μs) |
|-------------------|---------|----------------|--|
| Super Low Energy | SLE | >34/31 hits | 1.3 |
| Low Energy | LE | >47 hits | 40 |
| High Energy | HE | >50 hits | 40 |
| Super High Energy | SHE | >70/58 hits | 40 |
| Outer Detector | OD | >22 hits in OD | N/A |

Table 3.2: The trigger thresholds and extended time windows saved around an event which were utilised throughout the SK-IV period. The exact thresholds can change and the values listed here represent the thresholds at the start and end of the SK-IV period.

3.1.4 Cherenkov Radiation

Cherenkov light is emitted from any highly energetic charged particle traveling with relativistic velocity, β , greater than the local speed of light in a medium [105]. Cherenkov light is formed at the surface of a cone with characteristic pitch angle,

$$\cos(\theta) = \frac{1}{\beta n}. \quad (3.2)$$

where n is the refractive index of the medium. Consequently, the Cherenkov momentum threshold, P_{thres} , is dependent upon the mass, m , of the charged particle moving through the medium,

$$P_{thres} = \frac{m}{\sqrt{n^2 - 1}} \quad (3.3)$$

For water, where $n = 1.33$, the Cherenkov threshold momentum and energy for various particles are given in Table 3.3. In contrast, γ -rays are detected indirectly via the combination of photons generated by Compton scattering and pair production. The threshold for detection in the SK detector is typically higher than the threshold for photon production. This is due to the fact that the attenuation of photons in the water means that typically $\sim 75\%$ of Cherenkov photons reach the ID PMTs. Then the collection and quantum efficiencies described in subsection 3.1.1 result in the number of detected photons being lower than the number of photons which reach the PMTs.

| Particle | Threshold Momentum (MeV) | Threshold Energy (MeV) |
|----------|--------------------------|------------------------|
| Electron | 0.5828 | 0.7751 |
| Muon | 120.5 | 160.3 |
| Pion | 159.2 | 211.7 |
| Proton | 1070.0 | 1423.1 |

Table 3.3: The threshold momentum and energy for a particle to generate Cherenkov light in ultrapure water, as calculated in Equation 3.2 in ultrapure water which has refractive index $n = 1.33$.

The Frank-Tamm equation [106] describes the relationship between the number of Cherenkov photons generated per unit length, dN/dx , the wavelength of the photons generated, λ , and the relativistic velocity of the charged particle,

$$\frac{d^2N}{dxd\lambda} = 2\pi\alpha \left(1 - \frac{1}{n^2\beta^2}\right) \frac{1}{\lambda^2}. \quad (3.4)$$

where α is the fine structure constant. For a 100MeV momentum electron, approximately 330 photons will be produced per centimeter in the $300\text{nm} \leq \lambda \leq 700\text{nm}$ region which the ID PMTs are most sensitive to [87].

3.2 The Tokai to Kamioka Experiment

The Tokai to Kamioka (T2K) experiment is a long-baseline neutrino oscillation experiment located in Japan. Proposed in the early 2000s [107, 108] to replace K2K [109], T2K was designed to observe electron neutrino appearance whilst precisely measuring the oscillation parameters associated with muon neutrino disappearance [110]. The experiment consists of a neutrino beam generated at the Japan Proton Accelerator Research Complex (J-PARC), a suite of near detectors situated 280m from the beam target, and the Super Kamiokande far detector positioned at a 295km baseline. The cross-section view of the T2K experiment is drawn in Figure 3.4.

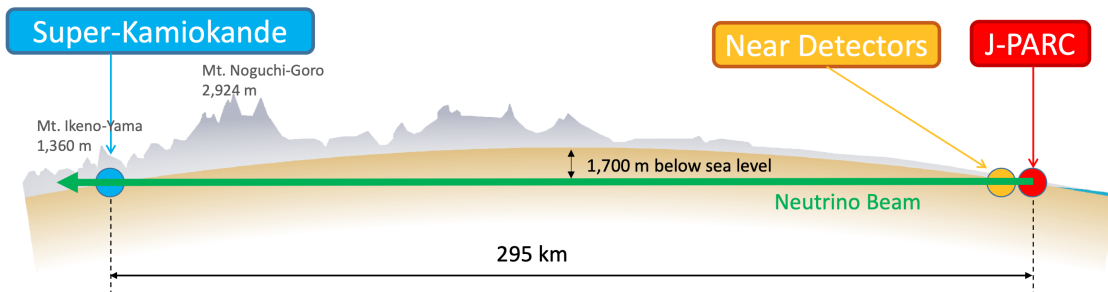


Figure 3.4: The cross-section view of the Tokai to Kamioka experiment illustrating the beam generation facility at J-PARC, the near detector situated at a baseline of 280m and the Super Kamiokande far detector situated 295km from the beam target.

⁷¹¹ The T2K collaboration makes world-leading measurements of the $\sin^2(\theta_{23})$, Δm_{23}^2 ,

⁷¹² and δ_{CP} oscillation parameters. Improvements in the precision and accuracy of param-

⁷¹³ eter estimates are still being made by including new data samples and developing the

⁷¹⁴ models which describe the neutrino interactions and detector responses [111]. Electron

⁷¹⁵ neutrino appearance was first observed at T2K in 2014 [112] with 7.3σ significance.

⁷¹⁶ The near detectors provide constraints on the beam flux and cross-section model

⁷¹⁷ parameters used within the oscillation analysis by observing the unoscillated neutrino

⁷¹⁸ beam. There are a host of detectors situated in the near detector hall (As illustrated

⁷¹⁹ in Figure 3.5): ND280 (subsection 3.2.2), INGRID (subsection 3.2.3), NINJA [113],

⁷²⁰ WAGASCI [114], and Baby-MIND [115]. The latter three are not currently used within

⁷²¹ the oscillation analysis presented within this thesis.

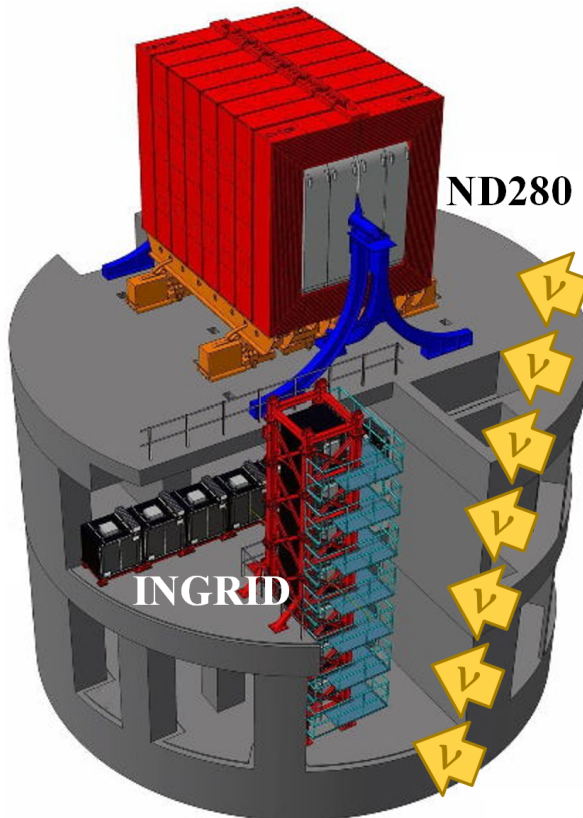


Figure 3.5: The near detector suite for the T2K experiment showing the ND280 and INGRID detectors. The distance between the detectors and the beam target is 280m.

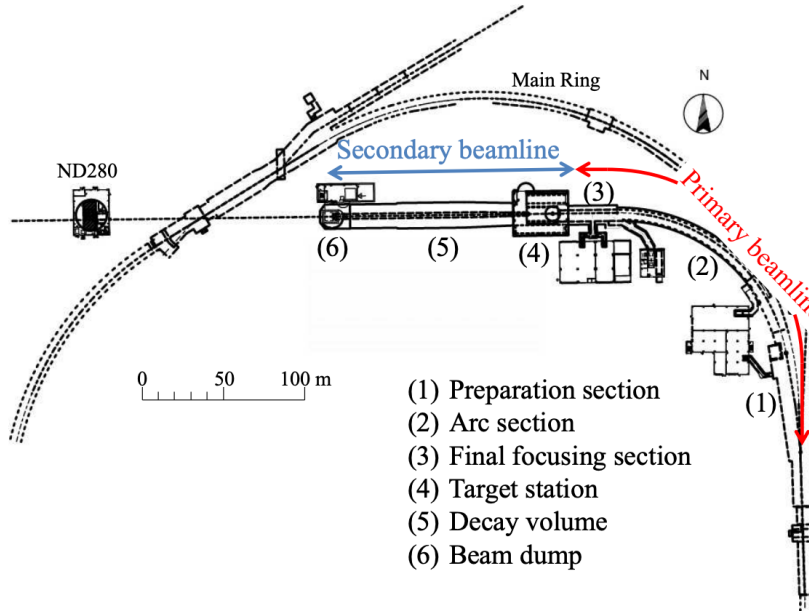
Whilst this thesis presents the ND280 in terms of its purpose for the oscillation analysis, the detector can also make many cross-section measurements at neutrino energies of $O(1)$ GeV for the different targets within the detector [116, 117]. These measurements are of equal importance as they can lead the way in determining the model parameters used in the interaction models for the future high-precision era of neutrino physics.

DB: Discuss BANFF, PTheta, MaCh3 and covariance

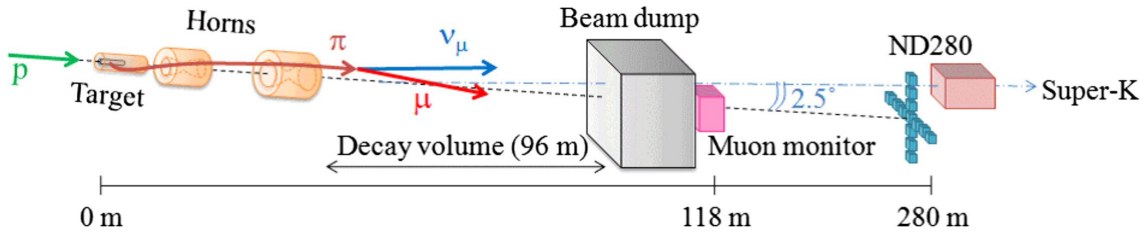
3.2.1 The Neutrino Beam

The neutrino beam used within the T2K experiment is described in [59, 118] and summarised below. The accelerating facility at J-PARC is composed of two sections; the primary and secondary beamlines. Figure 3.6 illustrates a schematic of the beamline, focusing mostly on the components of the secondary beamline. The primary beamline has three accelerators that progressively accelerate protons; a linear accelerator, a rapid-cycling synchrotron, and the main-ring (MR) synchrotron. Once fully accelerated by the MR, the protons have a kinetic energy of 30GeV. Eight bunches of these protons, separated by 500ns, are extracted per “spill” from the MR and directed towards a graphite target (a rod of length 91.4cm and diameter 2.6cm). Spills are extracted at 0.5Hz with $\sim 3 \times 10^{14}$ protons contained per spill.

The secondary beamline consists of three main components: the target station, the decay volume, and the beam dump. The target station is comprised of the target, beam monitors, and three magnetic focusing horns. The proton beam interacts with the graphite target to form a secondary beam of mostly pions and kaons. The secondary beam travels through a 96m long decay volume, generating neutrinos through the following decays [59],



(a) Primary and secondary beamline



(b) Secondary beamline

Figure 3.6: Top panel: Bird's eye view of the most relevant part of primary and secondary beamline used within the T2K experiment. The primary beamline is the main-ring proton synchrotron, kicker magnet, and graphite target. The secondary beamline consists of the three focusing horns, decay volume, and beam dump. Figure taken from [118]. Bottom panel: The side-view of the secondary beamline including the focusing horns, beam dump and neutrino detectors. Figure taken from [119].

$$\begin{array}{ll}
 \pi^+ \rightarrow \mu^+ + \nu_\mu & \pi^- \rightarrow \mu^- + \bar{\nu}_\mu \\
 K^+ \rightarrow \mu^+ + \nu_\mu & K^- \rightarrow \mu^- + \bar{\nu}_\mu \\
 \rightarrow \pi^0 + e^+ + \nu_e & \rightarrow \pi^0 + e^- + \bar{\nu}_e \\
 \rightarrow \pi^0 + \mu^+ + \nu_\mu & \rightarrow \pi^0 + \mu^- + \bar{\nu}_\mu \\
 K_L^0 \rightarrow \pi^- + e^+ + \nu_e & K_L^0 \rightarrow \pi^+ + e^- + \bar{\nu}_e \\
 \rightarrow \pi^- + \mu^+ + \nu_\mu & \rightarrow \pi^+ + \mu^- + \bar{\nu}_\mu \\
 \mu^+ \rightarrow e^+ + \bar{\nu}_\mu + \nu_e & \mu^- \rightarrow e^- + \nu_\mu + \bar{\nu}_e
 \end{array}$$

The electrically charged component of the secondary beam is focused towards the far detector by the three magnetic horns. These horns direct charged particles of a particular polarity towards SK whilst defocusing the oppositely charged particles. This allows a mostly neutrino or mostly antineutrino beam to be used within the experiment, denoted as “forward horn current (FHC)” or “reverse horn current (RHC)” respectively.

Figure 3.7 illustrates the different contributions to the FHC and RHC neutrino flux.

The low energy flux is dominated by the decay of pions whereas kaon decay becomes the dominant source of neutrinos for $E_\nu > 3\text{GeV}$. The “wrong-sign” component, which is the $\bar{\nu}_\mu$ background in a ν_μ beam, and the intrinsic irreducible ν_e background, are predominantly due to muon decay for $E_\nu < 2\text{GeV}$. As the antineutrino production cross-section is smaller than the neutrino cross-section, the wrong-sign component is more dominant in the RHC beam as compared to that in the FHC beam.

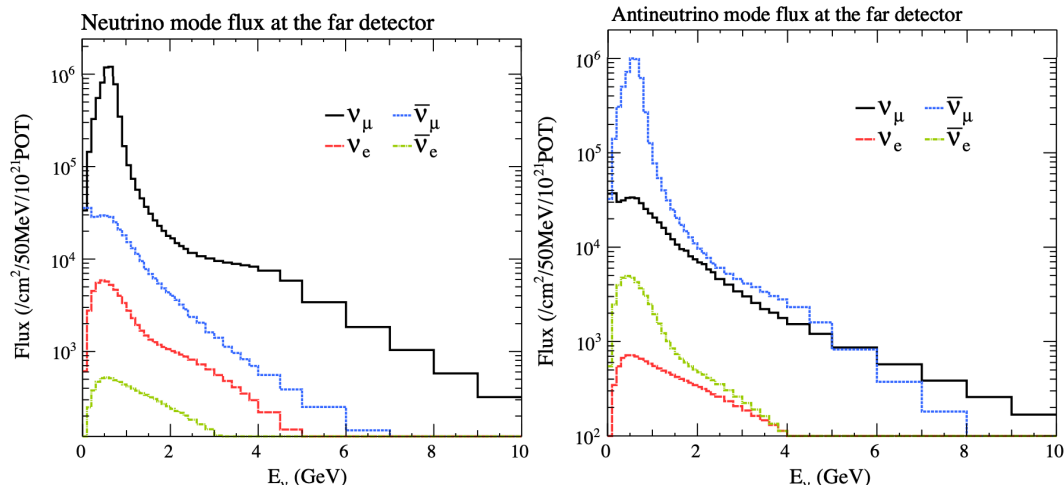


Figure 3.7: The Monte Carlo prediction of the energy spectrum for each flavour of neutrino (ν_e , $\bar{\nu}_e$, ν_μ and $\bar{\nu}_\mu$) in the neutrino dominated beam FHC mode (Left) and antineutrino dominated beam RHC mode (Right) expected at SK. Taken from [120].

The beam dump, situated at the end of the decay volume, stops all charged particles other than highly energetic muons ($p_\mu > 5\text{GeV}$). The MuMon detector monitors the

762 penetrating muons to determine the beam direction and intensity which is used to
763 constrain some of the beam flux systematics within the analysis [119, 121].

764 The T2K experiment uses an off-axis beam to narrow the neutrino energy distribution.
765 This was the first implementation of this technique in a long-baseline neutrino
766 oscillation experiment after its original proposal [122]. Pion decay, $\pi \rightarrow \mu + \nu_\mu$, is a
767 two-body decay. Consequently, the neutrino energy, E_ν , can be determined based on
768 the pion energy, E_π , and the angle at which the neutrino is emitted, θ ,

$$E_\nu = \frac{m_\pi^2 - m_\mu^2}{2(E_\pi - p_\pi \cos(\theta))}, \quad (3.5)$$

769 where m_π and m_μ are the mass of the pion and muon respectively. For a fixed
770 energy pion, the neutrino energy distribution is dependent upon the angle at which the
771 neutrinos are observed from the initial pion beam direction. For the 295km baseline at
772 T2K, $E_\nu = 0.6\text{GeV}$ maximises the electron neutrino appearance probability, $P(\nu_\mu \rightarrow \nu_e)$,
773 whilst minimising the muon disappearance probability, $P(\nu_\mu \rightarrow \nu_\mu)$. Figure 3.8
774 illustrates the neutrino energy distribution for a range of off-axis angles, as well as the
775 oscillation probabilities most relevant to T2K.

776 3.2.2 The Near Detector at 280m

777 Whilst all the near detectors are situated in the same “pit” located at 280m from the
778 beamline, the “ND280” detector is the off-axis detector which is situated at the same
779 off-axis angle as the Super-Kamiokande far detector. It has two primary functions;
780 firstly it measures the neutrino flux and secondly it counts the event rates of different
781 types of neutrino interactions. Both of these constrain the flux and cross-section

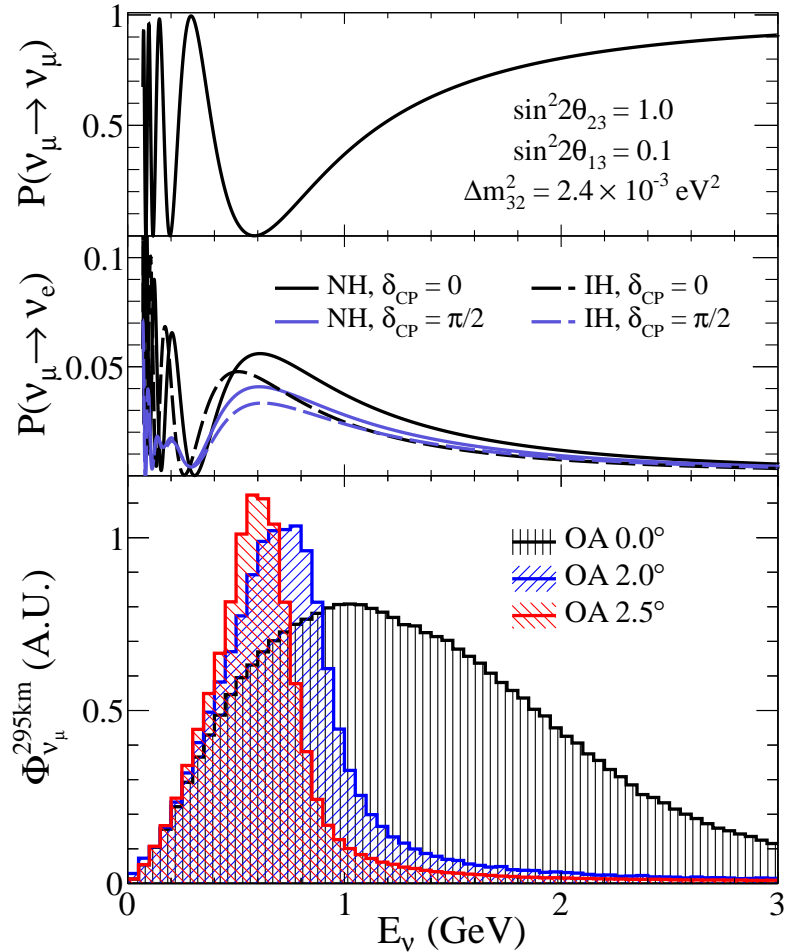


Figure 3.8: Top panel: T2K muon neutrino disappearance probability as a function of neutrino energy. Middle panel: T2K electron neutrino appearance probability as a function of neutrino energy. Bottom panel: The neutrino flux distribution for three different off-axis angles (Arbitrary units) as a function of neutrino energy.

782 systematics invoked within the model for a more accurate prediction of the expected
 783 event rate at the far detector.

784 As illustrated in Figure 3.9, the ND280 detector consists of several sub-detectors.
 785 The most important part of the detector for this analysis is the tracker region. This is
 786 comprised of two time projection chambers (TPCs) sandwiched between three fine
 787 grain detectors (FGDs). The FGDs contain both hydrocarbon plastics and water tar-
 788 gets for neutrino interactions and provide track reconstruction near the interaction
 789 vertex. The emitted charged particles can then propagate into the TPCs which pro-
 790 vide particle identification and momentum reconstruction. The FGDs and TPCs are

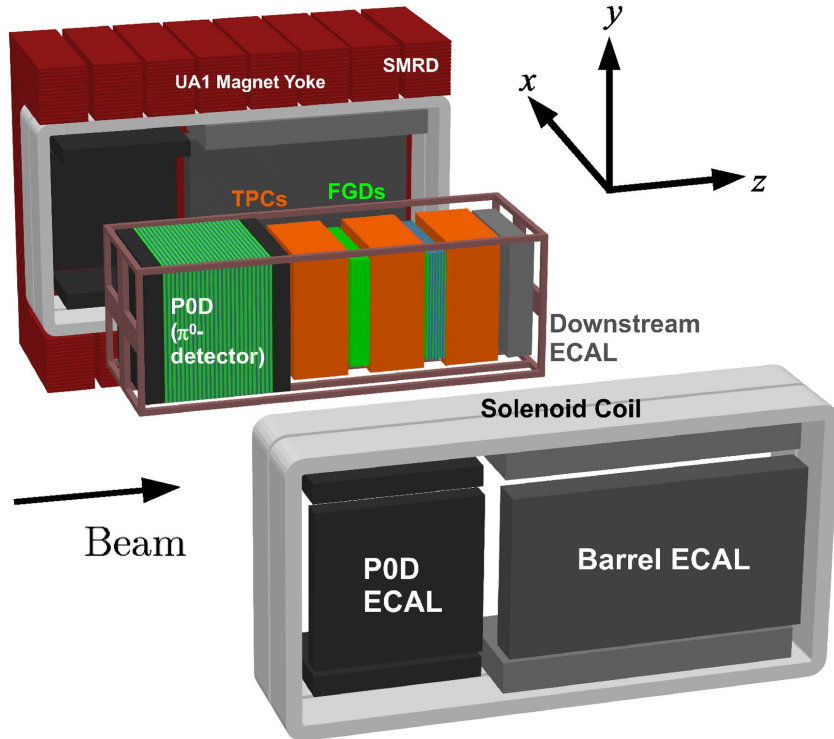


Figure 3.9: The components of the ND280 detector. The neutrino beam travels from left to right. Taken from [118].

791 further described in subsubsection 3.2.2.1 and subsubsection 3.2.2.2 respectively. The
 792 electromagnetic calorimeter (ECAL) encapsulates the tracker region alongside the π^0
 793 detector (P0D). The ECAL measures the deposited energy from photons emitted from
 794 interactions within the FGD. The P0D constrains the cross-section of neutral current
 795 interactions which generate neutral pions, which is one of the largest backgrounds in
 796 the electron neutrino appearance oscillation channel. The P0D and ECAL detectors
 797 are detailed in subsubsection 3.2.2.3 and subsubsection 3.2.2.4 respectively. The entire
 798 detector is located within a large yoke magnet which produces a 0.2T magnetic field.
 799 This design of the magnet also includes a scintillating detector called the side muon
 800 range detector (SMRD) which is used to track high-angle muons as well as acting as a
 801 cosmic veto. The SMRD is described in subsubsection 3.2.2.5.

802 3.2.2.1 Fine Grained Detectors

803 The T2K tracker region is comprised of two fine grained detectors (FGD) and three
804 Time Projection Chambers (TPC). A detailed description of the FGD design, construc-
805 tion, and assembly is found in [123] and summarised below. The FGDs are the primary
806 target for neutrino interactions with a mass of 1.1 tonnes per FGD. Alongside this,
807 the FGDs are designed to be able to track short-range particles which do not exit the
808 FGD. Typically, short-range particles are low momentum and are observed as tracks
809 that deposit a large amount of energy per unit length. This means the FGD needs
810 good granularity to resolve these particles. The FGDs have the best timing resolution
811 ($\sim 3\text{ns}$) of any of the sub-detectors of the ND280 detector. As such, the FGDs are
812 used for time of flight measurements to distinguish forward going positively charged
813 particles from backward going negatively charged particles. Finally, any tracks which
814 pass through multiple sub-detectors are required to be track matched to the FGD.

815 Both FGDs are made from square scintillator planes of side length 186cm and
816 width 2.02cm. Each plane consists of two layers of 192 scintillator bars in an X or Y
817 orientation. A wavelength shifting fiber is threaded through the center of each bar and
818 is read out by a multi-pixel photon counter (MPPC). FGD1 is the most upstream of
819 the two FGDs and contains 15 planes of carbon plastic scintillator which is a common
820 target in external neutrino scattering data. As the far detector is a pure water target, 7
821 of the 15 scintillator planes in FGD2 have been replaced with a hybrid water-scintillator
822 target. Due to the complexity of the nucleus, nuclear effects can not be extrapolated
823 between different nuclei. Therefore having the ability to take data on one target which
824 is the same as external data and another target which is the same as the far detector
825 target is beneficial for reliable model parameter estimates.

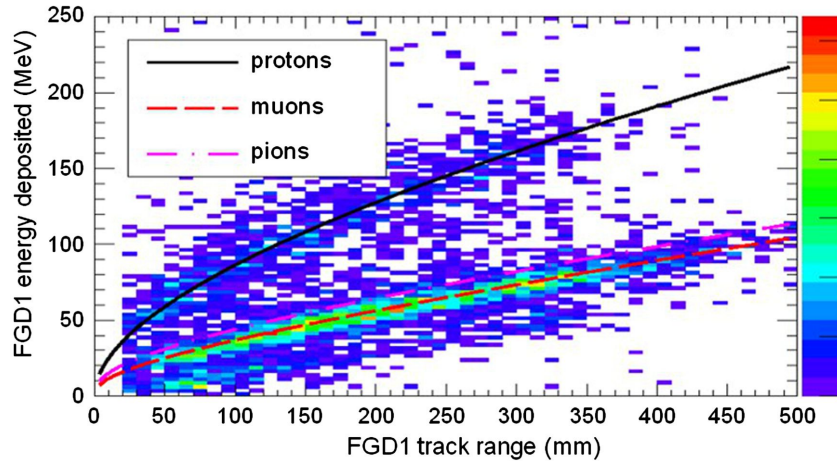


Figure 3.10: Comparison of data to Monte Carlo prediction of integrated deposited energy as a function of track length for particles that stopped in FGD1. Taken from [123].

The integrated deposited energy is used for particle identification. The FGD can distinguish protons from other charged particles by comparing the integrated deposited energy from data to Monte Carlo prediction as seen in Figure 3.10.

3.2.2.2 Time Projection Chambers

The majority of particle identification and momentum measurements within ND280 are provided by three Time Projection Chambers (TPCs) [124]. The TPCs are located on either side of the FGDs. They are located inside of the magnetic field meaning the momentum of a charged particle can be determined from the bending of the track.

Each TPC module consists of two gas-tight boxes, as shown in Figure 3.11, which are made of non-magnetic material. The outer box is filled with CO₂ which acts as an electrical insulator between the inner box and the ground. The inner box forms the field cage which produces a uniform electric drift field of $\sim 275\text{V/cm}$ and is filled with an argon gas mixture. Charged particles moving through this gas mixture ionize the gas and the ionised charge is drifted towards micromegas detectors which measure the ionization charge. The time and position information in the readout allows a three-dimensional image of the neutrino interaction.

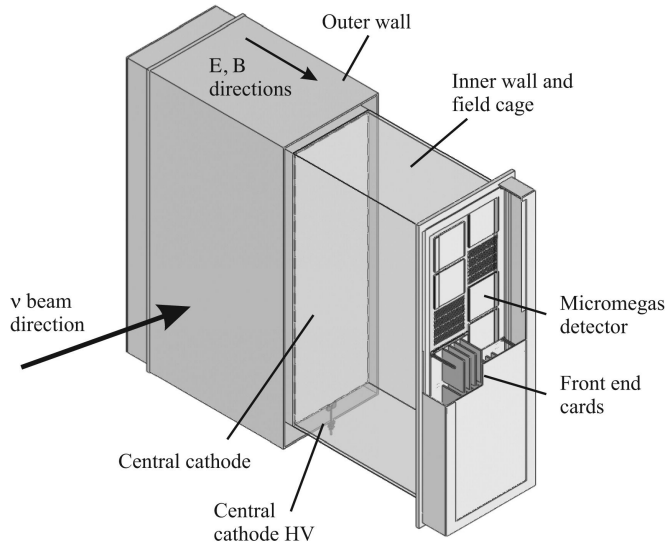


Figure 3.11: Schematic design of a Time Projection Chamber detector. Taken from [124].

The particle identification of tracks that pass through the TPCs is performed using

dE/dx measurements. Figure 3.12 illustrates the data to Monte Carlo distributions of the energy lost by a charged particle passing through the TPC as a function of the reconstructed particle momentum. The resolution is $7.8 \pm 0.2\%$ meaning that electrons and muons can be distinguished. This allows reliable measurements of the intrinsic ν_e component of the beam.

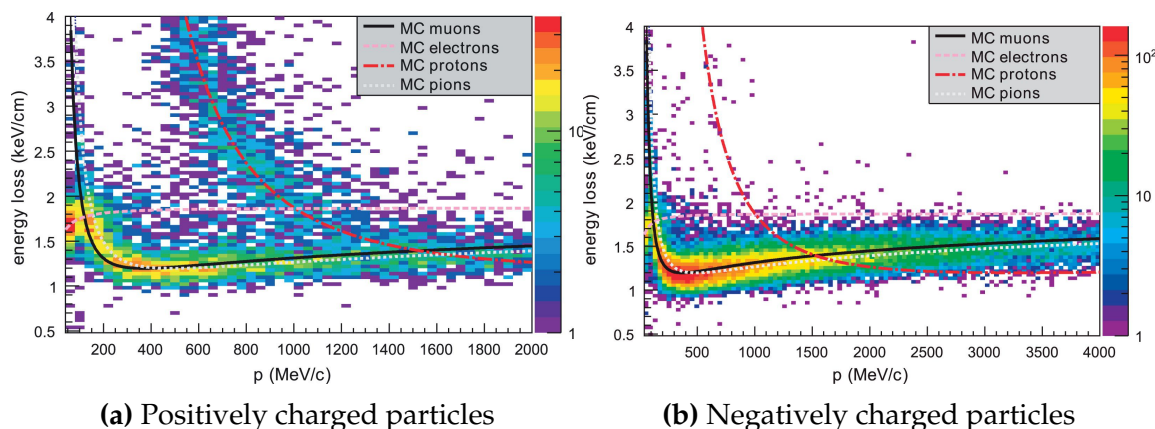


Figure 3.12: The distribution of energy loss as a function of reconstructed momentum for charged particles passing through the TPC, comparing data to Monte Carlo prediction. Taken from [124].

⁸⁴⁸ 3.2.2.3 π^0 Detector

⁸⁴⁹ If one of the γ -rays from a $\pi^0 \rightarrow 2\gamma$ decay is missed at the far detector, the recon-
⁸⁵⁰ struction will determine that event to be a charge current ν_e -like event. This is one of
⁸⁵¹ the main backgrounds hindering the electron neutrino appearance searches. The π^0
⁸⁵² detector (P0D) measures the cross-section of the neutral current induced neutral pion
⁸⁵³ production on a water target to constrain this background.

⁸⁵⁴ The P0D is a cube of approximately 2.5m length consisting of layers of scintillating
⁸⁵⁵ bars, brass and lead sheets, and water bags as illustrated in Figure 3.13. Two electro-
⁸⁵⁶ magnetic calorimeters are positioned at the most upstream and most downstream
⁸⁵⁷ position in the sub-detector and the water target is situated in between them. The
⁸⁵⁸ scintillator layers are built from two triangular bars orientated in opposite directions
⁸⁵⁹ to form a rectangular layer. Each triangular scintillator bar is threaded with optical
⁸⁶⁰ fiber which is read out by MPPCs. The high-Z brass and lead regions produce electron
⁸⁶¹ showers from the photons emitted in π^0 decay.

⁸⁶² The sub-detector can generate measurements of NC1 π^0 cross-sections on a water
⁸⁶³ target by measuring the event rate both with and without the water target, with the
⁸⁶⁴ cross-section on a water target being determined as the difference. The total active
⁸⁶⁵ mass is 16.1 tonnes when filled with water and 13.3 tonnes when empty.

⁸⁶⁶ 3.2.2.4 Electromagnetic Calorimeter

⁸⁶⁷ The electromagnetic calorimeter [126] (ECal) encapsulates the P0D and tracking sub-
⁸⁶⁸ detectors. Its primary purpose is to aid π^0 reconstruction from any interaction in
⁸⁶⁹ the tracker. To do this, it measures the energy and direction of photon showers from
⁸⁷⁰ $\pi^0 \rightarrow 2\gamma$ decay. It can also distinguish pion and muon tracks depending on the shape
⁸⁷¹ of the photon shower deposited.

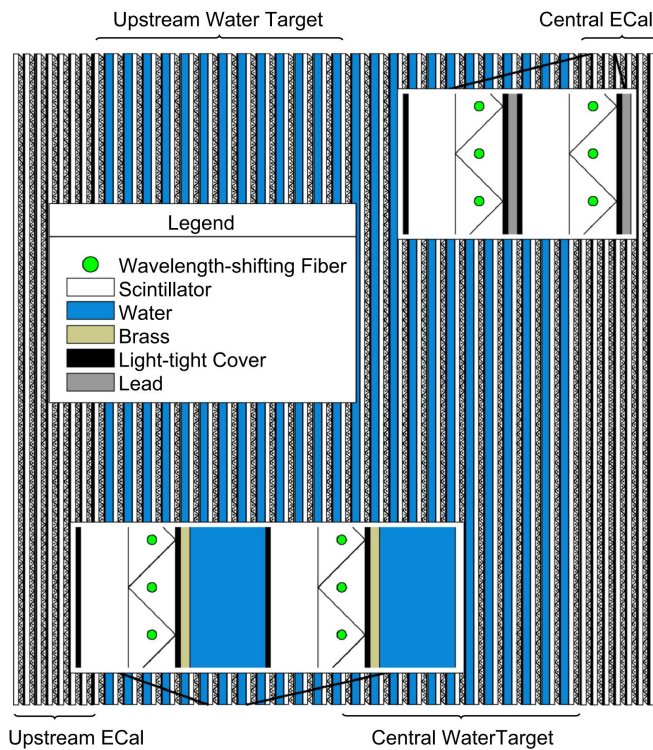


Figure 3.13: A schematic of the P0D side-view. Taken from [125].

872 The ECal is comprised of three sections; the P0D ECal which surrounds the P0D,
 873 the barrel ECal which encompasses the tracking region, and the downstream ECal
 874 which is situated downstream of the tracker region. The barrel and downstream
 875 ECals are tracking calorimeters that focus on electromagnetic showers from high-angle
 876 particles emitted from the tracking sub-detectors. Particularly in the TPC, high-angle
 877 tracks (those which travel perpendicularly to the beam-axis) can travel along a single
 878 scintillator bar resulting in very few hits. The width of the barrel and downstream
 879 ECal corresponds to ~ 11 electron radiation lengths to ensure a significant amount of
 880 the π^0 energy is contained. As the P0D has its own calorimetry which reconstructs
 881 showers, the P0D ECal determines the energy which escapes the P0D.

882 Each ECal is constructed of multiple layers of scintillating bars sandwiched between
 883 lead sheets. The scintillating bars are threaded with optical fiber and read out by
 884 MPPCs. Each sequential layer of the scintillator is orientated perpendicular to the
 885 previous which allows a three dimensional event reconstruction. The target mass

886 of the P0D ECal, barrel ECal, and downstream ECal are 1.50, 4.80 and 6.62 tonnes
887 respectively.

888 **3.2.2.5 Side Muon Range Detector**

889 As illustrated in Figure 3.9, the ECal, FGDs, P0D, and TPCs are enclosed within the
890 UA1 magnet. Originally designed for the NOMAD [127] experiment and reconditioned
891 for use in the T2K experiment [128], the UA1 magnet provides a uniform horizontal
892 magnetic field of 0.2T with an uncertainty of 2×10^{-4} T.

893 Built into the UA1 magnet, the side muon range detector (SMRD) [129] monitors
894 high-energy muons which leave the tracking region and permeate through the ECal.
895 It additionally acts as a cosmic muon veto and trigger.

896 **3.2.3 The Interactive Neutrino GRID**

897 The Interactive Neutrino GRID (INGRID) detector is situated within the same “pit” as
898 the other near detectors. It is aligned with the beam in the “on-axis” position and mea-
899 sures the beam direction, spread, and intensity. The detector was originally designed
900 with 16 identical modules [118] (two modules have since been decommissioned) and a
901 “proton” module. The design of the detector is cross-shaped with length and height
902 10m × 10m as illustrated in Figure 3.14.

903 Each module is composed of iron sheets interlaced with eleven tracking scintillator
904 planes for a total target mass of 7.1 tonnes per module. The scintillator design is an X-Y
905 pattern of 24 bars in both orientations, where each bar contains wave-length shifting
906 fibers which are connected to multi-pixel photon counters (MPPCs). Each module is
907 encapsulated inside veto planes to aid the rejection of charged particles entering the
908 module.

909 The proton module is different from the other modules in that it consists of entirely
 910 scintillator planes with no iron target. The scintillator bars are also smaller than those
 911 used in the other modules to increase the granularity of the detector and improve
 912 tracking capabilities. The module sits in the center of the beamline and is designed to
 913 give precise measurements of quasi-elastic charged current interactions to evaluate
 914 the performance of the Monte Carlo simulation of the beamline.

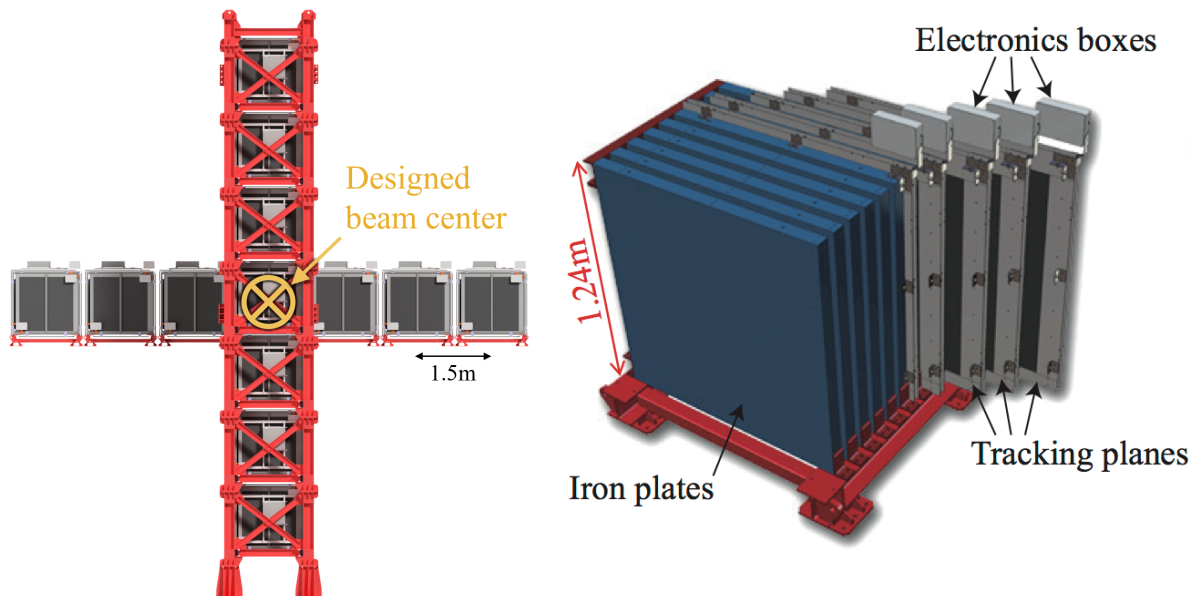


Figure 3.14: Left panel: The Interactive Neutrino GRID on-axis Detector. 14 modules are arranged in a cross-shape configuration, with the center modules being directly aligned with the on-axis beam. Right panel: The layout of a single module of the INGRID detector. Both figures are recreated from [118].

915 The INGRID detector can measure the beam direction to an uncertainty of 0.4mrad
 916 and the beam center within a resolution of 10cm [118]. The beam direction in both the
 917 vertical and horizontal directions is discussed in [130] and it is found to be in good
 918 agreement with the MUMON monitor described in subsection 3.2.1.

₉₁₉ **Chapter 4**

₉₂₀ **Bayesian Statistics and Markov Chain**
₉₂₁ **Monte Carlo Techniques**

₉₂₂ This thesis presents a Bayesian oscillation analysis. To extract the oscillation parameters,
₉₂₃ a Markov Chain Monte Carlo (MCMC) method is used. This chapter explains
₉₂₄ the theory of how parameter estimates can be determined using this technique and
₉₂₅ condenses the material found in the literature [131–134].

₉₂₆ The oscillation parameter determination presented within this thesis is built upon
₉₂₇ a simultaneous fit to neutrino beam data in the near detector, beam data at SK and
₉₂₈ atmospheric data at SK. In total, there are four oscillation parameters of interest
₉₂₉ ($\sin^2(\theta_{23})$, $\sin^2(\theta_{13})$, Δm_{23}^2 , and δ_{CP}), two oscillation parameters to which this study
₉₃₀ will not be sensitive ($\sin^2(\theta_{12})$, Δm_{12}^2) and many nuisance parameters that control the
₉₃₁ systematic uncertainty models invoked within this study.

₉₃₂ The MCMC technique generates a multi-dimensional probability distribution across
₉₃₃ all of the model parameters used in the fit. To determine the parameter estimate of a
₉₃₄ single parameter, this multi-dimensional object is integrated over all other parameters.
₉₃₅ This process is called Marginalisation and is further described in subsection 4.3.1.
₉₃₆ Monte Carlo techniques approximate the probability distribution of each parameter
₉₃₇ within the limit of generating infinite samples. As ever, generating a large number of
₉₃₈ samples is time and resource-dependent. Therefore, an MCMC technique is utilised
₉₃₉ within this analysis to reduce the required number of steps to sufficiently sample the
₉₄₀ parameter space. This technique is described in further detail in subsection 4.2.1.

941 4.1 Bayesian Statistics

942 Bayesian inference treats observable data, D , and model parameters, $\vec{\theta}$, on equal
943 footing such that a probability model of both data and parameters is required. This is
944 the joint probability distribution $P(D, \vec{\theta})$ and can be described by the prior distribution
945 for model parameters $P(\vec{\theta})$ and the likelihood of the data given the model parameters
946 $P(D|\vec{\theta})$,

$$P(D, \vec{\theta}) = P(D|\vec{\theta})P(\vec{\theta}). \quad (4.1)$$

947 The prior distribution, $P(\vec{\theta})$, describes all previous knowledge about the parameters
948 within the model. For example, if the risk of developing health problems is known
949 to increase with age, the prior distribution would describe the increase. For the
950 purpose of this analysis, the prior distribution is typically the best-fit values taken
951 from external data measurements with a Gaussian uncertainty. The prior distribution
952 can also contain correlations between model parameters. In an analysis using Monte
953 Carlo techniques, the likelihood of measuring some data assuming some set of model
954 parameters is calculated by comparing the Monte Carlo prediction generated at that
955 particular set of model parameters to the data.

956 It is parameter estimation that is important for this analysis and as such, we apply
957 Bayes' theorem [135] to calculate the probability for each parameter to have a certain
958 value given the observed data, $P(\vec{\theta}|D)$, which is known as the posterior distribution
959 (often termed the posterior). This can be expressed as

$$P(\vec{\theta}|D) = \frac{P(D|\vec{\theta})P(\vec{\theta})}{\int P(D|\vec{\theta})P(\vec{\theta})d\vec{\theta}}. \quad (4.2)$$

960 The denominator in Equation 4.2 is the integral of the joint probability distribution
 961 over all values of all parameters used within the fit. For brevity, we say that the
 962 posterior distribution is

$$P(\vec{\theta}|D) \propto P(D|\vec{\theta})P(\vec{\theta}). \quad (4.3)$$

963 In subsection 4.3.1, we see that for the cases used within this analysis, it is reason-
 964 able to know the posterior to some normalisation constant.

965 **4.2 Monte Carlo Simulation**

966 Monte Carlo techniques are used to numerically solve a complex problem that does
 967 not necessarily have an analytical solution. These techniques rely on building a large
 968 ensemble of samples from an unknown distribution and then using the ensemble to
 969 approximate the properties of the distribution.

970 An example that uses Monte Carlo techniques is to calculate the area underneath
 971 a curve. For example, take the problem of calculating the area under a straight line
 972 with gradient $M = 0.4$ and intercept $C = 1.0$. Analytically, one can calculate the area
 973 under the line is equal to 30 units for $0 \leq x \leq 10$. Using Monte Carlo techniques,
 974 one can calculate the area under this line by throwing many random values for the x
 975 and y components of each sample and then calculating whether that point falls below

the line. The area can then be calculated by the ratio of points below the line to the total number of samples thrown multiplied by the total area in which samples were scattered. The study is shown in Figure 4.1 highlights this technique and finds the area under the curve to be 29.9 compared to an analytical solution of 30.0. The deviation of the numerical to analytical solution can be attributed to the number of samples used in the study. The accuracy of the approximation in which the properties of the Monte Carlo samples replicate those of the desired distribution is dependent on the number of samples used. Replicating this study with a differing number of Monte Carlo samples used in each study (As shown in Figure 4.2) highlights how the Monte Carlo techniques are only accurate within the limit of a high number of samples.

Whilst the above example has an analytical solution, these techniques are just as applicable to complex solutions. Clearly, any numerical solution is only as useful as its efficiency. As discussed, the accuracy of the Monte Carlo technique is dependent upon the number of samples generated to approximate the properties of the distribution. Furthermore, if the positions at which the samples are evaluated are not ‘cleverly’ picked, the efficiency of the Monte Carlo technique significantly drops. Given the example in Figure 4.1, if the region in which the samples are scattered significantly extends passed the region of interest, many calculations will be calculated but do not add to the ability of the Monte Carlo technique to achieve the correct result. For instance, any sample evaluated at a $y \geq 5$ could be removed without affecting the final result. This does bring in an aspect of the ‘chicken and egg’ problem in that to achieve efficient sampling, one needs to know the distribution beforehand.

4.2.1 Markov Chain Monte Carlo

This analysis utilises a multi-dimensional probability distribution, with some dimensions being significantly more constrained than others. This could be from prior

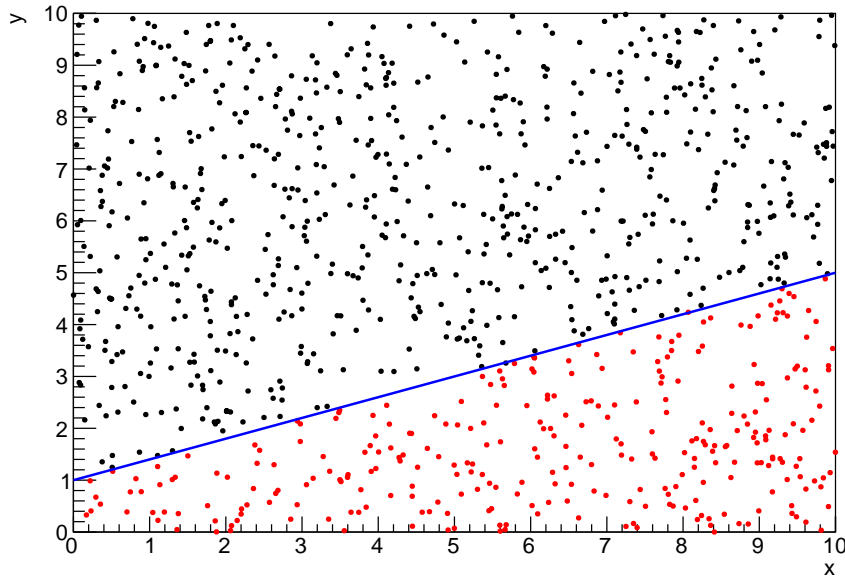


Figure 4.1: Example of using Monte Carlo techniques to find the area under the blue line. The gradient and intercept of the line are 0.4 and 1.0 respectively. The area found to be under the curve using one thousand samples is 29.9 units.

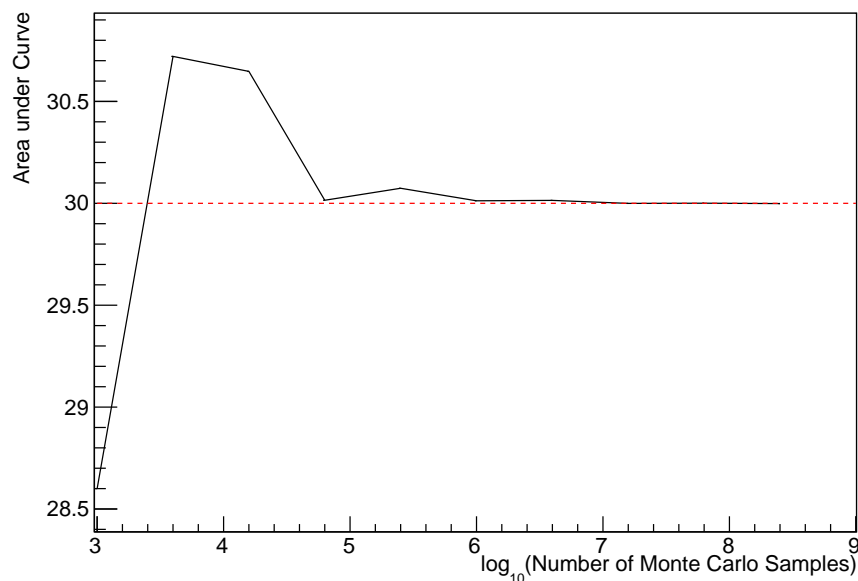


Figure 4.2: The area under a line of gradient 0.4 and intercept 1.0 for the range $0 \leq x \leq 10$ as calculated using Monte Carlo techniques as a function of the number of samples used in each repetition. The analytical solution to the area is 30 units as given by the red line.

knowledge of parameter distributions from external data or un-physical regions in which parameters can not exist. Consequently, the Monte Carlo techniques used need to be as efficient as possible. For this analysis, the Markov Chain Monte Carlo (MCMC) technique is chosen. An MCMC technique is a Monte Carlo technique that uses a Markov chain to select which points at which to sample the parameter distribution. This technique performs a semi-random stochastic walk through the allowable parameter space. This builds a posterior distribution which has the property that the density of sampled points is proportional to the probability density of that parameter. This does mean that the samples produced by this technique are not statistically independent but they will cover the space of the distribution.

A Markov chain functions by selecting the position of step \vec{x}_{i+1} based on the position of \vec{x}_i . The space in which the Markov chain selects samples is dependent upon the total number of parameters utilised within the fit, where a discrete point in this space is described by the N-dimensional space \vec{x} . In a perfectly operating Markov chain, the position of the next step depends solely on the previous step and not on the further history of the chain (\vec{x}_0, \vec{x}_1 , etc.). However, in solving the multi-dimensionality of the fit used within this analysis, each step becomes correlated with several of the steps preceding itself. This behaviour is further explained in subsection 4.2.3. Providing the MCMC chain is well optimised, it will begin to converge towards a unique stationary distribution. The period between the chain's initial starting point and the convergence to the unique stationary distribution is colloquially known as the burn-in period. This is discussed further in subsection 4.2.3. Once the chain reaches the stationary distribution, all points sampled after that point will look like samples from that distribution.

1025 Further details of the theories underpinning MCMC techniques are discussed
1026 in [132] but can be summarised by the requirement that the chain satisfies the three
1027 ‘regularity conditions’:

- 1028 • Irreducibility: From every position in the parameter space \vec{x} , there must exist a
1029 non-zero probability for every other position in the parameter space to be reached.
- 1030 • Recurrence: Once the chain arrives at the stationary distribution, every step fol-
1031 lowing from that position must be samples from the same stationary distribution.
- 1032 • Aperiodicity: The chain must not repeat the same sequence of steps at any point
1033 throughout the sampling period.

1034 The output of the chain after burn-in (ie. the sampled points after the chain
1035 has reached the stationary distribution) can be used to approximate the posterior
1036 distribution and model parameters $\vec{\theta}$. To achieve the requirement that the unique
1037 stationary distribution found by the chain be the posterior distribution, one can use
1038 the Metropolis-Hastings algorithm. This guides the stochastic process depending on
1039 the likelihood of the current proposed step compared to that of the previous step.
1040 Implementation and other details of this technique are discussed in subsection 4.2.2.

1041 4.2.2 Metropolis-Hastings Algorithm

1042 As a requirement for MCMCs, the Markov chain implemented in this technique must
1043 have a unique stationary distribution that is equivalent to the posterior distribution.
1044 To ensure this requirement and that the regularity conditions are met, this analysis
1045 utilises the Metropolis-Hastings (MH) algorithm [136,137]. For the i^{th} step in the chain,
1046 the MH algorithm determines the position in the parameter space to which the chain
1047 moves to based on the current step, \vec{x}_i , and the proposed step, \vec{y}_{i+1} . The proposed step
1048 is randomly selected from some proposal function $f(\vec{x}_{i+1}|\vec{x}_i)$, which depends solely

1049 on the current step (ie. not the further history of the chain). The next step in the chain
 1050 \vec{x}_{i+1} can be either the current step or the proposed step determined by whether the
 1051 proposed step is accepted or rejected. To decide if the proposed step is selected, the
 1052 acceptance probability, $\alpha(\vec{x}_i, \vec{y}_i)$, is calculated as

$$\alpha(\vec{x}_i, \vec{y}_{i+1}) = \min \left(1, \frac{P(\vec{y}_{i+1}|D)f(\vec{x}_i|\vec{y}_{i+1})}{P(\vec{x}_i|D)f(\vec{y}_{i+1}|\vec{x}_i)} \right). \quad (4.4)$$

1053 Where $P(\vec{y}_{i+1}|D)$ is the posterior distribution as introduced in section 4.1. To
 1054 simplify this calculation, the proposal function is required to be symmetric such that
 1055 $f(\vec{x}_i|\vec{y}_{i+1}) = f(\vec{y}_{i+1}|\vec{x}_i)$. In practice, a multi-variate Gaussian distribution is used to
 1056 throw parameter proposals from. This reduces Equation 4.4 to

$$\alpha(\vec{x}_i, \vec{y}_{i+1}) = \min \left(1, \frac{P(\vec{y}_{i+1}|D)}{P(\vec{x}_i|D)} \right). \quad (4.5)$$

1057 After calculating this quantity, a random number, β , is generated uniformly be-
 1058 tween 0 and 1. If $\beta \leq \alpha(\vec{x}_i, \vec{y}_{i+1})$, the proposed step is accepted. Otherwise, the chain
 1059 sets the next step equal to the current step and this procedure is repeated. This can be
 1060 interpreted as if the posterior probability of the proposed step is greater than that of
 1061 the current step, ($P(\vec{y}_{i+1}|D) \geq P(\vec{x}_i|D)$), the proposed step will always be accepted.
 1062 If the opposite is true, ($P(\vec{y}_{i+1}|D) \leq P(\vec{x}_i|D)$), the proposed step will be accepted
 1063 with probability $P(\vec{x}_i|D)/P(\vec{y}_{i+1}|D)$. This ensures that the Markov chain does not get
 1064 trapped in any local minima in the potentially non-Gaussian posterior distribution.
 1065 The outcome of this technique is that the density of steps taken in a discrete region is
 1066 directly proportional to the probability density in that region.

¹⁰⁶⁷ 4.2.3 MCMC Optimisation

¹⁰⁶⁸ As discussed in subsection 4.2.2, the proposal function invoked within the MH algo-
¹⁰⁶⁹ rithm can take any form and the chain will still converge to the stationary distribution.
¹⁰⁷⁰ At each set of proposed parameter values, a prediction of the same spectra has to be
¹⁰⁷¹ generated which requires significant computational resources. Therefore, the number
¹⁰⁷² of steps taken before the unique stationary distribution is found should be minimised
¹⁰⁷³ as only steps after convergence add information to the oscillation analysis. Further-
¹⁰⁷⁴ more, the chain should entirely cover the allowable parameter space to ensure that all
¹⁰⁷⁵ values have been considered. Tuning the distance that the proposal function jumps
¹⁰⁷⁶ between steps on a parameter-by-parameter basis can both minimise the length of the
¹⁰⁷⁷ burn-in period and ensure that the correlation between step \vec{x}_i and \vec{x}_j is sufficiently
¹⁰⁷⁸ small.

¹⁰⁷⁹ The effect of changing the width of the proposal function is highlighted in Figure 4.3.
¹⁰⁸⁰ Three scenarios, each with the same underlying stationary distribution (A Gaussian of
¹⁰⁸¹ width 1.0 and mean 0.), are presented. The only difference between the three scenarios
¹⁰⁸² is the width of the proposal function, colloquially known as the ‘step size σ ’. Each
¹⁰⁸³ scenario starts at an initial parameter value of 10.0 which would be considered an
¹⁰⁸⁴ extreme variation. For the case where $\sigma = 0.1$, it is clear to see that the chain takes
¹⁰⁸⁵ a long time to reach the expected region of the parameter. This indicates that this
¹⁰⁸⁶ chain would have a large burn-in period and does not converge to the stationary
¹⁰⁸⁷ distribution until step ~ 500 . Furthermore, whilst the chain does move towards the
¹⁰⁸⁸ expected region, each step is significantly correlated with the previous. Considering
¹⁰⁸⁹ the case where $\sigma = 5.0$, the chain approaches the expected parameter region almost
¹⁰⁹⁰ instantly meaning that the burn-in period is not significant. However, there are clearly
¹⁰⁹¹ large regions of steps where the chain does not move. This is likely due to the chain
¹⁰⁹² proposing steps in the tails of the distribution which have a low probability of being

1093 accepted. Consequently, this chain would take a significant number of steps to fully
 1094 span the allowable parameter region. For the final scenario, where $\sigma = 0.5$, you can see
 1095 a relatively small burn-in period of approximately 100 steps. Once the chain reaches
 1096 the stationary distribution, it moves throughout the expected region of parameter
 1097 values many times, sufficiently sampling the full parameter region. This example is a
 1098 single parameter varying across a continuous distribution and does not fully reflect
 1099 the difficulties in the many-hundred multi-variate parameter distribution used within
 1100 this analysis. However, it does give a conceptual idea of the importance of selecting
 1101 the proposal function and associated step size.

1102 As discussed, step size tuning directly correlates to the average step acceptance
 1103 rate. If the step size is too small, many steps will be accepted but the chain moves
 1104 slowly. If the opposite is true, many steps will be rejected as the chain proposes steps
 1105 in the tails of the distribution. Discussion in [138] suggests that the ‘ideal’ acceptance
 1106 rate of a high dimension MCMC chain should be approximately $\sim 25\%$. An “ideal”
 1107 step size [138] of

$$\sigma = \frac{2.4}{N_p}, \quad (4.6)$$

1108 where N_p is the number of parameters included in the MCMC fit. However, the
 1109 complex correlations between systematics mean that some parameters have to be hand
 1110 tuned and many efforts have been taken to select a set of parameter-by-parameter step
 1111 sizes to approximately reach the ideal acceptance rate.

1112 Figure 4.3 highlights the likelihood as calculated by the fit in [DB: Link to AsimovA](#)
 1113 **Sensitivity Section** as a function of the number of steps in each chain. In practice,
 1114 many independent MCMC chains are run simultaneously to parallelise the task of

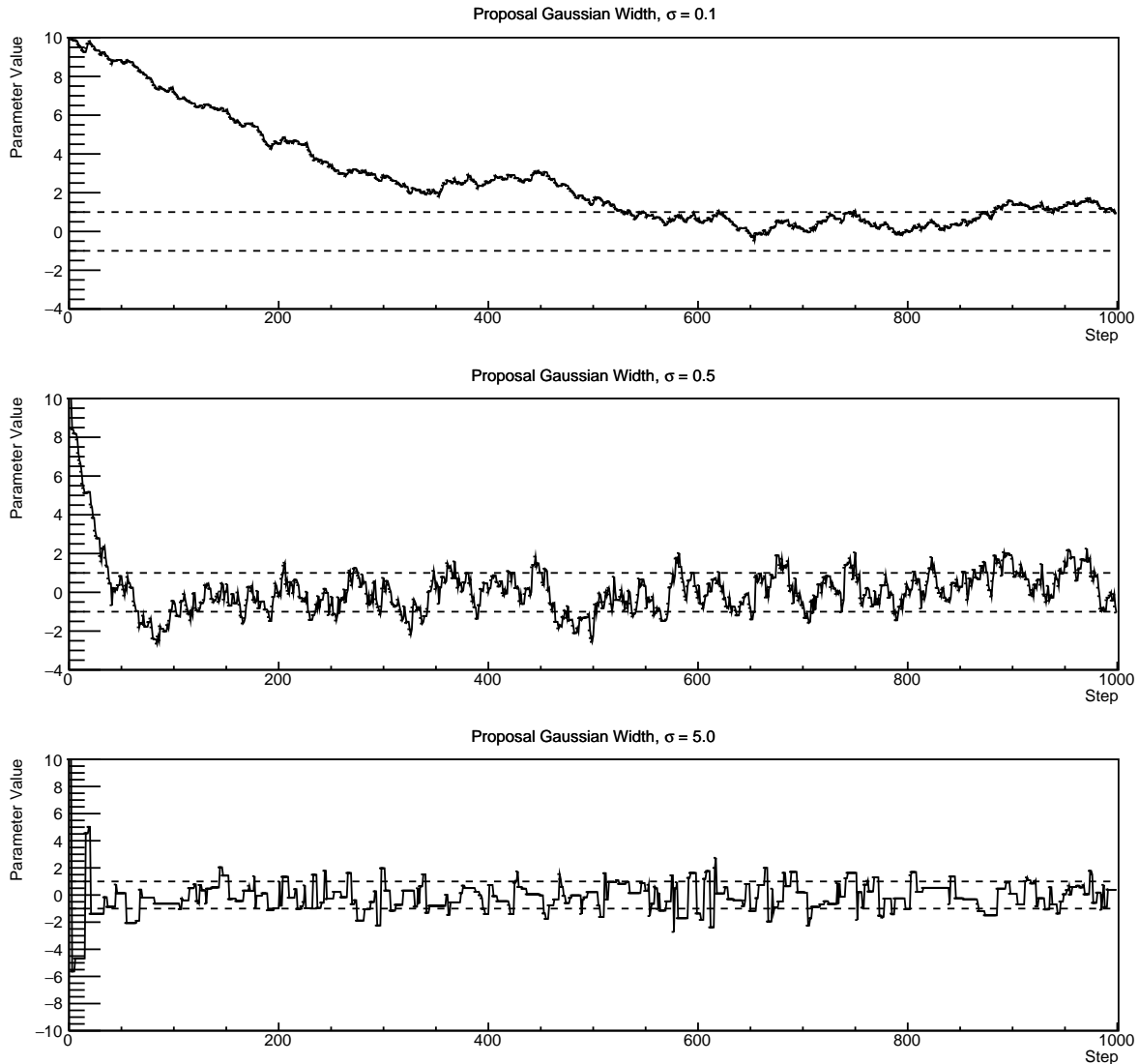


Figure 4.3: Three MCMC chains, each with a stationary distribution equal to a Gaussian centered at 0 and width 1 (As indicated by the black dotted lines). All of the chains use a Gaussian proposal function but have different widths (or ‘step size σ ’). The top panel has $\sigma = 0.1$, middle panel has $\sigma = 0.5$ and the bottom panel has $\sigma = 5.0$.

1115 performing the fit. This figure overlays the distribution found in each chain. As seen,
 1116 the likelihood decreases from its initial value and converges towards a stationary
 1117 distribution after $\sim 1 \times 10^5$ steps.

1118 Multiple configurations of this analysis have been performed throughout this thesis
 1119 where different samples or systematics have been used. For all of these configurations,
 1120 it was found that a burnin period of 1×10^5 was sufficient in all cases.

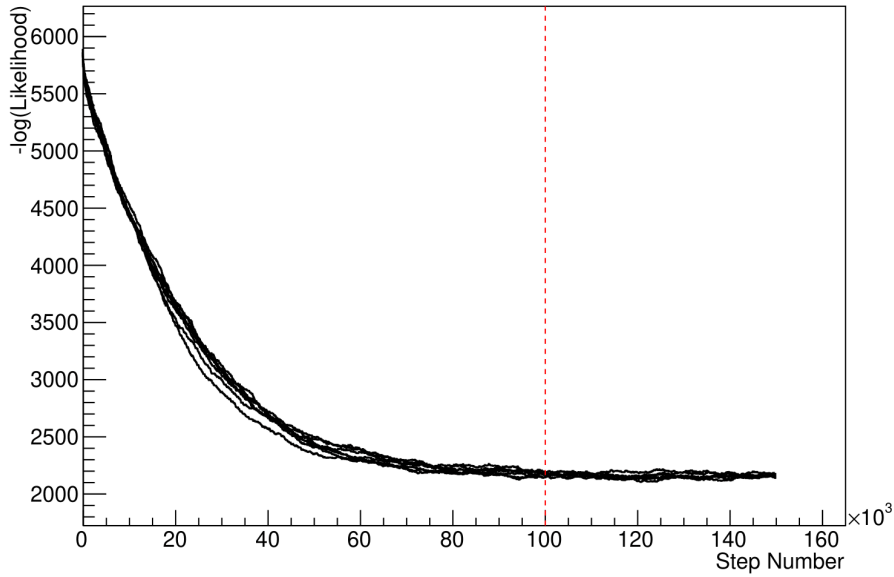


Figure 4.4: The log-likelihood from the fit detailed in DB: [Link to AsimovA Sensitivity Section](#) as a function of the number of steps accumulated in each fit. Many independent MCMC chains were run in parallel and overlaid on this plot. The red line indicates the 1×10^5 step burn-in period after which the log-likelihood becomes stable.

1121 4.3 Understanding the MCMC Results

1122 The previous sections have described how to generate the posterior probability distri-
 1123 bution using Bayesian MCMC techniques. However, this analysis focuses on oscillation
 1124 parameter determination. The posterior distribution output from the chain is a high
 1125 dimension object, with as many dimensions as there are parameters included in the os-
 1126 cillation analysis. However, this multi-dimensional object is difficult to conceptualize
 1127 so parameter estimations are often presented in one or two-dimensional projections
 1128 of this probability distribution. To do this, we invoke the marginalisation technique
 1129 highlighted in subsection 4.3.1.

1130 4.3.1 Marginalisation

1131 The output of the MCMC chain is a highly dimensional probability distribution
1132 which is very difficult to interpret. From the standpoint of an oscillation analysis
1133 experiment, the one or two-dimensional ‘projections’ of the oscillation parameters of
1134 interest are most relevant. Despite this, the best fit values and uncertainties on the
1135 oscillation parameters of interest should correctly encapsulate the correlations to the
1136 other systematic uncertainties (colloquially called ‘nuisance’ parameters). For this joint
1137 beam and atmospheric analysis, the oscillation parameters of interest are $\sin^2(\theta_{23})$,
1138 $\sin^2(\theta_{13})$, Δm_{23}^2 , and δ_{CP} . All other parameters (Including the oscillation parameter
1139 this fit is insensitive to) are deemed nuisance parameters. To generate these projections,
1140 we rely upon integrating the posterior distribution over all nuisance parameters. This
1141 is called marginalisation. A simple example of this technique is to imagine the scenario
1142 where two coins are flipped. To determine the probability that the first coin returned
1143 a ‘head’, the exact result of the second coin flip is disregarded and simply integrated
1144 over. For the parameters of interest, $\vec{\theta}_i$, we can calculate the marginalised posterior by
1145 integrating over the nuisance parameters, $\vec{\theta}_n$. In this case, Equation 4.2 becomes

$$P(\vec{\theta}_i|D) = \frac{\int P(D|\vec{\theta}_i, \vec{\theta}_n)P(\vec{\theta}_i, \vec{\theta}_n)d\vec{\theta}_n}{\int P(D|\vec{\theta})P(\vec{\theta})d\vec{\theta}} \quad (4.7)$$

1146 Where $P(\vec{\theta}_i, \vec{\theta}_n)$ encodes the prior knowledge about the uncertainty and correlations
1147 between the parameters of interest and the nuisance parameters. In practice, this
1148 is simply taking the one or two-dimensional projection of the multi-dimensional
1149 probability distribution.

Whilst in principle an easy solution to a complex problem, correlations between the interesting and nuisance parameters can bias the marginalised results. A similar effect is found when the parameters being marginalised over have non-Gaussian probability distributions. For example, Figure 4.5 highlights the marginalisation bias in the probability distribution found for a parameter when requiring a correlated parameter to have a positive parameter value. Due to the complex nature of this oscillation parameter fit presented in this thesis, there are correlations occurring between the oscillation parameters of interest and the other nuisance parameters included in the fit.

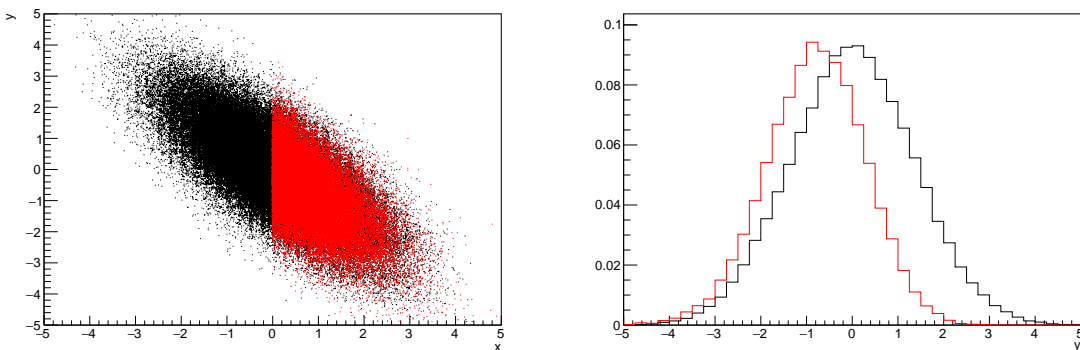


Figure 4.5: Left: The two dimensional probability distribution for two correlated parameters x and y . The red distribution shows the two dimensional probability distribution when $0 \leq x \leq 5$. Right: The marginalised probability distribution for the y parameter found when requiring the x to be bound between $-5 \leq x \leq 5$ and $0 \leq x \leq 5$ for the black and red distribution, respectively.

4.3.2 Parameter Estimation and Credible Intervals

The purpose of this analysis is to determine the best fit values for the oscillation parameters that the beam and atmospheric samples are sensitive to: $\sin^2(\theta_{23})$, $\sin^2(\theta_{13})$, Δm_{23}^2 , and δ_{CP} . Typically, the results presented take the form of one or two-dimension marginalised probability distributions for the appearance ($\sin^2(\theta_{13})$ and δ_{CP}) and disappearance ($\sin^2(\theta_{23})$ and Δm_{23}^2) parameters. The posterior probability density

₁₁₆₅ taken from the output MCMC chain is binned in these parameters. The parameter
₁₁₆₆ best-fit point is then taken to be the value that has the highest posterior probability.
₁₁₆₇ This is performed in both one and two-dimensional projections.

₁₁₆₈ However, the single best-fit point in a given parameter is not of much use on its
₁₁₆₉ own. We would also like to determine the uncertainty, or credible interval, on that
₁₁₇₀ best-fit point. The definition of the 1σ credible interval is that we have 68% belief that
₁₁₇₁ the parameter is within those bounds. For a more generalised definition, the credible
₁₁₇₂ interval is the region, R , of the posterior distribution that contains a specific fraction of
₁₁₇₃ the total probability, such that

$$\int_R P(\theta|D)d\theta = \alpha \quad (4.8)$$

₁₁₇₄ Where θ is the parameter on which we calculate the credible interval. This technique
₁₁₇₅ then calculates the $\alpha \times 100\%$ credible interval.

₁₁₇₆ In practice, this analysis uses the highest posterior density (HPD) credible intervals
₁₁₇₇ which are calculated through the following method. First, the probability distribution
₁₁₇₈ is area-normalised such that it has an integrated area equal to 1.0. The bins of proba-
₁₁₇₉ bility are then summed from the highest to lowest until the sum exceeds the 1σ level
₁₁₈₀ (0.68 in this example). This process is repeated for a range of credible intervals, notably
₁₁₈₁ the 1σ , 2σ and 3σ along with other levels where the critical values for each level can
₁₁₈₂ be found in [139]. This process can be repeated for the two-dimensional probability
₁₁₈₃ distributions by creating two-dimensional contours of credible intervals rather than a
₁₁₈₄ one-dimensional result.

¹¹⁸⁵ 4.3.3 Bayesian Model Comparisons

¹¹⁸⁶ Due to the matter resonance, this analysis has some sensitivity to the mass hierarchy
¹¹⁸⁷ of neutrino states (whether Δm_{23}^2 is positive or negative) and the octant of $\sin^2(\theta_{23})$
¹¹⁸⁸ . The Bayesian approach utilised within this analysis gives an intuitive method of
¹¹⁸⁹ model comparison by determining which hypothesis is most favourable. Taking the
¹¹⁹⁰ ratio of Equation 4.3 for the two hypotheses of normal hierarchy, NH , and inverted
¹¹⁹¹ hierarchy, IH , gives

$$\frac{P(\vec{\theta}_{NH}|D)}{P(\vec{\theta}_{IH}|D)} = \frac{P(D|\vec{\theta}_{NH})}{P(D|\vec{\theta}_{IH})} \times \frac{P(\vec{\theta}_{NH})}{P(\vec{\theta}_{IH})}. \quad (4.9)$$

¹¹⁹² The middle term defines the Bayes factor which is a data-driven interpretation of
¹¹⁹³ how strong the data prefers one hierarchy to the other. For this analysis, equal priors
¹¹⁹⁴ on both mass hierarchy hypotheses are chosen ($P(\vec{\theta}_{NH}) = P(\vec{\theta}_{IH}) = 0.5$). In practice,
¹¹⁹⁵ the MCMC chain proposes a value of $|\Delta m_{23}^2|$ and then applies a 50% probability
¹¹⁹⁶ that the value is sign flipped. Consequently, the Bayes factor can be calculated from
¹¹⁹⁷ the ratio of the probability density in either hypothesis. This equates to counting the
¹¹⁹⁸ number of steps taken in the normal and inverted hierarchies and taking the ratio. The
¹¹⁹⁹ same approach can be taken to compare the upper octant (UO) compared to the lower
¹²⁰⁰ octant (LO) hypothesis of $\sin^2(\theta_{23})$.

¹²⁰¹ Whilst the value of the Bayes factor should always be shown, the Jeffreys scale [140]
¹²⁰² (highlighted in Table 4.1) gives an indication of the strength of preference for one model
¹²⁰³ compared to the other. Other interpretations of the strength of preference of a model
¹²⁰⁴ exist, e.g. the Kass and Raferty Scale [141].

| $\log_{10}(B_{AB})$ | B_{AB} | Strength of Preference |
|---------------------|--------------|--|
| < 0.0 | < 1 | No preference for hypothesis A (Supports hypothesis B) |
| 0.0 – 0.5 | 1.0 – 3.16 | Preference for hypothesis A is weak |
| 0.5 – 1.0 | 3.16 – 10.0 | Preference for hypothesis A is substantial |
| 1.0 – 1.5 | 10.0 – 31.6 | Preference for hypothesis A is strong |
| 1.5 – 2.0 | 31.6 – 100.0 | Preference for hypothesis A is very strong |
| > 2.0 | > 100.0 | Decisive preference for hypothesis A |

Table 4.1: Jeffreys scale for strength of preference for two models A and B as a function of the calculated Bayes factor ($B_{AB} = B(A/B)$) between the two models [140]. The original scale is given in terms of $\log_{10}(B(A/B))$ but converted to linear scale for easy comparison throughout this thesis.

1205 4.3.4 Comparison of MCMC Output to Expectation

1206 To ensure the fit is performing well, a best-fit spectrum is produced using the pos-
1207 terior probability distribution and compared with the data, allowing easy by-eye
1208 comparisons to be made. A simple method of doing this is to perform a comparison
1209 in the fitting parameters (For instance, the reconstructed neutrino energy and lepton
1210 direction for T2K far detector beam samples) of the spectra generated by the MCMC
1211 chain to ‘data’. This ‘data’ could be true data or some variation of Monte Carlo predic-
1212 tion. This allows easy comparison of the MCMC probability distribution to the data.
1213 To perform this, N steps from the post burn-in MCMC chain are randomly selected
1214 (Where for all plots of this style in this thesis, $N = 3000$). From these, the Monte Carlo
1215 prediction at each step is generated by reweighting the model parameters to the values
1216 specified at that step. Due to the probability density being directly correlated with
1217 the density of steps in a certain region, parameter values close to the best fit value are
1218 most likely to be selected.

1219 In practice, for each bin of the fitting parameters has a probability distribution
1220 of event rates, with one entry per sampled MCMC step. This distribution is binned
1221 where the bin with the highest probability is selected as the mean and an error on

1222 the width of this probability distribution is calculated using the approach highlighted
1223 in subsection 4.3.2. Consequently, the best fit distribution in the fit parameter is not
1224 necessarily that which would be attained by reweighting the Monte Carlo prediction
1225 to the most probable parameter values.

1226 A similar study can be performed to illustrate the freedom of the model parameter
1227 space prior to the fit. This can be done by throwing parameter values from the prior
1228 uncertainty of each parameter. This becomes troublesome for parameters with no
1229 prior uncertainty as the range is technically infinite. Where applicable solutions to
1230 remove these have been addressed.

1231 **Chapter 5**

1232 **Simulation, Reconstruction, and Event
Reduction**

1234 As a crucial part of the oscillation analysis, an accurate prediction of the expected
1235 neutrino spectrum at the far detector is required. This includes modeling the flux
1236 generation, neutrino interactions, and detector effects. All of the simulation packages
1237 required to do this are briefly described in section 5.1. The reconstruction of neutrino
1238 events inside the far detector, including the `fitQun` algorithm, is documented in
1239 section 5.2. This also includes data quality checks of the SK-V data which the author
1240 performed for the T2K oscillation analysis presented at Neutrino 2020 [80]. Finally,
1241 section 5.3 describes the steps taken in the SK detector to trigger on events of interest
1242 whilst removing the comparatively large rate of cosmic ray muon events.

1243 **5.1 Simulation**

1244 In order to generate a Monte Carlo prediction of the expected event rate at the far
1245 detector, all the processes in the beam and atmospheric flux, neutrino interaction, and
1246 detector need to be modeled. Each of these parts is individually modeled and each of
1247 them is detailed below.

1248 The beamline simulation consists of three distinct parts: the initial hadron inter-
1249 action modeled by FLUKA [142], the target station geometry and particle tracking

performed by JNUBEAM, [143, 144] and any hadronic re-interactions simulated by GCALOR [145]. The primary hadronic interactions are $O(10)\text{GeV}$, where FLUKA matches external cross-section data better than GCALOR [146]. However, FLUKA is not very adaptable so a small simulation is built to model the interactions in the target and the output is then passed to JNUBEAM and GCALOR for propagation. The hadronic interactions are tuned to data from the NA61/SHINE [147–149] and HARP [150] experiments. The tuning is done by reweighting the FLUKA and GCALOR predictions to match the external data multiplicity and cross-section measurements, based on final state particle kinematics [146]. The culmination of this simulation package generates the predicted flux for neutrino and antineutrino beam modes which are illustrated in Figure 3.7.

The atmospheric neutrino flux **predictions are is** simulated by the HKKM model [43, 45]. The primary cosmic ray flux is tuned to AMS [151] and BESS [152] data assuming the US-standard atmosphere '76 [153] density profile and includes geomagnetic field effects. The primary cosmic rays interact to generate pions and muons. The interaction of these secondary particles to generate neutrinos is handled by DPMJET-III [154] for energies above 32GeV and JAM [45, 155] for energies below that value **DB:** **Question for Giles: Why different generators for above/below 32GeV?** These hadronic interactions are tuned to BESS and L3 data [156, 157] using the same methodology as the tuning of the beamline simulation. The energy and cosine zenith predictions of $\nu_e, \bar{\nu}_e, \nu_\mu, \bar{\nu}_\mu$ flux are given in Figure 2.3 and Figure 2.5, respectively. The flux is approximately symmetrical and peaked around the horizon ($\cos(\theta_Z) = 0.0$). This is because horizontally-going pions and kaons can travel further than their vertically-going counterparts resulting in a larger probability of decaying to neutrinos. The symmetry is broken in lower-energy neutrinos due to geomagnetic effects, which modify the track of the primary cosmic rays. Updates to the HKKM model are currently ongoing [158].

Once a flux prediction has been made for all three detectors, NEUT 5.4.0 [159, 160] models the interactions of the neutrinos in the detectors. For the purposes of this analysis, quasi-elastic (QE), meson exchange (MEC), single meson production (PROD), coherent pion production (COH), and deep inelastic scattering (DIS) interactions are simulated. These interaction categories can be further broken down by whether they were propagated via a W^\pm boson in Charged Current (CC) interactions or via a Z^0 boson in Neutral Current (NC) interactions. CC interactions have a charged lepton in the final state, which can be flavour-tagged in reconstruction to determine the flavour of the neutrino. In contrast, NC interactions have a neutrino in the final state so no flavour information can be determined from the observables left in the detector after an interaction. ~~This is the reason why NC events~~ ~~This is the reason why neutrinos which interact through NC modes~~ are assumed to not oscillate within this analysis. Both CC and NC interactions are modeled for all the above interaction categories, other than MEC interactions which are only modeled for CC events. ~~As the SK detector is only sensitive to charged particles above Cherenkov threshold, all charged current interactions are simulated whilst only neutral current processes that can produce charged particles (NCDIS, NCCOH, and NCPROD including π^0 production) are modeled. NC MEC interactions can only produce charged particles through secondary re-interactions which is a low cross-section process.~~

As illustrated in Figure 5.1, CCQE interactions dominate the ~~low-energy~~ cross-section of neutrino interactions ~~around $E_\nu \sim 0.5\text{GeV}$~~ . The NEUT implementation adopts the Llewellyn Smith [161] model for neutrino-nucleus interactions, where the nuclear ground state of any bound nucleons (neutrino-oxygen interactions) is approximated by a spectral-function [162] model that simulates the effects of Fermi momentum and Pauli blocking. The cross-section of QE interactions ~~are is~~ controlled by vector and axial-vector form factors parameterised by the BBBA05 [163] model and a dipole form factor with $M_A^{QE} = 1.21\text{GeV}$ fit to external data [164], respectively. NEUT

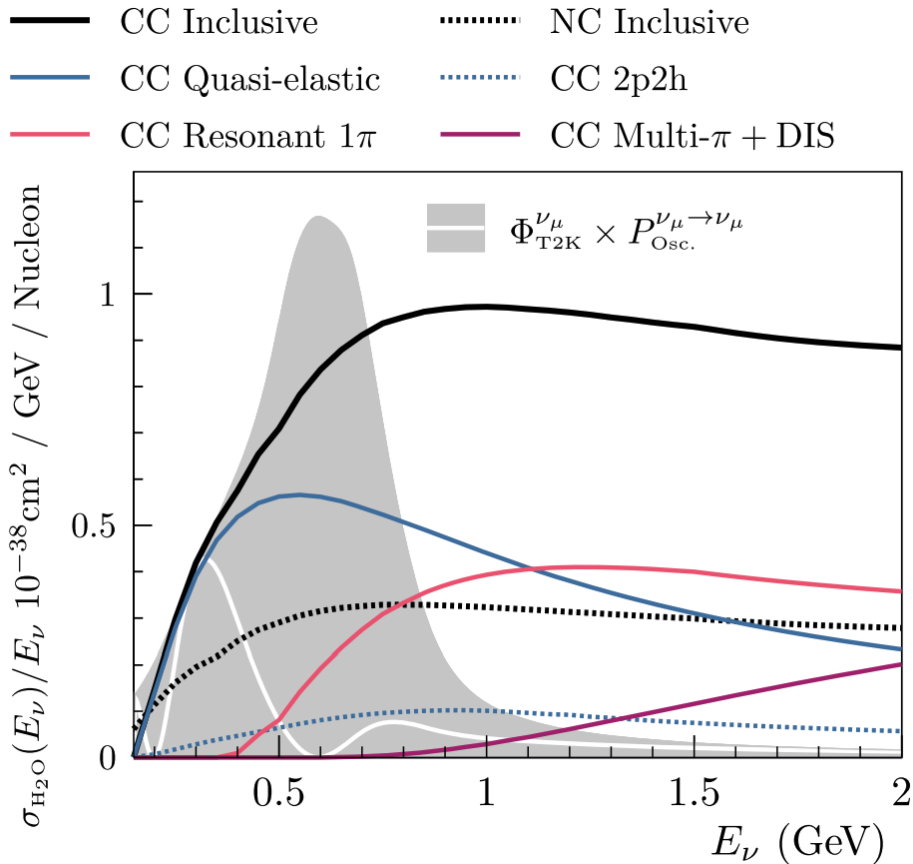


Figure 5.1: The NEUT prediction of the ν_μ -H₂O cross-section overlaid on the T2K ν_μ flux. The charged current (black, solid) and neutral current (black, dashed) inclusive, charged current quasi-elastic (blue, solid), charged current 2p2h (blue, dashed), charged current single pion production (pink), and charged current multi- π and DIS (Purple) cross-sections are illustrated. Figure taken from [159].

1303 implements the Valencia [165] model to simulate MEC events, where two nucleons
 1304 and two holes in the nuclear target are produced (Often called 2p2h interactions).

1305 For neutrinos of energy $O(1)\text{GeV}$, PROD interactions become dominant. These
 1306 predominantly produce charged and neutral pions although γ , kaon, and η production
 1307 is also considered. To simulate these interactions, the Berger-Sehgal [166] model is
 1308 implemented within NEUT. It simulates the excitation of a nucleon from a neutrino
 1309 interaction, production of an intermediate baryon, and the **consequential subsequent**
 1310 decay to a single meson or γ . Pions can also be produced through COH interactions,
 1311 which occur when the incoming neutrino interacts with the entire oxygen **nuclei**

1312 target nucleus leaving a single pion outside of the nucleus. NEUT utilises the Berger-
1313 Sehgal [167] model to simulate these COH interactions.

1314 DIS and multi- π producing interactions become the most dominant for energies
1315 $> O(5)\text{GeV}$. PYTHIA [168] is used to simulate any interaction with invariant mass
1316 $W > 2\text{GeV}/c^2$, which produces at least one meson. For any interaction which produces
1317 at least two mesons but has $W < 2\text{GeV}/c^2$, the Bronner model is **invoked used** [169].
1318 Both of these models use parton distribution functions based on the Bodek-Yang
1319 model [170–172].

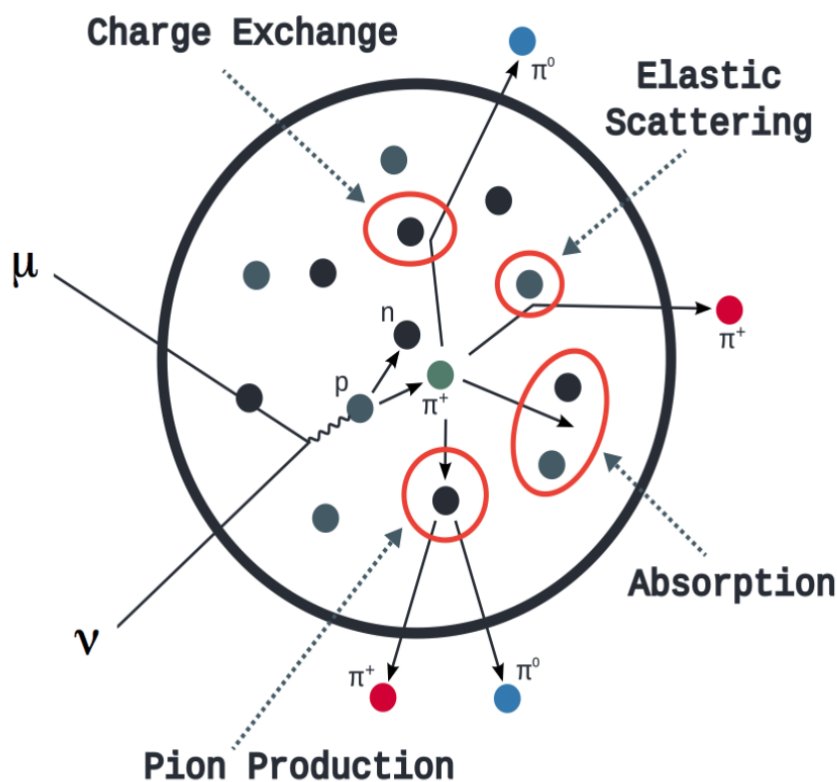


Figure 5.2: Illustration of the various processes which a pion can undergo before exiting the nucleus. Taken from [173].

1320 Any pion which is produced within the nucleus can re-interact through final state
1321 interactions before it exits, as illustrated by the scattering, absorption, production, and
1322 exchange interactions in Figure 5.2. These re-interactions alter the observable particles

1323 within the detector. For instance, if the charged pion from a CC PROD interaction is
1324 absorbed, the observables would mimic a CC QE interaction. To simulate these effects,
1325 NEUT uses a semi-classical intranuclear cascade model [159]. This cascade functions by
1326 stepping the pion through the nucleus in fixed-length steps equivalent to $dx = R_N/100$,
1327 where R_N is the radius of the nucleus. At each step, the simulation allows the pion
1328 to interact through scattering, charged exchange, absorption, or production with an
1329 interaction-dependent probability calculated from a fit to external data [174]. This
1330 cascade continues until the pion is absorbed or exits the nucleus.

1331 Once the final state particle kinematics have been determined **from by** NEUT, they
1332 are passed into the detector simulation. The near detectors, ND280 and INGRID, are
1333 simulated using a GEANT4 package [118,175] to simulate the detector geometry, particle
1334 tracking, and energy deposition. The response of the detectors is simulated using
1335 the elecSim package [118]. The far detector simulation is based upon the original
1336 Kamiokande experiment software which uses the GEANT3-based SKDETSIM [118,176]
1337 package. This **controls simulates** the interactions of particles in the water as well as
1338 Cherenkov light production. The water quality and PMT calibration measurements
1339 detailed in subsection 3.1.2 are also used within this simulation to make accurate
1340 predictions of the detector response.

1341 5.2 Event Reconstruction at SK

1342 **Any above Cherenkov threshold event which Any event which generates optical**
1343 **photons that** occurs in SK will be **recorded observed** by the PMT array, where each
1344 PMT records the time and accumulated charge. This recorded information is shown
1345 in event displays similar to those illustrated in Figure 5.3. To be useful for physics
1346 analyses, this series of PMT hit information needs to be reconstructed to determine

the particle's identity and kinematics (or track parameters): four-vertex, direction, and momenta. ~~This is because The reconstruction uses the fact that~~ the charge and timing distribution of photons generated by a particular particle in an event is dependent upon its initial kinematics. ~~The concept of distinguishing electron and muon events is from the “fuzziness” of the ring.~~ Electron and muon rings are distinguished by their “fuzziness”. Muons are heavier and less affected by scattering or showering meaning they typically produce “crisp” rings. Electrons are more likely to interact via electromagnetic showering or scattering which results in larger variations of their direction from the initial direction. Consequently, electrons typically produce “fuzzier” rings compared to muons.

1357 The below paragraph has been reordered

For the purposes of this analysis, the `fitQun` reconstruction algorithm is utilised. Its core function is to compare a prediction of the accumulated charged and timing distribution from each PMT, generated for a particular particle identity and track parameters, to that observed in the neutrino event. It determines the preferred values by minimising a likelihood function which includes information from PMTs which were hit and those that were not hit. `fitQun` performs a simultaneous fit of particle kinematics and identity, improving both the accuracy of the fit parameters and the rejection of neutral current π^0 events [177, 178]. The `fitQun` algorithm is based on the key concepts of the MiniBooNE reconstruction algorithm [179] and is described in [180] which is summarised below. The `fitQun` algorithm improves upon the APFit reconstruction algorithm which has been used for many previous SK analyses. APFit fits the vertex from timing information and then fits the momentum and direction of the particle from PMT hits within a 43 deg Cherenkov cone (which assumes an ultra-relativistic particle). It then fits the particle identity once the track parameters have been fit.

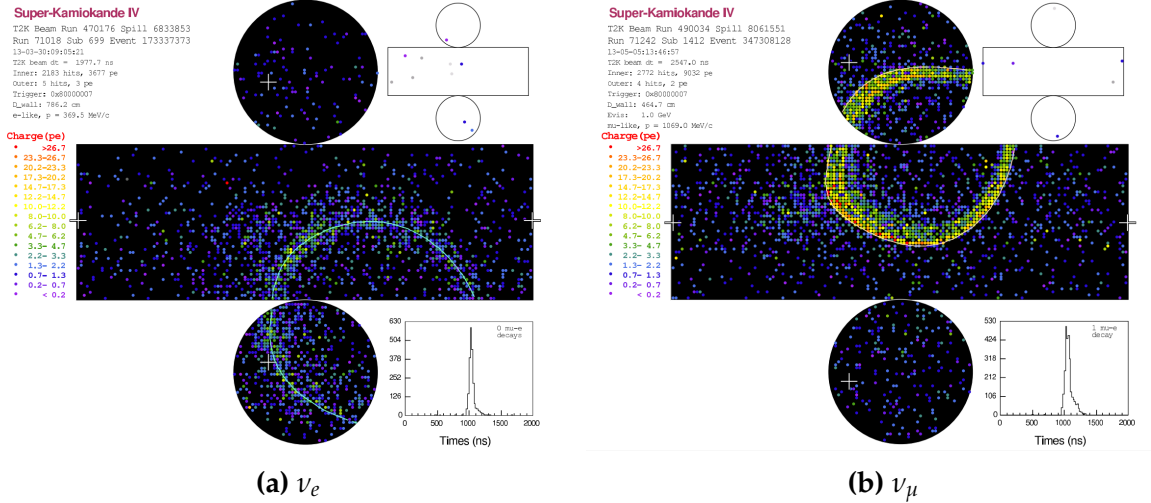


Figure 5.3: Event displays from Super Kamiokande illustrating the “crisp” ring from a muon and the typically “fuzzy” electron ring. Each pixel represents a PMT and the color scheme denotes the accumulated charge deposited on that PMT. Figures taken from [181].

1373 The below has been added as an overview of fiTQun

1374 The fiTQun reconstruction algorithm proceeds by:

- 1375 • **Vertex pre-fitting:** An estimate of the vertex is made using a goodness-of-fit metric
- 1376 • **Peak finding:** The initial time of the event is determined by clustering events by time residuals
- 1377 • **Single-ring fits:** Given the pre-fit vertex and estimated time of interaction, a maximum likelihood technique searches for a single particle generating light
- 1378 • **Multi-ring fits:** Seeded from the single-ring fits, hypotheses with multiple light-producing particles are considered using the same maximum likelihood technique

1383 An event in SK can consist of a primary and decay particles. An event in SK can
 1384 consist of multiple particles. For example, a charge current muon neutrino interaction
 1385 can generate two particles that have the potential of generating Cherenkov photons:
 1386 the primary muon, and the secondary decay-electron from the muon. To ensure both

¹³⁸⁷ particle are reconstructed separately, each event is divided into time clusters which
¹³⁸⁸ are called “subevents”. The number of subevents is equal to the number of decay
¹³⁸⁹ electrons plus one (the primary event). To find all the subevents in an event, a vertex
¹³⁹⁰ goodness metric is calculated for some vertex position \vec{x} and time t ,

$$G(\vec{x}, t) = \sum_i^{\text{hit PMTs}} \exp \left(-\frac{1}{2} \left(\frac{T_{Res}^i(\vec{x}, t)}{\sigma} \right)^2 \right) \quad (5.1)$$

¹³⁹¹ where

$$T_{Res}^i(\vec{x}, t) = t^i - t - |R_{PMT}^i - \vec{x}| / c_n \quad (5.2)$$

¹³⁹² is the residual hit time. It is the difference in time between the PMT hit time, t^i ,
¹³⁹³ of the i^{th} PMT and the expected time of the PMT hit if the photon was emitted at
¹³⁹⁴ the start of the vertex. R_{PMT}^i is the position of the i^{th} PMT, c_n is the speed of light in
¹³⁹⁵ water and $\sigma = 4\text{ns}$ which is comparable to the time resolution of the PMT. When the
¹³⁹⁶ proposed fit values of time and vertex are close to the true values, $T_{Res}^i(\vec{x}, t)$ tends to
¹³⁹⁷ zero resulting in subevents appearing as spikes in the goodness metric. The proposed
¹³⁹⁸ fit vertex and time are grid-scanned, and the values which maximise the goodness
¹³⁹⁹ metric are selected as the “pre-fit vertex”. Whilst this predicts a vertex for use in
¹⁴⁰⁰ the clustering algorithm, the final vertex is fit using the higher-precision maximum
¹⁴⁰¹ likelihood method described below.

¹⁴⁰² Once the pre-fit vertex has been determined, the goodness metric is scanned as
¹⁴⁰³ a function of t to determine the number of subevents. A peak-finding algorithm is
¹⁴⁰⁴ then used on the goodness metric, requiring the goodness metric to exceed some

1405 threshold and drop below a reduced threshold before any subsequent additional
 1406 peaks are considered. The thresholds are set such that the rate of false peak finding
 1407 is minimised while still attaining good data to Monte Carlo agreement. To improve
 1408 performance, the pre-fit vertex for each delayed subevent is re-calculated after PMT
 1409 hits from the previous subevent are masked. This improves the decay-electron tagging
 1410 performance. Once all subevents have been determined, the time window around
 1411 each subevent is then defined by the earliest and latest time which satisfies $-180 <$
 1412 $T_{Res}^i < 800\text{ns}$. The subevents and associated time windows are then used as seeds for
 1413 further reconstruction.

1414 For a given subevent, the `fitQun` algorithm constructs a likelihood based on the
 1415 accumulated charge q_i and time information t_i from the i^{th} PMT,

$$L(\Gamma, \vec{\theta}) = \prod_j^{\text{unhit}} P_j(\text{unhit}|\Gamma, \vec{\theta}) \prod_i^{\text{hit}} \{1 - P_i(\text{unhit}|\Gamma, \vec{\theta})\} f_q(q_i|\Gamma, \vec{\theta}) f_t(t_i|\Gamma, \vec{\theta}), \quad (5.3)$$

1416 where $\vec{\theta}$ defines the track parameters; vertex position, direction vector and mo-
 1417 ments, and Γ represents the particle hypothesis. $P_i(\text{unhit}|\Gamma, \vec{\theta})$ is the probability of the
 1418 i^{th} tube to not register a hit given the track parameters and particle hypothesis. The
 1419 charge likelihood, $f_q(q_i|\Gamma, \vec{\theta})$, and time likelihood, $f_t(t_i|\Gamma, \vec{\theta})$, represents the probability
 1420 density function of observing charge q_i and time t_i on the i^{th} PMT given the specified
 1421 track parameters and particle hypothesis.

1422 **I don't think the below paragraph is actually needed?**

1423 As the generation and propagation of the optical photons are independent of the
 1424 PMT and electronics response, it is natural to split the calculation into two. This split
 1425 was also performed to . Firstly, the expected number of photoelectrons (or predicted

1426 charge), $\mu_i = \mu_i(\vec{\theta}, \Gamma)$, at the i^{th} PMT is calculated. This value is then substituted into
1427 the likelihood function. This allows the charge likelihood density $f_q(q_i|\mu_i)$ and unhit
1428 probability $P_i(\text{unhit}|\mu_i)$ to be expressed via quantities that are only dependent on the
1429 response of the PMT.

1430 The predicted charge is calculated based on contributions from both the direct
1431 light and the scattered light. The direct light contribution is determined based on the
1432 integration of the Cherenkov photon profile along the track. PMT angular acceptance,
1433 water quality, and calibration measurements discussed in subsection 3.1.2 are included
1434 to accurately predict the charge probability density at each PMT. The scattered light
1435 is calculated in a similar way, although it includes a scattering function that depends
1436 on the vertex of the particle and the position of the PMT. The charge likelihood is
1437 calculated by comparing the prediction to the observed charge in the PMT.

1438 The time likelihood is approximated to depend on the vertex \vec{x} , direction \vec{d} , and
1439 time t of the track **parameters** as well as the particle hypothesis. The expected time
1440 for PMT hits is calculated by assuming unscattered photons being emitted from the
1441 midpoint of the track, S_{mid} ,

$$t_{exp}^i = t + S_{mid}/c + |R_{PMT}^i - \vec{x} - S_{mid}\vec{d}|/c_n, \quad (5.4)$$

1442 where c is the speed of light in a vacuum. The time likelihood is then expressed in
1443 terms of the residual difference between the PMT hit time and the expected hit time,
1444 $t_{Res}^i = t^i - t_{exp}^i$. The particle hypothesis and momentum also affect the Cherenkov
1445 photon distribution. These parameters modify the shape of the time likelihood density
1446 since in reality not all photons are emitted at the midpoint of the track. As with the
1447 charge likelihood, the contributions from both the direct and scattered light to the time

1448 likelihood density are calculated separately, which are both calculated from particle
1449 gun studies.

1450 **Below paragraphs, figures and equations are changed**

1451 The track parameters and particle identity which maximise $L(\Gamma, \vec{\theta})$ are defined as
1452 the best-fit parameters. In practice MINUIT [182] is used to minimise the value of
1453 $-\ln L(\Gamma, \vec{\theta})$. The `fitQun` algorithm considers an electron-like, muon-like, and charged
1454 pion-like hypothesis for events with a single final state particle, denoted “single-ring
1455 events”. The particle’s identity is determined by taking the ratio of the likelihood
1456 of each of the hypotheses. For instance, electrons and muons are distinguished by
1457 considering the value of $\ln(L(e, \vec{\theta}_e)/L(\mu, \vec{\theta}_\mu))$ in comparison to the reconstructed
1458 momentum of the electron hypothesis, as illustrated by Figure 5.4. The coefficients
1459 of the discriminator between electron-like and muon-like events is determined from
1460 Monte Carlo studies [180]. Similar distributions exist for distinguishing electron-like
1461 events from π^0 -like events, and muon-like events from pion-like events. They are
1462 defined as,

$$\begin{aligned} \text{Electron/Muon} : & \ln(L_e/L_\mu > 0.2 \times p_e^{rec} [\text{MeV}], \\ \text{Electron}/\pi^0 : & \ln(L_e/L_{\pi^0} < 175 - 0.875 \times m_{\gamma\gamma} [\text{MeV}], \\ \text{Muon/Pion} : & \ln(L_\mu/L_{\pi^\pm} < 0.15 \times p_\mu^{rec} [\text{MeV}], \end{aligned} \quad (5.5)$$

1463 as taken from [183], where p_e^{rec} and p_μ^{rec} are the reconstructed momentum of the
1464 single-ring electron and muon fits, respectively. $m_{\gamma\gamma}$ represents the reconstructed
1465 invariant mass of the two photons emitted from π^0 decay. Typically, the distance
1466 between a particular entry in these two-dimensional distributions and the cut-line is
1467 termed the PID parameter and is illustrated in Figure 5.5.

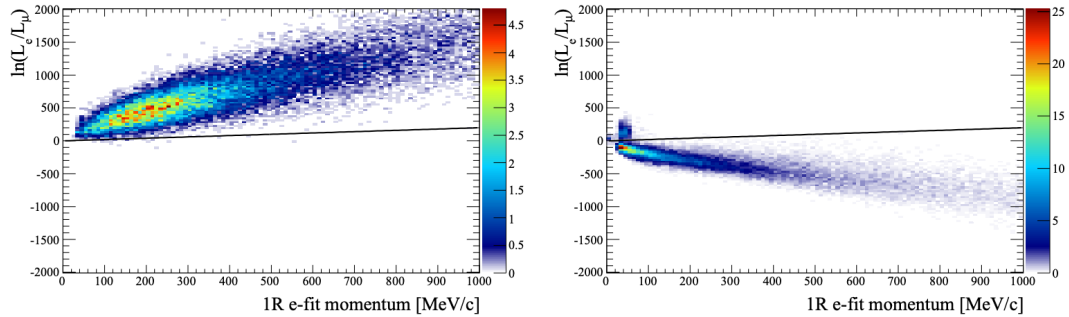


Figure 5.4: The difference of the electron-like and muon-like log-likelihood compared to the reconstructed single-ring fit momentum for atmospheric ν_e (left) and ν_μ (right) samples. The black line represents the cut used to discriminate electron-like and muon-like events, which coefficients obtained from Monte Carlo studies. Figures taken from [180].

1468

Review stop

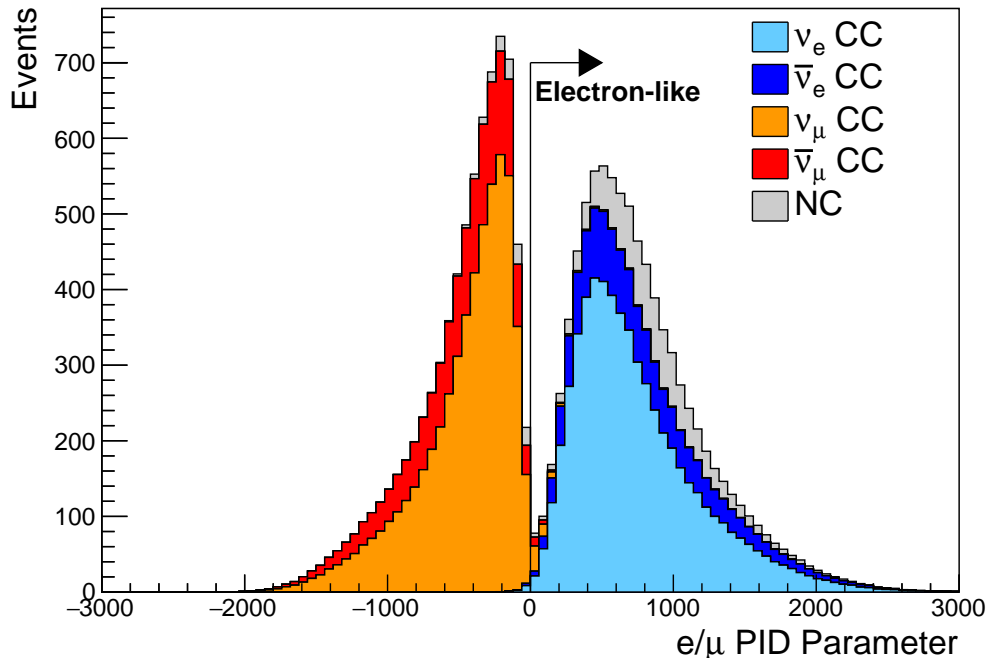


Figure 5.5: The electron/muon PID separation parameter for all sub-GeV single-ring events in SK-IV. The charged current (CC) component is broken down in four flavours of neutrino (ν_μ , $\bar{\nu}_\mu$, ν_e and $\bar{\nu}_e$). Events with positive values of the parameter are determined to be electron-like.

1469

The `fitQun` algorithm also considers a π^0 hypothesis. To do this, it performs a fit looking for two standard electron-hypothesis tracks which point to the same

1470

1471 four-vertex. This assumes the electron tracks are generated from photon-conversion so
1472 the electron tracks actually appear offset from the proposed π^0 vertex. For these fits,
1473 the conversion length, direction, and momentum of each photon are also considered
1474 as track parameters which are then fit in the same methodology as the standard
1475 single-ring hypotheses.

1476 Whilst lower energy events are predominately single-ring events, higher energy
1477 neutrino events can generate final states with multiple particles which generate
1478 Cherenkov photons. These “multi-ring” hypotheses are also considered in the `fiTQuN`
1479 algorithm. When calculating the charge likelihood density, the predicted charge asso-
1480 ciated with each ring is calculated separately and then summed to calculate the total
1481 accumulated charge on each PMT. Similarly, the time likelihood for the multi-ring
1482 hypothesis is calculated assuming each ring is independent. Each track is time-ordered
1483 based on the time of flight from the center of the track to the PMT and the direct light
1484 from any ring incident on the PMT is assumed to arrive before any scattered light. To
1485 reduce computational resource [usage](#), the multi-ring fits only consider electron-like
1486 and charged pion-like rings as the pion fit can be used as a proxy for a muon fit due to
1487 their similar mass.

1488 Multi-ring fits proceed by proposing another ring to the previous fit and then
1489 fitting the parameters in the method described above. Typically, multi-ring fits have
1490 the largest likelihood because of the additional degrees of freedom introduced. **A**
1491 [likelihood value is calculated for the \$n\$ -ring and \$\(n + 1\)\$ -ring hypotheses, where](#)
1492 [the additional ring is only included if the likelihood value is above 9.35, based](#)
1493 [on Monte Carlo studies in \[184\]. Consequently, the additional ring is only added](#)
1494 [if the ratio of likelihoods passes a criterion, which is determined by Monte Carlo](#)
1495 [studies.](#)

¹⁴⁹⁶ 5.2.1 Validation of Reconstruction in SK-V

¹⁴⁹⁷ As an example of how the reconstruction depends on the detector conditions, the
¹⁴⁹⁸ author of this thesis assessed the quality of event reconstruction for SK-V data. The
¹⁴⁹⁹ detector systematics ~~invoked-within used in~~ the T2K-only oscillation analysis are
¹⁵⁰⁰ determined using data-to-Monte Carlo comparisons of the SK-IV data [185]. Due to
¹⁵⁰¹ tank-open maintenance occurring between SK-IV and SK-V, the dark rate of each PMT
¹⁵⁰² was observed to increase in SK-V due to light exposure for a significant time during
¹⁵⁰³ the repairs. This increase can be seen in Figure 5.6. Run-10 of the T2K experiment was
¹⁵⁰⁴ conducted in the SK-V period, so the consistency of SK-IV and SK-V data needs to
¹⁵⁰⁵ be studied to determine whether the SK-IV-defined systematics can be applied to the
¹⁵⁰⁶ run-10 data. This comparison study was performed using the stopping muon data set
¹⁵⁰⁷ for both the SK-IV and SK-V periods. This data sample is used due to the high rate of
¹⁵⁰⁸ interactions ($O(200)$ events per hour) as well as having similar energies to muons from
¹⁵⁰⁹ CCQE ν_μ interactions from beam interactions. The rate of cosmic muons does depend
¹⁵¹⁰ on the solar activity cycle [186] but has been neglected in this comparison study. This
¹⁵¹¹ is because the shape of the distributions is most important for the purposes of being
¹⁵¹² compared to the detector systematics. The SK-IV and SK-V data samples consist of
¹⁵¹³ 2398.42 and 626.719 hours of data which equates to 686k and 192k events respectively.

¹⁵¹⁴ The predicted charge calculated in the `fitQun` ~~charge-likelihood prediction al-~~
¹⁵¹⁵ ~~gorithm~~ includes a contribution from the photoelectron emission due to dark noise.
¹⁵¹⁶ Therefore, the increase in the SK-V dark rate needs to be accounted for. In practice, the
¹⁵¹⁷ average dark rate in each SK period is calculated and used as an input in the reconstruc-
¹⁵¹⁸ tion. This is calculated by averaging the dark rate per run for each period separately,
¹⁵¹⁹ using the calibration measurements detailed in subsection 3.1.2. The average dark
¹⁵²⁰ rate from SK-IV and SK-V were found to be 4.57kHz and 6.30kHz, respectively. The
¹⁵²¹ ~~associated-charge charges associated~~ with the muon and decay electron subevents

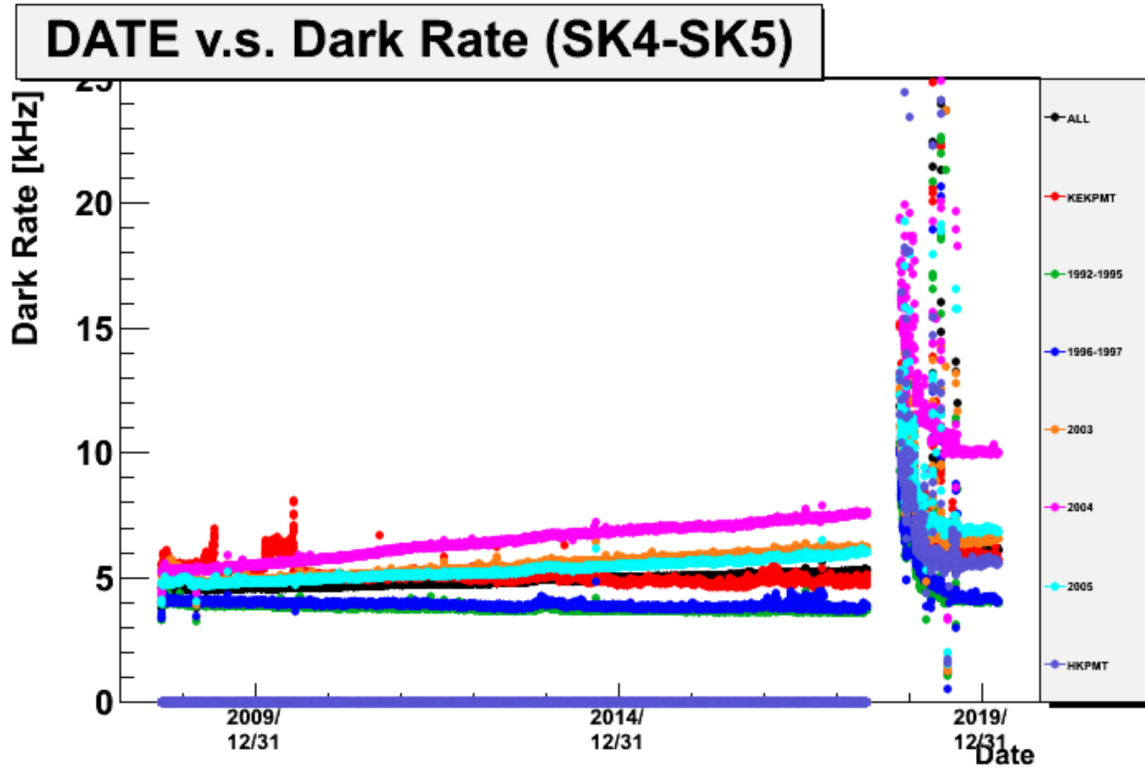


Figure 5.6: The variation of the measured dark rate as a function of date, broken down by PMT type. The SK-IV and SK-V periods span September 2008 to May 2018 and January 2019 to July 2020, respectively. The break in measurement in 2018 corresponds to the period of tank repair and refurbishment. Figure adapted from [185].

are illustrated in Figure 5.7. The photoelectron emission from dark noise ~~will be more noticeable is more significant~~ for events that have lower energy. This is because this contribution becomes more comparable to the number of photoelectrons emitted from incident photons in lower-energy events. This behaviour is observed in the data, where the charge deposited by the muon subevent is mostly unaffected by the increase in dark rate, whilst the charge associated with the decay-electron is clearly affected.

~~The energy scale systematic for the SK-IV period was determined to be 2.1%. It is defined to be equal to the difference between data and Monte Carlo prediction in the stopping muon data sample. The energy scale systematic is estimated from data-to-Monte Carlo differences in the stopping muon sample in [187] and found to be 2.1%.~~ To determine the consistency of SK-IV and SK-V with respect to the energy

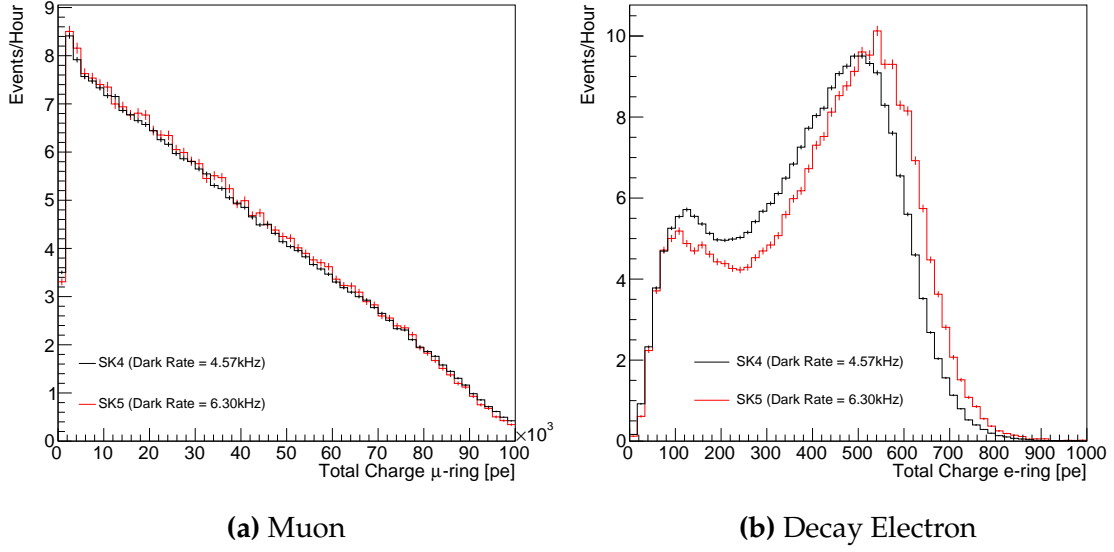


Figure 5.7: Comparison of the measured raw charge deposited per event from the stopping muon data samples between SK-IV (Blue) and SK-V (Red), split by the primary muon subevent and the associated decay electron subevent.

scale systematic, the muon momentum distribution is compared between the two SK periods. As the total number of Cherenkov photons is integrated across the track length, the reconstructed momentum divided by track length (or range) is compared between SK-IV and SK-V as illustrated in Figure 5.8.

The consistency between these distributions has been computed in two ways. Firstly, a Gaussian is fit to *the peak of* each distribution separately, whose *mean* *of* which is found to be $(2.272 \pm 0.003)\text{MeV/cm}$ and $(2.267 \pm 0.006)\text{MeV/cm}$ for SK-IV and SK-V respectively. The ratio of these is equal to 1.002 ± 0.003 . The means of the Gaussian fits are consistent with the expected stopping power of a minimum ionising muon for a target material (water) with $Z/A \sim 0.5$ [188]. The second consistency check is performed by introducing a nuisance parameter, α , which modifies the SK-V distribution. The value of α which minimises the χ^2 value between the SK-IV and SK-V is determined by scanning across a range of values. This is repeated by applying the nuisance parameter as both a multiplicative factor and an additive shift. The χ^2 distributions for different values of α is illustrated in Figure 5.9. The

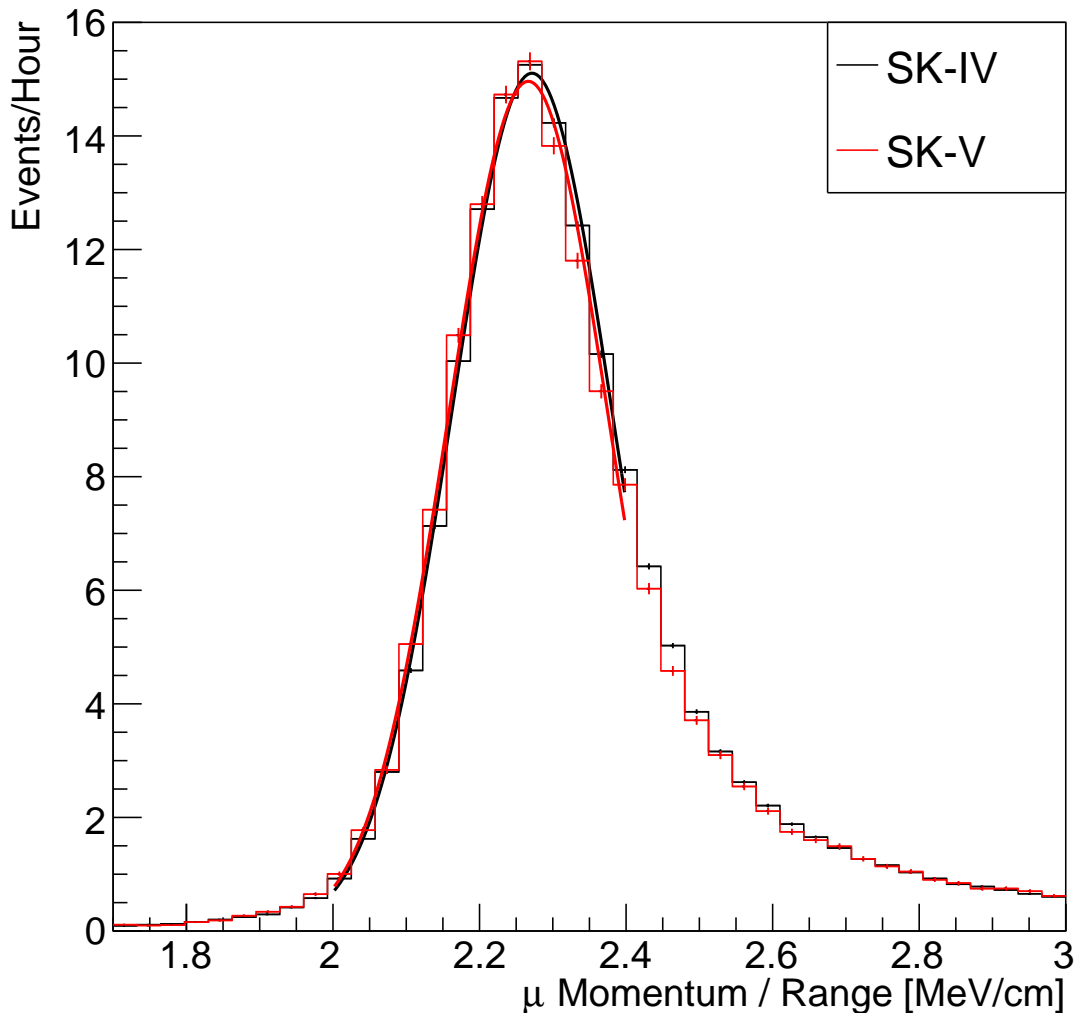


Figure 5.8: The distribution of the reconstructed momentum from the muon ring divided by the distance between the reconstructed muon and decay electron vertices as found in the stopping muon data sets of SK-IV (Black) and SK-IV (Red). Only events with one tagged decay electron are considered. A Gaussian fit is considered in the range [2.0, 2.4] MeV/cm and illustrated as the solid curve.

₁₅₄₈ values which minimise the χ^2 are found to be 0.0052 and 1.0024 for the additive and
₁₅₄₉ multiplicative implementations, respectively. No evidence of shifts larger than the
₁₅₅₀ 2.1% uncertainty on the energy scale systematic has been found in the reconstructed
₁₅₅₁ momentum distribution of SK-IV and SK-V.

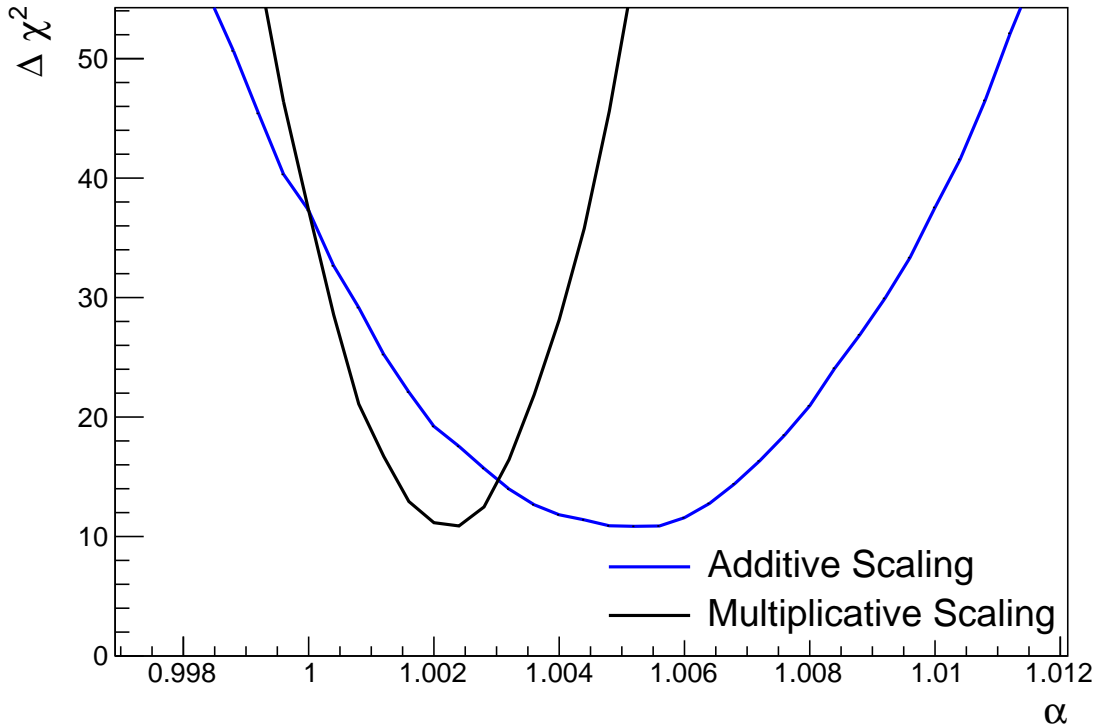


Figure 5.9: The χ^2 difference between the SK-IV and SK-V reconstructed muon momentum divided by range when the SK-V is modified by the scaling parameter α . Both additive (Blue) and multiplicative (Black) scaling factors have been considered. In practice, the additive scaling factor actually uses the value of $(\alpha - 1.0)$ but is illustrated like this so the results can be shown on the same axis range.

1552 5.3 Event Reduction at SK

1553 Atmospheric neutrino events observed in the SK detector are categorised into three
 1554 different types of samples: fully contained (FC), partially contained (PC) and up-going
 1555 muon (Up- μ), using PMT hit signatures in the inner and outer detector (ID and OD,
 1556 respectively). To identify FC neutrino events, it is required that the neutrino interacts
 1557 inside the fiducial volume of the ID and that no significant OD activity is observed. For
 1558 this analysis, an event is defined to be in the fiducial volume provided the event vertex
 1559 is at least 0.5m away from the ID walls. PC events have the same ID requirements
 1560 but can have a larger signal present inside the OD. **Typically these events are higher**

1561 **energy muon interactions that penetrate the ID walls** Typically, only high energy
 1562 **muons from ν_μ interactions can penetrate the ID wall.** The Up- μ sample contains
 1563 events where muons are created from neutrino interactions in the OD water or rock
 1564 below the tank. They then propagate upwards through the detector. Downward-going
 1565 muons generated from neutrino interactions above the tank are neglected is because of
 1566 the difficulty in separating their signature from the cosmic muon shower background.
 1567 The sample categories are visually depicted in Figure 5.10.

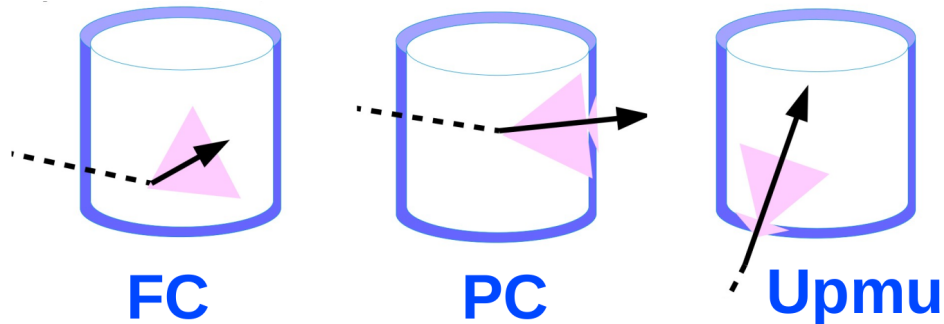


Figure 5.10: A depiction of the topology patterns for fully-contained (FC), partially-contained (PC) and up-going muon (Up- μ) samples included in this analysis.

1568 Based on the event characteristics, as defined by the `fitQun` event reconstruction
 1569 software, the FC events are categorised by

- 1570 • **Visible Energy:** equal to the sum of the reconstructed kinetic energy of particles
 1571 above the Cerenkov threshold for all rings present in the event. The purpose is to
 1572 separate events into sub-GeV and multi-GeV categories.
- 1573 • **Number of observed Cerenkov rings.** The purpose is to separate single-ring and
 1574 multi-ring events, where single-ring events predominantly consist of quasi-elastic
 1575 interactions and multi-ring events are typically resonant pion production or deep
 1576 inelastic scattering events.

- 1577 • **Particle identification parameter of the most energetic ring:** A value deter-
1578 mined from the maximum likelihood value based on `fitQun`'s electron, muon, or
1579 pion hypothesis. The purpose is to separate electron-like and muon-like events.
- 1580 • **Number of decay electrons:** The purpose is to separate quasi-elastic events
1581 (which have one decay electron emitted from the muon decay) and resonant pion
1582 production events (which have two decay electrons emitted from the muon and
1583 pion).

1584 The PC and Up- μ categories are broken down into “through-going” and “stopping”
 1585 samples depending on whether the muon leaves the detector. This is because the **PC**
 1586 stopping events deposit the entire energy of the interaction into the detector, resulting
 1587 in better reconstruction. The energy of events that exit the detector has to be estimated,
 1588 **with typically worse resolution**, which introduces much larger systematic uncertain-
 1589 ties. Through-going Up- μ samples are further broken down by whether any hadronic
 1590 showering was observed in the event which typically indicates DIS interactions. The
 1591 expected neutrino energy for the different categories is given in Figure 5.11. FC sub-
 1592 GeV and multi-GeV events peak around 0.7GeV and 3GeV respectively, with slightly
 1593 different peak energies for ν_e and $n\nu_\mu$ oscillation channels. PC and Up- μ are almost
 1594 entirely comprised of ν_μ events and peak around 7GeV and 100GeV, respectively.

1595 In normal data-taking operations, the SK detector observes many background
 1596 events alongside the beam and atmospheric neutrino signal events of physics inter-
 1597 est **for this thesis**. Cosmic ray muons and flasher events, which are the spontaneous
 1598 discharge of a given PMT, contribute the largest amount of background events in the en-
 1599 ergy range relevant to **any analysis searching for neutrino events this thesis**. Lower
 1600 energy analyses like DSNB searches are also subject to radioactive backgrounds [189].
 1601 Therefore the data recorded is reduced with the aim of removing these background
 1602 events. The reduction process is detailed in [47, 89] and briefly summarised below.

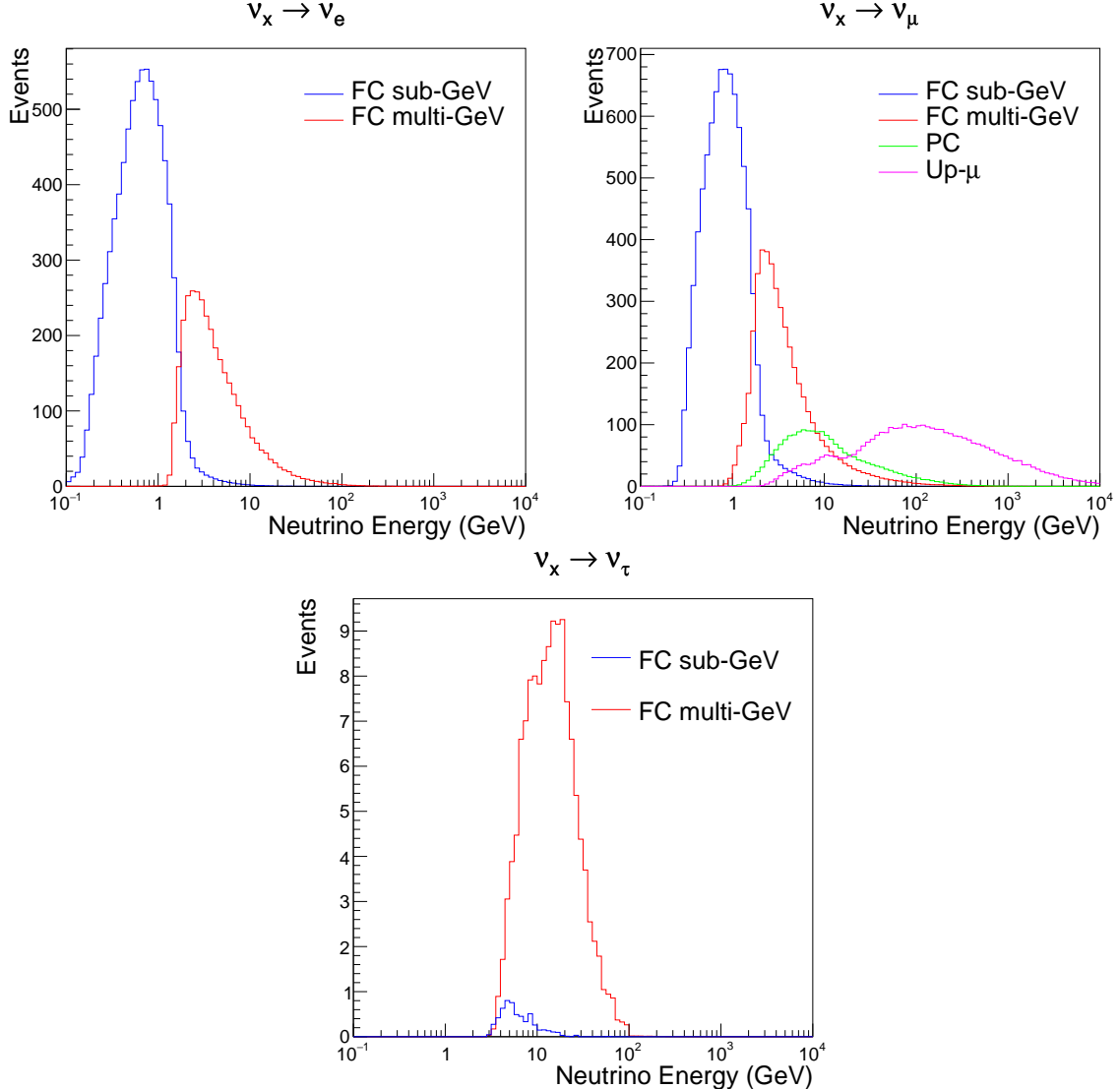


Figure 5.11: The predicted neutrino flux of the fully contained (FC) sub-GeV and multi-GeV, partially contained (PC), and upward-going muon (Up- μ) events. The prediction is broken down by the $\nu_x \rightarrow \nu_e$ prediction (top left), $\nu_x \rightarrow \nu_\mu$ prediction (top right) and $\nu_x \rightarrow \nu_\tau$ prediction (bottom). Asimov A oscillation parameters are assumed (given in Table 2.2).

1603 The first two steps in the FC reconstruction remove the majority of cosmic ray
 1604 muons by requiring a significant amount of ID activity compared to that measured in
 1605 the OD. Events that pass this cut are typically very high momentum muons or events
 1606 that leave very little activity in the OD. Consequently, a third reduction step is then
 1607 applied to select cosmic-ray muons that pass the initial reduction step. A purpose-built
 1608 cosmic muon fitter is used to determine the entrance (or exit) position of the muon and

1609 a cut is applied to OD activity contained within 8m of this position. Flasher events are
 1610 removed in the fourth reduction step which is based on the close proximity of PMT
 1611 hits surrounding the PMT producing the flash. Events that pass all these reduction
 1612 steps are reconstructed with the APFit algorithm. The fifth step of the reduction uses
 1613 information from the more precise fitter to repeat the previous two steps with tighter
 1614 cuts. Muons below the Cherenkov threshold can not generate optical photons in the
 1615 ID but the associated decay electron can due to its lower mass. These are the types of
 1616 events targeted in the fifth reduction step. The final cuts require the event vertex to be
 1617 within the fiducial volume (0.5m from the wall although the nominal distance is 2.0m),
 1618 visible energy $E_{vis} > 30\text{MeV}$ and fewer than 16 hits within the higher energy OD
 1619 cluster. The culmination of the fully contained reduction results in 8.09 events/day in
 1620 the nominal fiducial volume [190]. The uncertainty in the reconstruction is calculated
 1621 by comparing Monte Carlo prediction to data. The largest discrepancy is found to be
 1622 1.3% in the fourth reduction step.

1623 The PC and Up- μ events are processed through their own reduction processes
 1624 detailed in [47]. Both of these samples are reconstructed with the APFit algorithm
 1625 rather than fitQun. This is because the efficiency of reconstructing events that leave
 1626 the detector has not been sufficiently studied for reliable systematic uncertainties wth
 1627 fitQun. The PC and Up- μ samples acquire events at approximately 0.66 and 1.44
 1628 events/day.

1629 Events due to beam neutrinos undergo the same reduction steps as FC events and
 1630 are then subject to further cuts [191]. The GPS system which links the timing between
 1631 the beam facility and SK needs to be operating correctly and there should be no activity
 1632 within the detector in the previous $100\mu\text{s}$ before the trigger. The events then need to
 1633 triggered between $-2\mu\text{s}$ and $10\mu\text{s}$ of the expected spill timing.

1634 Due to the lower energy beam neutrinos, the T2K samples are not dependent
 1635 upon the visible energy neutrino as the range of neutrino energies are smaller than
 1636 that found in atmospheric neutrinos. Furthermore, the 2020 T2K-only oscillation
 1637 analysis only considers events which contain a single ring. Similar to atmospheric
 1638 event selection, the number of decay electrons is used as a proxy for distinguishing
 1639 CCQE and CCRES events. The expected neutrino energy, broken down by number
 1640 of decay electrons, is given in ???. The beam neutrinos samples are not split by
 1641 visible energy since their energy range is smaller than the atmospheric neutrino
 1642 events. Following the T2K analysis in [80], only single-ring beam neutrino events
 1643 are considered. Similar to atmospheric event selection, the number of decay electrons
 1644 is used as a proxy for distinguishing CCQE and CCRES events. The expected neutrino
 1645 energy, broken down by number of decay electrons, is given in Figure 5.12.

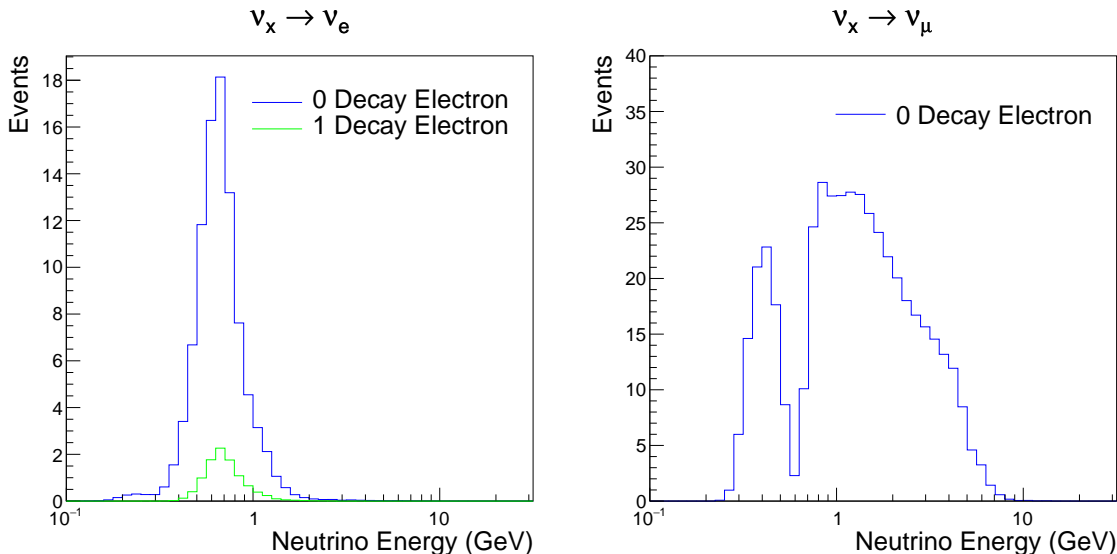


Figure 5.12: The predicted flux of beam neutrinos, as a function of neutrino energy. The predictions are broken down by the number of decay electrons associated with the particular events. Asimov A oscillation parameters are assumed (given in Table 2.2).

1646 **Chapter 6**

1647 **Sample Selections and Systematics**

1648 The oscillation analysis presented within this thesis is built upon a simultaneous
1649 fit to atmospheric data at SK, neutrino beam data in the near detector, and beam
1650 data measured at SK. The definitions of these samples are documented in section 6.1,
1651 section 6.2, and section 6.3, respectively. The data collected and used within this
1652 analysis is detailed in Table 6.1. The near and far detector data corresponds to T2K
1653 runs 2-9 and runs 1-10, respectively. The accumulated POT and beam power for runs
1654 1 – 10 are illustrated in Figure 6.1.

| Data Type | Total |
|-------------------|---------------------------|
| Near Detector FHC | 1.15×10^{21} POT |
| Near Detector RHC | 8.34×10^{20} POT |
| Far Detector FHC | 1.97×10^{21} POT |
| Far Detector RHC | 1.63×10^{21} POT |
| Atmospheric SK-IV | 3244.4 days |

Table 6.1: The amount of data collected in each detector used within this analysis. The data collected at the near and far detector, for both neutrino beam (FHC) and antineutrino beam (RHC), is measured as the number of protons on target (POT).

1655 The difference in POT recorded at the near and far detector is due to the difference
1656 in downtime of the respective detector. The SK detector is very stable with almost 100%
1657 of data recorded during beam operation. Due to various technical and operational
1658 issues, the downtime of the near detector is significantly higher due to its more
1659 complex design and operating requirements.

1660 The systematic parameters invoked within the flux, detector, and interaction models
 1661 used within this analysis are documented in section 6.4. The standard configuration of
 1662 the joint beam and atmospheric data fit utilises far detector systematics provided in
 1663 the official inputs from the two experiments. Additionally, a correlated detector model
 1664 which fits the parameters used in sample selections to data has been developed and
 1665 documented in subsection 6.4.5.

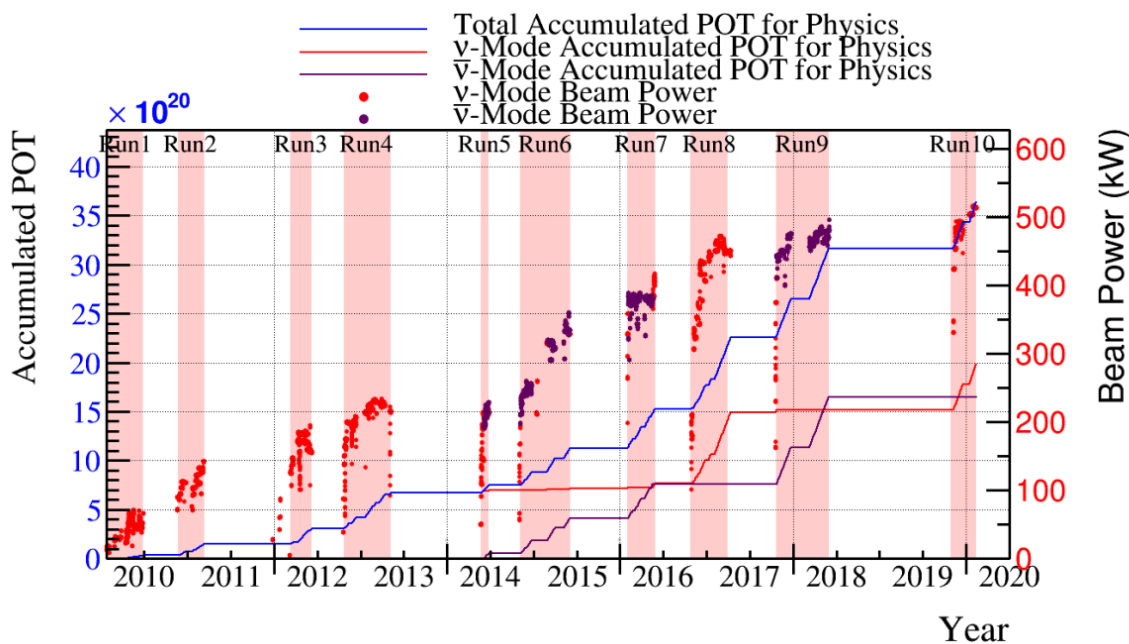


Figure 6.1: The accumulated beam data, measured as the number of protons on target (POT). The total data (blue) is given which comprises of the neutrino beam (red) and antineutrino (purple) components. The beam power for neutrino and antineutrino beams is given as the markers using the same colour scheme. The timescale runs from Run 1 which started in January 2010 until Run 10 which ended in February 2020. The ratio of accumulated data in neutrino and antineutrino beam is 54.7% : 45.3%.

1666 6.1 Atmospheric Samples

1667 The atmospheric event selection follows the official SK-IV analysis presented in [89]
1668 and is documented below. The Monte Carlo prediction used within this analysis
1669 corresponds to 500 years worth of neutrino events, which is scaled down to match the
1670 SK-IV livetime of 3244.4 days.

1671 The fully contained (FC), partially contained (PC), and upward going muon events
1672 ($\text{up-}\mu$) which pass the reduction cuts discussed in section 5.3 are further broken down
1673 into different samples based on reconstruction information. This section details the
1674 samples used within this oscillation analysis, alongside the chosen binning, used
1675 within the fit.

1676 FC events are first separated by the visible energy deposited within the detector.
1677 This is calculated as the sum of the reconstructed kinetic energy above the Cherenkov
1678 threshold for all rings present in the event. Events are separated by whether they were
1679 above or below $E_{\text{vis}} = 1.33\text{GeV}$. This separates “subGeV” and “multiGeV” events.
1680 Typically, lower energy events consist of charge current quasi-elastic (CCQE) inter-
1681 actions which are better understood and simpler to reconstruct resulting in smaller
1682 systematic uncertainties. Events are further separated by the number of rings as-
1683 sociated with the event due to similar reasoning. As the oscillation probability is
1684 dependent upon the flavour of neutrino, electron and muon events are separated
1685 using a similar likelihood method to that discussed in section 5.2. To reduce computa-
1686 tional resources required for the reconstruction, only electron and pion hypotheses are
1687 considered so this separation cut depends on the ratio of the electron to pion likeli-
1688 hoods, $\log(L_e/L_\pi)$. Finally, the number of decay electrons is used to classify events.
1689 Charged current resonant pion production (CCRES) interactions generate a final-state
1690 pion. This can decay, mostly likely through a muon, into a decay electron. Therefore

- any electron-like event with one decay electron or muon-like event with two decay electrons was most likely produced by a CCRES interaction. Consequently, the number of decay electrons can be used to distinguish CCQE and CCRES interaction modes. Ultimately, FC subGeV events are separated into the samples listed in Table 6.2.

| Sample Name | Description |
|--------------------|---|
| SubGeV-e-like-0dcy | Single ring e -like events with zero decay electrons |
| SubGeV-e-like-1dcy | Single ring e -like events with one or more decay electrons |
| SubGeV-mulike-0dcy | Single ring μ -like events with zero decay electrons |
| SubGeV-mulike-1dcy | Single ring μ -like events with one decay electrons |
| SubGeV-mulike-2dcy | Single ring μ -like events with two or more decay electrons |
| SubGeV-pi0like | Two e -like ring events with zero decay electrons and reconstructed π^0 mass $85 \leq m_{\pi^0} < 215\text{MeV}$ |

Table 6.2: The fully contained subGeV samples, defined as events with visible energy $E_{vis} < 1.33\text{GeV}$, used within this oscillation analysis.

- In addition to the cuts discussed above, multiGeV samples also have additional cuts to separate samples which target neutrino and antineutrino separation. As discussed in section 7.1, the matter resonance only occurs for neutrinos in normal hierarchy and antineutrinos in an inverted mass hierarchy. Therefore, having flavour-enriched samples aids in the determination of the mass hierarchy. For a CCRES interaction,

$$\begin{aligned}
 \bar{\nu}_e + N &\rightarrow e^+ + N' + \pi^-, \\
 \nu_e + N &\rightarrow e^- + N' + \pi^+ \\
 &\quad \downarrow \mu^+ + \nu_\mu \\
 &\quad \downarrow e^+ + \nu_e + \bar{\nu}_\mu.
 \end{aligned} \tag{6.1}$$

- The π^- emitted from a $\bar{\nu}_e$ interaction is more likely to be absorbed within the oxygen nucleus compared to the π^+ from ν_e interactions [192]. These pions then

1702 decay, mostly through muons, to electrons. Therefore the number of tagged decay
 1703 electrons associated with an event gives an indication of whether the interaction
 1704 was due to a neutrino or antineutrino: zero for $\bar{\nu}_e$ events, and one for ν_e events.
 1705 The ability to separate neutrino from antineutrino events is illustrated in Table 6.4,
 1706 where the MultiGeV-*e*like-nue has 78% purity of neutrino interactions with only 7%
 1707 antineutrino background in that sample and the rest of the sample comprising of
 1708 neutral current backgrounds.

1709 This relatively simple discriminator works reasonably well for single-ring events.
 1710 However, this is not the case for multi-ring events. A multiGeV multiring separation
 1711 (MME) likelihood cut which specifically targets multiGeV multiRing electron-like
 1712 events was introduced in [193, 194]. This is a two-stage likelihood selection cut. Four
 1713 observables are used within the first likelihood cut to distinguish CC ν_e and CC $\bar{\nu}_e$
 1714 events from background:

- 1715 • The number of decay electrons
- 1716 • The maximum distance between the vertex of the neutrino and the decay electrons
- 1717 • The energy deposited by the leading energy ring
- 1718 • The reconstructed particle identification of that highest energy ring

1719 Background events consist of CC ν_μ and NC interactions. Typically these produce
 1720 events where the majority of the energy is carried by the hadronic system. Additionally,
 1721 muons tend to travel further than the pions from CC ν_e before decaying. Consequently,
 1722 the parameters used within the likelihood cut target the typical background interaction
 1723 kinematics.

1724 Neutrino and antineutrino events are then separated by a second likelihood method
 1725 ($\nu/\bar{\nu}$ separation) detailed in [52]. This uses the number of decay electrons, the number
 1726 of reconstructed rings, and the event's transverse momentum. The last two parameters

| Sample Name | Description |
|----------------------------------|--|
| MultiGeV- <i>e</i> -like-nue | Single ring <i>e</i> -like events with zero decay electrons |
| MultiGeV- <i>e</i> -like-nuebar | Single ring <i>e</i> -like events with one or more decay electrons |
| MultiGeV- <i>μ</i> -like | Single ring <i>μ</i> -like events |
| MultiRing- <i>e</i> -like-nue | Two or more ring events with leading energy <i>e</i> -like ring and passed both MME and $\nu/\bar{\nu}$ separation cuts |
| MultiRing- <i>e</i> -like-nuebar | Two or more ring events with leading energy <i>e</i> -like ring and passed MME and failed $\nu/\bar{\nu}$ separation cuts |
| MultiRing- <i>μ</i> -like | Two or more ring events with leading energy <i>μ</i> -like ring and only requires $E_{vis} > 0.6\text{GeV}$ DB: Why is this not }1.33\text{GeV? N |
| MultiRing-Other1 | Two or more ring events with leading energy <i>e</i> -like ring and failed the MME likelihood cut |

Table 6.3: The fully contained multiGeV samples used within this oscillation analysis. Both the sample name and description are given.

1727 are used because higher-energy samples tend to have more pions produced above
 1728 the Cherenkov threshold which results in more rings compared to an antineutrino
 1729 interaction. Furthermore, the angular distribution also tends to be more forward
 1730 peaked in antineutrino interactions as compared to neutrino interactions [89]. These
 1731 FC multiGeV sample definitions are detailed in Table 6.3.

1732 The PC and up- μ events are split by the amount of energy deposited within the
 1733 outer detector, into “stopping” and “through-going” samples. This is because the
 1734 momentum of events leaving the detector has to be approximated, which increases the
 1735 systematic uncertainty. This estimate is particularly poor for very high-energy events.
 1736 This is why up- μ through-going events are not binned in reconstructed momentum.
 1737 If an event leaves the detector, the energy it takes with it has to be estimated which
 1738 increases the systematic uncertainty compared to events entirely contained within the
 1739 inner detector. The through-going up- μ are further separated by the presence of any
 1740 electromagnetic showering in the event, as the assumption of non-showering muon

- ₁₇₄₁ does not give reliable reconstruction for these types of events [47]. In total, 13 FC, 2
₁₇₄₂ PC, and 3 up- μ atmospheric samples are included within this analysis.

| Sample | CC ν_e | CC $\bar{\nu}_e$ | CC($\nu_\mu + \bar{\nu}_\mu$) | CC($\nu_\tau + \bar{\nu}_\tau$) | NC |
|------------------------|------------|------------------|---------------------------------|-----------------------------------|-------|
| SubGeV-elike-0dcy | 72.17 | 23.3 | 0.724 | 0.033 | 3.77 |
| SubGeV-elike-1dcy | 86.81 | 1.773 | 7.002 | 0.062 | 4.351 |
| SubGeV-mulike-0dcy | 1.003 | 0.380 | 90.07 | 0.036 | 8.511 |
| SubGeV-mulike-1dcy | 0.023 | 0. | 98.46 | 0.029 | 1.484 |
| SubGeV-mulike-2dcy | 0.012 | 0. | 99.25 | 0.030 | 0.711 |
| SubGeV-pi0like | 6.923 | 2.368 | 0.928 | 0.011 | 89.77 |
| MultiGeV-elike-nue | 78.18 | 7.041 | 3.439 | 1.886 | 9.451 |
| MultiGeV-elike-nuebar | 56.68 | 37.81 | 0.174 | 0.614 | 4.718 |
| MultiGeV-mulike | 0.024 | 0.005 | 99.67 | 0.245 | 0.058 |
| MultiRing-elike-nue | 59.32 | 12.39 | 4.906 | 3.385 | 20 |
| MultiRing-elike-nuebar | 52.39 | 31.03 | 1.854 | 1.585 | 13.14 |
| MultiRing-mulike | 0.673 | 0.080 | 97.33 | 0.342 | 1.578 |
| MultiRingOther-1 | 27.98 | 2.366 | 34.93 | 4.946 | 29.78 |
| PCStop | 8.216 | 3.118 | 84.45 | 0. | 4.214 |
| PCThrus | 0.564 | 0.207 | 98.65 | 0. | 0.576 |
| UpStop-mu | 0.829 | 0.370 | 98.51 | 0. | 0.289 |
| UpThruNonShower-mu | 0.206 | 0.073 | 99.62 | 0. | 0.103 |
| UpThruShower-mu | 0.128 | 0.054 | 99.69 | 0. | 0.132 |

Table 6.4: The purity of each atmospheric sample used within this analysis, broken down by charged current (CC) and neutral current (NC) interactions and which neutrino flavour interacted within the detector. Asimov A oscillation parameter sets are assumed (given in Table 2.2). Electron neutrino and antineutrino events are separated to illustrate the ability of the separation likelihood cuts used within the multiGeV and multiring sample selections.

- ₁₇₄₃ The atmospheric samples are binned in direct observables: reconstructed lepton
₁₇₄₄ momentum and direction, as given by Table 6.5. The distribution of the reconstructed
₁₇₄₅ lepton momentum (for samples that only have one bin reconstructed zenith angle)
₁₇₄₆ and reconstructed direction for each atmospheric sample used within this analysis is
₁₇₄₇ illustrated in Figure 6.2.

| Sample | $\cos(\theta_Z)$ Bins | Momentum Bin Edges ($\log_{10}(P)$ MeV) |
|---------------------------------|-----------------------|--|
| SubGeV- <i>e</i> like-0dcy | 10 | 2.0, 2.4, 2.6, 2.8, 3.0, 3.2 |
| SubGeV- <i>e</i> like-1dcy | 1 | 2.0, 2.4, 2.6, 2.8, 3.0, 3.2 |
| SubGeV- <i>m</i> ulike-0dcy | 10 | 2.0, 2.4, 2.6, 2.8, 3.0, 3.2 |
| SubGeV- <i>m</i> ulike-1dcy | 10 | 2.0, 2.4, 2.6, 2.8, 3.0, 3.2 |
| SubGeV- <i>m</i> ulike-2dcy | 1 | 2.0, 2.4, 2.6, 2.8, 3.0, 3.2 |
| SubGeV- <i>p</i> i0like | 1 | 2.0, 2.2, 2.4, 2.6, 2.8, 3.2 |
| MultiGeV- <i>e</i> like-nue | 10 | 3.0, 3.4, 3.7, 4.0, 5.0 |
| MultiGeV- <i>e</i> like-nuebar | 10 | 3.0, 3.4, 3.7, 4.0, 5.0 |
| MultiGeV- <i>m</i> ulike | 10 | 3.0, 3.4, 5.0 |
| MultiRing- <i>e</i> like-nue | 10 | 3.0, 3.4, 3.7, 5.0 |
| MultiRing- <i>e</i> like-nuebar | 10 | 3.0, 3.4, 3.7, 5.0 |
| MultiRing- <i>m</i> ulike | 10 | 2.0, 3.124, 3.4, 3.7, 5.0 |
| MultiRing- <i>O</i> ther1 | 10 | 3.0, 3.4, 3.7, 4.0, 5.0 |
| PC-Stop | 10 | 2.0, 3.4, 5.0 |
| PC-Through | 10 | 2.0, 3.124, 3.4, 3.7, 5.0 |
| Upmu-Stop | 10 | 3.2, 3.4, 3.7, 8.0 |
| Upmu-Through-Showering | 10 | 2.0, 8.0 |
| Upmu-Through-NonShowering | 10 | 2.0, 8.0 |

Table 6.5: The reconstructed cosine zenith and lepton momentum binning assigned to the atmospheric samples. The “ $\cos(\theta_Z)$ Bins” column illustrates the number of bins uniformly distributed over the $-1.0 \leq \cos(\theta_Z) \leq 1.0$ region for fully and partially contained samples and $-1.0 \leq \cos(\theta_Z) \leq 0.0$ region for up- μ samples. **DB: Does this belong in the appendix?**

1748

DB: By-mode spectra of each sample needed? ie. Figure 6.3 for atmospherics?

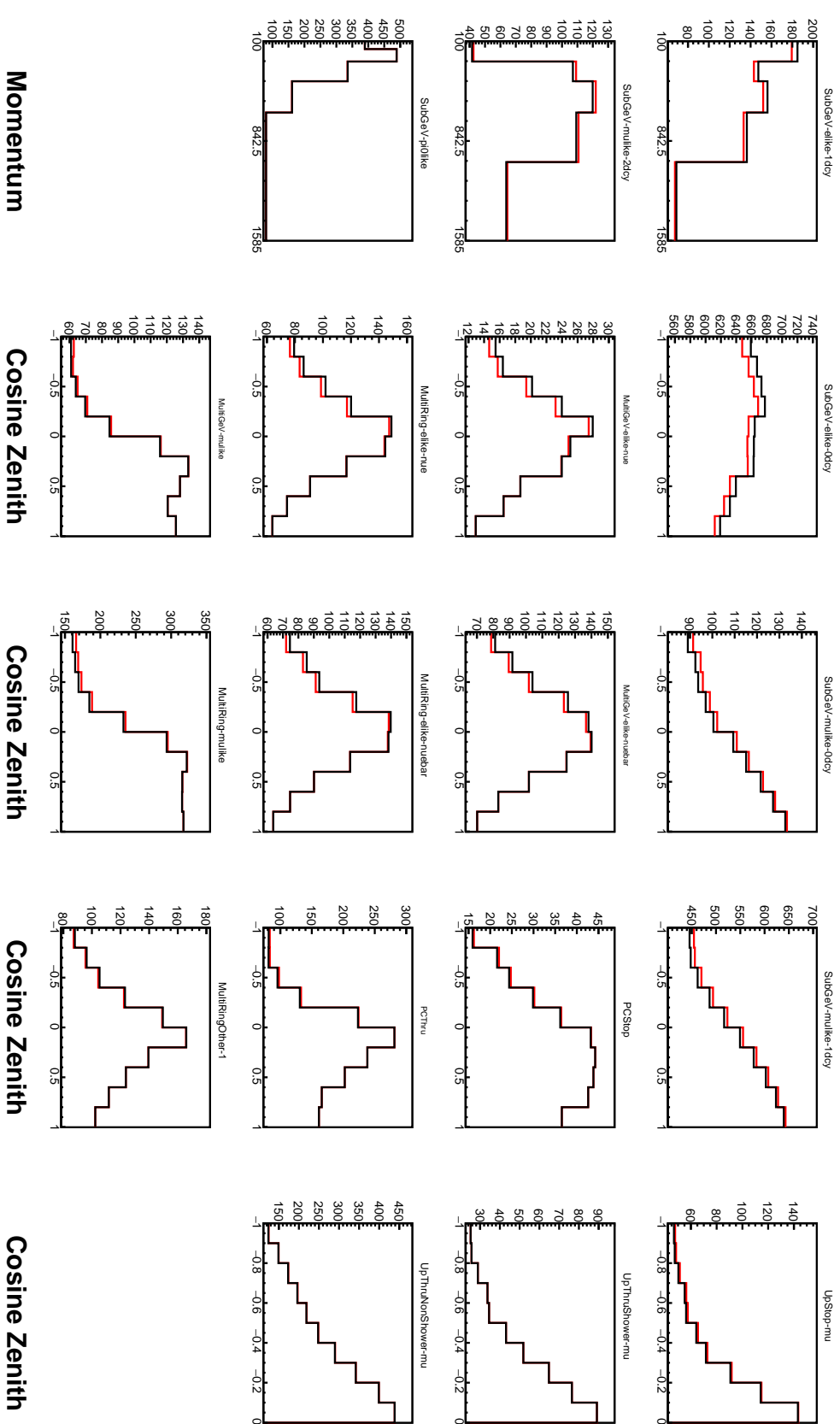


Figure 6.2: Comparison of the SK-IV atmospheric samples between predictions made with the CP-violating Asimov A (Black) and CP-conserving Asimov B (Red) oscillation parameter sets (given in Table 2.2). The subGeV samples CCRES and π^0 -like samples are given in their reconstructed lepton momentum. All other samples are presented in their reconstructed zenith angle projection.

¹⁷⁴⁹ 6.2 Near Detector Beam Samples

¹⁷⁵⁰ The near detector sample selections are documented in detail within [195] and sum-
¹⁷⁵¹ marised below. Samples are selected based upon the particular FGD in which the
¹⁷⁵² vertex of the neutrino interaction is in as well as the operating mode of the beam:
¹⁷⁵³ FHC or RHC. For additional constraints on model parameters, wrong-sign neutrino
¹⁷⁵⁴ samples are also considered when the beam is operating in RHC mode. Samples
¹⁷⁵⁵ from the wrong-sign component of the FHC beam mode are not included as they are
¹⁷⁵⁶ statistically insignificant compared to those samples already listed.

¹⁷⁵⁷ Before being assigned a sample, all events must undergo CC-inclusive cuts, as
¹⁷⁵⁸ defined in [196]:

- ¹⁷⁵⁹ • Event Timing: The DAQ must be operational and the event must occur within
¹⁷⁶⁰ the expected beam time window
- ¹⁷⁶¹ • TPC Requirement: The track path must intercept one or more TPCs
- ¹⁷⁶² • Fiducial volume: The event must originate from within the fiducial volume. The
¹⁷⁶³ fiducial volumes are defined as a region within each sub-detector [197].
- ¹⁷⁶⁴ • Upstream Background: Remove events that have muons tracks that originate
¹⁷⁶⁵ upstream of the FGDs by requiring no high-momentum tracks within 150mm
¹⁷⁶⁶ upstream of the candidate vertex. Additionally, events that occur within the
¹⁷⁶⁷ downstream FGD are vetoed if a secondary track starts within the upstream FGD
- ¹⁷⁶⁸ • Broken track removal: All candidates where the muon candidate is broken in two
¹⁷⁶⁹ are removed
- ¹⁷⁷⁰ • Muon PID: Measurements of dE/dx in a TPC are used to distinguish muon-like
¹⁷⁷¹ events using a likelihood cut

₁₇₇₂ In addition to these cuts, RHC neutrino events also have to undergo the following
₁₇₇₃ cuts to aid in the separation of neutrino and antineutrino [198]:

- ₁₇₇₄ • TPC Requirement: The track path must intercept TPC2
- ₁₇₇₅ • Positive Track: The highest momentum track must be positive
- ₁₇₇₆ • TPC1 Veto: Remove any events originating upstream of TPC1

₁₇₇₇ Once all CC-inclusive events have been determined, they are further segregated
₁₇₇₈ into sub-samples that target the constraints on interaction modes most relevant at
₁₇₇₉ the far detector. They are split by pion multiplicity: CC0 π , CC1 π , and CCOther.
₁₇₈₀ These target specific interaction modes CCQE, CCRES, and other CC background
₁₇₈₁ interactions, respectively. Pions in the TPCs and FGDs are selected by requiring a
₁₇₈₂ second track to be observed, which is separate from the muon track and is in the same
₁₇₈₃ beam spill window and sub-detector. If the pion originated within a FGD, it must also
₁₇₈₄ pass through the sequential downstream TPC (TPC2 for FGD1, TPC3 for FGD2).

₁₇₈₅ CC0 π , CC1 π , and CCOther samples are defined with the following cuts:

- ₁₇₈₆ • ν_μ CC0 π Selection: No electrons in TPC and no charged pions or decay electrons
₁₇₈₇ within the TPC or FGD
- ₁₇₈₈ • ν_μ CC1 π Selection: Exactly one charged pion in either the TPC or FGD, where
₁₇₈₉ the number of charged pions in the FGD is equal to the number of decay electrons
- ₁₇₉₀ • ν_μ CCOther Selection: All events which are not classified into the above two
₁₇₉₁ selections.

₁₇₉₂ Counting the three selections for each FGD in FHC and RHC running, including
₁₇₉₃ the wrong-sign background in RHC, 18 near detector samples are used within this
₁₇₉₄ analysis. These samples are binned in reconstructed lepton momentum (illustrated in
₁₇₉₅ Figure 6.3) and direction with respect to the beam. The binning is chosen such that

each event has at least 20 Monte Carlo events in each bin [197]. This is to ensure that the bins are coarse enough to ensure the reduction of statistical errors, whilst also being fine enough to sample the high-resolution peak regions. The exact binning is detailed in [197].

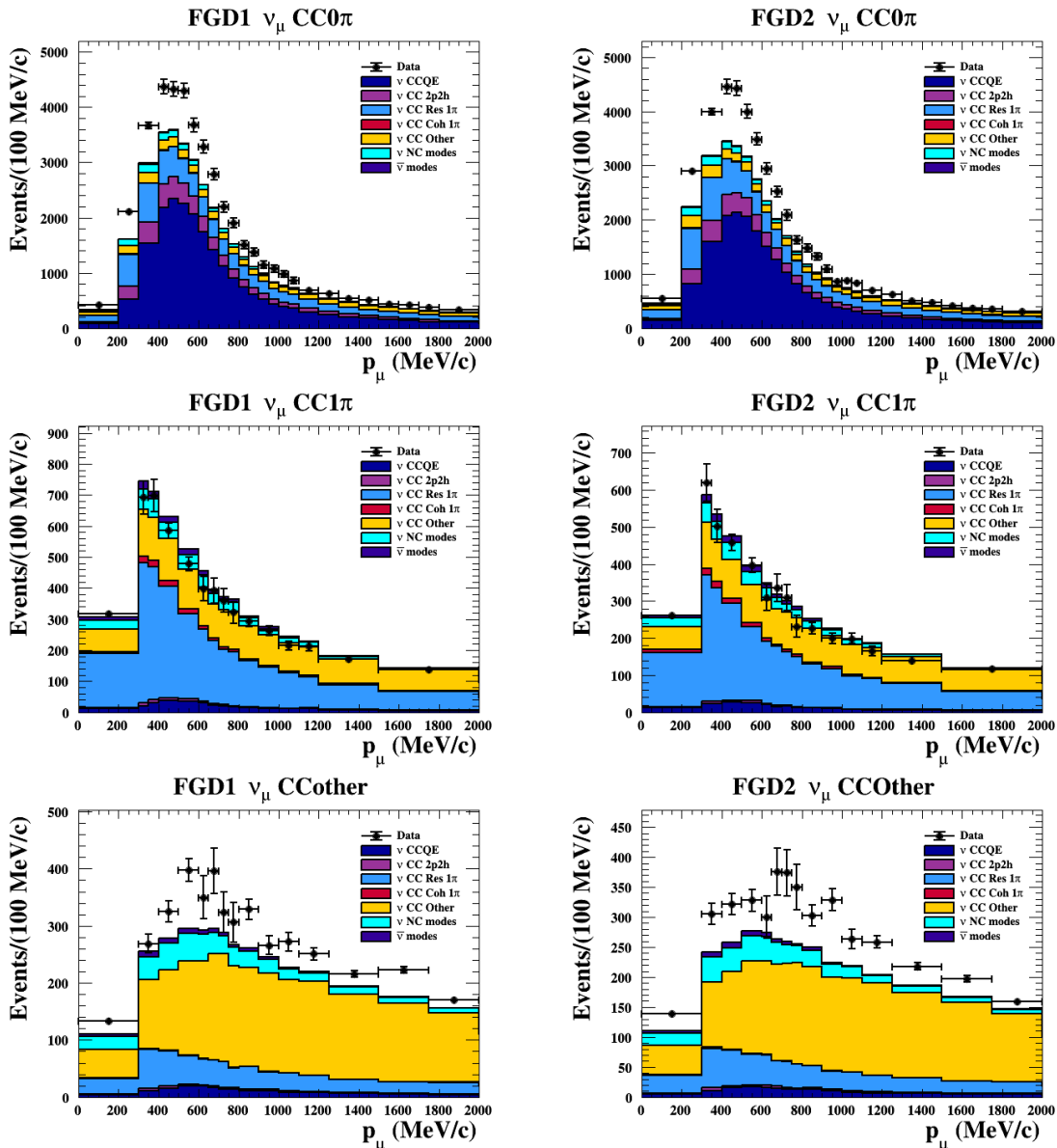


Figure 6.3: The nominal Monte Carlo predictions for the FGD1 and FGD2 samples in neutrino beam mode, broken down into the $\text{CC}\nu_\mu 0\pi$, $\text{CC}\nu_\mu 1\pi$ and $\text{CC}\nu_\mu$ Other categories. Figures taken from [195].

1800 6.3 Far Detector Beam Samples

1801 The beam neutrino events which occur at the SK detector, which pass the reduction cuts
1802 detailed in section 5.3, are separated depending on whether the beam was operating
1803 in FH or RHC mode. The events are then separated into three samples: electron-like
1804 ($1Re$), muon-like ($1R\mu$), and CC $1\pi^+$ -like ($1Re1de$) which are observed as electron-like
1805 events with an associated decay electron [185]. As discussed in section 6.1, positively
1806 charged pions emitted from neutrino interactions are more likely to produce decay
1807 electrons than negatively charged pions. Consequently, the CC $1\pi^+$ -like sample is only
1808 selected when the beam is operating in FHC mode. Therefore, five beam samples
1809 measured at SK are used in this analysis.

1810 The fiducial volume definition for beam samples is slightly different from that used
1811 within the atmospheric samples. It uses both the distance to the closest wall (d_{Wall})
1812 and the distance to the wall along the trajectory of the particle (to_{Wall}). This allows
1813 events that originate close to the wall but are facing into the tank to be included within
1814 the analysis, which would have otherwise been removed. These additional events are
1815 beneficial for a statistics-limited experiment. The exact cut values for both d_{Wall} and
1816 to_{Wall} are different for each of the three types of sample and are optimised based on
1817 T2K sensitivity to δ_{CP} [183, 199]. They are:

1818 DB: Diagram of d_{Wall} and to_{Wall} needed?

1819 **1Re event selection** For an event to be classified as a $1Re$ -like, the event must follow:

- 1820 • Fully-contained and within $d_{Wall} > 80\text{cm}$ and $to_{Wall} > 170\text{cm}$
- 1821 • Total of one ring which is reconstructed as electron-like with reconstructed mo-
1822 mentum $P_e > 100\text{MeV}$

- ₁₈₂₃ • Zero decay electrons are associated with the event

- ₁₈₂₄ • Passes π^0 rejection cut discussed in section 5.2

₁₈₂₅ The zero decay electron cut specifically targets CCQE interactions. Whereas, the π^0
₁₈₂₆ rejection cut is designed to remove neutral current π^0 background events which can
₁₈₂₇ be easily reconstructed as 1Re-like events.

₁₈₂₈ **CC1 π^+ event selection** This event selection is very similar to that of the 1Re sample.
₁₈₂₉ The only difference is that the dWall and toWall criteria are changed to $> 50\text{cm}$ and
₁₈₃₀ $> 270\text{cm}$, respectively. Furthermore, exactly one decay electron is required from the
₁₈₃₁ π^+ decay.

₁₈₃₂ **1R μ event selection** A 1R μ -like event is determined by the following cuts:

- ₁₈₃₃ • Fully-contained and within $\text{dWall} > 50\text{cm}$ and $\text{toWall} > 250\text{cm}$

- ₁₈₃₄ • Total of one ring which is reconstructed as muon-like with reconstructed momen-
₁₈₃₅ tum $P_\mu > 200\text{MeV}$

- ₁₈₃₆ • Fewer than two decay electrons are associated with the event

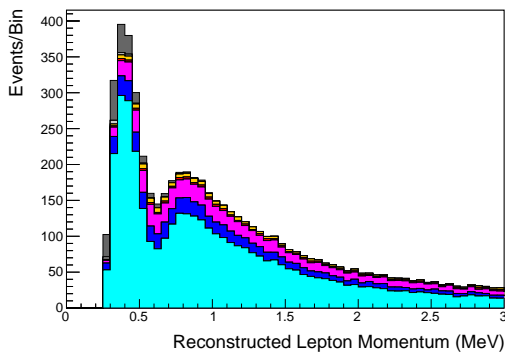
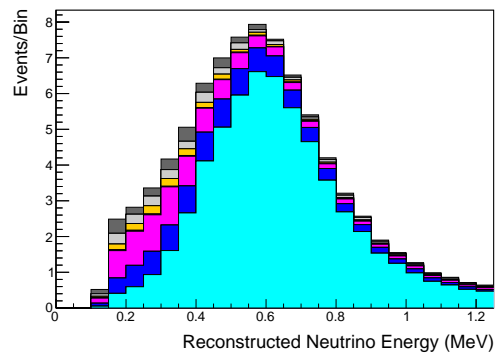
- ₁₈₃₇ • Passes π^+ rejection cut discussed in section 5.2

₁₈₃₈ As pions and muons have similar masses, the Cherenkov rings they generate have
₁₈₃₉ similar opening angles. To enhance the purity, the events have to pass the π^+ rejection
₁₈₄₀ cut which is specifically optimised to separate the two types of events.

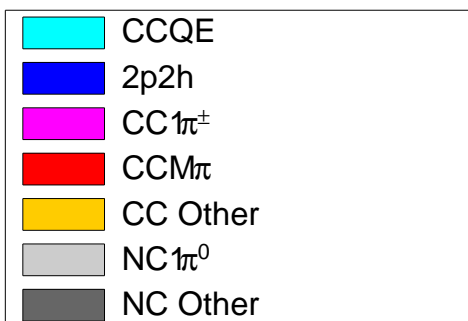
₁₈₄₁ All of these samples are binned in reconstructed neutrino energy. This is possible
₁₈₄₂ as the direction from the source is known extremely well. This value is calculated for
₁₈₄₃ the 1Re-like and 1R μ -like samples assuming CCQE interactions,

$$E_\nu^{rec} = \frac{(M_N - V_{nuc})E_l - m_l^2/2 + M_N V_{nuc} - V_{nuc}^2/2 + (M_P^2 + M_N^2)/2}{M_N - V_{nuc} - E_l + P_l \cos(\theta_{beam})} \quad (6.2)$$

Where M_N , M_P and m_l are the masses of the neutron, proton and outgoing lepton, respectively. $V_{nuc} = 27\text{MeV}$ is the binding energy of the oxygen nuclei [185], θ_{beam} is the angle between the beam and the direction of the outgoing lepton, and E_l and P_l are the energy and momentum of that outgoing lepton.

(a) FHC 1R μ 

(b) FHC 1Re



(c)

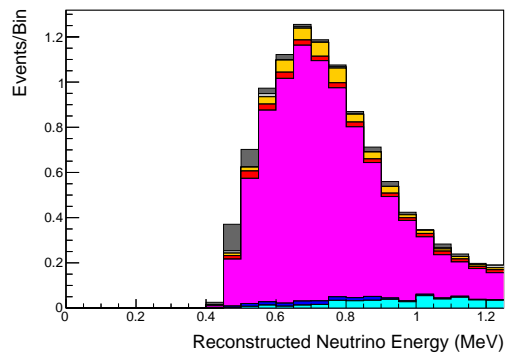
(d) FHC CC1 π^+

Figure 6.4: The reconstructed neutrino energy, as defined by Equation 6.2 and Equation 6.3, for the 1R μ -like, 1Re-like and CC1 π^+ -like samples. Asimov A oscillation parameter sets are assumed (given in Table 2.2). These samples are the FHC mode samples. For ease of viewing, the 1R μ sample only shows the $0. \leq E_\nu^{rec} < 3.0\text{GeV}$ but the binning extends to 30.0GeV.

₁₈₄₈ The reconstructed neutrino energy of the CC1 π^+ -like events is modified to include
₁₈₄₉ the delta resonance produced within the interaction,

$$E_\nu^{rec} = \frac{2M_N E_l + M_{\Delta^{++}}^2 - M_N^2 - m_l^2}{2(M_N - E_l + P_l \cos(\theta_{beam}))} \quad (6.3)$$

₁₈₅₀ Where $M_{\Delta^{++}}$ is the mass of the delta baryon. Binding energy effects are not
₁₈₅₁ considered as a two-body process with the delta baryon is assumed. This follows
₁₈₅₂ the T2K oscillation analysis presented in [80], although recent developments of the
₁₈₅₃ interaction model in the latest T2K oscillation analysis do include effects from binding
₁₈₅₄ energy in this calculation [200].

₁₈₅₅ The reconstructed neutrino energy for the FHC samples is illustrated in Figure 6.4.
₁₈₅₆ As expected, the 1R μ -like and 1Re-like samples are heavily dominated by CCQE in-
₁₈₅₇ teractions, with smaller contributions from 2p2h meson exchange and resonant pion
₁₈₅₈ production interactions. The CC1 π^+ -like sample predominantly consists of charged
₁₈₅₉ current resonant pion production interactions. The 1Re-like and CC1 π^+ -like samples
₁₈₆₀ are also binned by the angle between the neutrino beam and the reconstructed lepton
₁₈₆₁ momentum. This is to aid in charged current and neutral current separation, as indi-
₁₈₆₂ cated in Figure 6.5. This is because the neutral current backgrounds are predominantly
₁₈₆₃ due to π^0 -decays, where the opening angle of the two gammas alongside the different
₁₈₆₄ final state kinematics produces a slightly broader angular distribution compared to
₁₈₆₅ the final state particles originating from charged current ν_e interactions.

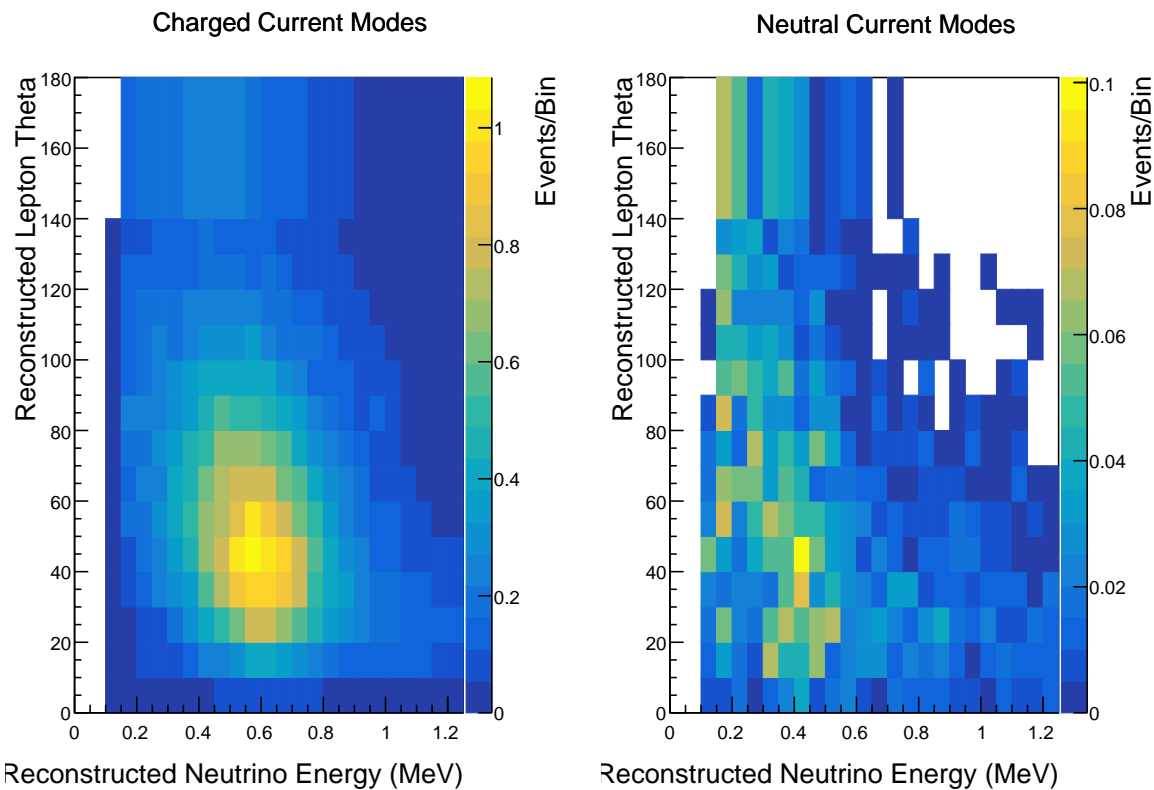


Figure 6.5: The distribution of the angle between the neutrino beam direction and the reconstructed final state lepton, for the FHC 1Re-like sample. The distribution is broken down by neutrino interaction mode into charged current (left) and neutral current (right) components. Asimov A oscillation parameter sets are assumed (given in Table 2.2). DB: Is this needed or will it just bring up more questions?

1866 6.4 Systematic Uncertainties

1867 The systematic model parameters for this analysis are split into groups, or blocks,
1868 depending on their purpose. They consist of flux uncertainties, neutrino-matter
1869 interaction systematics, and detector efficiencies. There are also uncertainties on the
1870 oscillation parameters which this analysis will not be sensitive to, Δm_{12}^2 and $\sin^2(\theta_{12})$.
1871 These uncertainties are taken from the 2018 PDG measurements [81]. As described in
1872 chapter 4, each model parameter used within this analysis requires a prior uncertainty.
1873 This is provided via separate covariance matrices for each block. The covariance
1874 matrices can include prior correlations between parameters within a single block, but
1875 the separate treatment means prior uncertainties can not be included for parameters
1876 in different groups. Some parameters in these models have no reasonably motivated
1877 uncertainties and are assigned flat priors which do not modify the likelihood penalty.
1878 The flux, neutrino interaction, and detector modeling simulations have already been
1879 discussed in section 5.1 and section 5.2. The uncertainties invoked within each of these
1880 models are described below.

1881 6.4.1 Beam Flux

1882 The neutrino beam flux systematics is based upon the uncertainty in the modeling of
1883 the components of the beam. This includes the hadron production model and their re-
1884 interactions, the shape, intensity, and alignment of the beam with respect to the target,
1885 and the uniformity of the magnetic field produced by the horn, alongside other effects.
1886 The uncertainty, as a function of neutrino energy, is illustrated in Figure 6.6 which
1887 includes a depiction of the total uncertainty as well as the contribution from individual
1888 components. The uncertainty around the peak of the energy distribution ($E_\nu \sim 0.6\text{GeV}$)

1889 is dominated by the measurements of the beam profile and alignment. Outside of this
1890 region, the uncertainties within hadron production dominate the uncertainty.

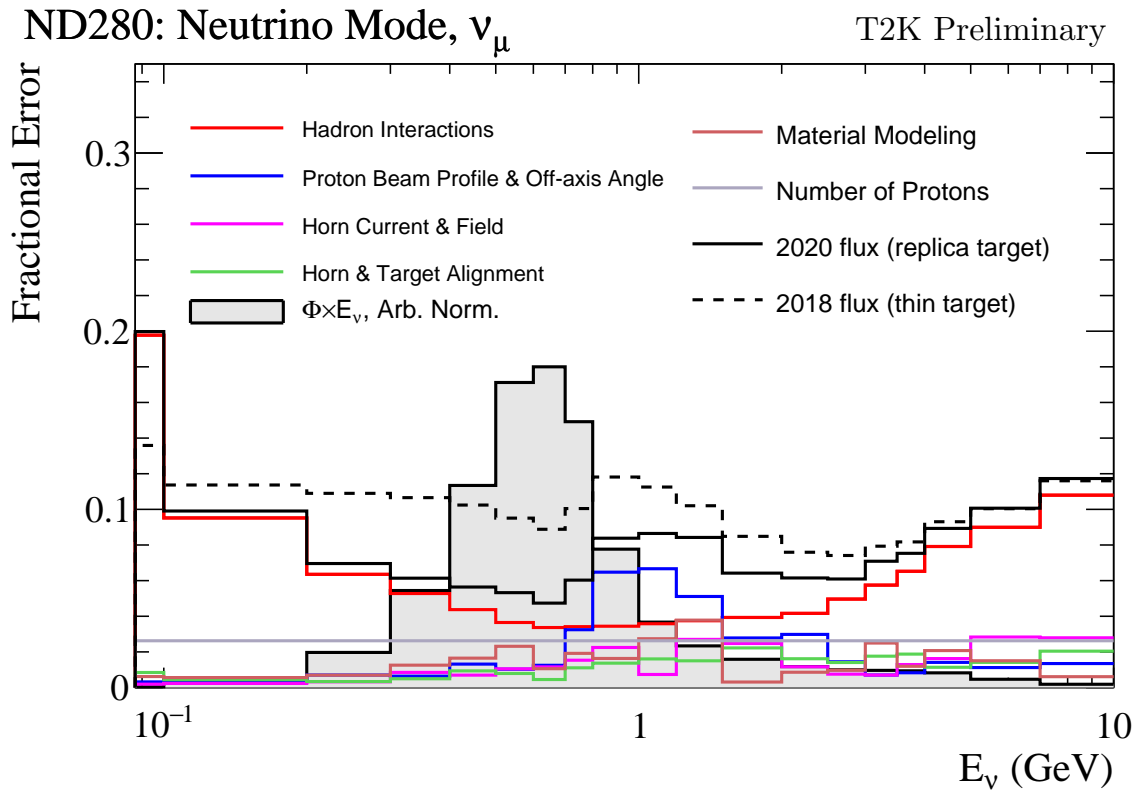


Figure 6.6: The total uncertainty evaluated on the near detector ν_μ flux prediction constrained by the replica-target data, illustrated as a function of neutrino energy. The solid(dashed) line indicates the uncertainty used within this analysis(the T2K 2018 analysis [201]). The solid histogram indicates the neutrino flux as a function of energy. Figure taken from [202].

1891 The beam flux uncertainties are described by one hundred parameters. They are
1892 split between the ND280 and SK detectors and binned by neutrino flavour: ν_μ , $\bar{\nu}_\mu$, ν_e
1893 and $\bar{\nu}_e$. The response is then broken down as a function of neutrino energy. The bin
1894 density in the neutrino energy is the same for the ν_μ in FHC and $\bar{\nu}_\mu$ in RHC beams,
1895 and narrows for neutrino energies close to the oscillation maxima of $E_\nu = 0.6\text{GeV}$.
1896 This binning is specified in Table 6.6. All of these systematic uncertainties are applied
1897 as normalisation parameters with Gaussian priors centered at 1.0 and error specified
1898 from a covariance matrix provided by the T2K beam group [202].

| Neutrino Flavour | Sign | Neutrino Energy Bin Edges (GeV) |
|------------------|-------|--|
| μ | Right | 0., 0.4, 0.5, 0.6, 0.7, 1., 1.5, 2.5, 3.5, 5., 7., 30. |
| μ | Wrong | 0., 0.7, 1., 1.5, 2.5, 30. |
| e | Right | 0., 0.5, 0.7, 0.8, 1.5, 2.5, 4., 30. |
| e | Wrong | 0., 2.5, 30. |

Table 6.6: The neutrino energy binning for the different neutrino flavours. “Right” sign indicates neutrinos in the FHC beam and antineutrinos in the RHC beam. “Wrong” sign indicates antineutrinos in the FHC beam and neutrinos in the RHC beam. The binning of the detector response is identical for the FHC and RHC modes as well as at ND280 and SK.

1899 6.4.2 Atmospheric Flux

1900 The atmospheric neutrino flux is modeled by the HKKM model [43]. 16 systematic
 1901 uncertainties are applied to control the normalisation of each neutrino flavour, energy,
 1902 and direction. All of the parameters are given Gaussian priors centered at 0 and width
 1903 equal to one. They are summarised below:

- 1904 • **Absolute Normalisation:** The overall normalisation of each neutrino flavour is
 1905 controlled by two independent systematic uncertainties, for $E_\nu < 1\text{GeV}$ and $E_\nu >$
 1906 1GeV , respectively. This is driven mostly by hadronic interaction uncertainties for
 1907 the production of pions and kaons [43]. The strength of the response is dependent
 1908 upon the neutrino energy.
- 1909 • **Relative Normalisation:** Uncertainties on the ratio of $(\nu_\mu + \bar{\nu}_\mu) / (\nu_e + \bar{\nu}_e)$ are
 1910 controlled by the difference between the HKKM model [43], FLUKA [46] and
 1911 Bartol models [42]. Three independent parameters are applied in the energy
 1912 ranges: $E_\nu < 1\text{GeV}$, $1\text{GeV} < E_\nu < 10\text{GeV}$, and $E_\nu > 10\text{GeV}$.
- 1913 • **$\nu/\bar{\nu}$ Normalisation:** The uncertainties in the π^+/π^- (and kaon equivalent) pro-
 1914 duction uncertainties in the flux of $\nu/\bar{\nu}$. The response is applied using the same
 1915 methodology as the relative normalisation parameters.

1916 • **Up/Down and Vertical/Horizontal Ratio:** Similar to the above two systematics,
1917 the difference between the HKKM, FLUKA, and Bartol model predictions, as a
1918 function of $\cos(\theta_Z)$, is used to control the normalisation of events as a function of
1919 zenith angle.

1920 • **K/π Ratio:** Higher energy neutrinos ($E_\nu > 10\text{GeV}$) become dependent upon
1921 kaon decay as the dominant source of neutrinos. Measurements of the ratio of
1922 K/π [203] are used to control the systematic uncertainty of the expected ratio of
1923 pion and kaon production.

1924 • **Solar Activity:** As the 11-year solar cycle can affect the Earth's magnetic field,
1925 the flux of primary cosmic rays varies across the same period. The uncertainty is
1926 calculated by taking a ± 1 year variation, equating to a 10% uncertainty for the
1927 SK-IV period.

1928 • **Atmospheric Density:** The height of the interaction of the primary cosmic rays is
1929 dependent upon the atmospheric density. The HKKM assumes the US standard
1930 1976 [153] profile. This systematic controls the uncertainty in that model.

1931 Updates to the HKKM and Bartol models are underway [158] to use a similar
1932 tuning technique to that used in the beam flux predictions. After those updates, it may
1933 be possible to include correlations in the hadron production uncertainty systematics
1934 for beam and atmospheric flux predictions.

1935 6.4.3 Neutrino Interaction

1936 The neutrino interactions which occur within all the detectors are modeled by NEUT.
1937 The two independent oscillation analyses, T2K-only [204] and the SK-only [52], have
1938 developed separate interaction models. To leverage the most sensitivity out of this
1939 simultaneous beam and atmospheric analysis, a correlated interaction model has been

1940 defined. Where applicable, correlations allow the systematic uncertainties applied to
1941 the atmospheric samples to be constrained by measurements of the near detector in
1942 the beam experiment. This can lead to stronger sensitivity to oscillation parameters as
1943 compared to an uncorrelated model.

1944 The low energy T2K systematic model has a more sophisticated treatment of CCQE,
1945 CCMEC, and CCRES uncertainties which is due to the purpose-made cross-section
1946 measurements made by the near detector. Furthermore, extensive comparisons of this
1947 model have been performed to external data [204]. However, the model is not designed
1948 for high-energy atmospheric events, like those illustrated in Figure 5.11. Therefore
1949 the high energy systematic model from the SK-only analysis is implemented for the
1950 relevant multiGeV, PC, and up- μ samples. The CCQE systematic parameters invoked
1951 within the SK high energy model are actually contained within T2K's CCQE model.
1952 Consequently, the more sophisticated CCQE and CCMEC T2K model parameters
1953 have been incorporated into the high energy model but are uncorrelated from the low
1954 energy counterparts.

1955 The high energy systematic model includes parameters developed from com-
1956 parisons of Nieves and Rein-Seghal models which affect resonant pion producing
1957 interactions, comparisons of the GRV98 and CKMT models which control DIS interac-
1958 tions, and hadron multiplicity measurements which modulate the normalisation of
1959 multi-pion producing events. The uncertainty of the ν_τ cross-section is particularly
1960 large and is controlled by a 25% normalisation uncertainty. These parameters are
1961 applied via normalisation or shape parameters. The former linearly scales the weight
1962 of all affected Monte-Carlo events, whereas the latter can increase or decrease a partic-
1963 ular event's weight depending on its neutrino energy and mode of interaction. The
1964 response of the shape parameters is defined by third-order polynomial splines which
1965 return a weight for a particular neutrino energy. To reduce computational resources

for the far detector fit, the response is binned by neutrino energy and sample binning: lepton momentum and cosine zenith binning for atmospheric splined responses and reconstructed neutrino energy and direction binning for beam samples. In total, 17 normalisation and 15 shape parameters are included in the high-energy model within this analysis.

Figure 6.7 indicates the predicted neutrino energy distribution for both beam and subGeV atmospheric samples. There is clearly significant overlap in neutrino energy between the subGeV atmospheric and beam samples, allowing similar kinematics in the final state particles. Figure 6.8 illustrates the fractional contribution of the different interaction modes per sample.

Comparing beam and atmospheric samples which target CCQE interactions (S.G. e-like 0de, S.G. μ -like [0,1]de, [FHC,RHC] 1R μ -like and [FHC,RHC] 1R e-like samples), there is a very similar contribution of CCQE, CC 2p2h, and CC1 π^\pm interactions. The samples which target CC1 π^\pm interactions, (S.G. e-like 0de, S.G. μ -like 2de and FHC 1R+1d.e e-like) also consist of very similar mode interactions.

As a consequence of the similarity in energy and mode contributions, correlating the systematic model between the beam and subGeV atmospheric samples ensures that this analysis attains the largest sensitivity to oscillation parameters while still ensuring neutrino interaction systematics are correctly accounted for. Due to its more sophisticated CCQE and 2p2h model, the T2K systematic model was chosen as the basis of the correlated model.

The T2K systematic model [204] is applied in a similar methodology to the SK model parameters. It consists of 19 shape parameters and 24 normalisation parameters. Four additional parameters, which model the uncertainty in the binding energy, are applied in a way to shift the momentum of the lepton emitted from a nucleus. This controls the uncertainty specified on the 27MeV binding energy assumed within Equation 6.2.

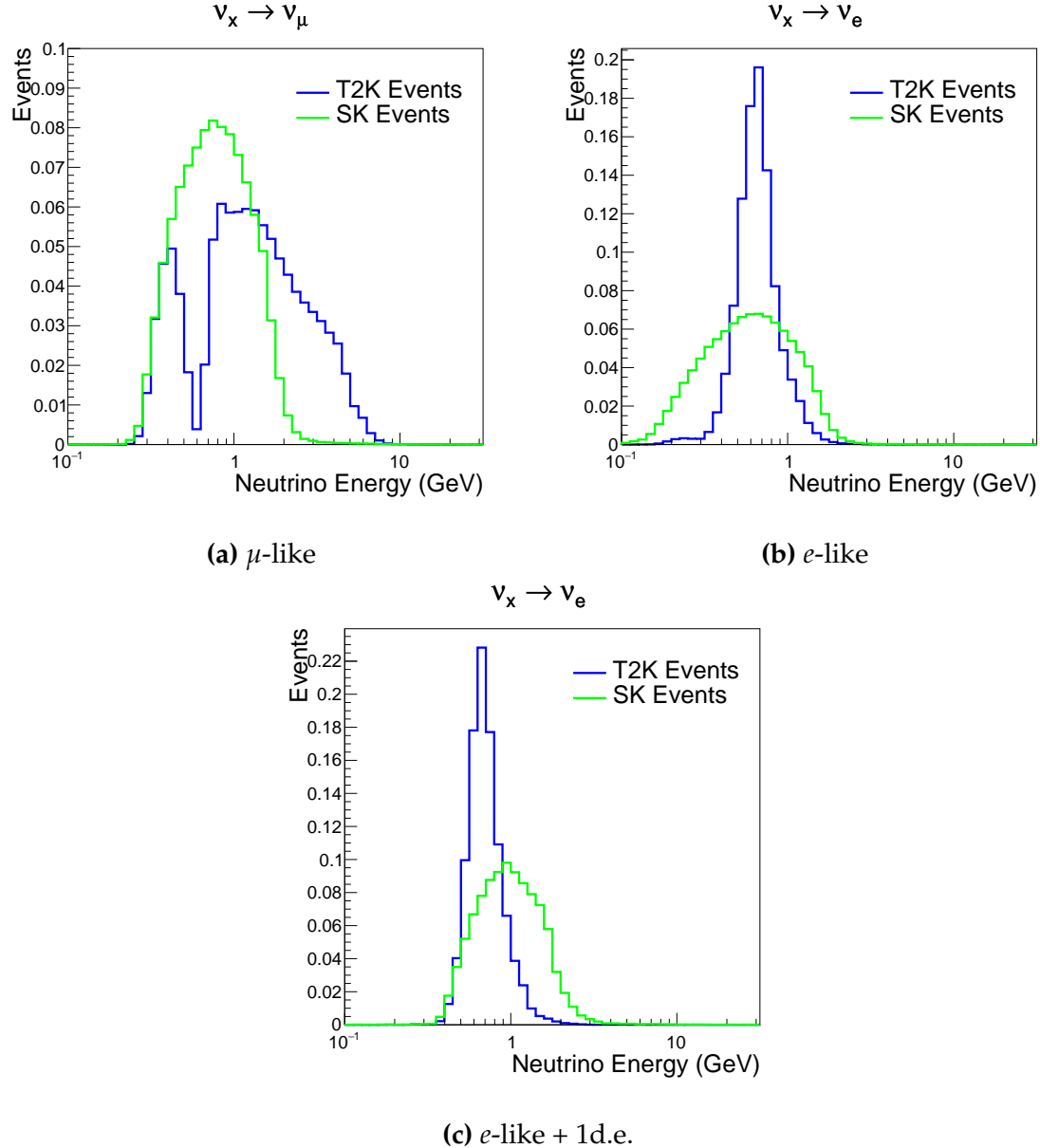


Figure 6.7: The predicted neutrino energy distribution for subGeV atmospheric and beam samples. FHC and RHC beam samples are summed together Asimov A oscillation parameters are assumed (given in Table 2.2). Beam and atmospheric samples with similar cuts are compared against one another.

1992 The majority of these parameters are assigned a Gaussian prior uncertainty. Those
 1993 that have no reasonably motivated uncertainty, or those which have not been fit to
 1994 external data, are assigned a flat prior which does not affect the penalty term.

1995 There are three particular tunes of the T2K flux and low energy cross section model
 1996 typically considered. Firstly, the “generated” tune which is the set of dial values with

| | CC QE | CC 2p2h | CC $1\pi^\pm$ | CC $M\pi$ | CC Other | NC π^0 | NC $1\pi^\pm$ | NC $M\pi$ | NC Coh. | NC Other |
|----------------------|-------------|-------------|---------------|-------------|-------------|-------------|---------------|-------------|-------------|-------------|
| FHC 1R+1d.e. e-like | 0.04 | 0.02 | 0.83 | 0.03 | 0.04 | 0.01 | 0.01 | 0.01 | 0.00 | 0.01 |
| RHC 1R e-like | 0.62 | 0.12 | 0.11 | 0.01 | 0.02 | 0.06 | 0.01 | 0.01 | 0.01 | 0.04 |
| FHC 1R e-like | 0.68 | 0.12 | 0.10 | 0.00 | 0.02 | 0.04 | 0.01 | 0.00 | 0.00 | 0.02 |
| RHC 1R μ -like | 0.62 | 0.13 | 0.17 | 0.02 | 0.03 | 0.00 | 0.02 | 0.00 | 0.00 | 0.00 |
| FHC 1R μ -like | 0.62 | 0.12 | 0.16 | 0.02 | 0.03 | 0.00 | 0.03 | 0.00 | 0.00 | 0.00 |
| S.G. π^0 -like | 0.05 | 0.01 | 0.02 | 0.00 | 0.01 | 0.68 | 0.06 | 0.07 | 0.06 | 0.04 |
| S.G. μ -like 2de | 0.04 | 0.01 | 0.80 | 0.10 | 0.04 | 0.00 | 0.00 | 0.00 | 0.00 | 0.00 |
| S.G. μ -like 1de | 0.72 | 0.11 | 0.12 | 0.01 | 0.02 | 0.00 | 0.01 | 0.00 | 0.00 | 0.00 |
| S.G. μ -like 0de | 0.68 | 0.11 | 0.10 | 0.01 | 0.02 | 0.01 | 0.05 | 0.01 | 0.00 | 0.02 |
| S.G. e-like 1de | 0.05 | 0.01 | 0.75 | 0.10 | 0.05 | 0.00 | 0.01 | 0.02 | 0.00 | 0.01 |
| S.G. e-like 0de | 0.73 | 0.11 | 0.10 | 0.01 | 0.02 | 0.02 | 0.00 | 0.00 | 0.00 | 0.00 |

Figure 6.8: The interaction mode contribution of each sample given as a fraction of the total event rate in that sample. Asimov A oscillation parameters are assumed (given in Table 2.2). The Charged Current (CC) modes are broken into quasi-elastic (QE), 2p2h, resonant charged pion production ($1\pi^\pm$), multi-pion production ($M\pi$), and other interaction categories. Neutral Current (NC) interaction modes are given in interaction mode categories: π^0 production, resonant charged pion production, multi-pion production, and others.

which the Monte Carlo was generated. Secondly, the set of dial values which are taken from external data measurements and used as inputs. These are the “pre-fit” dial values. The reason these two sets of dial values are different is that the external data measurements are continually updated but it is very computationally intensive to regenerate a Monte Carlo prediction after each update. The final tune is the “post-fit”, “post-ND fit” or “post-BANFF” dial values. These are the values taken from a fit to the beam near detector data. This fit is performed by two independent fitting frameworks, MaCh3 and BANFF, which ensures reliable measurements. The output of each fitter is converted into a covariance matrix to describe the error and correlations between all the flux and cross-section parameters. This is then propagated to the far-detector

2007 oscillation analysis group for use in the P-Theta fitting framework. As MaCh3 can
2008 perform a near detector fit, it is included within the simultaneous fit of the far-detector
2009 beam and atmospheric oscillation analysis. This is because this technique does not
2010 require any assumption of Gaussian posterior distributions which is required in the
2011 covariance matrix methodology.

2012 On top of the combination of the SK and T2K interaction models, several other
2013 parameters have been specifically developed for the joint oscillation analysis. The
2014 majority of the atmospheric samples' δ_{CP} sensitivity comes from the normalisation
2015 of subGeV electron-like events. These are modeled using a spectral function model
2016 to approximate the nuclear ground state. However, the near detector is not able to
2017 constrain the model. Therefore, an additional systematic is introduced which models
2018 an alternative Continous Random Phase Approximation (CRPA) nuclear ground
2019 state. The reasoning is documented in [205]. As the near detector can not sufficiently
2020 constrain the model, this dial approximates the event weights if a CRPA model had
2021 been assumed rather than a spectral function. This dial only effects ν_e and $\bar{\nu}_e$ and is
2022 applied as a shape parameter.

2023 Further additions to the model have been introduced due to the inclusion of the
2024 subGeV π^0 atmospheric sample. This particularly targets charged current and neutral
2025 current π^0 producing interactions to help constrain the systematic uncertainties. There
2026 is no analogous sample in the T2K beam-only analysis so no significant effort has
2027 been placed into building a sufficient uncertainty model. Therefore, an uncertainty
2028 that affects neutral current resonant π^0 production is incorporated into this analysis.
2029 Comparisons of NEUT's NC resonant pion production predictions have been made to
2030 MiniBooNE [206] data and a consistent 16% to 21% underprediction is observed [205].
2031 Consequently, a conservative 30% normalisation parameter is invoked.

2032 Down-going events are mostly insensitive to oscillation parameters and can act
 2033 similar to the near detector within an accelerator experiment (Details will be dis-
 2034 cussed in chapter 7). This region of phase space can act as a sideband and allows the
 2035 cross-section model and near detector constraint to be studied. The distribution of
 2036 events in this region is calculated using the technique outlined in subsection 4.3.4. For
 2037 CCQE-targeting samples, the application of the near detector constraint is well within
 2038 the statistical fluctuation of the down-going data such that no significant tension is
 2039 observed between the data and the Monte Carlo prediction after the near detector
 2040 constraint is applied. This is not the case for samples with target CCRES interac-
 2041 tions. The electron-like data is consistent with the constrained prediction at high
 2042 reconstructed momenta but diverges at lower momentum, whereas the muon-like
 2043 sample is under-predicted throughout the range of momenta. To combat this disagree-
 2044 ment, an additional cross-section systematic dial, specifically designed to inflate the
 2045 low pion momentum systematics was developed in [205]. This is a shape parameter
 2046 implemented through a splined response.

2047 6.4.4 Near Detector

2048 The systematics applied due to uncertainties arising from the response of the near
 2049 detector is documented in [133]. The response is described by 574 normalisation param-
 2050 eters binned in the selected sample as well as momentum and angle, P_μ and $\cos(\theta_\mu)$,
 2051 of the final-state muon. These are applied via a covariance matrix with each parameter
 2052 being assigned a Gaussian prior from that covariance matrix. These normalisation
 2053 parameters are built from underlying systematics, e.g. pion secondary interaction
 2054 systematics, which are randomly thrown and the variation in each $P_\mu \times \cos(\theta_\mu)$ bin is
 2055 determined. Two thousand throws are evaluated and a covariance matrix response is
 2056 created. This allows significant correlations between FGD1 and FGD2 samples, as well

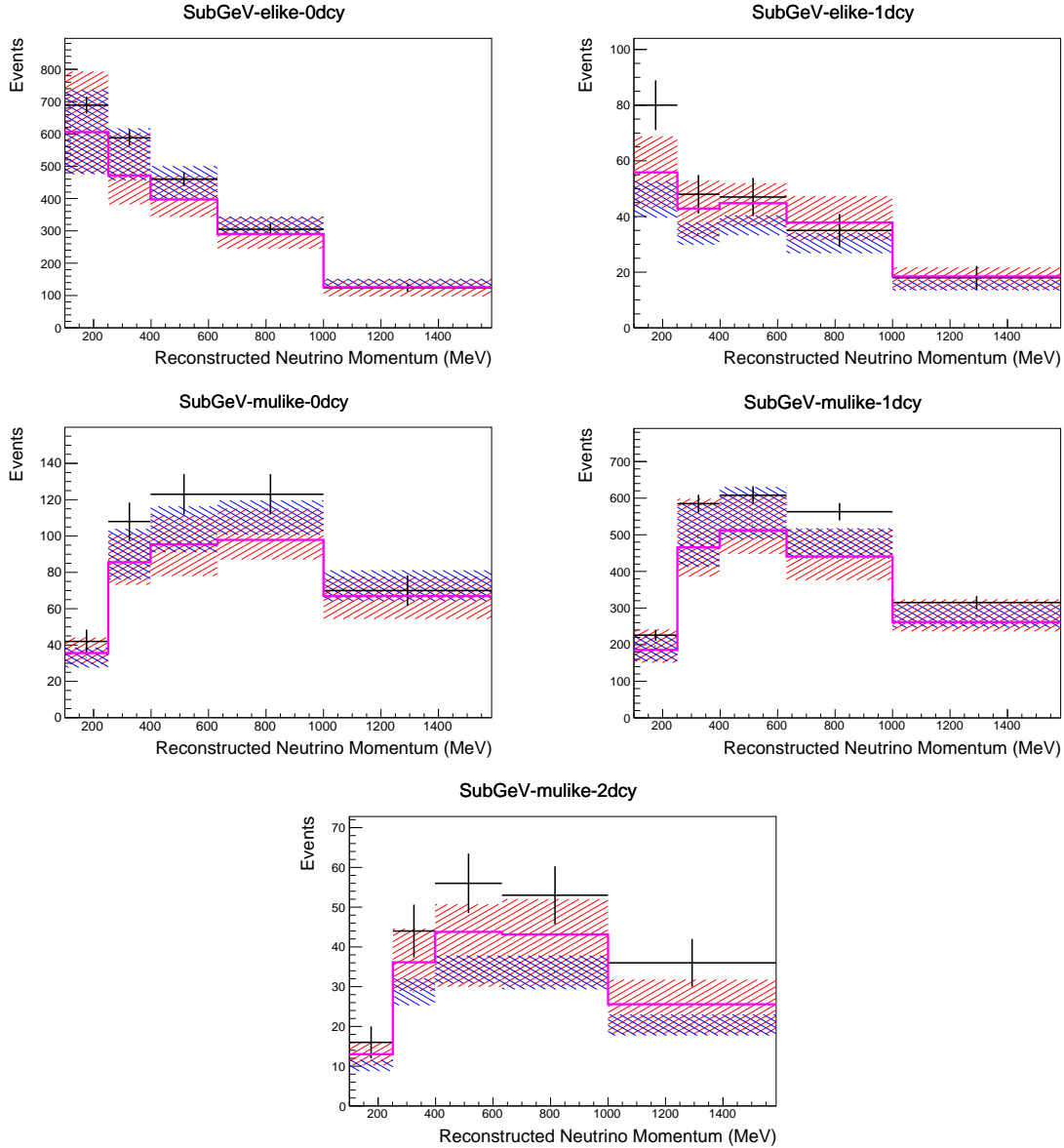


Figure 6.9: Down-going atmospheric subGeV single-ring samples comparing the mean and error of the pre-fit and post-fit Monte Carlo predictions in red and blue, respectively. The magenta histogram illustrates the Monte Carlo prediction using the generated dial values. The black points illustrate the down-going data with statistical errors given. The mean and errors of the Monte Carlo predictions are calculated by the techniques documented in subsection 4.3.4. The pre-fit spectrum is calculated by throwing the cross-section and atmospheric flux dial values from the pre-fit covariance matrix. The post-fit spectrum is calculated by sampling the cross-section dial values from an ND fit MCMC chain, whilst still throwing the atmospheric flux dials from the pre-fit covariance.

as adjacent $P_\mu \times \cos(\theta_\mu)$ bins. Statistical uncertainties are accounted for by including fluctuations of each event's weight from a Poisson distribution.

2059 Similar to the cross-section systematics, MaCh3 and BANFF are used to constrain
2060 the uncertainty of these systematics through independent validations. Each fitter
2061 generates a post-fit covariance matrix which is compared and passed to the far-detector
2062 oscillation analysis working group. As the analysis presented within this thesis uses
2063 the MaCh3 framework, a joint oscillation analysis fit of all three sets of samples and
2064 their respective systematics is performed.

2065 **6.4.5 Far Detector**

2066 Two configurations of the far detector systematic model implementation have been
2067 considered. Firstly, the far detector systematic uncertainties for beam and atmospheric
2068 samples are taken from their respective analysis inputs, denoted “official inputs” anal-
2069 ysis. Consequently, no correlations are assumed between the beam and atmospheric
2070 samples. The generation of the beam- and atmospheric-specific inputs are documented
2071 in subsubsection 6.4.5.1 and subsubsection 6.4.5.2. Secondly, a correlated detector
2072 model has been developed. Here, the distribution of parameters used for applying
2073 event cuts (e.g. electron-muon PID separation) is modified within the fit. It follows
2074 a similar methodology to the beam far detector systematics implementation but per-
2075 forms a joint fit of the beam and atmospheric data. This alternative implementation is
2076 detailed in subsubsection 6.4.5.3.

2077 **6.4.5.1 Beam Samples**

2078 There are 45 systematics which describe the response of the far detector to beam
2079 events [185], split into 44 normalisation parameters and one energy scale systematic.
2080 The energy scale systematic is applied as a multiplicative scaling of the reconstructed
2081 neutrino energy. It is described by a Gaussian, centered at one with equal to the

2082 difference in Monte Carlo to data comparisons performed in [187]. The normalisation
 2083 parameters are assigned a Gaussian error centralised at one with width taken from a
 2084 covariance matrix. A detailed breakdown of the generation of the covariance matrix
 2085 is found in [199]. To build the covariance matrix, a fit is performed on atmospheric
 2086 data which has been selected using beam sample selection cuts. These cuts use the
 2087 variables, L^i , where the index i is detailed in Table 6.7. Each L^i is a smear, α , and shift,
 2088 β parameter such that,

$$L_j^i \rightarrow \bar{L}_j^i = \alpha_j^i L + \beta_j^i \quad (6.4)$$

2089 Where L_j^i (\bar{L}_j^i) correspond to nominal(varied) PID cut parameters given in Table 6.7.
 2090 The shift and smear parameters are binned by final-state topology, j , where the binning
 2091 is given in Table 6.8. The final-state topology binning is because the detector will
 2092 respond differently to events that have one or multiple rings. For example, the detector
 2093 will be able to distinguish single-ring events better than two overlapping ring events,
 2094 resulting in smaller systematic uncertainty for one-ring events compared to two-ring
 2095 events. This approach is used to allow the cut parameter distributions to be modified
 2096 within the fit, allowing for better data to Monte Carlo agreement. Only the shape
 2097 of each of the cut variables is used within this fit, such that physics effects are not
 2098 considered.

| Cut Variable | Parameter Name |
|--------------|---|
| 0 | <code>fitQun e/mu PID</code> |
| 1 | <code>fitQun e/pi0 PID</code> |
| 2 | <code>fitQun mu/pi PID</code> |
| 3 | <code>fitQun Ring-Counting Parameter</code> |

Table 6.7: List of cut variables that are included within the shift/smear fit documented in [199].

| Category | Description |
|--------------------|---|
| $1e$ | Only one electron above Cherenkov threshold in the final state |
| 1μ | Only one muon above Cherenkov threshold in the final state |
| $1e+other$ | One electron and one or more other charged particles above Cherenkov threshold in the final state |
| $1\mu+other$ | One muon and one or more other charged particles above Cherenkov threshold in the final state |
| $1\pi^0$ | Only one π^0 in the final state |
| $1\pi^\pm$ or $1p$ | Only one hadron (typically charged pion or proton) in the final state |
| Other | Any other final state |

Table 6.8: Reconstructed event topology categories on which the SK detector systematics [199] are based.

2099 Beyond the uncertainty on the PID cut criteria, the mis-modeling of π^0 events
 2100 is also considered. If one of the two rings from a π^0 event is missed, this will be
 2101 reconstructed as a $CC\nu_e$ -like event. This is one of the largest systematics hindering the
 2102 electron neutrino appearance analyses. Consequently, additional systematics has been
 2103 introduced to constrain the mis-modeling of π^0 events in SK, binned by reconstructed
 2104 neutrino energy. To evaluate this systematic uncertainty, a set of “hybrid- π^0 ” samples
 2105 is constructed. These events are built by overlaying one electron-like ring from the
 2106 SK atmospheric neutrino samples or decay electron ring from a stopping cosmic ray
 2107 muon with one simulated photon ring. Both rings are chosen so that momenta and
 2108 opening angle follow the decay kinematics of NC π^0 events from the T2K-MC. Hybrid-
 2109 π^0 Monte Carlo samples with both rings from the SK Monte Carlo are produced
 2110 to compare with the hybrid- π^0 data samples and the difference in the fraction of
 2111 events that pass the ν_e selection criteria is used to assign the systematic errors. In
 2112 order to investigate any data to Monte Carlo differences that may originate from
 2113 either the higher energy ring or lower energy ring, two samples are built; a sample
 2114 in which the electron constitutes the higher energy ring from the π^0 decay called the
 2115 primary sample and another one in which it constitutes the lower energy ring called

2116 the secondary sample. The standard T2K ν_e fiTQun event selection criteria are used to
2117 select events.

2118 Final contributions to the covariance matrix are determined by supplementary
2119 uncertainties attained by comparing stopping muon data to Monte Carlo prediction,
2120 as first introduced in section 5.2. The efficiency of tagging decay electrons is estimated
2121 by the stopping muon data to Monte Carlo differences by comparing the number
2122 of one decay electron events to the number of events with one or fewer decay elec-
2123 trons. Similarly, the rate at which fake decay electrons are reconstructed by fiTQun
2124 is estimated by comparing the number of two decay electron events to the number
2125 of events with one or two reconstructed decay electrons. The two sources of sys-
2126 tematics are added in quadrature weighted by the number of events with one true
2127 decay electron yielding a 0.2% systematic uncertainty. A fiducial volume systematic of
2128 $\pm 2.5\text{cm}$ which corresponds to a 0.5% shift in the normalisation of events. Additional
2129 normalisation uncertainties based on neutrino flavour and interaction mode are also
2130 defined in [185, 207, 208].

2131 Two additional sources of uncertainty are included: secondary and photo-nuclear
2132 interactions. These are estimated by varying the underlying parameters are building a
2133 distribution of sample event rates. These contributions are then added in quadrature
2134 to the above covariance matrix.

2135 6.4.5.2 Atmospheric Samples

2136 The systematic parameters which control the detector systematics for atmospheric
2137 samples, documented in [89], are split into two sub-groups. Those which are related
2138 to particle identification and ring counting systematics and those which are related to
2139 calibration, separation, and reduction uncertainties.

2140 The particle identification systematics consist of five parameters. The ring separation systematic enforces an anti-correlated response between the single-ring and
 2141 multi-ring samples. This is implemented as a fractional increase/decrease in the
 2142 overall normalisation of each sample, depending on the distance to the nearest wall
 2143 from an event's vertex. The coefficients of the normalisation are estimated prior to the
 2144 fit and depend on the particular atmospheric sample. The single-ring and multi-ring
 2145 PID systematics encode the detector's ability to separate electron-like and muon-like
 2146 events and are implemented in a similar way to the ring separation systematic.
 2147

2148 The multi-ring electron-like separation likelihood, discussed in section 6.1, encodes
 2149 the ability of the detector to separate neutrino from anti-neutrino events. As an impor-
 2150 tant systematic in the mass hierarchy determination, systematic uncertainties control
 2151 the relative normalisations of the ν_e and $\bar{\nu}_e$ enriched samples. Two normalisation
 2152 parameters are implemented which vary the event rate of each multi-ring sample,
 2153 whilst ensuring the total event rate is conserved.

2154 There are 22 systematics related to calibration measurements, including effects
 2155 from backgrounds, reduction, and showering effects. They are documented in [89] and
 2156 briefly summarised in Table 6.9. They are applied via normalisation parameters, with
 2157 the separation systematics requiring the conservation of event rate across all samples.

2158 6.4.5.3 Correlated Detector Model

2159 A complete uncertainty model of the SK detector would be able to determine the
 2160 systematic shift on the sample spectra for a variation of the underlying parameters,
 2161 e.g. PMT angular acceptance. However, this is computationally intensive, requiring
 2162 Monte Carlo predictions to be made for each plausible variation. Consequently, an
 2163 effective parameter model has been utilised for a correlated detector model following
 2164 from the T2K-only model implementation documented in subsubsection 6.4.5.1. The

Table 6.9: Sources of systematic errors specified within the grouped into the “calibration” systematics model.

| Index | Description |
|-------|--|
| 0 | Partially contained reduction |
| 1 | Fully contained reduction |
| 2 | Separation of fully contained and partially contained events |
| 3 | Separation of stopping and through-going partially contained events in top of detector |
| 4 | Separation of stopping and through-going partially contained events in barrel of detector |
| 5 | Separation of stopping and through-going partially contained events in bottom of detector |
| 6 | Background due to cosmic rays |
| 7 | Background due to flasher events |
| 8 | Vertex systematic moving events into and out of fiducial volume |
| 9 | Upward going muon event reduction |
| 10 | Separation of stopping and through-going in upward going muon events |
| 11 | Energy systematic in upward going muon events |
| 12 | Reconstruction of the path length of upward going muon events |
| 13 | Separation of showering and non-showering upward going muon events |
| 14 | Background of stopping upward going muon events |
| 15 | Background of non-showering through-going upward going muon events |
| 16 | Background of showering through-going upward going muon events |
| 17 | Efficiency of tagging two rings from π^0 decay |
| 18 | Efficiency of decay electron tagging |
| 19 | Background from downgoing cosmic muons |
| 20 | Asymmetry of energy deposition in tank |
| 21 | Energy scale deposition |

²¹⁶⁵ implementation performs a simultaneous fit of detector and oscillation parameters,

²¹⁶⁶ for the detector parameters given in Table 6.7.

²¹⁶⁷ The correlated detector model utilises the same smear and shift parameters docu-

²¹⁶⁸ mented in subsubsection 6.4.5.1, split by final state topology. Beyond this, the shift

²¹⁶⁹ and smear parameters are split by visible energy deposited within the detector, with

2170 binning specified in Table 6.10. This is because atmospheric events are categorised
2171 by subGeV and multiGeV events based on visible energy, so this splitting is required
2172 when correlating the systematic model for beam and atmospheric events. Alongside
2173 the technical requirement, higher energy events will be better reconstructed due to
2174 fractionally less noise within the detector. This implementation correlates the detector
2175 systematics between the far-detector beam and subGeV atmospheric samples due
2176 to their similar energies and interaction types. As a result of the inclusion of visible
2177 energy binning, Equation 6.4 becomes

$$L_{jk}^i \rightarrow \bar{L}_{jk}^i = \alpha_{jk}^i L + \beta_{jk}^i, \quad (6.5)$$

2178 where k is the visible energy bin. As there are no equivalent beam samples, the
2179 multiGeV, multiring, PC, and Up- μ samples will be subject to the ATMPD particle
2180 identification systematics implementation as described in subsubsection 6.4.5.2 rather
2181 than using this correlated detector model. The calibration systematics also described
2182 in the aforementioned chapter still apply to all atmospheric samples.

| Index | Range (MeV) |
|-------|---------------------|
| 0 | $30 \geq x > 300$ |
| 1 | $300 \geq x > 700$ |
| 2 | $700 \geq x > 1330$ |
| 3 | $1330 \geq x$ |

Table 6.10: Visible energy binning for which the correlated SK detector systematics are based

2183 The implementation of this systematic model takes the events reconstructed values
2184 of the cut parameters, modifies them by the particular shift and smear parameter for
2185 that event, and then re-applies event selection. This invokes event migration, which is

2186 a new feature incorporated into the MaCh3 framework which is only achievable due
2187 to the event-by-event reweighting scheme.

2188 Particular care has to be taken when varying the ring counting parameter. This
2189 is because the number of rings is a finite value (one-ring, two-rings, etc.) which can
2190 not be continuously varied through this shift and smear technique. Consequently a
2191 ring counting parameter, RC_i , is calculated for the i^{th} event, following the definition
2192 in [184]. The likelihood from all considered one-ring (L_{1R}) and two-ring (L_{2R}) fits
2193 are compared to determine the preferred hypothesis. The difference is computed as
2194 $\Delta_{LLH} = \log(L_{1R}) - \log(L_{2R})$. The ring counting parameter is then defined as,

$$RC_i = \text{sgn}(\Delta_{LLH}) \times \sqrt{|\Delta_{LLH}|}, \quad (6.6)$$

2195 where $\text{sgn}(x) = x/|x|$. This ring counting parameter corresponds to an intermedi-
2196 ate likelihood value used within the `fitQun` algorithm to decide the number of rings
2197 associated with a particular event. However, fake-ring merging algorithms are applied
2198 after this likelihood value is used. Consequently, this ring counting parameter does
2199 not always exactly correspond to the number of reconstructed rings. This can be seen
2200 in Figure 6.10.

2201 As the `fitQun` algorithm does not provide a likelihood value after the fake-ring
2202 algorithms have been applied, the ring counting parameter distribution is correlated to
2203 the final number of reconstructed rings through “maps”. These are two-dimensional
2204 distributions of the ring counting parameter and the final number of reconstructed
2205 rings. An example is illustrated in Figure 6.11. In principle, the `fitQun` reconstruction
2206 algorithm should be re-run after the variation in the ring counting parameter. However,

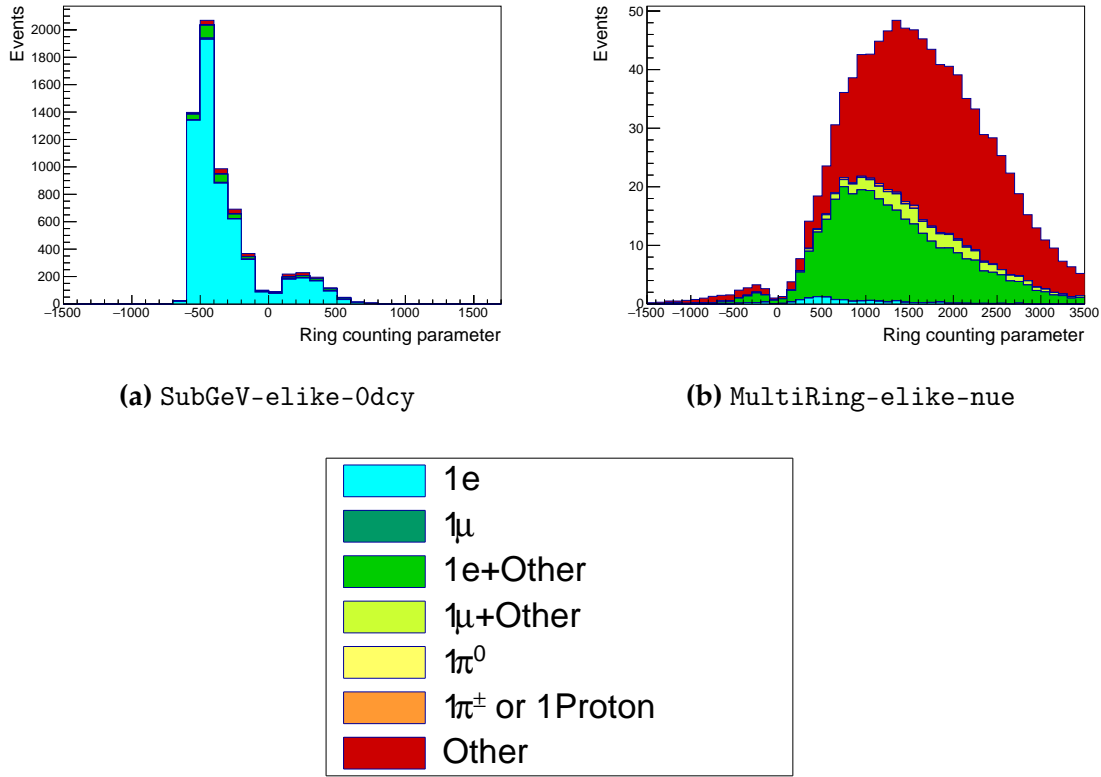


Figure 6.10: The ring counting parameter as defined in Equation 6.6 for the SubGeV-else-0dcy and MultiRing-else-nue samples.

2207 this is not computationally viable. Therefore the “maps” are used as a reweighting
 2208 template.

2209 The maps are split by final state topology and true neutrino flavour and all `fitQun`
 2210 -reconstructed Monte Carlo events are used to fill them. The maps are row-normalised
 2211 to represent the probability of X number of rings for a given RC_i value. Prior to the
 2212 fit, an event’s nominal weight is calculated as $W^i(N_{Rings}^i, L_{jk}^i)$, where N_{Rings}^i is the
 2213 reconstructed number of rings for the i^{th} event and $W^i(x, y)$ is the bin content in map
 2214 associated with the i^{th} event, where x number of rings and y is ring counting parameter.
 2215 Then during the fit, the value of $R = W^i(N_{Rings}^i, \bar{L}_{jk}^i) / W^i(N_{Rings}^i, L_{jk}^i)$ is calculated as
 2216 the event weight for the i^{th} event. This is the only cut variable that uses a reweighting
 2217 scheme rather than event migration.

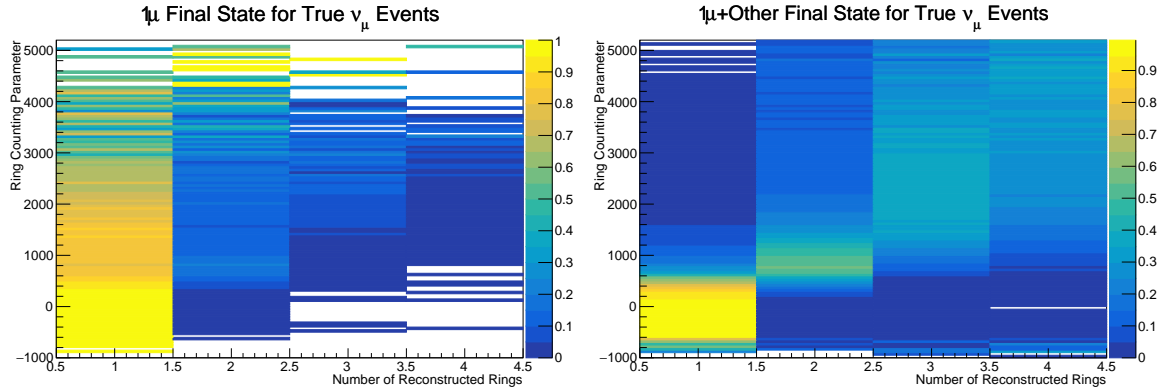


Figure 6.11: The ring counting parameter, defined in Equation 6.6, as a function of the number of reconstructed rings as found by the `fitQun` reconstruction algorithm. Left: true ν_μ events with only one muon above the Cherenkov threshold in the final state. Right: true ν_μ events with one muon and at least one other charged particle above the Cherenkov threshold in the final state.

2218 The π^0 systematics introduced in subsection 6.4.4 are applied via a covariance
 2219 matrix. This is not possible in the alternative model as no covariance matrix is used.
 2220 Thus, the implementation of the π^0 systematics has been modified. The inputs from
 2221 the hybrid π^0 sample is included via the use of “ χ^2 maps”, which are two-dimensional
 2222 histograms in α_{jk}^i and β_{jk}^i parameters over some range. Illustrative examples of the χ^2
 2223 maps are given in Figure 6.12. Due to their nature, the shift and smear parameters are
 2224 typically very correlated. A map is produced for each cut parameter given in Table 6.7
 2225 and for each visible energy bin given in Table 6.10.

2226 The maps are filled through the χ^2 comparison of the hybrid π^0 Monte Carlo and
 2227 data in the particle identification parameters documented in Table 6.7. The Monte
 2228 Carlo distribution is modified by the α_{jk}^i and β_{jk}^i scaling, whilst cross-section and flux
 2229 nuisance parameters are thrown from their prior uncertainties. The χ^2 between the
 2230 scaled Monte Carlo and data is calculated and the relevant point in the χ^2 map is filled.

2231 The implementation within this alternative detector model is to add the bin contents
 2232 of the maps, for the relevant values of the α_{jk}^i and β_{jk}^i parameters, to the likelihood
 2233 penalty. Only $1\pi^0$ final state topology shift and smear parameters use this prior
 2234 uncertainty.

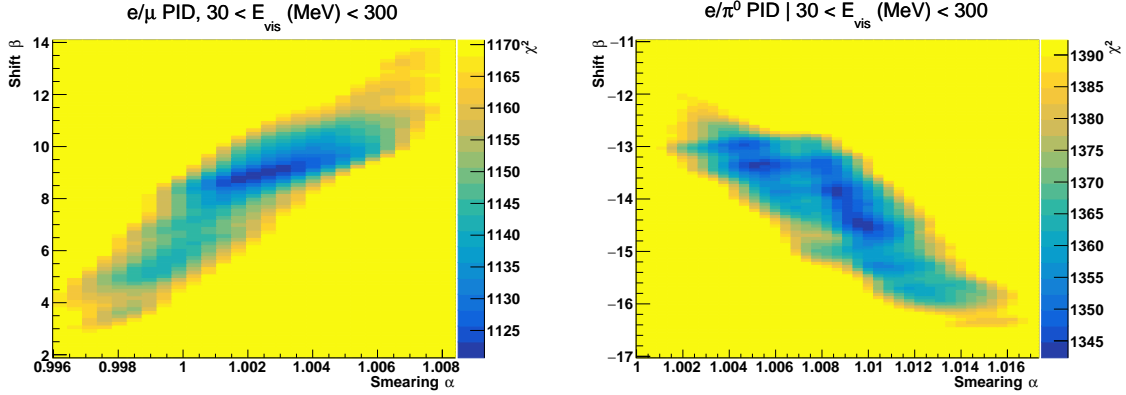


Figure 6.12: The χ^2 between the hybrid- π^0 Monte Carlo and data samples, as a function of smear (α) and shift (β) parameters, for events which have $1\pi^0$ final state topology. Left: Electron-muon separation PID parameter for events with $30 \geq E_{vis}(\text{MeV}) < 300$. Right: Electron- π^0 separation PID parameter for events with $30 \geq E_{vis}(\text{MeV}) < 300$.

Similarly, the implementation of the supplementary systematics documented in subsubsection 6.4.5.1 needs to be modified. A new framework [209] was built in tandem with the T2K-SK working group [185] so the additional parameters can be incorporated into the MaCh3 framework. These are applied as normalisation parameters, depending on the particular interaction mode, number of tagged decay electrons, and whether the primary particle generated Cherenkov light. They are assigned Gaussian uncertainties with widths described by a covariance matrix. Furthermore, the secondary interaction and photo-nuclear effects need to be accounted for in this detector model using a different implementation than that in subsubsection 6.4.5.1. This was done by including a shape parameter for each of the secondary interactions and the photo-nuclear systematic parameters.

There are a total of 224 α_{jk}^i and β_{jk}^i parameters, of which 32 have prior constraints from the hybrid π^0 samples.

One final complexity of this correlated detector model is that the two sets of samples, beam and subGeV atmospheric, use slightly different parameters to distinguish electron and muon-like events. The T2K samples use the value of $\log(L_e/L_\mu)$ whereas the atmospheric samples use the value of $\log(L_e/L_\pi)$, where L_X is the likelihood for

2252 hypothesis X. This is because the T2K fits use single-ring `fitQun` fitting techniques,
 2253 whereas multi-ring fits are applied to the atmospheric samples where only the electron
 2254 and pion hypothesis are considered. The correlation between the two likelihood ratios
 2255 is illustrated in Figure 6.13. As discussed in section 5.2, the pion hypothesis is a very
 2256 good approximation of the muon hypothesis due to their similar mass. Consequently,
 2257 using the same shift and smear parameters correlated between the beam and subGeV
 2258 atmospheric samples is deemed a good approximation.

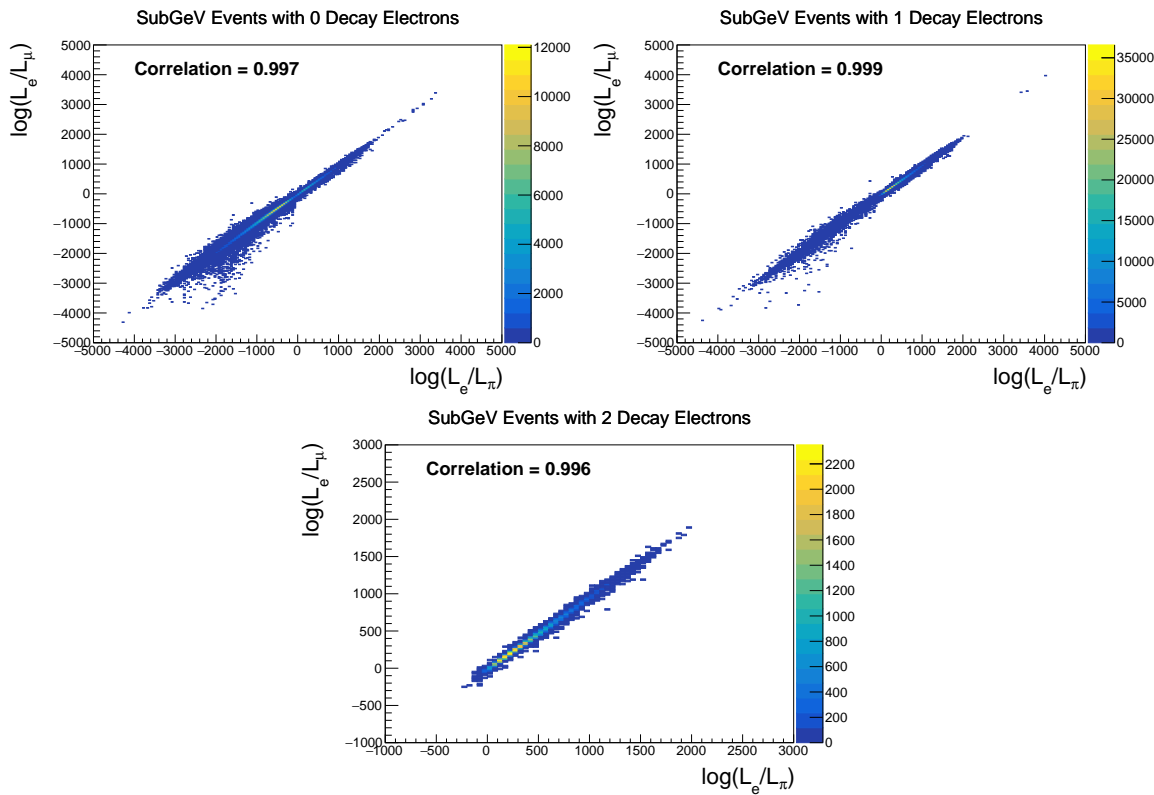


Figure 6.13: The distribution of $\log(L_e/L_\mu)$ compared to $\log(L_e/L_\pi)$ for subGeV events with zero (top left), one (top right) or two (bottom) decay electrons. The correlation in the distribution is calculated as 0.997, 0.999 and 0.996, respectively.

2259

Chapter 7

2260

Oscillation Probability Calculation

2261 It is important to understand how and where the sensitivity to the oscillation pa-
2262 rameters comes from for both atmospheric and beam samples. An overview of how
2263 these samples observe changes in δ_{CP} , Δm_{23}^2 , and $\sin^2(\theta_{23})$ is given in section 7.1. It
2264 also explains the additional complexities involved when performing an atmospheric
2265 neutrino analysis as compared to a beam-only analysis.

2266 Without additional techniques, atmospheric sub-GeV upward-going neutrinos
2267 ($E_\nu < 1.33\text{GeV}, \cos(\theta_Z) < 0.$) can artificially inflate the sensitivity to δ_{CP} due to the
2268 quickly varying oscillation probability in this region. Therefore, a “sub-sampling”
2269 approach has been developed to reduce these biases ensuring accurate and reliable
2270 sensitivity measurements. This technique ensures that small-scale unresolvable fea-
2271 tures of the oscillation probability have been averaged over whilst the large-scale
2272 features in the oscillation probability are unaffected. The documentation and valida-
2273 tion of this technique are found in section 7.2. The oscillation probability calculation is
2274 computationally intensive due to the large number of matrix multiplications needed.
2275 Consequently, the CUDAProb3 implementation choice made within the fitting frame-
2276 work, as detailed in section 7.3, ensures that the analysis can be done in a timely
2277 manner.

2278 Whilst the beam neutrinos are assumed to propagate through a constant density
2279 slab of material, the density variations through the Earth result in more complex
2280 oscillation patterns. Furthermore, the uncertainty in the electron density can modify
2281 the oscillation probability for the denser core layers of the Earth. The model of the

2282 Earth used within this analysis is detailed in section 7.4. This includes information
2283 about the official SK-only methodology as well as improvements that can be made
2284 to remove some of the approximations made in that analysis. Another complexity of
2285 atmospheric neutrinos oscillation studies is that the height of production in the atmo-
2286 sphere is not known on an event-by-event basis. An analytical averaging technique
2287 that approximates the uncertainty of the oscillation probability has been followed,
2288 with the author of this thesis being responsible for the implementation and validation.
2289 This implementation of an external technique is illustrated in section 7.5.

2290 7.1 Overview

2291 DB: Should this be moved into an earlier chapter? The selections chapter references
2292 the matter resonance which has not yet been explained at that point

2293 The analysis presented within this thesis focuses on the determination of oscillation
2294 parameters from atmospheric and beam neutrinos. Whilst subject to the same oscil-
2295 lation formalism, the way in which the two samples have sensitivity to the different
2296 oscillation parameters differs quite significantly.

2297 Atmospheric neutrinos have a varying baseline, or “path length”, L , such that
2298 the distance each neutrino travels before interacting is dependent upon the zenith
2299 angle, θ_Z . As primary cosmic rays can interact anywhere between the Earth’s surface
2300 and $\sim 50\text{km}$ above that, the height, h , in the atmosphere at which the neutrino was
2301 generated also affects the path length,

$$L = \sqrt{(R_E + h)^2 - R_E^2 (1 - \cos^2(\theta_Z))} - R_E \cos(\theta_Z). \quad (7.1)$$

2302 Where $R_E = 6,371\text{km}$ is the Earth's radius. Consequently, the oscillation probability
2303 is dependent upon two parameters, $\cos(\theta_Z)$ and E_ν .

2304 The oscillation probability used within this analysis is based on [21]. The neutrino
2305 wavefunction in the vacuum Hamiltonian evolves in each layer of constant matter
2306 density via

$$i \frac{d\psi_j(t)}{dt} = \frac{m_j^2}{2E_\nu} \psi_j(t) - \sum_k \sqrt{2} G_F N_e U_{ej} U_{ke}^\dagger \psi_k(t), \quad (7.2)$$

2307 where m_j^2 is the square of the j^{th} vacuum eigenstate mass, E_ν is the neutrino
2308 energy, G_F is Fermi's constant, N_e is the electron number density and U is the PMNS
2309 matrix. The transformation $N_e \rightarrow -N_e$ and $\delta_{CP} \rightarrow -\delta_{CP}$ is applied for antineutrino
2310 propagation. Thus, a model of the Earth's density is required for atmospheric neutrino
2311 propagation. Following the official SK-only methodology [210], this analysis uses the
2312 Preliminary Reference Earth Model (PREM) [211]. This model provides piecewise cubic
2313 polynomials as a function of the Earth's radius which results in the density profile
2314 illustrated in Figure 7.1. As discussed, the propagator requires layers of constant
2315 density. The SK methodology approximates the PREM model by using four layers of
2316 constant density [210]. The details of these layers are detailed in Table 7.1.

| Layer | Outer Radius [km] | Density [g/cm^3] | Chemical composition (Z/A) |
|-----------------|-------------------|------------------------------------|----------------------------|
| Inner Core | 1220 | 13 | 0.468 ± 0.029 |
| Outer Core | 3480 | 11.3 | 0.468 ± 0.029 |
| Lower Mantle | 5701 | 5.0 | 0.496 |
| Transition Zone | 6371 | 3.3 | 0.496 |

Table 7.1: Description of the four layers of the Earth invoked within the constant density approximation of the PREM model [211].

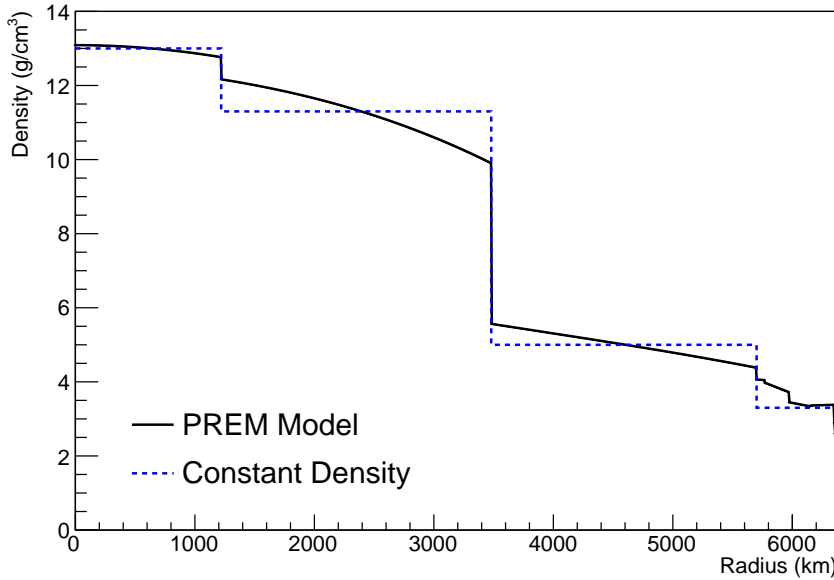


Figure 7.1: The density of the Earth given as a function of the radius, as given by the PREM model (Black), and the constant density four-layer approximation (Blue), as used in the official SK-only analysis.

2317 The atmospheric neutrino oscillation probabilities can be presented as two dimen-
 2318 sional “oscillograms” as illustrated in Figure 7.2. The distinct discontinuities, as a
 2319 function of $\cos(\theta_Z)$, are due to the discrete change in density invoked within the PREM
 2320 model.

2321 Atmospheric neutrinos do have sensitivity to δ_{CP} through a normalisation term.
 2322 Figure 7.3 illustrates the difference in oscillation probability between CP-conserving
 2323 ($\delta_{CP} = 0$) and a CP-violating ($\delta_{CP} = -1.601$) value taken from Asimov A oscillation
 2324 parameter set (Table 2.2). The result is a complicated oscillation pattern in the appear-
 2325 ance probability for sub-GeV upgoing neutrinos. The detector does not have sufficient
 2326 resolution to resolve these individual patterns so the sensitivity to δ_{CP} for atmospheric
 2327 neutrinos comes via the overall normalisation of these events.

2328 The presence of matter means that the effect δ_{CP} has on the oscillation probability
 2329 is not equal between neutrinos and antineutrinos, which would be expected when
 2330 propagating through a vacuum. This is further extenuated by the fact that SK can

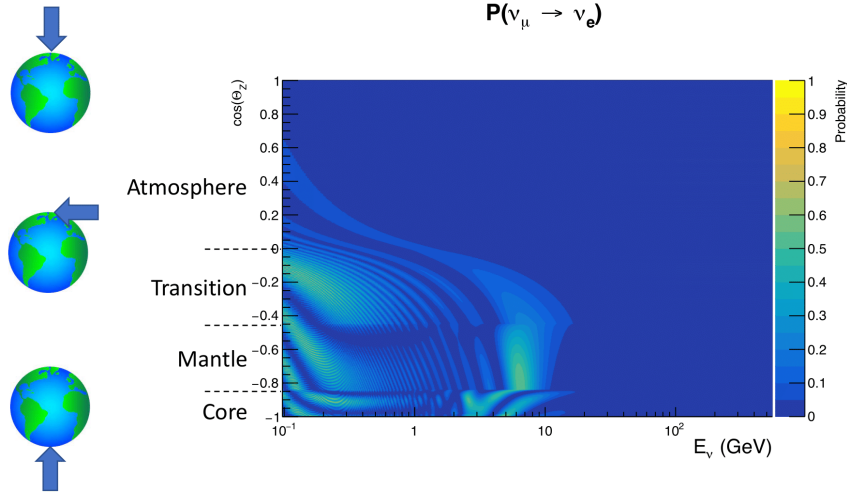


Figure 7.2: An “oscillogram” that depicts the $P(\nu_\mu \rightarrow \nu_e)$ oscillation probability as a function of neutrino energy and cosine of the zenith angle. The zenith angle is defined such that $\cos(\theta_Z) = 1.0$ represents neutrinos that travel from directly above the detector. The four-layer constant density PREM model approximation is used and Asimov A oscillation parameters are assumed (Table 2.2).

not distinguish neutrinos and antineutrinos well and that the cross-section neutrino interaction is larger than that for antineutrinos. Finally, sample selections (discussed in section 6.1) targeting different neutrino interaction modes result in an imbalance in the percentage of neutrinos to anti-neutrinos. This is because negatively charged pions from antineutrino interactions are more likely to be captured by a nucleus compared to a positively charged pion. All of these effects lead to a difference in the number of neutrinos detected compared to antineutrinos. This changes how the δ_{CP} normalisation term is observed, resulting in a very complex sensitivity to δ_{CP} .

Atmospheric neutrinos are subject to matter effects as they travel through the dense matter in the Earth. The vacuum and matter oscillation probabilities for $P(\nu_e \rightarrow \nu_e)$ and $P(\bar{\nu}_e \rightarrow \bar{\nu}_e)$ are presented in Figure 7.4, where the PREM model has been assumed. The oscillation probability for both neutrinos and antineutrinos is affected in the presence of matter. However, the resonance effects around $O(5)\text{GeV}$ only occur for neutrinos in normal mass hierarchy and antineutrinos in inverse mass hierarchy. The

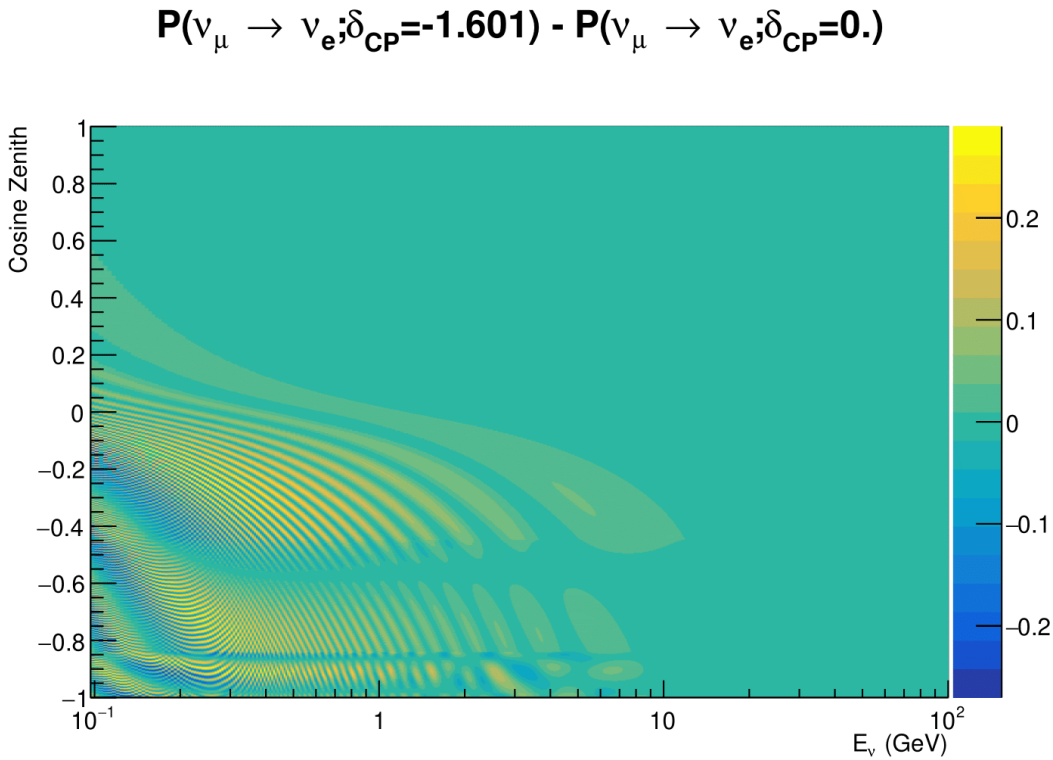


Figure 7.3: The effect of δ_{CP} for atmospheric neutrinos given in terms of the neutrino energy and zenith angle. This oscillogram compares the $P(\nu_\mu \rightarrow \nu_e)$ oscillation probability for a CP conserving ($\delta_{CP} = 0.0$) and a CP violating ($\delta_{CP} = -1.601$) value taken from the Asimov A parameter set. The other oscillation parameters assume the Asimov A oscillation parameter set given in Table 2.2.

exact position and amplitude of the resonance depend on $\sin^2(\theta_{23})$ meaning that the atmospheric neutrinos have sensitivity to $\sin^2(\theta_{23})$.

As the T2K beam flux is centered at the first oscillation maximum ($E_\nu = 0.6\text{GeV}$), the sensitivity to δ_{CP} is predominantly observed as a change in the event-rate of e-like samples in $\nu/\bar{\nu}$ modes. Figure 7.5 illustrates the $P(\nu_\mu \rightarrow \nu_e)$ oscillation probability for a range of δ_{CP} values. A circular modulation of the first oscillation peak (in both magnitude and position) is observed when varying throughout the allowable values of δ_{CP} . The CP-conserving values of $\delta_{CP} = 0, \pi$ have a lower(higher) oscillation maximum than the CP-violating values of $\delta_{CP} = -\pi/2(\delta_{CP} = \pi/2)$. A sub-dominant

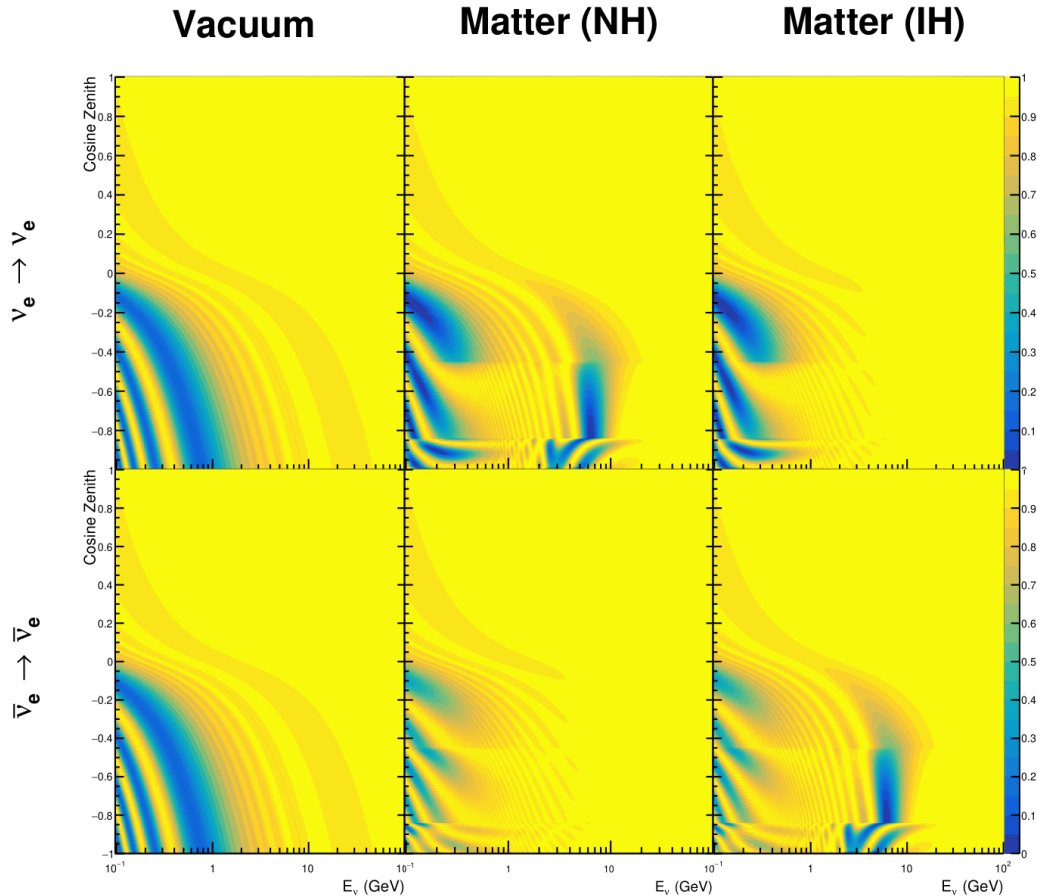


Figure 7.4: An illustration of the matter-induced effects on the oscillation probability, given as a function of neutrino energy and zenith angle. The top row of panels gives the $P(\nu_e \rightarrow \nu_e)$ oscillation probability and the bottom row illustrates the $P(\bar{\nu}_e \rightarrow \bar{\nu}_e)$ oscillation probability. The left column highlights the oscillation probability in a vacuum, whereas the middle and right column represents the oscillation probabilities when the four-layer fixed density PREM model is assumed. All oscillation probabilities assume the “Asimov A” set given in Table 2.2, but importantly, the right column sets an inverted mass hierarchy. The “matter resonance” effects at $E_\nu \sim 5\text{GeV}$ can be seen in the $P(\nu_e \rightarrow \nu_e)$ for normal mass hierarchy and $P(\bar{\nu}_e \rightarrow \bar{\nu}_e)$ for inverted hierarchy.

shift in the energy of the oscillation peak is also present to aid in separating the two
 CP-conserving values of δ_{CP} .

T2K’s sensitivity to the $\sin^2(\theta_{23})$ and Δm_{23}^2 is observed as a shape-based variation
 of the muon-like samples, as illustrated in Figure 7.5. The value of Δm_{32}^2 laterally shifts
 the position of the oscillation dip (around $E_\nu \sim 0.6\text{GeV}$) in the $P(\nu_\mu \rightarrow \nu_\mu)$ oscillation

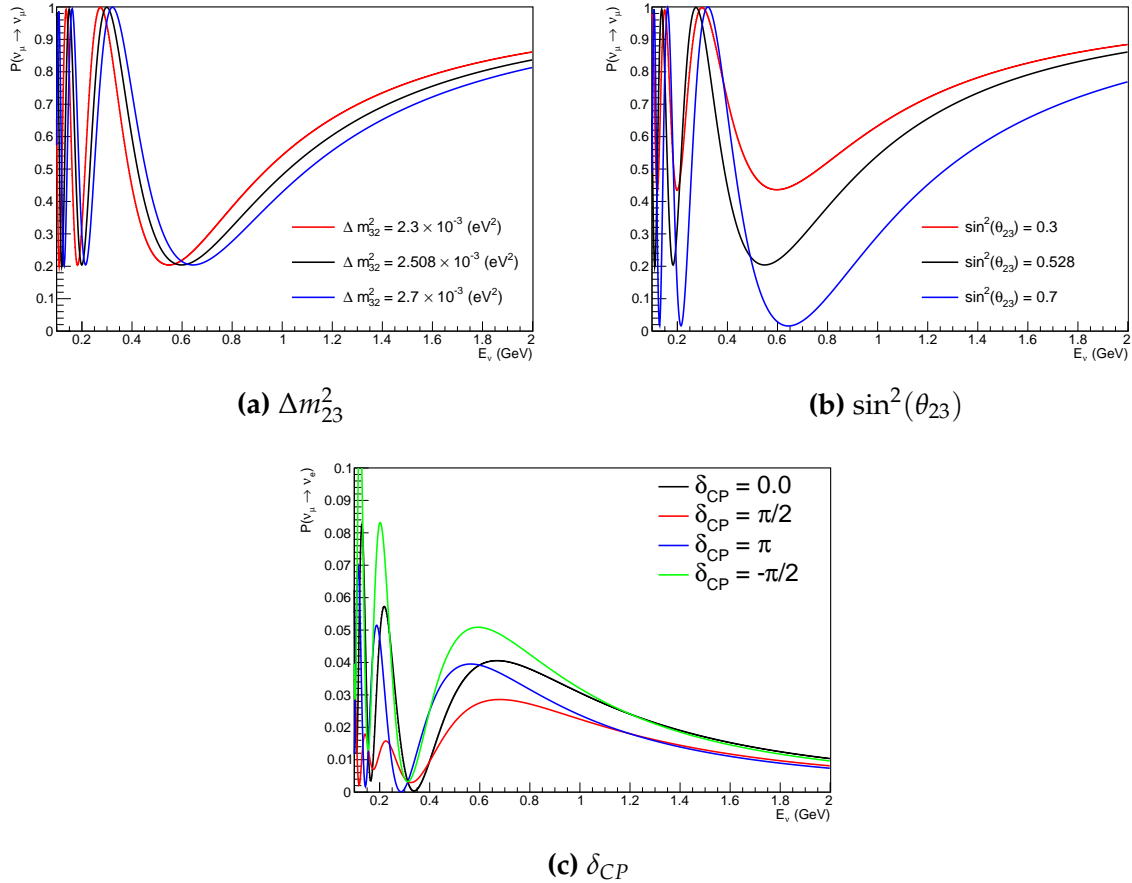


Figure 7.5: The oscillation probability for beam neutrino events given as a function of neutrino energy. All oscillation parameters assume the “Asimov A” set given in Table 2.2 unless otherwise stated. Each panel represents a change in one of the oscillation parameters whilst keeping the remaining parameters fixed.

probability. A variation of $\sin^2(\theta_{23})$ is predominantly observed as a vertical shift of the oscillation dip with second-order horizontal shifts being due to matter effects. The beam neutrinos have limited sensitivity to matter effects due to the relatively shorter baseline as well as the Earth’s mantle being a relatively low-density material (as compared to the Earth’s core). For some values of δ_{CP} , the degeneracy in the number of e-like events allows the mass hierarchy to be resolved. This leads to a δ_{CP} -dependent mass hierarchy sensitivity which can be seen in Figure 7.6.

Whilst all oscillation channels should be included for completeness, the computational resources required to run a fit are limited and any reasonable approximations

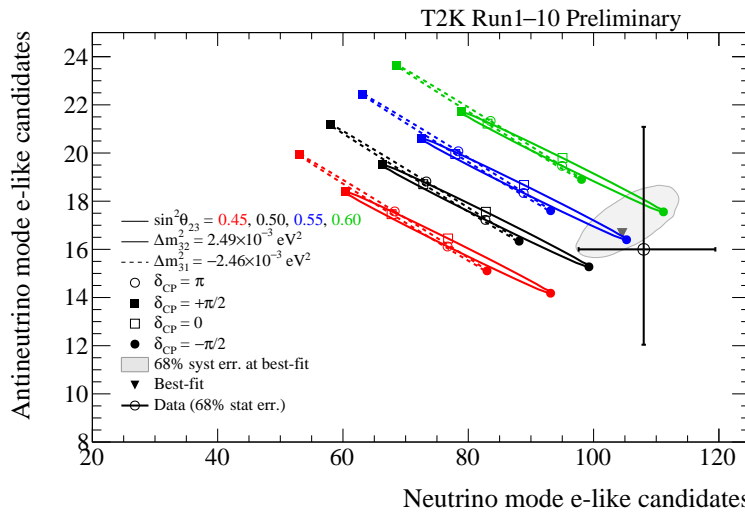


Figure 7.6: The number of electron-like events in the FHC and RHC operating mode of the beam, as a function of the oscillation probabilities. Both normal hierarchy (Solid) and inverse hierarchy (Dashed) values of Δm_{23}^2 are given.

which reduce the number of oscillation probability calculations that need to be made should be applied. The $\nu_e \rightarrow \nu_{e,\mu,\tau}$ (and antineutrino equivalent) oscillations can be ignored for beam neutrinos as the $\nu_e/\bar{\nu}_e$ fluxes are approximately two orders of magnitude smaller than the corresponding $\nu_\mu/\bar{\nu}_\mu$ flux. Furthermore, as the peak neutrino energy of the beam is well below the threshold for charged current tau production ($E_\nu = 3.5\text{GeV}$ [51], only a small proportion of the neutrinos produced in the beam have the required energy. For the few neutrinos that have sufficient energy, the oscillation probability is very small due to the short baseline. Whilst these approximations can be made for the beam neutrinos, the atmospheric flux of ν_e is of the same order of magnitude as the ν_μ flux and the energy distribution of atmospheric neutrinos extends well above the tau production threshold.

²³⁷⁹ 7.2 Treatment of Fast Oscillations

²³⁸⁰ As shown in Figure 7.7, atmospheric neutrino oscillations have a significantly more
²³⁸¹ complex structure for upgoing neutrinos with energy below 1GeV. This is because the
²³⁸² L/E dependence of the oscillation probability in this region induces rapid variations
²³⁸³ for small changes in L or E . As discussed in section 7.1, this is also the region in which
²³⁸⁴ atmospheric neutrinos have sensitivity to δ_{CP} . In practice, the direction of the neutrino
²³⁸⁵ is inferred from the direction of the final state particles traveling in the detector, which
²³⁸⁶ can be poor for low-energy neutrino interactions. This creates a distinct difference
²³⁸⁷ from the beam neutrinos where the position of the source is very precisely known.

²³⁸⁸ As a consequence of the unresolvable structure, an average oscillation probability
²³⁸⁹ is observed in the subGeV upgoing region. This creates a computational problem; A
²³⁹⁰ significantly large amount of Monte Carlo statistics would be required to accurately
²³⁹¹ predict the number of events if Monte Carlo averaging was the only technique used.
²³⁹² This section describes the ‘sub-sampling’ approach developed for this analysis and
²³⁹³ compares it to the methodology used within the SK-only analysis.

²³⁹⁴ The official SK-only analysis uses the osc3++ oscillation parameter fitter [210].
²³⁹⁵ To perform the fast oscillation averaging, it uses a ‘nearest-neighbour’ technique.
²³⁹⁶ For a given neutrino event, the nearest twenty neighbours in reconstructed lepton
²³⁹⁷ momentum and zenith angle are found and a distribution of their neutrino energies is
²³⁹⁸ built. The RMS, σ , of this distribution is then used to compute an average oscillation
²³⁹⁹ probability for the given neutrino Monte Carlo event.

²⁴⁰⁰ For the i^{th} event, the oscillation weight is calculated as

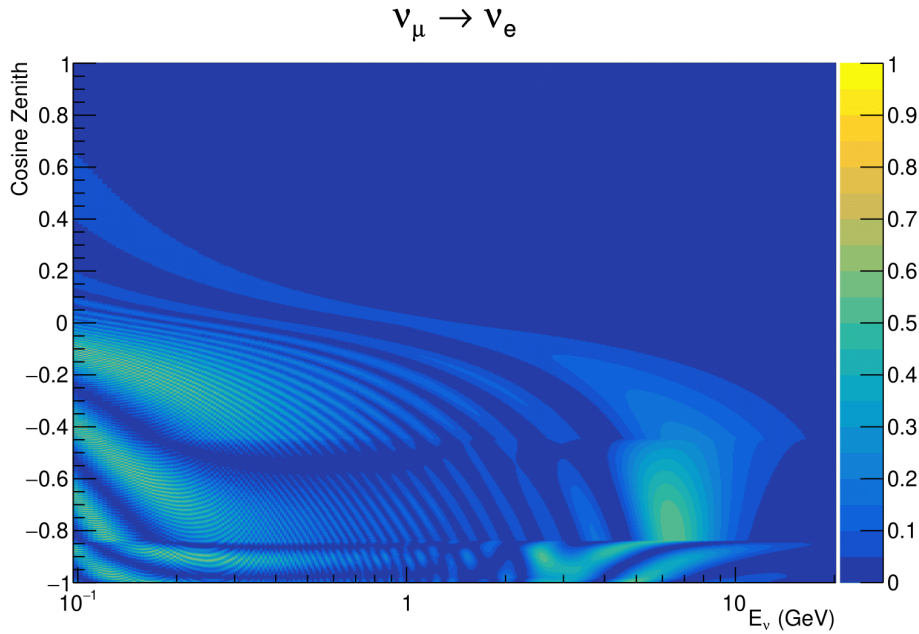


Figure 7.7: The oscillation probability $P(\nu_\mu \rightarrow \nu_e)$, given as a function of neutrino energy and zenith angle, which highlights an example of the “fast” oscillations in the sub-GeV upgoing region.

$$W_i = \frac{1}{5}P(E_i, \bar{L}_i) + \frac{1}{5} \sum_{\beta=-1,-0.5,0.5,1} P(E_i + \beta\sigma_i, L_\beta), \quad (7.3)$$

where $P(E, L)$ is the oscillation probability calculation for neutrino energy E and path length L and the two path lengths, \bar{L}_i and L_β are discussed below. All of the oscillation probability calculations are performed with a fixed zenith angle such that the same density profile is used.

The uncertainty in the production height is controlled by using an “average” production height, \bar{L}_i , which represents the average path length computed using twenty production heights taken from the Honda flux model’s prediction [45]. For a given event, the production heights are sampled in steps of 5% of their cumulative distribution function. L_β values are similarly calculated but instead use different combinations of four production heights,

$$\begin{aligned}
 L_{-1.0} &= \frac{1}{4}L(45, 50, 55, 60), \\
 L_{-0.5} &= \frac{1}{4}L(35, 40, 65, 70), \\
 L_{+0.5} &= \frac{1}{4}L(25, 30, 75, 68), \\
 L_{+1.0} &= \frac{1}{4}L(15, 20, 85, 89).
 \end{aligned} \tag{7.4}$$

2411 This averaging technique works because of the inference between the zenith angle
 2412 and the reconstructed direction of final state particles in the detector. For low-energy
 2413 neutrinos, where the resolution of the true neutrino direction is poor, σ_i will be large,
 2414 resulting in significant averaging effects. Contrary to this, the inferred direction of
 2415 high-energy neutrinos will be much closer to the true value, meaning that σ_i will be
 2416 smaller, culminating in small averaging effects.

2417 In practice, this technique is performed before the fit in order to deal with the
 2418 computational cost. This is possible as the Osc3++ framework uses binned oscillation
 2419 parameters rather than continuous so the oscillation parameters used in the fit are
 2420 known prior to run-time. The framework used in this analysis uses continuous
 2421 oscillation parameters, and due to the MCMC fitting technique, there is no way to
 2422 know which oscillation parameter values will be selected *a priori*. Therefore, the
 2423 oscillation parameter calculation has to be performed at run-time. Computing five
 2424 oscillation probabilities per event would require far too many computational resources
 2425 to be viable. Therefore SK technique can not be used within this analysis. However,
 2426 the concept of the averaging technique can be taken from it.

2427 To perform a similar averaging as the SK analysis, a sub-sampling approach using
 2428 binned oscillograms has been devised. The technique can be explained by considering
 2429 a “fine” and “coarse” oscillogram. The fine oscillograms are used to define the array of

2430 $\cos(\theta_Z)$ and E_ν used in the oscillation engine. The coarse oscillograms cover the same
2431 phase-space but have fewer bins, where the value of a particular coarse bin is taken
2432 as the linear average (flat prior in E_ν and $\cos(\theta_Z)$) of all fine bins which falls into it.
2433 The coarse oscillogram is then used for determining the oscillation weight for a given
2434 event. The binning which is used to calculate the oscillation probabilities, known as
2435 the ‘fine’ binning, has $N \times N$ subdivisions per coarse bin. Figure 7.8 illustrates the
2436 $N = 2$ example where the assigned value to a coarse bin is the average of the four fine
2437 bins which fall in that coarse bin. Whilst the coarse bin edges do not have to be linear
2438 on either axis, the sub-division of the fine bins is linear over the range of a coarse bin.

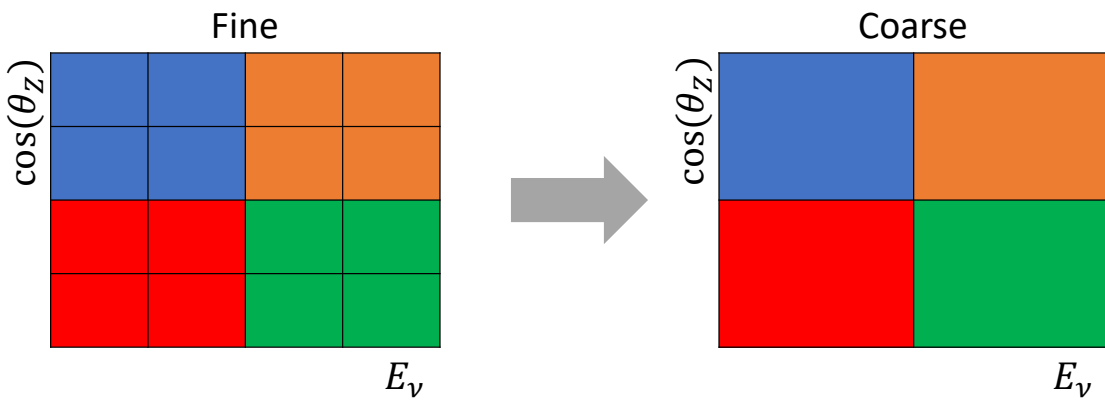


Figure 7.8: Illustration of the averaging procedure for $N = 2$. The oscillation probabilities calculated on the finer left binning are averaged to obtain the oscillation probabilities in the coarser right binning. These averaged oscillation probabilities with the coarser binning are then applied to each event during the fit.

2439 The coarse binning is defined with 67×52 bins in true neutrino energy \times cosine
2440 zenith. It is picked to be identical to that provided in [212]. In general, the binning is
2441 logarithmically spaced in neutrino energy but has some hand-picked bin edges. Firstly,
2442 the bin density around the matter resonance is smoothly increased around the matter
2443 resonance region. This is to avoid smearing this region which can be well sampled by
2444 the Monte Carlo. Secondly, bin edges are selected to hit $0.4, 0.6, 1, 10, 30, 50, 100\text{GeV}$.
2445 This is to ensure that the Coulomb correction systematic and the atmospheric flux
2446 systematics definitions in neutrino energy can be hit. The cosine zenith binning is

2447 approximately linearly spaced across the allowable range but the values of layer
2448 transitions are hit precisely: -0.8376 (core-mantle) and -0.4464 (mantle/transition
2449 zone). Bins are spread further apart for downgoing events as this is a region unaffected
2450 by the fast oscillation wavelengths and reduces the total number of calculations
2451 required to perform the calculation.

2452 The choice of N is justified based on two studies. Firstly, the variation of event rates
2453 of each sample is studied as a function of N . For a given set of oscillation parameters
2454 thrown from the PDG prior constraints (detailed in Table 2.1), the oscillation probabili-
2455 ties are calculated using a given value of N . Each sample is re-weighted and the event
2456 rate is stored. The value of N is scanned from 1, which corresponds to no averaging, to
2457 24, which corresponds to the largest computationally viable subdivision binning. The
2458 event rate of each sample at large N is expected to converge to a stationary value due
2459 to the fine binning fully sampling the small-scale structure. Figure 7.9 illustrates this
2460 behaviour for the SubGeV_elike_0dcy sample for 30 different throws of the oscillation
2461 parameters.

2462 Denoting the event rate for one sample for a given throw t at each N by λ_t^N , the
2463 average over all considered N values ($\bar{\lambda}_t = \frac{1}{24} \sum_{N=1}^{24} \lambda_t^N$) is computed. The variance in
2464 the event rate at each N is then calculated as

$$\text{Var}[\lambda^N] = \frac{1}{N_{\text{throws}}} \sum_{t=1}^{N_{\text{throws}}} (\lambda_t^N - \bar{\lambda}_t)^2 - \left[\frac{1}{N_{\text{throws}}} \sum_{t=1}^{N_{\text{throws}}} (\lambda_t^N - \bar{\lambda}_t) \right]^2. \quad (7.5)$$

2465 The aim of the study is to find the lowest value of N such that this variance is
2466 below 0.001. This is the typical threshold used by T2K fitters to validate systematic
2467 implementation so has been set as the same criteria. The results of this study for
2468 each atmospheric sample used within this thesis are illustrated in Figure 7.10 for

SubGeV-elike-0dcy

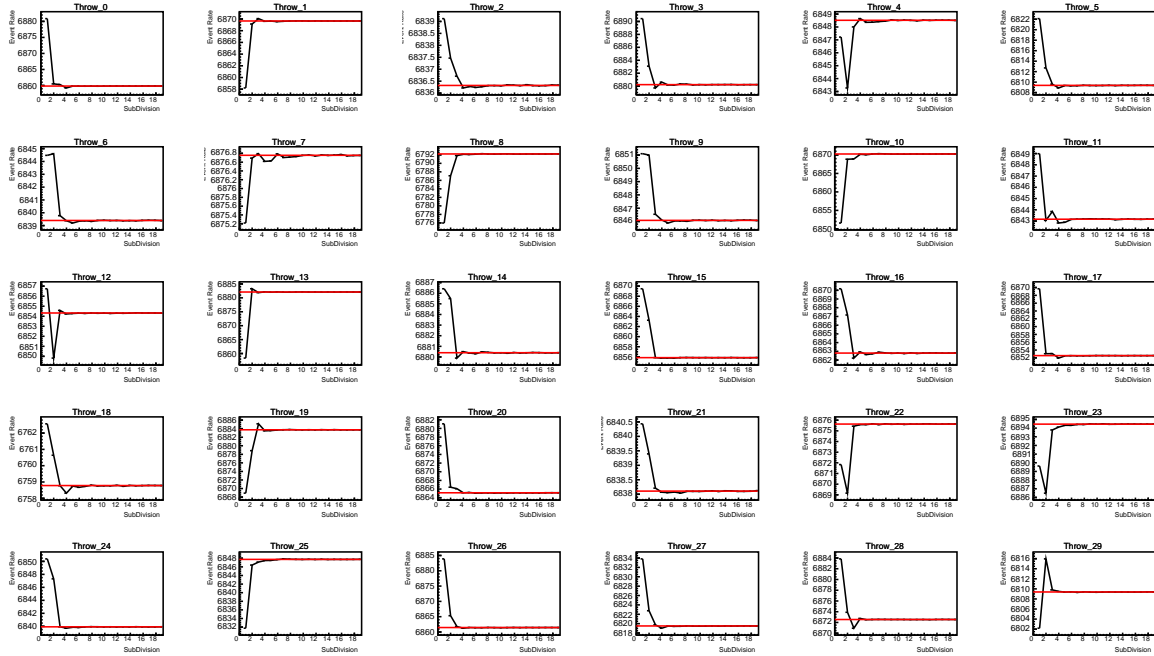


Figure 7.9: Event rate of the SubGeV_elike_0dcy sample as a function of the number of subdivisions per coarse bin. Each subplot represents the event rate of the sample at a different oscillation parameter set thrown from the PDG priors detailed in Table 2.1. The red line in each subplot represents the mean of the event rate over the different values of sub-divisions for that particular oscillation parameter throw.

2469 2000 throws of the oscillation parameters. As can be seen, the variance is below
 2470 the threshold at $N = 10$, and is driven primarily by the SubGeV_mulike_1dcy and
 2471 SubGeV_elike_0dcy samples.

2472 The second study to determine the value of N is as follows. The likelihood for each
 2473 sample is computed against an Asimov data set created with Asimov A oscillation
 2474 parameters (Table 2.2). Following Equation 7.5, the variance of the log-likelihood over
 2475 all considered N is computed. The results are shown in Figure 7.11.

2476 A choice of $N = 10$ sub-divisions per coarse bin has a variance in both event rate
 2477 and log-likelihood residuals less than the required threshold of 0.001. The largest
 2478 value of the likelihood variance is of order 10^{-7} , corresponding to an error on the log-

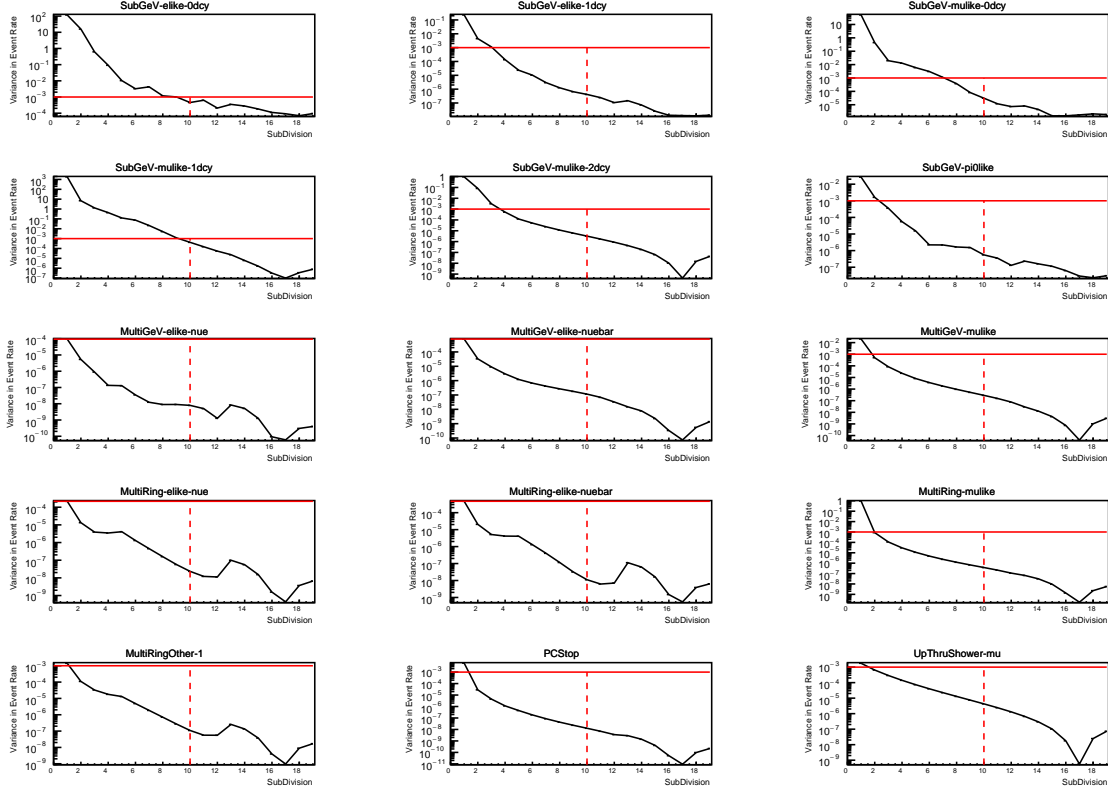


Figure 7.10: Variance of event rate for each atmospheric sample as a function of the number of sub-divisions per coarse bin. The solid red line indicates the 0.1% threshold and the dashed red line indicates the variance at a sub-division $N = 10$.

2479 likelihood of about 3×10^{-4} which is small enough to be negligible for the oscillation
 2480 analysis.

2481 Figure 7.12 illustrates the effect of the smearing using $N = 10$. The fast oscillations
 2482 in the sub-GeV upgoing region have been replaced with a normalisation effect whilst
 2483 the large matter resonance structure remains.

2484 7.3 Calculation Engine

2485 As previously discussed in section 7.2, the calculation of oscillation probabilities is per-
 2486 formed at run-time due to utilising continuous oscillation parameters. Consequently,
 2487 the time per calculation is crucial for fit performance. The initial fitting framework

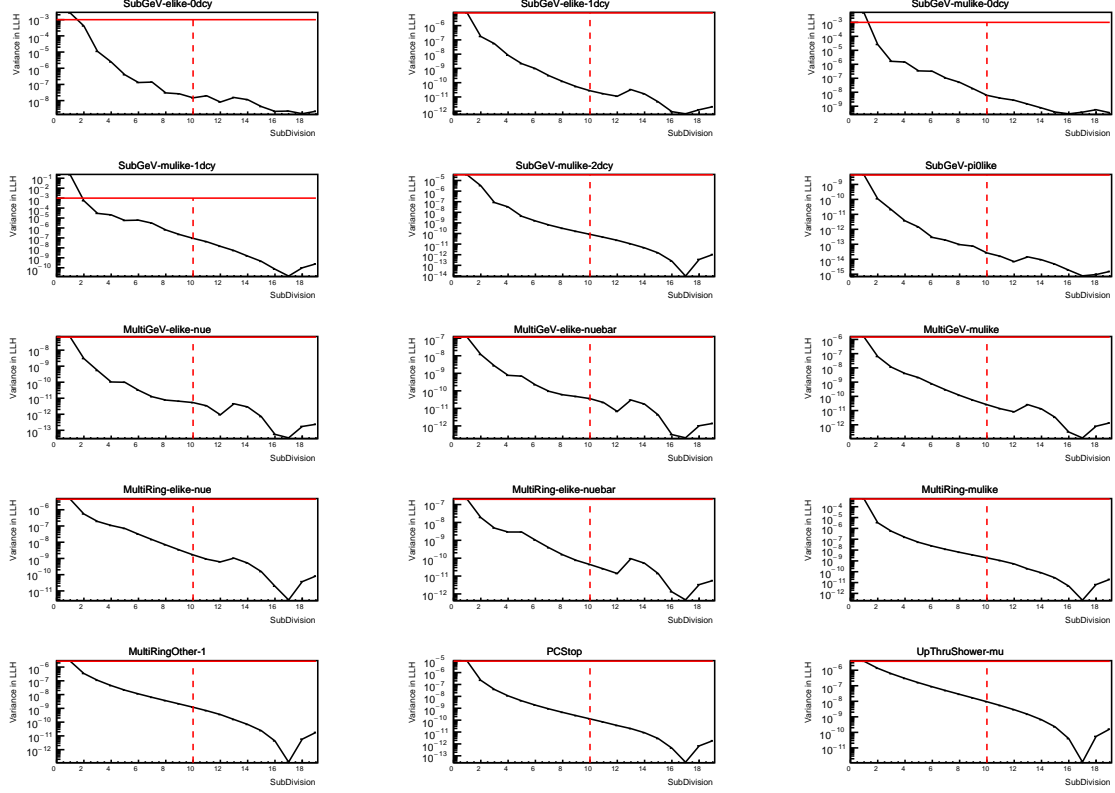


Figure 7.11: Variance of sample likelihood, when compared to ‘Asimov data’ set at Asimov A, for each atmospheric sample as a function of the number of sub-divisions per coarse bin. The solid red line indicates the 0.1% threshold and the dashed red line is a graphical indication of the variance at a sub-division $N = 10$.

used for this analysis was developed with ProbGPU [213]. This is a GPU-only implementation of the prob3 engine [214]. It is primarily designed for neutrino propagation in a beam experiment (single layer of constant density) with the atmospheric propagation code not being used prior to the analysis in this thesis.

Another engine, CUDAProb3 [215], has been implemented within the fitting framework used in this analysis. It has been specifically optimised for atmospheric neutrino oscillation calculation so does not contain the code to replace the beam oscillation calculation. The engine utilises object-orientated techniques as compared to the functional implementation of ProbGPU. This allows the energy and cosine zenith arrays to be kept on GPU memory, rather than having to load these arrays onto GPU memory for each calculation. General memory interfacing is one of the slowest tasks which

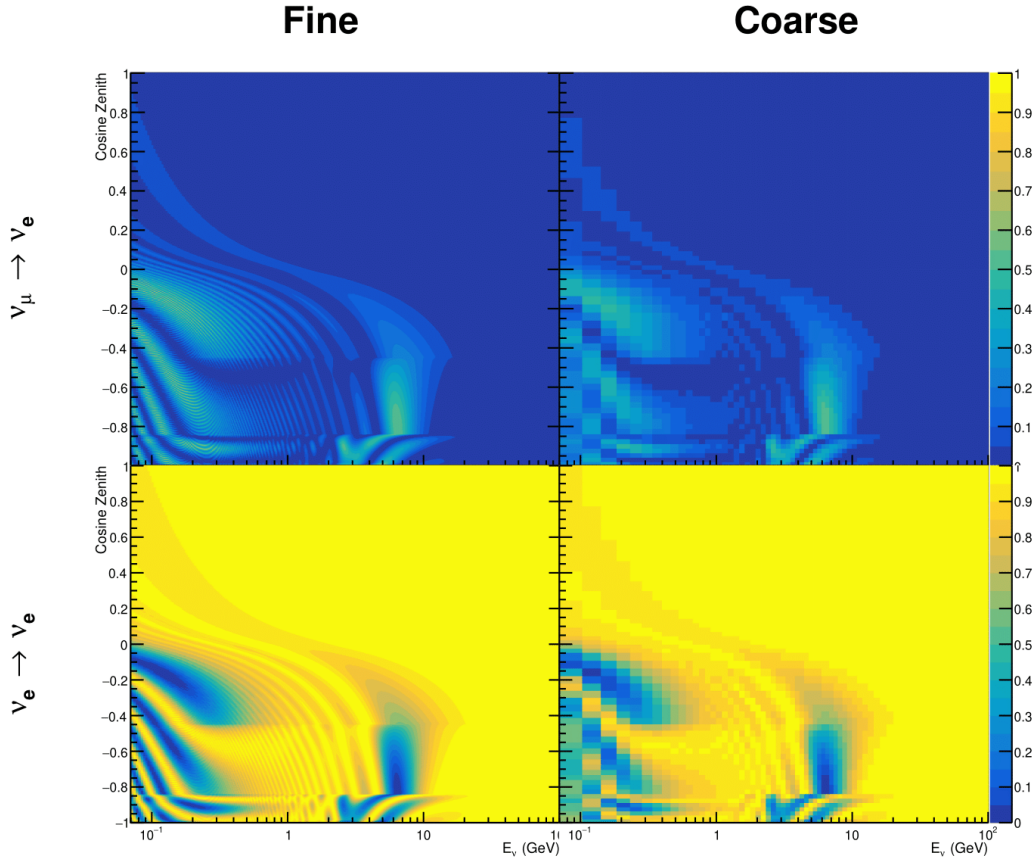


Figure 7.12: The oscillation probability, $P(\nu_\mu \rightarrow \nu_e)$ (top row) and $P(\nu_e \rightarrow \nu_\mu)$ (bottom row), given as a function of neutrino energy and zenith angle. The left column gives the “fine” binning used to calculate the oscillation probabilities and the right column illustrates the “coarse” binning used to reweight the Monte Carlo events. The fine binning choice is given with $N = 10$, which was determined to be below the threshold from Figure 7.10 and Figure 7.11.

2499 GPUs can do, so being able to eliminate this significantly reduces the time required
 2500 for calculation. This can be seen in Figure 7.13, where the GPU implementation of
 2501 CUDAProb3 is approximately three times faster than the ProbGPU engine.

2502 Another significant advantage of CUDAProb3 is that it contains a CPU multithreaded
 2503 implementation which is not possible with the ProbGPU or prob3 engines. This elimi-
 2504 nates the requirement for GPU resources when submitting jobs to batch systems. As
 2505 illustrated in Figure 7.13, the calculation speed depends on the number of available

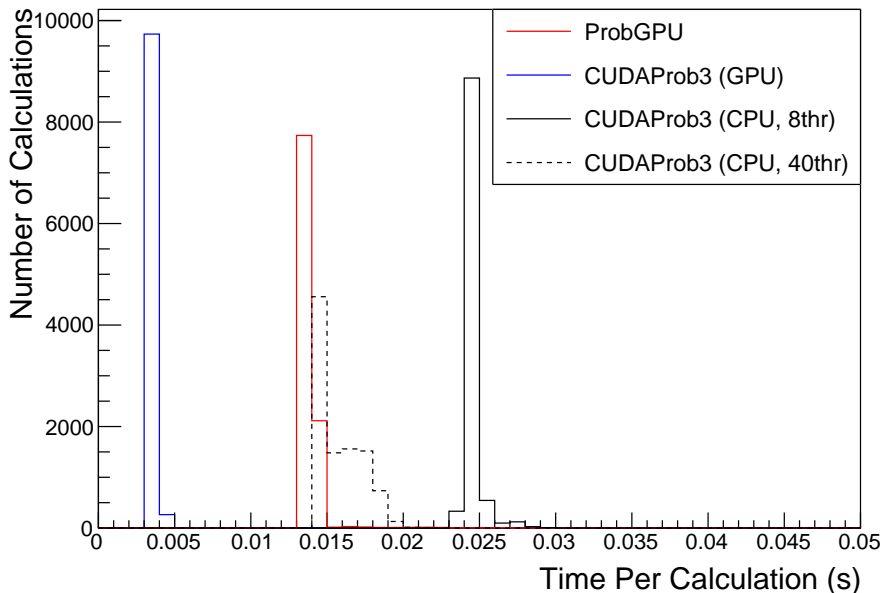


Figure 7.13: The calculation time taken to both calculate the oscillation probabilities and fill the “coarse” oscillograms, following the technique given in section 7.2, for the CUDAProb3 and ProbGPU (Red) calculation engines. CUDAProb3 has both a GPU (Blue) and CPU (Black) implementation, where the CPU implementation is multithreaded. Therefore, 8-threads (solid) and 40-threads (dashed) configurations have been tested. Prob3, which is a CPU single-thread implementation has a mean step time of 1.142s.

2506 threads. Using 8 threads (which is typical of the batch systems being used) is ap-
 2507 proximately twice as slow as the ProbGPU engine implementation, but would allow
 2508 the fitting framework to be run on many more resources. This fact is utilised for any
 2509 SK-only fits but GPU resources are required for any fits which include beam samples
 2510 due to the ProbGPU requirement. Based on the benefits shown by the implementa-
 2511 tion in this section, efforts are being placed into including linear propagation for beam
 2512 neutrino propagation into the engine [216].

2513 7.4 Matter Density Profile

2514 For an experiment observing atmospheric neutrinos propagating through the Earth, a
 2515 model of the Earth’s density profile is required. The model used within this analysis is

2516 the Preliminary Reference Earth Model (PREM) [211], as illustrated in Figure 7.1. As
2517 discussed in section 7.1, the propagator used within the calculation engine requires
2518 constant density layers. To follow the official SK-only analysis [210], the average
2519 density of each layer has been taken from the PREM model. Table 7.1 documents
2520 the density and radii of the layers used within this approximation. The density
2521 measurements provided in the PREM model are provided in terms of mass density,
2522 whereas neutrino oscillations are sensitive to the electron number density. This value
2523 can be computed as the product of the chemical composition, or the Z/A value, and
2524 the mass density of each layer. Currently, the only way to calculate the chemical
2525 composition value for layers close to the Earth’s core is through neutrino oscillations.
2526 The chemical composition of the upper layers of the Earth’s Mantle and the Transition
2527 zone is well known due to it being predominantly pyrolite which has a chemical
2528 composition value of 0.496 [217]. The components of the Earth’s core region are less
2529 well known. Consequently, the chemical composition dial for the core layers is set to a
2530 value of 0.468, as calculated in [218]. This value is assigned a Gaussian error with a
2531 standard deviation equivalent to the difference in chemical composition in core and
2532 mantle layers. Figure 7.14 illustrates the effect of moving from the $Z/A = 0.5$ method
2533 which is used in the official SK-only analysis [210] to these more precise values.

2534 The beam oscillation probability in this thesis uses a baseline of 295km, density
2535 2.6g/cm^3 , and chemical composition 0.5 as is done by the official T2K-only analysis
2536 [219].

2537 Whilst the propagator requires a fixed density layer model of the Earth, the density
2538 only has to be fixed for a specific $E_\nu \times \cos(\theta_Z)$ bin in a given layer. As the density is a
2539 function of radius, which is a function of the direction in which a neutrino propagates,
2540 a better approximation of the PREM model can be made if a $\cos(\theta_Z)$ -specific density is
2541 calculated.

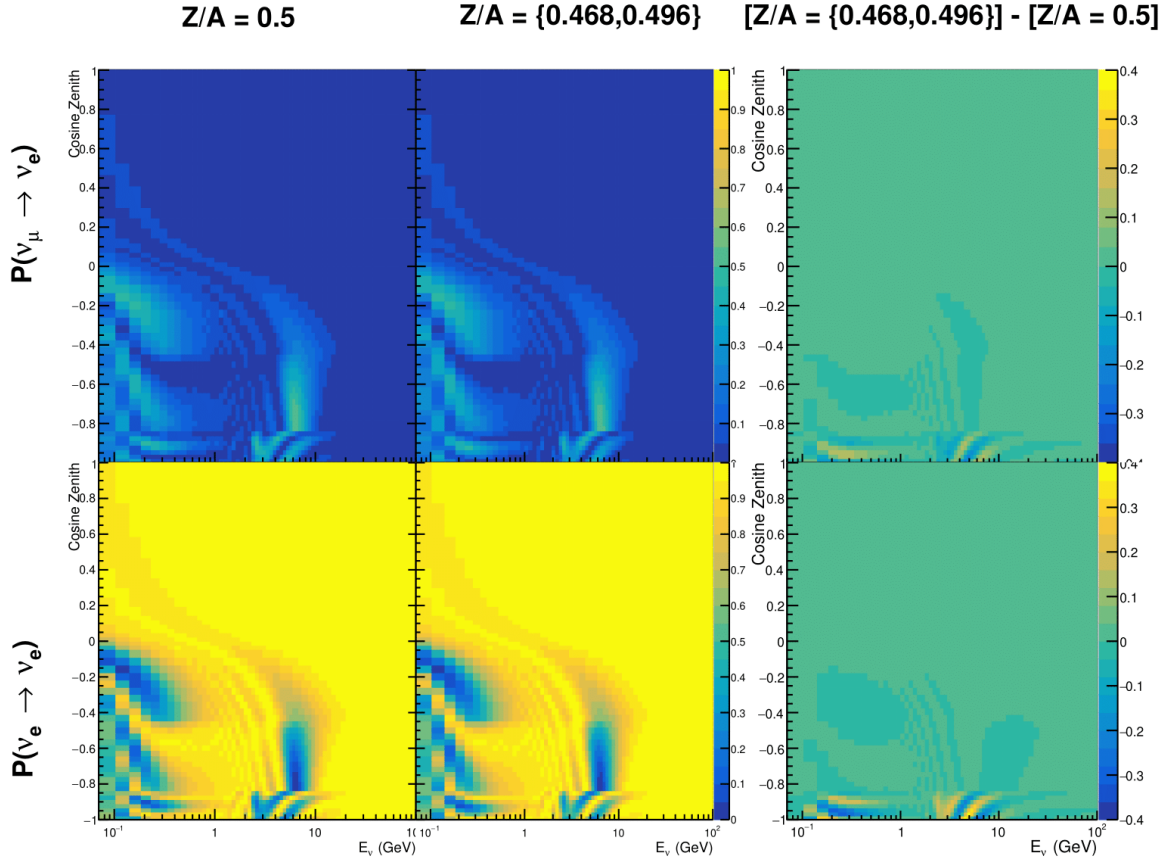


Figure 7.14: The oscillation probability, $P(\nu_\mu \rightarrow \nu_e)$ (top row) and $P(\nu_e \rightarrow \nu_\mu)$ (bottom row), given as a function of neutrino energy and zenith angle. The left column gives probabilities where the constant $Z/A = 0.5$ approximation which is used in the official SK-only analysis. The middle column gives the probabilities where $Z/A = [0.468, 0.498]$ values are used, as given in Table 7.1. The right column illustrates the difference in oscillation probability between the two different techniques.

2542 To achieve this, the average density, $\langle \rho \rangle_i$, in the i^{th} layer, is calculated as the density,
 2543 $\rho(t)$, integrated over the track a given $\cos(\theta_Z)$,

$$\langle \rho \rangle_i = \frac{1}{t_{i+1} - t_i} \int_{t_i}^{t_{i+1}} \rho(t) dt \quad (7.6)$$

2544 where t_i are the intersection points between each layer and t is the path length of
 2545 the trajectory across the layer.

2546 The oscillation probability calculation speed is approximately linear in the number
 2547 of layers invoked within the Earth model. Therefore a four-layer model is still utilized
 2548 with the only difference to the official SK-only analysis being that the four-layer model
 2549 used for each value of $\cos(\theta_Z)$ is different. Following the method outlined in [220],
 2550 a four-layer piecewise quadratic polynomial is fit to the PREM model for the four
 2551 layers defined in Table 7.1. This fit was not performed by the author of the thesis
 2552 and is documented in [212]. The coefficients of the quadratic fit to each layer are
 2553 given in Table 7.2 with the final distribution illustrated in Figure 7.15. The quadratic
 2554 approximation is clearly much closer to the PREM model as compared to the constant
 2555 density approximation.

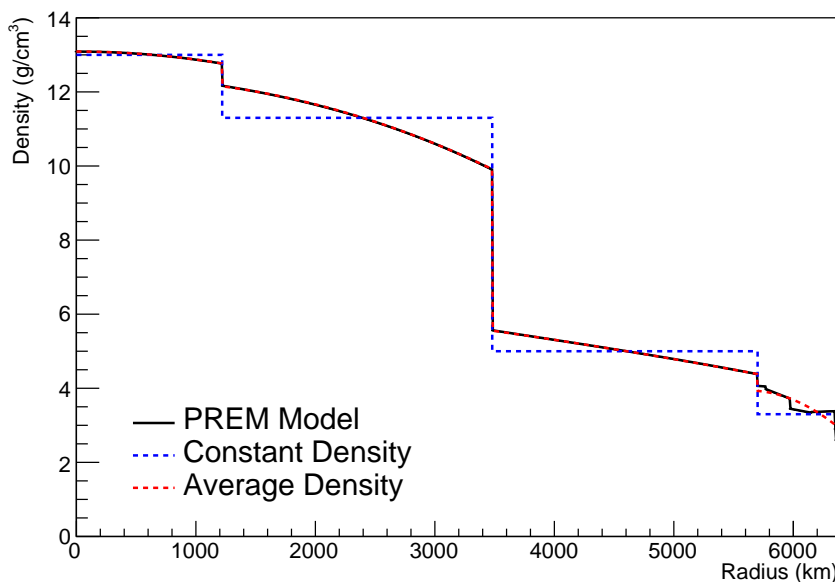


Figure 7.15: The density of the Earth given as a function of the radius, as given by the PREM model (Black), the constant density four-layer approximation (Blue), as used in the official SK-only analysis, and the quadratic approximation of the PREM model (Red).

| Layer | Outer Radius [km] | Density [g/cm ³] |
|-----------------|-------------------|-------------------------------|
| Inner Core | 1220 | $13.09 - 8.84x^2$ |
| Outer Core | 3480 | $12.31 + 1.09x - 10.02x^2$ |
| Lower Mantle | 5701 | $6.78 - 1.56x - 1.25x^2$ |
| Transition Zone | 6371 | $-50.42 + 123.33x - 69.95x^2$ |

Table 7.2: The quadratic polynomial fits to the PREM model for four assumed layers of the PREM model. The fit to calculate the coefficients is given in [212], where $x = R/R_{Earth}$.

The effect of using the quadratic density per $\cos(\theta_Z)$ model is highlighted in Figure 7.16. The slight discontinuity in the oscillation probability around $\cos(\theta_Z) \sim -0.45$ in the fixed density model, which is due to the transition to mantle layer boundary, has been reduced. This is expected as the difference in the density across this boundary is significantly smaller in the quadratic density model as compared to the constant density model. Whilst the difference in density across the other layer transitions is reduced, there is still a significant difference. This means the discontinuities in the oscillation probabilities remain but are significantly reduced. However, as the quadratic density approximation matches the PREM model well in this region, these discontinuities are due to the Earth model rather than an artifact of the oscillation calculation.

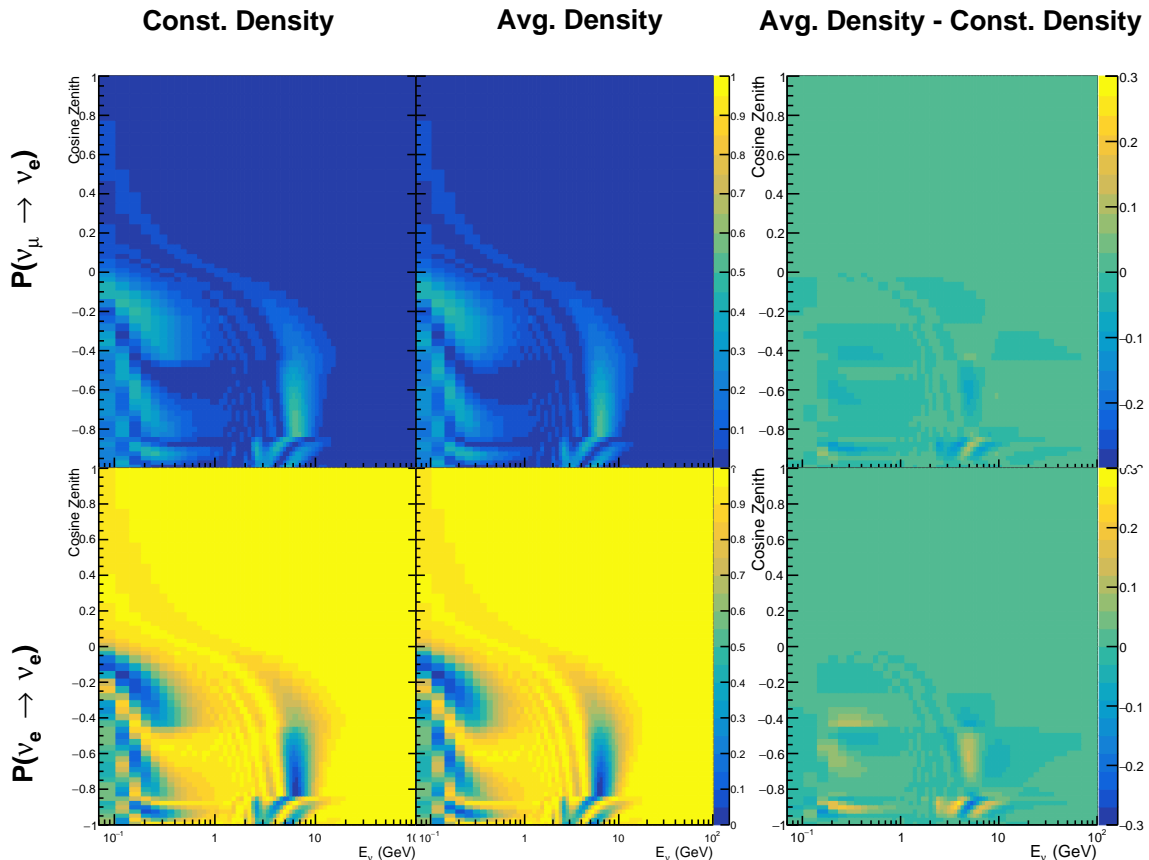


Figure 7.16: The oscillation probability, $P(\nu_\mu \rightarrow \nu_e)$ (top row) and $P(\nu_e \rightarrow \nu_\mu)$ (bottom row), given as a function of neutrino energy and zenith angle. The left column gives probabilities where the four-layer constant density approximation is used. The middle column gives the probabilities where the density is integrated over the trajectory, using the quadratic PREM approximation, for each $\cos(\theta_Z)$ is used. The right column illustrates the difference in oscillation probability between the two different techniques.

2567 7.5 Production Height Averaging

2568 As discussed in section 7.1, the height at which the cosmic ray flux interacts in the
2569 atmosphere is not known on an event-by-event basis. The production height can vary
2570 from the Earth’s surface to $\sim 50\text{km}$ above that. The SK-only analysis methodology
2571 (described in section 7.2) for including the uncertainty on the production height is
2572 to include variations from the Honda model when pre-calculating the oscillation
2573 probabilities prior to the fit. This technique is not possible for this analysis which
2574 uses continuous oscillation parameters that can not be known prior to the fit. Conse-
2575 quently, an analytical averaging technique was developed in [212]. The author of this
2576 thesis was not responsible for the derivation of the technique but has performed the
2577 implementation and validation of the technique for this analysis alone.

2578 Using the 20 production heights per Monte Carlo neutrino event, provided as 5%
2579 percentiles from the Honda flux model, a production height distribution $p_j(h|E_\nu, \cos \theta_Z)$
2580 is built for each neutrino flavour $j = \nu_e, \bar{\nu}_e, \nu_\mu, \bar{\nu}_\mu$. In practice, a histogram is filled with
2581 20 evenly spaced bins in production height h between 0 and 50km. The neutrino energy
2582 and cosine zenith binning of the histogram is the same as that provided in section 7.2.
2583 The average production height, $\bar{h} = \int dh \frac{1}{4} \sum_j p_j(h|E_\nu, \cos(\theta_Z))$, is calculated. The
2584 production height binning of this histogram is then translated into $\delta t(h) = t(\bar{h}) - t(h)$,
2585 where $t(h)$ is the distance travelled along the trajectory.

2586 For the i^{th} traversed layer, the transition amplitude, $D_i(t_{i+1}, t_i)$, is computed. The
2587 time-ordered product of these is then used as the overall transition amplitude via

$$A(t_{n+1}, t_0) = D_n(t_{n+1}, t_n) \dots D_1(t_2, t_1) D_0(t_1, t_0), \quad (7.7)$$

2588

where,

$$\begin{aligned} D_n(t_{n+1}, t_n) &= \exp[-iH_n(t_{n+1} - t_n)] \\ &= \sum_{k=1}^3 C_k \exp[ia_k(t_{n+1} - t_n)] \end{aligned} \quad (7.8)$$

2589

is expressed as a diagonalised time-dependent solution to the Schrodinger equation.

2590

The 0^{th} layer is the propagation through the atmosphere and is the only term that depends on the production height. Using the substitution $t_0 = t(\bar{h}) - \delta t(h)$, it can be shown that

2593

Thus Equation 7.7 becomes

$$\begin{aligned} A(t_{n+1}, t_0) &= D_n(t_{n+1}, t_n) \dots D_1(t_2, t_1) D_0(t_1, \bar{h}) D(\delta t) \\ &= A(t_{n+1}, \bar{h}) \sum_{k=1}^3 C_k \exp[ia_k \delta t], \\ &= \sum_{k=1}^3 B_k \exp[ia_k \delta t]. \end{aligned} \quad (7.10)$$

2594

The oscillation probability averaged over production height is then calculated as

$$\begin{aligned}
 \bar{P}(\nu_j \rightarrow \nu_i) &= \int d(\delta t) p_j(\delta t | E_\nu, \cos \theta_Z) P(\nu_j \rightarrow \nu_i) \\
 &= \int d(\delta t) p_j(\delta t | E_\nu, \cos \theta_Z) A(t_{n+1}, t_0) A^*(t_{n+1}, t_0) \\
 &= \sum_{km} (B_k)_{ij} (B_m)_{ij}^* \int d(\delta t) p_j(\delta t | E_\nu, \cos \theta_Z) \exp[i(a_k - a_m)\delta t]
 \end{aligned} \tag{7.11}$$

2595 In practice, implementation in CUDAProb3 [215] is relatively straightforward as
 2596 the majority of these terms are already calculated in the standard oscillation calculation.
 2597 Figure 7.17 illustrates the results of the production height averaging. As expected,
 2598 the main effect is observed in the low-energy downward-going and horizontal-going
 2599 events. Upward-going events have to travel the radius of the Earth, $R_E = 6371\text{km}$,
 2600 where the production height uncertainty is a small fraction of the total path length.

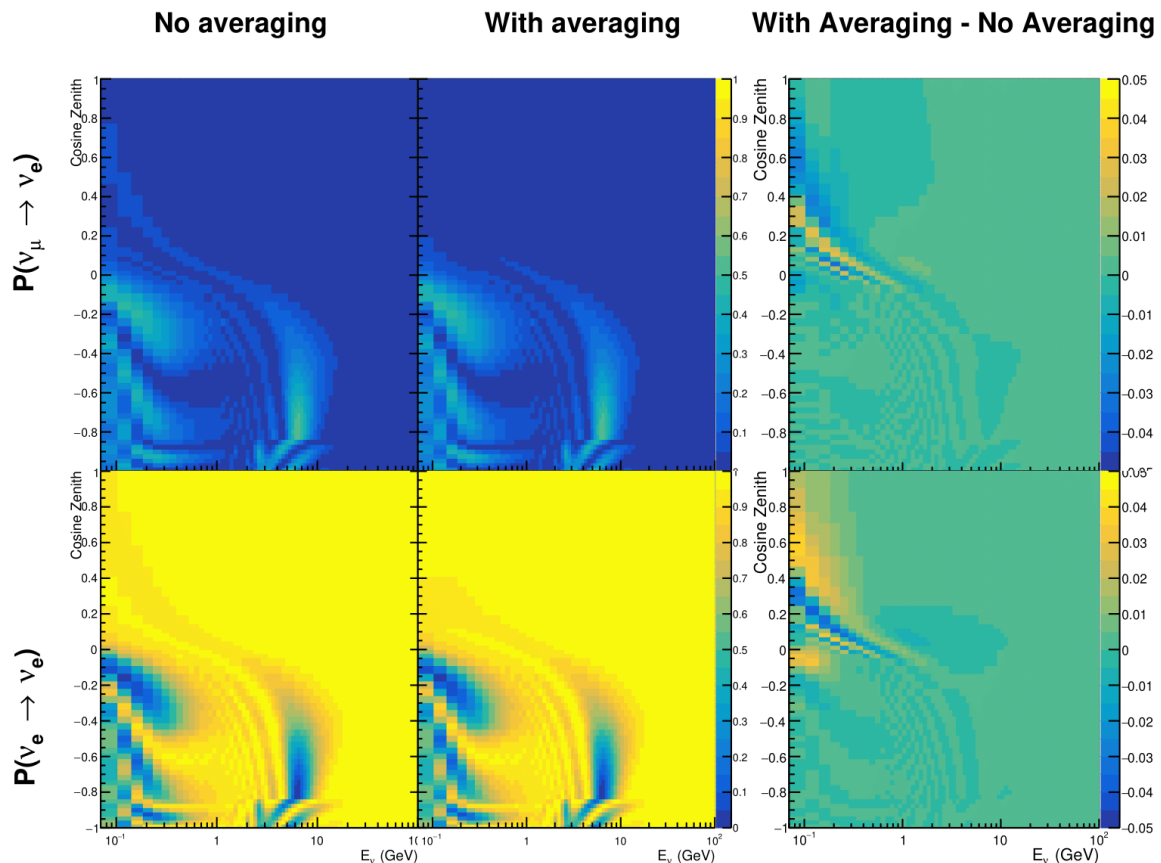


Figure 7.17: The oscillation probability, $P(\nu_\mu \rightarrow \nu_e)$ (top row) and $P(\nu_e \rightarrow \nu_\mu)$ (bottom row), given as a function of neutrino energy and zenith angle. The left column gives probabilities where a fixed production height of 25km is used. The middle column gives the probabilities where the production height is analytically averaged. The right column illustrates the difference in oscillation probability between the two different techniques.

2601 **Chapter 8**

2602 **Oscillation Analysis**

2603 **8.1 Likelihood Calculation**

2604 This analysis performs a joint oscillation parameter fit of the ND280, and the SK
2605 atmospheric samples.

2606 Once the Monte Carlo predictions of each beam and atmospheric sample has been
2607 built, following from chapter 6, a likelihood needs to be constructed. This is done
2608 by comparing the Monte Carlo prediction to “data”. The data can consist of either
2609 an Asmiov Monte Carlo prediction, which is typically used for sensitivity studies,
2610 or real data. The Monte Carlo prediction is calculated at a particular point, $\vec{\theta}$, in the
2611 model parameter space, $N_i^{MC} = N_i^{MC}(\vec{\theta})$. Both the data and Monte Carlo spectra are
2612 binned, where the i^{th} bin content is represented by N_i^D and N_i^{MC} , respectively. The bin
2613 contents for the beam near detector, beam far detector and atmospheric samples are
2614 denoted with ND , FD and Atm , respectively. The binning index, i , runs over all the
2615 bins within the sample and all samples with that set. Taking the beam far detector
2616 samples as example, it would run over all the reconstructed neutrino energy bins in all
2617 samples (FHC1R μ , RHC1R μ , etc.). The likelihood calculation between data and Monte
2618 Carlo for a particular bin follows a Poisson distribution, where the data is treated as a
2619 fluctuation of the simulation.

2620 Following the T2K analysis presented in [80], the likelihood contribution from the
2621 near detector also includes a Monte Carlo statistical uncertainty term, derived from

the Barlow and Beeston statistical treatment [221, 222]. In addition to treating the data as a fluctuation of the Monte Carlo prediction, it includes a contribution from the likelihood that the generated simulation is a statistical fluctuation of the actual true simulation assuming infinite statistics. The technical implementation of this additional likelihood term is documented in [195]. The term is defined as,

$$\frac{(\beta_i - 1)^2}{2\sigma_{\beta_i}^2}, \quad (8.1)$$

where β_i represents a scaling parameter for each bin i , which is a value based on the amount of Monte Carlo statistics in a bin [195]. $\sigma_{\beta_i} = \sqrt{\sum_i w_i^2 / N_i^{MC}}$, and $\sqrt{\sum_i w_i^2}$ represents the sum of the square of the weights of the Monte Carlo events which fall into bin i .

Additional contributions to the likelihood come from the variation of the systematic model parameters. For those parameters with well-motivated uncertainty estimates, a covariance matrix, V describes the prior knowledge of each parameter as well as any correlations between the parameters. Due to the technical implementation, a single covariance matrix describes each “block” of model parameters, e.g. beam flux systematics. For simplicity, the covariance matrix associated with the k^{th} block is denoted V^k . This substitution results in $\vec{\theta} = \sum_k^{N_b} \vec{\theta}^k$ and $V = \sum_k^{N_b} V^k$, for N_b number of blocks describing: oscillation parameters, beam flux, atmospheric flux, neutrino interaction, near detector, beam far detector and atmospheric far detector systematics detailed in section 6.4. The number of parameters in the k^{th} block is defined as $n(k)$.

The final likelihood term is defined as,

$$\begin{aligned}
& -\ln(\mathcal{L}) = & (8.2) \\
& \sum_i^{\text{NDbins}} N_i^{\text{ND},MC}(\vec{\theta}) - N_i^{\text{ND},D} + N_i^{\text{ND},D} \times \ln \left[N_i^{\text{ND},D} / N_i^{\text{ND},MC}(\vec{\theta}) \right] + \frac{(\beta_i - 1)^2}{2\sigma_{\beta_i}^2} \\
& + \sum_i^{\text{FDbins}} N_i^{\text{FD},MC}(\vec{\theta}) - N_i^{\text{FD},D} + N_i^{\text{FD},D} \times \ln \left[N_i^{\text{FD},D} / N_i^{\text{FD},MC}(\vec{\theta}) \right] \\
& + \sum_i^{\text{Atmbins}} N_i^{\text{Atm},MC}(\vec{\theta}) - N_i^{\text{Atm},D} + N_i^{\text{Atm},D} \times \ln \left[N_i^{\text{Atm},D} / N_i^{\text{Atm},MC}(\vec{\theta}) \right] \\
& + \frac{1}{2} \sum_k^{\text{N}_b} \sum_i^{n(k)} \sum_j^{n(k)} (\vec{\theta}^k)_i (V^k)_{ij}^{-1} (\vec{\theta}^k)_j.
\end{aligned}$$

2642 This is the value determined at each step of the MCMC to build the posterior
2643 distribution, as discussed in chapter 4.

2644 8.1.1 Likelihood Scans

2645 Using the defintion of the likelihood presented in section 8.1, the response of each
2646 sample to a variation particular parameter can be studied. Figure 8.1 presents the
2647 variation of all the samples (beam and atmospheric) at SK. Each plot represents a
2648 “scan”, where a particular parameter is scanned in the range of -3σ to $+3\sigma$, where σ is
2649 the uncertainty defined by the covariance matrix. The “data” being used within the
2650 definition of the likelihood equation is built using the Asimov A oscillation parameter
2651 values defined in Table 2.2 alongside the pre-fit dial values as discussed in subsec-
2652 tion 6.4.3. Due to the correlations between oscillation parameters, the value of $\chi^2 \sim 1$
2653 does not equate to the typical 1σ sensitivity. However, it does give an indication of
2654 which samples response the strongest to a variation in the oscillation parameters. The
2655 point at which the likelihood tends to zero illustrates the value of the parameter used

2656 to build the Asimov data prediction. The likelihood scans only include the sample
 2657 response and ignore the penalty contribution term from the variation of the parameter.

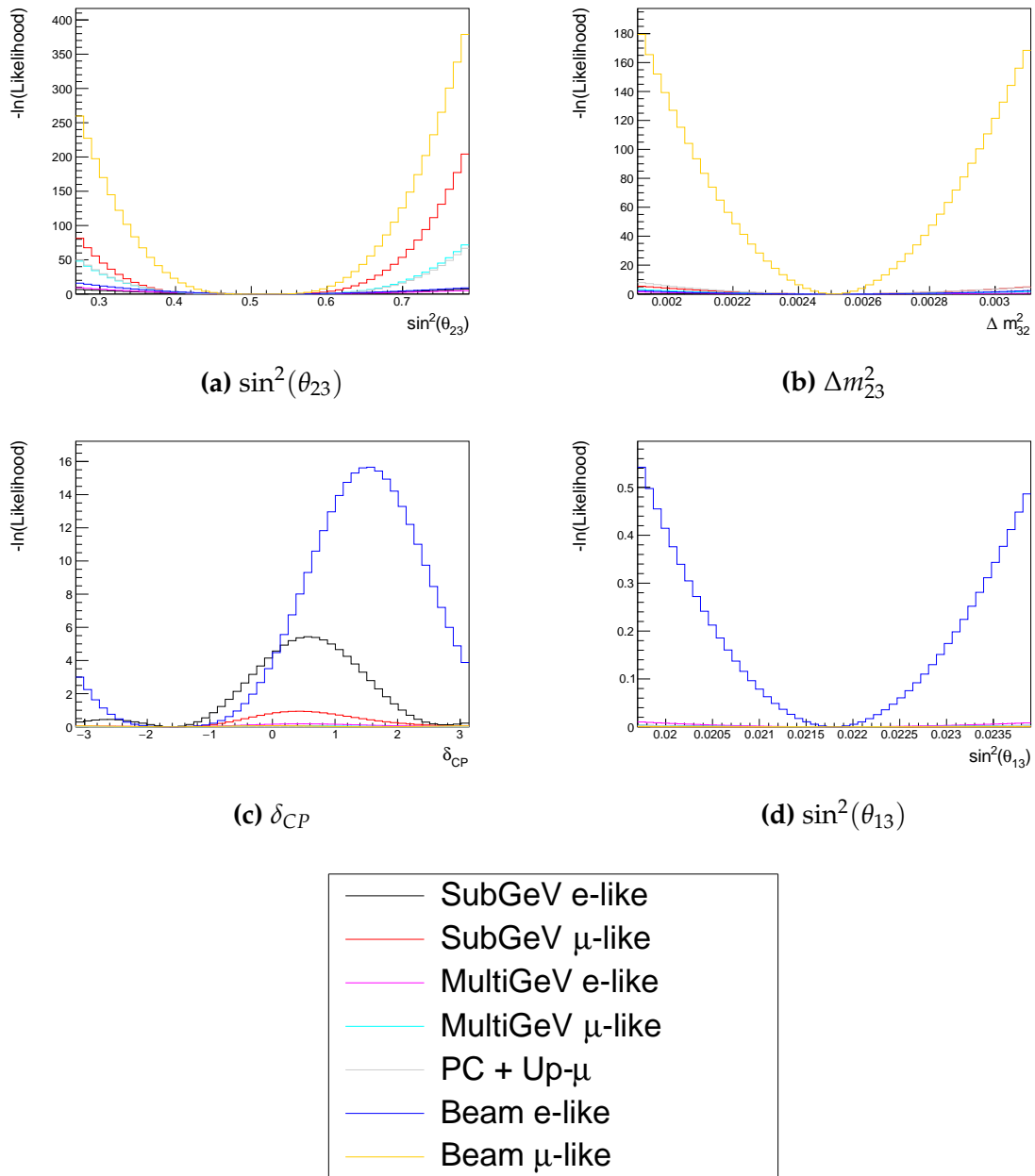


Figure 8.1: The response of the likelihood, as defined in section 8.1, illustrating the response of the samples to the oscillation parameters. Δm_{12}^2 and $\sin^2(\theta_{12})$ are negated because these samples have no sensitivity to those parameters. The Asimov data set is built using the pre-fit dial values assuming Asimov A oscillation parameters defined in Table 2.2.

₂₆₅₉ **Bibliography**

- ₂₆₆₀ [1] J. Chadwick, Verhandl. Dtsc. Phys. Ges. **16**, 383 (1914).
- ₂₆₆₁ [2] C. D. Ellis and W. A. Wooster, Proc. R. Soc. Lond. A Math. Phys. Sci. **117**, 109
₂₆₆₂ (1927).
- ₂₆₆₃ [3] W. Pauli, Phys. Today **31N9**, 27 (1978).
- ₂₆₆₄ [4] E. Fermi, Z. Phys. **88**, 161 (1934).
- ₂₆₆₅ [5] F. Reines and C. L. Cowan, Phys. Rev. **92**, 830 (1953).
- ₂₆₆₆ [6] C. L. Cowan, F. Reines, F. B. Harrison, H. W. Kruse, and A. D. McGuire, Science
₂₆₆₇ **124**, 103 (1956), <http://science.sciencemag.org/content/124/3212/103.full.pdf>.
- ₂₆₆₈ [7] G. Danby *et al.*, Phys. Rev. Lett. **9**, 36 (1962).
- ₂₆₆₉ [8] K. Kodama *et al.*, Physics Letters B **504**, 218 (2001).
- ₂₆₇₀ [9] LSND, A. Aguilar-Arevalo *et al.*, Phys. Rev. **D64**, 112007 (2001), hep-ex/0104049.
- ₂₆₇₁ [10] MiniBooNE Collaboration, A. A. Aguilar-Arevalo *et al.*, Phys. Rev. Lett. **110**,
₂₆₇₂ 161801 (2013).
- ₂₆₇₃ [11] Planck Collaboration *et al.*, aap **641** (2020).
- ₂₆₇₄ [12] The ALEPH Collaboration, The Delphi Collaboration, The L3 Collaboration, The
₂₆₇₅ SLD Collaboration, The LEP Electroweak Working Group, The SLD Electroweak
₂₆₇₆ and Heavy Flavour Groups, J. A. Bagger *et al.*, Physics Reports **427**, 257 (2006).
- ₂₆₇₇ [13] B. Pontecorvo, Sov. Phys. JETP **26**, 984 (1968), [Zh. Eksp. Teor. Fiz. 53, 1717 (1967)].
- ₂₆₇₈ [14] B. Pontecorvo, Sov. Phys. JETP **7**, 172 (1958), [Zh. Eksp. Teor. Fiz. 34, 247 (1957)].
- ₂₆₇₉ [15] M. Kobayashi and T. Maskawa, Progress of Theoretical Physics **49**, 652 (1973).
- ₂₆₈₀ [16] N. Cabibbo, Phys. Rev. Lett. **10**, 531 (1963).
- ₂₆₈₁ [17] A. M. and, Journal of Physics: Conference Series **587**, 012030 (2015).
- ₂₆₈₂ [18] A. Y. Smirnov, (2003).
- ₂₆₈₃ [19] S. Mikheyev and A. Smirnov, Soviet Journal of Nuclear Physics **42**, 913 (1985).

- 2684 [20] L. Wolfenstein, Phys. Rev. D **17**, 2369 (1978).
- 2685 [21] V. D. Barger, K. Whisnant, S. Pakvasa, and R. J. N. Phillips, Phys. Rev. D **22**, 2718
2686 (1980).
- 2687 [22] The Super-Kamiokande Collaboration, Y. Ashie *et al.*, Phys. Rev. Lett. **93**, 101801
2688 (2004).
- 2689 [23] SNO Collaboration, Q. R. Ahmad *et al.*, Phys. Rev. Lett. **89**, 011301 (2002).
- 2690 [24] 2015 Nobel prize in Physics as listed by Nobelprize.org, [https://www.](https://www.nobelprize.org/nobel_prizes/physics/laureates/2015/)
2691 [nobelprize.org/nobel_prizes/physics/laureates/2015/](https://www.nobelprize.org/nobel_prizes/physics/laureates/2015/), Accessed: 22-06-
2692 2022.
- 2693 [25] J. A. Formaggio and G. P. Zeller, Rev. Mod. Phys. **84**, 1307 (2012), 1305.7513.
- 2694 [26] A. Bellerive, Int. J. Mod. Phys. A **19**, 1167 (2004).
- 2695 [27] R. Davis, D. S. Harmer, and K. C. Hoffman, Phys. Rev. Lett. **20**, 1205 (1968).
- 2696 [28] N. Vinyoles *et al.*, Astrophys. J. **835**, 202 (2017).
- 2697 [29] V. Gribov and B. Pontecorvo, Phys. Lett. B **28**, 493 (1969).
- 2698 [30] K. S. Hirata *et al.*, Phys. Rev. Lett. **63**, 16 (1989).
- 2699 [31] W. Hampel *et al.*, Phys. Lett. B **447**, 127 (1999).
- 2700 [32] SAGE Collaboration, J. N. Abdurashitov *et al.*, Phys. Rev. C **60**, 055801 (1999).
- 2701 [33] Q. R. Ahmad *et al.*, Phys. Rev. Lett. **89** (2002).
- 2702 [34] Borexino Collaboration, Nature **562**, 505 (2018).
- 2703 [35] B. Aharmim *et al.*, Astrophys. J. **653**, 1545 (2006).
- 2704 [36] M. Agostini *et al.*, (2020).
- 2705 [37] S. Andringa *et al.*, Adv. High Energy Phys. **2016**, 1 (2016).
- 2706 [38] J. F. Beacom *et al.*, Chin. phys. C **41**, 023002 (2017).
- 2707 [39] F. An *et al.*, J. Phys. G Nucl. Part. Phys. **43**, 030401 (2016).
- 2708 [40] J. Aalbers *et al.*, (2020), 2006.03114.
- 2709 [41] T. K. Gaisser and M. Honda, (2002).

- 2710 [42] G. D. Barr, T. K. Gaisser, P. Lipari, S. Robbins, and T. Stanev, Physical Review D
2711 **70** (2004).
- 2712 [43] M. Honda, T. Kajita, K. Kasahara, S. Midorikawa, and T. Sanuki, Physical Review
2713 D **75** (2007).
- 2714 [44] M. Honda, T. Kajita, K. Kasahara, and S. Midorikawa, Phys. Rev. D **70**, 043008
2715 (2004).
- 2716 [45] M. Honda, T. Kajita, K. Kasahara, and S. Midorikawa, Phys. Rev. D **83**, 123001
2717 (2011).
- 2718 [46] A. Fasso, A. Ferrari, P. R. Sala, and J. Ranft, (2001).
- 2719 [47] Y. Ashie *et al.*, Physical Review D **71** (2005).
- 2720 [48] F. Reines *et al.*, Phys. Rev. Lett. **15**, 429 (1965).
- 2721 [49] D. Casper *et al.*, Phys. Rev. Lett. **66**, 2561 (1991).
- 2722 [50] K. S. Hirata *et al.*, Phys. Lett. B **280**, 146 (1992).
- 2723 [51] Z. Li *et al.*, Physical Review D **98** (2018).
- 2724 [52] Kamiokande Collaboration *et al.*, (2017).
- 2725 [53] T2K Collaboration, Nature **580**, 339 (2020).
- 2726 [54] M. A. Acero *et al.*, Phys. Rev. Lett. **123**, 151803 (2019).
- 2727 [55] M. G. Aartsen *et al.*, Phys. Rev. Lett. **120** (2018).
- 2728 [56] P. Adamson *et al.*, Phys. Rev. Lett. **112** (2014).
- 2729 [57] M. S. Athar *et al.*, Progress in Particle and Nuclear Physics **124**, 103947 (2022).
- 2730 [58] G. Danby *et al.*, Phys. Rev. Lett. **9**, 36 (1962).
- 2731 [59] K. Abe *et al.*, Physical Review D **87** (2013).
- 2732 [60] MINOS Collaboration, D. G. Michael *et al.*, Phys. Rev. Lett. **97**, 191801 (2006).
- 2733 [61] G. Danby *et al.*, Phys. Rev. Lett. **9**, 36 (1962).
- 2734 [62] NOvA Collaboration, M. A. Acero *et al.*, Phys. Rev. Lett. **123**, 151803 (2019).
- 2735 [63] B. Abi, R. Acciarri, M. A. Acero, and G. e. a. Adamov, Eur. Phys. J. C Part. Fields

- 2736 **80** (2020).
- 2737 [64] Hyper-Kamiokande Proto-Collaboration *et al.*, Prog. Theor. Exp. Phys. **2015**,
2738 53C02 (2015).
- 2739 [65] C. Blanco, D. Hooper, and P. Machado, Physical Review D **101** (2020).
- 2740 [66] MicroBooNE Collaboration *et al.*, Search for an Excess of Electron Neutrino
2741 Interactions in MicroBooNE Using Multiple Final State Topologies, 2021.
- 2742 [67] KARMEN Collaboration, B. Armbruster *et al.*, Phys. Rev. D **65**, 112001 (2002).
- 2743 [68] S.-B. Kim, T. Lasserre, and Y. Wang, Adv. High Energy Phys. **2013**, 1 (2013).
- 2744 [69] M. Sajjad Athar *et al.*, Prog. Part. Nucl. Phys. **124**, 103947 (2022), 2111.07586.
- 2745 [70] K. Abe *et al.*, Nucl. Instrum. Methods Phys. Res. A **1027**, 166248 (2022).
- 2746 [71] F. P. An *et al.*, Phys. Rev. Lett. **108**, 171803 (2012).
- 2747 [72] RENO Collaboration, J. K. Ahn *et al.*, Phys. Rev. Lett. **108**, 191802 (2012).
- 2748 [73] Double Chooz Collaboration, Y. Abe *et al.*, Phys. Rev. Lett. **108**, 131801 (2012).
- 2749 [74] J. Collaboration *et al.*, TAO Conceptual Design Report: A Precision Measurement
2750 of the Reactor Antineutrino Spectrum with Sub-percent Energy Resolution, 2020,
2751 2005.08745.
- 2752 [75] for the RENO Collaboration, New results from RENO and the 5 MeV excess,
2753 AIP Publishing LLC, 2015.
- 2754 [76] Y. Abe *et al.*, Journal of High Energy Physics **2014** (2014).
- 2755 [77] Daya Bay Collaboration, D. Adey *et al.*, Phys. Rev. Lett. **123**, 111801 (2019).
- 2756 [78] M. P. Decowski, Nucl. Phys. B. **908**, 52 (2016).
- 2757 [79] The KamLAND Collaboration, A. Gando *et al.*, Phys. Rev. D **83**, 052002 (2011).
- 2758 [80] P. Dunne, Latest Neutrino oscillation results from T2K, 2020.
- 2759 [81] M. Tanabashi *et al.*, Phys. Rev. D. **98** (2018).
- 2760 [82] Particle Data Group, R. L. Workman and Others, PTEP **2022**, 083C01 (2022).
- 2761 [83] T2K Collaboration, K. Abe *et al.*, Phys. Rev. Lett. **112**, 181801 (2014).

- [84] Y. Fukuda *et al.*, Phys. Rev. Lett. **81**, 1562 (1998).
- [85] Linyan Wan, (2022).
- [86] K. Abe *et al.*, Nuclear Instruments and Methods in Physics Research Section A: Accelerators, Spectrometers, Detectors and Associated Equipment **737**, 253 (2014).
- [87] S. Fukuda *et al.*, Nucl. Instrum. Methods Phys. Res. A **501**, 418 (2003).
- [88] Y. Itow *et al.*, (2001).
- [89] M. Jiang *et al.*, Prog. Theor. Exp. Phys. **2019** (2019).
- [90] S. Fukuda *et al.*, Nuclear Instruments and Methods in Physics Research Section A: Accelerators, Spectrometers, Detectors and Associated Equipment **501**, 418 (2003), <http://www.sciencedirect.com/science/article/pii/S016890020300425X>.
- [91] Y. Nakano *et al.*, Nucl. Instrum. Methods Phys. Res. A **977**, 164297 (2020).
- [92] Hamamatsu, Hamamatsu Photonics Photomultiplier Tubes Handbook.
- [93] K. Abe *et al.*, Nucl. Instrum. Methods Phys. Res. A **1027**, 166248 (2022).
- [94] J. F. Beacom and M. R. Vagins, Phys. Rev. Lett. **93**, 171101 (2004).
- [95] L. Marti *et al.*, Nucl. Instrum. Methods Phys. Res. A **959**, 163549 (2020).
- [96] L. Marti *et al.*, (2019).
- [97] M. Vagins, Solar/DSNB Neutrino_SK-Gd, 2022.
- [98] J. Focht, PhD thesis, Massachusetts Institute of Technology, 2004.
- [99] T. Tanimori *et al.*, IEEE Transactions on Nuclear Science **36**, 497 (1989).
- [100] Super-Kamiokande Collaboration, J. Hosaka *et al.*, Phys. Rev. D **73**, 112001 (2006).
- [101] H. Nishino *et al.*, Nucl. Instrum. Methods Phys. Res. A **610**, 710 (2009).
- [102] S. Yamada *et al.*, IEEE Transactions on Nuclear Science **57**, 428 (2010).
- [103] S. Yamada, Y. Hayato, Y. Obayashi, and M. Shiozawa, New online system without hardware trigger for the Super-Kamiokande experiment, in *2007 IEEE Nuclear Science Symposium Conference Record*, IEEE, 2007.

- 2789 [104] G. Carminati, Phys. Procedia **61**, 666 (2015).
- 2790 [105] P. A. Čerenkov, Phys. Rev. **52**, 378 (1937).
- 2791 [106] I. Frank and I. Tamm, Coherent visible radiation of fast electrons passing
2792 through matter, in *Selected Papers*, pp. 29–35, Springer Berlin Heidelberg, Berlin,
2793 Heidelberg, 1991.
- 2794 [107] The T2K Collaboration, KEK Proposal (2001),
2795 <http://neutrino.kek.jp/jhfnu/loi/loi.v2.030528.pdf>.
- 2796 [108] Y. Itow *et al.*, (2001), hep-ex/0106019.
- 2797 [109] The K2K Collaboration and S. H. Ahn, (2001), hep-ex/0103001.
- 2798 [110] The T2K Collaboration, KEK Proposal (2006), http://j-parc.jp/researcher/Hadron/en/pac_0606/pdf/p11-Nishikawa.pdf.
- 2800 [111] C. Bronner, Accelerator Neutrino I_Recent results from T2K, 2022.
- 2801 [112] T2K Collaboration, K. Abe *et al.*, Phys. Rev. Lett. **112**, 061802 (2014),
2802 <https://link.aps.org/doi/10.1103/PhysRevLett.112.061802>.
- 2803 [113] NINJA Collaboration, T. Fukuda *et al.*, Proposal for precise measurement of
2804 neutrino-water cross-section in NINJA physics run, Proposal for J-PARC and
2805 KEK, 2017.
- 2806 [114] T. Ovsiannikova *et al.*, Physics of Particles and Nuclei **48**, 1014 (2017),
2807 <https://doi.org/10.1134/S1063779617060478>.
- 2808 [115] M. Antonova *et al.*, Journal of Instrumentation **12**, C07028 (2017),
2809 <http://stacks.iop.org/1748-0221/12/i=07/a=C07028>.
- 2810 [116] The T2K Collaboration, K. Abe *et al.*, Phys. Rev. D **102**, 012007 (2020).
- 2811 [117] K. Abe *et al.*, Progress of Theoretical and Experimental Physics **2021** (2021).
- 2812 [118] The T2K Collaboration, K. Abe *et al.*, Nuclear Instruments
2813 and Methods in Physics Research Section A: Accelerators, Spectrometers,
2814 Detectors and Associated Equipment **659**, 106 (2011),
2815 <http://www.sciencedirect.com/science/article/pii/S0168900211011910>.
- 2816 [119] K. Matsuoka *et al.*, Nuclear Instruments and Methods in Physics Research Section
2817 A: Accelerators, Spectrometers, Detectors and Associated Equipment **624**, 591

- 2818 (2010), <http://www.sciencedirect.com/science/article/pii/S016890021002098X>.
- 2819 [120] K. Abe *et al.*, Phys. Rev. D. **103** (2021).
- 2820 [121] T. Vladisavljevic, *Predicting the T2K neutrino flux and measuring oscillation parameters* Springer theses, 1 ed. (Springer Nature, Cham, Switzerland, 2020).
- 2821
- 2822 [122] D. Beavis, A. Carroll, and I. Chiang, (1995).
- 2823 [123] P.-A. Amaudruz *et al.*, Nuclear Instruments and Methods in Physics Research
2824 Section A: Accelerators, Spectrometers, Detectors and Associated Equipment
2825 **696**, 1 (2012).
- 2826 [124] N. Abgrall *et al.*, Nuclear Instruments and Methods in Physics Research Section
2827 A: Accelerators, Spectrometers, Detectors and Associated Equipment **637**, 25
2828 (2011).
- 2829 [125] S. Assylbekov *et al.*, Nuclear Instruments and Methods in Physics Research
2830 Section A: Accelerators, Spectrometers, Detectors and Associated Equipment
2831 **686**, 48 (2012).
- 2832 [126] D. Allan *et al.*, Journal of Instrumentation **8**, P10019 (2013).
- 2833 [127] F. Vannucci, Advances in High Energy Physics **2014**, 1 (2014).
- 2834 [128] UA1 magnet sets off for a second new life, 2022.
- 2835 [129] S. Aoki *et al.*, Nuclear Instruments and Methods in Physics Research Section
2836 A: Accelerators, Spectrometers, Detectors and Associated Equipment **698**, 135
2837 (2013).
- 2838 [130] K. Suzuki *et al.*, Progress of Theoretical and Experimental Physics **2015**, 53C01
2839 (2015).
- 2840 [131] S. Brooks, A. Gelman, G. L. Jones, and X.-L. Meng, *Handbook of Markov Chain
Monte Carlo* (CRC Press, 2011).
- 2841
- 2842 [132] W. R. Gilks, S. Richardson, and D. J. Spiegelhalter, *Markov Chain Monte Carlo in
Practice* (Chapman & Hall/CRC Interdisciplinary Statistics, 1995).
- 2843
- 2844 [133] C. Wret, *Minimising systematic uncertainties in the T2K experiment using near-
detector and external data*, PhD thesis, Imperial College London, 2018.
- 2845
- 2846 [134] K. E. Duffy, *Measurement of the Neutrino Oscillation Parameters $\sin^2 \theta_{23}$, Δm_{32}^2 ,*

- 2847 $\sin^2 \theta_{13}$, and δ_{CP} in Neutrino and Antineutrino Oscillation at T2K, PhD thesis, Oriel
2848 College, University of Oxford, 2016.
- 2849 [135] T. Bayes, Rev. Phil. Trans. Roy. Soc. Lond. **53**, 370 (1764).
- 2850 [136] N. Metropolis, A. W. Rosenbluth, M. N. Rosenbluth, A. H. Teller, and E. Teller,
2851 Journal of Chemical Physics **21** (1970).
- 2852 [137] W. K. Hastings, Biometrika **57** (1970).
- 2853 [138] J. Dunkley, M. Bucher, P. G. Ferreira, K. Moodley, and C. Skordis, Mon. Not. R.
2854 Astron. Soc. **356**, 925 (2005).
- 2855 [139] Particle Data Group *et al.*, Prog. Theor. Exp. Phys. **2020** (2020).
- 2856 [140] H. Jeffreys, *The Theory of Probability* Oxford Classic Texts in the Physical Sciences
2857 (, 1939).
- 2858 [141] R. E. Kass and A. E. Raftery, J. Am. Stat. Assoc. **90**, 773 (1995).
- 2859 [142] T. Böhlen *et al.*, Nuclear Data Sheets **120**, 211 (2014),
2860 <http://www.sciencedirect.com/science/article/pii/S0090375214005018>.
- 2861 [143] R. Brun *et al.*, GEANT: Detector Description and Simulation Tool; Oct 1994 CERN
2862 Program Library (CERN, Geneva, 1993), <http://cds.cern.ch/record/1082634>,
2863 Long Writeup W5013.
- 2864 [144] T2K Collaboration, K. Abe *et al.*, Phys. Rev. D **87**, 012001 (2013).
- 2865 [145] C. Zeitnitz and T. Gabriel, Nuclear Instruments and Methods in Physics Research Section A: Accelerators, Spectrometers, Detectors and Associated Equipment **349**, 106 (1994),
2866 <http://www.sciencedirect.com/science/article/pii/0168900294906130>.
- 2867 [146] A. Fiorentini *et al.*, T2K Technical Note **217** (2017).
- 2868 [147] N. Abgrall *et al.*, Physical Review C **84** (2011).
- 2869 [148] N. Abgrall *et al.*, Physical Review C **85** (2012).
- 2870 [149] N. Abgrall *et al.*, Nuclear Instruments and Methods in Physics Research Section
2871 A: Accelerators, Spectrometers, Detectors and Associated Equipment **701**, 99
2872 (2013), <http://www.sciencedirect.com/science/article/pii/S016890021201234X>.

- 2875 [150] HARP Collaboration, M. Apollonio *et al.*, Phys. Rev. C **80**, 035208 (2009),
2876 <https://link.aps.org/doi/10.1103/PhysRevC.80.035208>.
- 2877 [151] B. Blau *et al.*, Nuclear Physics B - Proceedings Supplements **113**, 125 (2002).
- 2878 [152] S. Haino *et al.*, Physics Letters B **594**, 35 (2004).
- 2879 [153] NASA, U.S. Standard Atmosphere, 1976, 1976.
- 2880 [154] S. Roesler, R. Engel, and J. Ranft, The Monte Carlo Event Generator DPMJET-III,
2881 in *Advanced Monte Carlo for Radiation Physics, Particle Transport Simulation and*
2882 *Applications*, pp. 1033–1038, Springer Berlin Heidelberg, 2001.
- 2883 [155] K. Niita *et al.*, Radiation Measurements **41**, 1080 (2006).
- 2884 [156] T. Sanuki *et al.*, Physics Letters B **541**, 234 (2002).
- 2885 [157] P. Achard *et al.*, Physics Letters B **598**, 15 (2004).
- 2886 [158] K. Sato, Atmospheric Neutrino_Reviews on neutrino fluxes (low E atm nu),
2887 2022.
- 2888 [159] Y. Hayato and L. Pickering, The European Physical Journal Special Topics **230**,
2889 4469 (2021).
- 2890 [160] Y. Hayato, Acta Physica Polonica B **40** (2009).
- 2891 [161] C. L. Smith, Physics Reports **3**, 261 (1972),
2892 <http://www.sciencedirect.com/science/article/pii/0370157372900105>.
- 2893 [162] O. Benhar, A. Fabrocini, and S. Fantoni, Nuclear Physics A **497**, 423 (1989).
- 2894 [163] R. Bradford, A. Bodek, H. Budd, and J. Arrington, Nuclear Physics B - Proceedings Supplements **159**, 127 (2006),
2895 <http://www.sciencedirect.com/science/article/pii/S0920563206005184>,
2896 Proceedings of the 4th International Workshop on Neutrino-Nucleus Interac-
2897 tions in the Few-GeV Region.
- 2898
- 2899 [164] A. A. Aguilar-Arevalo *et al.*, Physical Review D **81** (2010).
- 2900 [165] R. Gran, J. Nieves, F. Sanchez, and M. J. V. Vacas, Phys. Rev. D **88**, 113007 (2013),
2901 <https://link.aps.org/doi/10.1103/PhysRevD.88.113007>.
- 2902 [166] C. Berger and L. M. Sehgal, Phys. Rev. D **76**, 113004 (2007).

- 2903 [167] C. Berger and L. M. Sehgal, Phys. Rev. D **79**, 053003 (2009),
2904 <https://link.aps.org/doi/10.1103/PhysRevD.79.053003>.
- 2905 [168] T. Sjöstrand, Computer Physics Communications **82**, 74 (1994).
- 2906 [169] C. Bronner and M. Hartz, Tuning of the Charged Hadrons Multiplicities for Deep
2907 Inelastic Interactions in NEUT, in *Proceedings of the 10th International Workshop on*
2908 *Neutrino-Nucleus Interactions in Few-GeV Region (NuInt15)*, Journal of the Physical
2909 Society of Japan, 2016.
- 2910 [170] M. Glück, E. Reya, and A. Vogt, The European Physical Journal C **5**, 461 (1998).
- 2911 [171] A. Bodek and U.-k. Yang, Axial and Vector Structure Functions for Electron- and
2912 Neutrino- Nucleon Scattering Cross Sections at all Q^2 using Effective Leading
2913 order Parton Distribution Functions, 2010.
- 2914 [172] A. Bodek and U.-K. Yang, (2010).
- 2915 [173] S. Gollapinni, (2016).
- 2916 [174] E. S. P. Guerra *et al.*, Phys. Rev. D **99**, 052007 (2019).
- 2917 [175] GEANT4, S. Agostinelli *et al.*, Nucl. Instrum. Meth. **A506**, 250 (2003).
- 2918 [176] R. Brun, F. Bruyant, M. Maire, A. C. McPherson, and P. Zanarini, (1987).
- 2919 [177] K. Abe *et al.*, Physical Review Letters **121** (2018).
- 2920 [178] K. Abe *et al.*, Physical Review D **91** (2015).
- 2921 [179] R. Patterson *et al.*, Nuclear Instruments and Methods in Physics Research Section
2922 A: Accelerators, Spectrometers, Detectors and Associated Equipment **608**, 206
2923 (2009).
- 2924 [180] e. a. S. Berkman, T2K Technical Note **146** (2013).
- 2925 [181] e. a. A. Himmel, T2K Technical Note **219** (2015).
- 2926 [182] F. a. James, (1998), CERN Program Library Long Writeups.
- 2927 [183] X. Li and M. Wilking, T2K Technical Note **319** (2017).
- 2928 [184] S. Tobayama, *An Analysis of the Oscillation of Atmospheric Neutrinos*, PhD thesis,
2929 British Columbia U., 2016.

- 2930 [185] e. a. D. Barrow, T2K Technical Note **399** (2020).
- 2931 [186] A. Maghrabi, A. Aldosari, and M. Almutairi, Advances in Space Research **68**,
2932 2941 (2021).
- 2933 [187] Super-Kamiokande Collaboration, K. Abe *et al.*, Phys. Rev. D **97**, 072001 (2018),
2934 <https://link.aps.org/doi/10.1103/PhysRevD.97.072001>.
- 2935 [188] Particle Data Group, J. Beringer *et al.*, Phys. Rev. D **86**, 010001 (2012).
- 2936 [189] Y. N. and, Journal of Physics: Conference Series **888**, 012191 (2017).
- 2937 [190] M. Jiang, *Study of the neutrino mass hierarchy with the atmospheric neutrino data*
2938 *collected in Super-Kamiokande IV*, PhD thesis, Kyoto University, 2019.
- 2939 [191] S. N. K. Iyogi and Y. Obayashi., T2K Technical Note **027** (2011).
- 2940 [192] LeeKaPik, *Study of the neutrino mass hierarchy with the atmospheric neutrino data*
2941 *observed in Super-Kamiokande*, PhD thesis, Tokyo University, 2012.
- 2942 [193] The Super-Kamiokande Collaboration, R. Wendell *et al.*, Phys. Rev. D **81**, 092004
2943 (2010).
- 2944 [194] Super-Kamiokande Collaboration, J. Hosaka *et al.*, Phys. Rev. D **74**, 032002
2945 (2006).
- 2946 [195] L. M. et al, T2K Technical Note **395** (2020).
- 2947 [196] P. B. et al., T2K Technical Note **212** (2015).
- 2948 [197] W. Parker, *Constraining Systematic Uncertainties at T2K using Near Detector Data*,
2949 PhD thesis, Royal Holloway University of London, 2020.
- 2950 [198] V. B. et al., T2K Technical Note **246** (2015).
- 2951 [199] J. Missert, T2K Technical Note **318** (2017).
- 2952 [200] e. a. J. Chakrani, T2K Technical Note **414** (2022).
- 2953 [201] T2K Collaboration, M. Wascko, T2K Status, Results, and Plans, Neutrino 2018,
2954 2018.
- 2955 [202] e. a. Tomislav Vladisavljevic, T2K Technical Note **354** (2020).
- 2956 [203] G. Ambrosini *et al.*, Phys. Lett. B **420**, 225 (1998).

- 2957 [204] e. a. Edward Atkin, T2K Technical Note **344** (2019).
- 2958 [205] e. a. D. Barrow, T2K Technical Note **422** (2022).
- 2959 [206] The MiniBooNE Collaboration, A. A. Aguilar-Arevalo *et al.*, Phys. Rev. D **81**,
2960 013005 (2010), <https://link.aps.org/doi/10.1103/PhysRevD.81.013005>.
- 2961 [207] P. de Perio and J. Imber, T2K Technical Note **186** (2014).
- 2962 [208] P. de Perio and J. Imber, T2K Technical Note **107** (2012).
- 2963 [209] C. V. Daniel Barrow, T2K-SK Detector Matrix Uncertainties - MaCh3 In-
2964 tegration, <https://git.t2k.org/t2k-sk/t2ksk-detcovmat/-/tree/feature/MaCh3Integration>, Accessed: 22-06-2022.
- 2966 [210] R. Wendell, *Three Flavor Oscillation Analysis of Atmospheric Neutrinos in Super-*
2967 *Kamiokande*, PhD thesis, University of North Carolina, 2008.
- 2968 [211] A. M. Dziewonski and D. L. Anderson, Phys. Earth Planet. Inter. **25**, 297 (1981).
- 2969 [212] e. a. D. Barrow, T2K Technical Note **425** (2022).
- 2970 [213] R. G. Calland, A. C. Kaborth, and D. Payne, **9**, P04016 (2014).
- 2971 [214] R. Wendell, <http://www.phy.duke.edu/raw22/public/Prob3++/>.
- 2972 [215] F. Kallenborn, C. Hundt, S. Böser, and B. Schmidt, Computer Physics Communi-
2973 cations **234**, 235 (2019).
- 2974 [216] L. Warsame, MaCh3 Analysis Progress.
- 2975 [217] S. Bourret, J. A. B. Coelho, and V. V. E. and, Journal of Physics: Conference Series
2976 **888**, 012114 (2017).
- 2977 [218] C. Rott, A. Taketa, and D. Bose, Scientific Reports **5** (2015).
- 2978 [219] K. Hagiwara, N. Okamura, and K. ichi Senda, Journal of High Energy Physics
2979 **2011** (2011).
- 2980 [220] D. Typinski, Earth Gravity, <http://www.typnet.net/Essays/EarthGravGraphics/EarthGrav.pdf>, Accessed: 24-06-2022.
- 2982 [221] R. Barlow and C. Beeston, Comput. Phys. Commun. **77**, 219 (1993).
- 2983 [222] J. S. Conway, Incorporating nuisance parameters in likelihoods for multisource

2984 *spectra*, 2011.

2985 List of Figures

| | | | |
|---------------------|-----|---|------------------------|
| <small>2986</small> | 2.1 | The cross-section of neutrinos from various natural and man-made sources as a function of neutrino energy. Taken from [25] | <small>2987</small> 10 |
| <small>2988</small> | 2.2 | The solar neutrino flux as a function of neutrino energy for various fusion reactions and decay chains as predicted by the Standard Solar Model. Taken from [26]. | <small>2989</small> 11 |
| <small>2990</small> | 2.3 | Left panel: The atmospheric neutrino flux for different neutrino flavours as a function of neutrino energy as predicted by the 2007 Honda model (“This work”) [43], the 2004 Honda model (“HKKM04”) [44], the Bartol model [42] and the FLUKA model [46]. Right panel: The ratio of the muon to electron neutrino flux as predicted by all the quoted models. Both figures taken from [43]. | <small>2991</small> 14 |
| <small>2992</small> | 2.4 | A diagram illustrating the definition of zenith angle as used in the Super Kamiokande experiment [47]. | <small>2993</small> 14 |
| <small>2994</small> | 2.5 | Prediction of $\nu_e, \bar{\nu}_e, \nu_\mu, \bar{\nu}_\mu$ fluxes as a function of zenith angle as calculated by the HKKM model [45]. The left, middle and right panels represent three values of neutrino energy, 0.32GeV, 1.0GeV and 3.2GeV respectively. Predictions for other models including Bartol [42], Honda [43] and FLUKA [46] are given in [47]. | <small>2995</small> 15 |
| <small>2996</small> | 2.6 | Constraints on the atmospheric oscillation parameters, $\sin^2(\theta_{23})$ and Δm_{23}^2 , from atmospheric and long baseline experiments: SK [52], T2K [53], NO ν A [54], IceCube [55] and MINOS [56]. Figure taken from [57]. | <small>2997</small> 16 |
| <small>2998</small> | 2.7 | Reactor electron antineutrino fluxes for ^{235}U (Black), ^{238}U (Green), ^{239}Pu (Purple), and ^{241}Pu (Orange) isotopes. The inverse β -decay cross-section (Blue) and corresponding measurable neutrino spectrum (Red) are also given. Top panel: Schematic of Inverse β -decay interaction including the eventual capture of the emitted neutron. This capture emits a γ -ray which provides a second signal of the event. Taken from [69]. | <small>2999</small> 19 |
| <small>3000</small> | 3.1 | A schematic diagram of the Super-Kamiokande Detector. Taken from [88]. | <small>3001</small> 25 |

| | | | |
|------|------|--|----|
| 3014 | 3.2 | The location of “standard PMTs” (red) inside the SK detector. Taken from [86]. | 29 |
| 3015 | | | |
| 3016 | 3.3 | Schematic view of the data flow through the data acquisition and online system. Taken from [102]. | 32 |
| 3017 | | | |
| 3018 | 3.4 | The cross-section view of the Tokai to Kamioka experiment illustrating the beam generation facility at J-PARC, the near detector situated at a baseline of 280m and the Super Kamiokande far detector situated 295km from the beam target. | 35 |
| 3019 | | | |
| 3020 | | | |
| 3021 | | | |
| 3022 | 3.5 | The near detector suite for the T2K experiment showing the ND280 and INGRID detectors. The distance between the detectors and the beam target is 280m. | 36 |
| 3023 | | | |
| 3024 | | | |
| 3025 | 3.6 | Top panel: Bird’s eye view of the most relevant part of primary and secondary beamline used within the T2K experiment. The primary beamline is the main-ring proton synchrotron, kicker magnet, and graphite target. The secondary beamline consists of the three focusing horns, decay volume, and beam dump. Figure taken from [118]. Bottom panel: The side-view of the secondary beamline including the focusing horns, beam dump and neutrino detectors. Figure taken from [119]. | 38 |
| 3026 | | | |
| 3027 | | | |
| 3028 | | | |
| 3029 | | | |
| 3030 | | | |
| 3031 | | | |
| 3032 | 3.7 | The Monte Carlo prediction of the energy spectrum for each flavour of neutrino (ν_e , $\bar{\nu}_e$, ν_μ and $\bar{\nu}_\mu$) in the neutrino dominated beam FHC mode (Left) and antineutrino dominated beam RHC mode (Right) expected at SK. Taken from [120]. | 39 |
| 3033 | | | |
| 3034 | | | |
| 3035 | | | |
| 3036 | 3.8 | Top panel: T2K muon neutrino disappearance probability as a function of neutrino energy. Middle panel: T2K electron neutrino appearance probability as a function of neutrino energy. Bottom panel: The neutrino flux distribution for three different off-axis angles (Arbitrary units) as a function of neutrino energy. | 41 |
| 3037 | | | |
| 3038 | | | |
| 3039 | | | |
| 3040 | | | |
| 3041 | 3.9 | The components of the ND280 detector. The neutrino beam travels from left to right. Taken from [118]. | 42 |
| 3042 | | | |
| 3043 | 3.10 | Comparison of data to Monte Carlo prediction of integrated deposited energy as a function of track length for particles that stopped in FGD1. Taken from [123]. | 44 |
| 3044 | | | |
| 3045 | | | |

| | | |
|------|--|----|
| 3046 | 3.11 Schematic design of a Time Projection Chamber detector. Taken from [124]. | 45 |
| 3047 | 3.12 The distribution of energy loss as a function of reconstructed momentum for charged particles passing through the TPC, comparing data to Monte Carlo prediction. Taken from [124]. | 45 |
| 3049 | | |
| 3050 | 3.13 A schematic of the P0D side-view. Taken from [125]. | 47 |
| 3051 | 3.14 Left panel: The Interactive Neutrino GRID on-axis Detector. 14 modules are arranged in a cross-shape configuration, with the center modules being directly aligned with the on-axis beam. Right panel: The layout of a single module of the INGRID detector. Both figures are recreated from [118]. | 49 |
| 3052 | | |
| 3053 | | |
| 3054 | | |
| 3055 | | |
| 3056 | 4.1 Example of using Monte Carlo techniques to find the area under the blue line. The gradient and intercept of the line are 0.4 and 1.0 respectively. The area found to be under the curve using one thousand samples is 29.9 units. | 54 |
| 3057 | | |
| 3058 | | |
| 3059 | | |
| 3060 | 4.2 The area under a line of gradient 0.4 and intercept 1.0 for the range $0 \leq x \leq 10$ as calculated using Monte Carlo techniques as a function of the number of samples used in each repetition. The analytical solution to the area is 30 units as given by the red line. | 54 |
| 3061 | | |
| 3062 | | |
| 3063 | | |
| 3064 | 4.3 Three MCMC chains, each with a stationary distribution equal to a Gaussian centered at 0 and width 1 (As indicated by the black dotted lines). All of the chains use a Gaussian proposal function but have different widths (or 'step size σ '). The top panel has $\sigma = 0.1$, middle panel has $\sigma = 0.5$ and the bottom panel has $\sigma = 5.0$. | 60 |
| 3065 | | |
| 3066 | | |
| 3067 | | |
| 3068 | | |
| 3069 | 4.4 The log-likelihood from the fit detailed in DB: Link to AsimovA Sensitivity Section as a function of the number of steps accumulated in each fit. Many independent MCMC chains were run in parallel and overlaid on this plot. The red line indicates the 1×10^5 step burn-in period after which the log-likelihood becomes stable. | 61 |
| 3070 | | |
| 3071 | | |
| 3072 | | |
| 3073 | | |

| | | |
|------|--|----|
| 3074 | 4.5 Left: The two dimensional probability distribution for two correlated parameters x and y . The red distribution shows the two dimensional probability distribution when $0 \leq x \leq 5$. Right: The marginalised probability distribution for the y parameter found when requiring the x to be bound between $-5 \leq x \leq 5$ and $0 \leq x \leq 5$ for the black and red distribution, respectively. | 63 |
| 3080 | 5.1 The NEUT prediction of the ν_μ -H ₂ O cross-section overlaid on the T2K ν_μ flux. The charged current (black, solid) and neutral current (black, dashed) inclusive, charged current quasi-elastic (blue, solid), charged current 2p2h (blue, dashed), charged current single pion production (pink), and charged current multi- π and DIS (Purple) cross-sections are illustrated. Figure taken from [159]. | 71 |
| 3086 | 5.2 Illustration of the various processes which a pion can undergo before exiting the nucleus. Taken from [173]. | 72 |
| 3088 | 5.3 Event displays from Super Kamiokande illustrating the “crisp” ring from a muon and the typically “fuzzier” electron ring. Each pixel represents a PMT and the color scheme denotes the accumulated charge deposited on that PMT. Figures taken from [181]. | 75 |
| 3092 | 5.4 The difference of the electron-like and muon-like log-likelihood compared to the reconstructed single-ring fit momentum for atmospheric ν_e (left) and ν_μ (right) samples. The black line represents the cut used to discriminate electron-like and muon-like events, which coefficients obtained from Monte Carlo studies. Figures taken from [180]. | 80 |
| 3097 | 5.5 The electron/muon PID separation parameter for all sub-GeV single-ring events in SK-IV. The charged current (CC) component is broken down in four flavours of neutrino (ν_μ , $\bar{\nu}_\mu$, ν_e and $\bar{\nu}_e$). Events with positive values of the parameter are determined to be electron-like. | 80 |
| 3101 | 5.6 The variation of the measured dark rate as a function of date, broken down by PMT type. The SK-IV and SK-V periods span September 2008 to May 2018 and January 2019 to July 2020, respectively. The break in measurement in 2018 corresponds to the period of tank repair and refurbishment. Figure adapted from [185]. | 83 |

| | | |
|------|---|----|
| 3106 | 5.7 Comparison of the measured raw charge deposited per event from the 3107 stopping muon data samples between SK-IV (Blue) and SK-V (Red), 3108 split by the primary muon subevent and the associated decay electron 3109 subevent. | 84 |
| 3110 | 5.8 The distribution of the reconstructed momentum from the muon ring 3111 divided by the distance between the reconstructed muon and decay 3112 electron vertices as found in the stopping muon data sets of SK-IV 3113 (Black) and SK-IV (Red). Only events with one tagged decay electron are 3114 considered. A Gaussian fit is considered in the range [2.0, 2.4] MeV/cm 3115 and illustrated as the solid curve. | 85 |
| 3116 | 5.9 The χ^2 difference between the SK-IV and SK-V reconstructed muon 3117 momentum divided by range when the SK-V is modified by the scaling 3118 parameter α . Both additive (Blue) and multiplicative (Black) scaling 3119 factors have been considered. In practice, the additive scaling factor 3120 actually uses the value of $(\alpha - 1.0)$ but is illustrated like this so the 3121 results can be shown on the same axis range. | 86 |
| 3122 | 5.10 A depiction of the topology patterns for fully-contained (FC), partially- 3123 contained (PC) and up-going muon (Up- μ) samples included in this 3124 analysis. | 87 |
| 3125 | 5.11 The predicted neutrino flux of the fully contained (FC) sub-GeV and 3126 multi-GeV, partially contained (PC), and upward-going muon (Up- μ) 3127 events. The prediction is broken down by the $\nu_x \rightarrow \nu_e$ prediction (top 3128 left), $\nu_x \rightarrow \nu_\mu$ prediction (top right) and $\nu_x \rightarrow \nu_\tau$ prediction (bottom). 3129 Asimov A oscillation parameters are assumed (given in Table 2.2). . . . | 89 |
| 3130 | 5.12 The predicted flux of beam neutrinos, as a function of neutrino energy. 3131 The predictions are broken down by the number of decay electrons 3132 associated with the particular events. Asimov A oscillation parameters 3133 are assumed (given in Table 2.2). | 91 |

| | | |
|---------------|---|-----|
| 3134 6.1 | The accumulated beam data, measured as the number of protons on target (POT). The total data (blue) is given which comprises of the neutrino beam (red) and antineutrino (purple) components. The beam power for neutrino and antineutrino beams is given as the markers using the same colour scheme. The timescale runs from Run 1 which started in January 2010 until Run 10 which ended in February 2020. The ratio of accumulated data in neutrino and antineutrino beam is 54.7% : 45.3%. | 93 |
| 3142 6.2 | Comparison of the SK-IV atmospheric samples between predictions made with the CP-violating Asimov A (Black) and CP-conserving Asimov B (Red) oscillation parameter sets (given in Table 2.2). The subGeV samples CCRES and π^0 -like samples are given in their reconstructed lepton momentum. All other samples are presented in their reconstructed zenith angle projection. | 100 |
| 3148 6.3 | The nominal Monte Carlo predictions for the FGD1 and FGD2 samples in neutrino beam mode, broken down into the $CC\nu_\mu 0\pi$, $CC\nu_\mu 1\pi$ and $CC\nu_\mu$ Other categories. Figures taken from [195]. | 103 |
| 3151 6.4 | The reconstructed neutrino energy, as defined by Equation 6.2 and Equation 6.3, for the $1R\mu$ -like, $1Re$ -like and $CC1\pi^+$ -like samples. Asimov A oscillation parameter sets are assumed (given in Table 2.2). These samples are the FHC mode samples. For ease of viewing, the $1R\mu$ sample only shows the $0. \leq E_\nu^{rec} < 3.0\text{GeV}$ but the binning extends to 30.0GeV | 106 |
| 3156 6.5 | The distribution of the angle between the neutrino beam direction and the reconstructed final state lepton, for the FHC $1Re$ -like sample. The distribution is broken down by neutrino interaction mode into charged current (left) and neutral current (right) components. Asimov A oscillation parameter sets are assumed (given in Table 2.2). DB: Is this needed or will it just bring up more questions? | 108 |
| 3162 6.6 | The total uncertainty evaluated on the near detector ν_μ flux prediction constrained by the replica-target data, illustrated as a function of neutrino energy. The solid(dashed) line indicates the uncertainty used within this analysis(the T2K 2018 analysis [201]). The solid histogram indicates the neutrino flux as a function of energy. Figure taken from [202]. | 110 |

| | | |
|------|---|-----|
| 3167 | 6.7 The predicted neutrino energy distribution for subGeV atmospheric 3168 and beam samples. FHC and RHC beam samples are summed together 3169 Asimov A oscillation parameters are assumed (given in Table 2.2). Beam 3170 and atmospheric samples with similar cuts are compared against one 3171 another. | 115 |
| 3172 | 6.8 The interaction mode contribution of each sample given as a fraction 3173 of the total event rate in that sample. Asimov A oscillation parameters 3174 are assumed (given in Table 2.2). The Charged Current (CC) modes are 3175 broken into quasi-elastic (QE), 2p2h, resonant charged pion production 3176 ($1\pi^\pm$), multi-pion production ($M\pi$), and other interaction categories. 3177 Neutral Current (NC) interaction modes are given in interaction mode 3178 categories: π^0 production, resonant charged pion production, multi- 3179 pion production, and others. | 116 |
| 3180 | 6.9 Down-going atmospheric subGeV single-ring samples comparing the 3181 mean and error of the pre-fit and post-fit Monte Carlo predictions 3182 in red and blue, respectively. The magenta histogram illustrates the 3183 Monte Carlo prediction using the generated dial values. The black 3184 points illustrate the down-going data with statistical errors given. The 3185 mean and errors of the Monte Carlo predictions are calculated by the 3186 techniques documented in subsection 4.3.4. The pre-fit spectrum is 3187 calculated by throwing the cross-section and atmospheric flux dial 3188 values from the pre-fit covariance matrix. The post-fit spectrum is 3189 calculated by sampling the cross-section dial values from an ND fit 3190 MCMC chain, whilst still throwing the atmospheric flux dials from the 3191 pre-fit covariance. | 119 |
| 3192 | 6.10 The ring counting parameter as defined in Equation 6.6 for the SubGeV-elike-0dcy 3193 and MultiRing-elike-nue samples. | 128 |
| 3194 | 6.11 The ring counting parameter, defined in Equation 6.6, as a function 3195 of the number of reconstructed rings as found by the <code>fitQun</code> recon- 3196 struction algorithm. Left: true ν_μ events with only one muon above 3197 the Cherenkov threshold in the final state. Right: true ν_μ events with 3198 one muon and at least one other charged particle above the Cherenkov 3199 threshold in the final state. | 129 |

| | | | |
|------|------|--|-----|
| 3200 | 6.12 | The χ^2 between the hybrid- π^0 Monte Carlo and data samples, as a function of smear (α) and shift (β) parameters, for events which have $1\pi^0$ final state topology. Left: Electron-muon separation PID parameter for events with $30 \geq E_{vis}(MeV) < 300$. Right: Electron- π^0 separation PID parameter for events with $30 \geq E_{vis}(MeV) < 300$ | 130 |
| 3205 | 6.13 | The distribution of $\log(L_e/L_\mu)$ compared to $\log(L_e/L_\pi)$ for subGeV events with zero (top left), one (top right) or two (bottom) decay electrons. The correlation in the distribution is calculated as 0.997, 0.999 and 0.996, respectively. | 131 |
| 3209 | 7.1 | The density of the Earth given as a function of the radius, as given by the PREM model (Black), and the constant density four-layer approximation (Blue), as used in the official SK-only analysis. | 135 |
| 3212 | 7.2 | An ‘‘oscillogram’’ that depicts the $P(\nu_\mu \rightarrow \nu_e)$ oscillation probability as a function of neutrino energy and cosine of the zenith angle. The zenith angle is defined such that $\cos(\theta_Z) = 1.0$ represents neutrinos that travel from directly above the detector. The four-layer constant density PREM model approximation is used and Asimov A oscillation parameters are assumed (Table 2.2). | 136 |
| 3218 | 7.3 | The effect of δ_{CP} for atmospheric neutrinos given in terms of the neutrino energy and zenith angle. This oscillogram compares the $P(\nu_\mu \rightarrow \nu_e)$ oscillation probability for a CP conserving ($\delta_{CP} = 0.0$) and a CP violating ($\delta_{CP} = -1.601$) value taken from the Asimov A parameter set. The other oscillation parameters assume the Asimov A oscillation parameter set given in Table 2.2. | 137 |

| | | |
|---------------|---|-----|
| 3224 7.4 | An illustration of the matter-induced effects on the oscillation probability, given as a function of neutrino energy and zenith angle. The top row of panels gives the $P(\nu_e \rightarrow \nu_e)$ oscillation probability and the bottom row illustrates the $P(\bar{\nu}_e \rightarrow \bar{\nu}_e)$ oscillation probability. The left column highlights the oscillation probability in a vacuum, whereas the middle and right column represents the oscillation probabilities when the four-layer fixed density PREM model is assumed. All oscillation probabilities assume the “Asimov A” set given in Table 2.2, but importantly, the right column sets an inverted mass hierarchy. The “matter resonance” effects at $E_\nu \sim 5\text{GeV}$ can be seen in the $P(\nu_e \rightarrow \nu_e)$ for normal mass hierarchy and $P(\bar{\nu}_e \rightarrow \bar{\nu}_e)$ for inverted hierarchy. | 138 |
| 3235 7.5 | The oscillation probability for beam neutrino events given as a function of neutrino energy. All oscillation parameters assume the “Asimov A” set given in Table 2.2 unless otherwise stated. Each panel represents a change in one of the oscillation parameters whilst keeping the remaining parameters fixed. | 139 |
| 3240 7.6 | The number of electron-like events in the FHC and RHC operating mode of the beam, as a function of the oscillation probabilities. Both normal hierarchy (Solid) and inverse hierarchy (Dashed) values of Δm_{23}^2 are given. | 140 |
| 3244 7.7 | The oscillation probability $P(\nu_\mu \rightarrow \nu_e)$, given as a function of neutrino energy and zenith angle, which highlights an example of the “fast” oscillations in the sub-GeV upgoing region. | 142 |
| 3247 7.8 | Illustration of the averaging procedure for $N = 2$. The oscillation probabilities calculated on the finer left binning are averaged to obtain the oscillation probabilities in the coarser right binning. These averaged oscillation probabilities with the coarser binning are then applied to each event during the fit. | 144 |
| 3252 7.9 | Event rate of the SubGeV_elike_0dcy sample as a function of the number of sub-divisions per coarse bin. Each subplot represents the event rate of the sample at a different oscillation parameter set thrown from the PDG priors detailed in Table 2.1. The red line in each subplot represents the mean of the event rate over the different values of subdivisions for that particular oscillation parameter throw. | 146 |

| | | |
|------|---|-----|
| 3258 | 7.10 Variance of event rate for each atmospheric sample as a function of the number of sub-divisions per coarse bin. The solid red line indicates the 0.1% threshold and the dashed red line indicates the variance at a sub-division $N = 10$ | 147 |
| 3262 | 7.11 Variance of sample likelihood, when compared to ‘Asimov data’ set at Asimov A, for each atmospheric sample as a function of the number of sub-divisions per coarse bin. The solid red line indicates the 0.1% threshold and the dashed red line is a graphical indication of the variance at a sub-division $N = 10$ | 148 |
| 3267 | 7.12 The oscillation probability, $P(\nu_\mu \rightarrow \nu_e)$ (top row) and $P(\nu_e \rightarrow \nu_e)$ (bottom row), given as a function of neutrino energy and zenith angle. The left column gives the “fine” binning used to calculate the oscillation probabilities and the right column illustrates the “coarse” binning used to reweight the Monte Carlo events. The fine binning choice is given with $N = 10$, which was determined to be below the threshold from Figure 7.10 and Figure 7.11. | 149 |
| 3274 | 7.13 The calculation time taken to both calculate the oscillation probabilities and fill the “coarse” oscillograms, following the technique given in section 7.2, for the CUDAProb3 and ProbGPU (Red) calculation engines. CUDAProb3 has both a GPU (Blue) and CPU (Black) implementation, where the CPU implementation is multithreaded. Therefore, 8-threads (solid) and 40-threads (dashed) configurations have been tested. Prob3, which is a CPU single-thread implementation has a mean step time of 1.142s. | 150 |
| 3282 | 7.14 The oscillation probability, $P(\nu_\mu \rightarrow \nu_e)$ (top row) and $P(\nu_e \rightarrow \nu_e)$ (bottom row), given as a function of neutrino energy and zenith angle. The left column gives probabilities where the constant $Z/A = 0.5$ approximation which is used in the official SK-only analysis. The middle column gives the probabilities where $Z/A = [0.468, 0.498]$ values are used, as given in Table 7.1. The right column illustrates the difference in oscillation probability between the two different techniques. | 152 |

- 3289 7.15 The density of the Earth given as a function of the radius, as given by
 3290 the PREM model (Black), the constant density four-layer approxima-
 3291 tion (Blue), as used in the official SK-only analysis, and the quadratic
 3292 approximation of the PREM model (Red). 153
- 3293 7.16 The oscillation probability, $P(\nu_\mu \rightarrow \nu_e)$ (top row) and $P(\nu_e \rightarrow \nu_e)$ (bot-
 3294 tom row), given as a function of neutrino energy and zenith angle. The
 3295 left column gives probabilities where the four-layer constant density ap-
 3296 proximation is used. The middle column gives the probabilities where
 3297 the density is integrated over the trajectory, using the quadratic PREM
 3298 approximation, for each $\cos(\theta_Z)$ is used. The right column illustrates the
 3299 difference in oscillation probability between the two different techniques. 155
- 3300 7.17 The oscillation probability, $P(\nu_\mu \rightarrow \nu_e)$ (top row) and $P(\nu_e \rightarrow \nu_e)$ (bot-
 3301 tom row), given as a function of neutrino energy and zenith angle. The
 3302 left column gives probabilities where a fixed production height of 25km
 3303 is used. The middle column gives the probabilities where the produc-
 3304 tion height is analytically averaged. The right column illustrates the
 3305 difference in oscillation probability between the two different techniques. 159
- 3306 8.1 The response of the likelihood, as defined in section 8.1, illustrating
 3307 the response of the samples to the oscillation parameters. Δm_{12}^2 and
 3308 $\sin^2(\theta_{12})$ are negated because these samples have no sensitivity to those
 3309 parameters. The Asimov data set is built using the pre-fit dial values
 3310 assuming Asimov A oscillation parameters defined in Table 2.2. 163

List of Tables

| | | |
|---------------|---|----|
| 3312 2.1 | The 2018 Particle Data Group constraints of the oscillation parameters taken from [81]. The value of Δm_{23}^2 is given for both normal hierarchy (N.H.) and inverted hierarchy (I.H.) and $\sin^2(\theta_{23})$ is broken down by whether its value is below (Q1) or above (Q2) 0.5. | 21 |
| 3316 2.2 | Reference values of the neutrino oscillation parameters for two different oscillation parameter sets. | 22 |
| 3318 3.1 | The various SK periods and respective live-time. The SK-VI live-time is calculated until 1 st April 2022. SK-VII started during the writing of this thesis. | 24 |
| 3321 3.2 | The trigger thresholds and extended time windows saved around an event which were utilised throughout the SK-IV period. The exact thresholds can change and the values listed here represent the thresholds at the start and end of the SK-IV period. | 33 |
| 3325 3.3 | The threshold momentum and energy for a particle to generate Cherenkov light in ultrapure water, as calculated in Equation 3.2 in ultrapure water which has refractive index $n = 1.33$ | 34 |
| 3328 4.1 | Jeffreys scale for strength of preference for two models A and B as a function of the calculated Bayes factor ($B_{AB} = B(A/B)$) between the two models [140]. The original scale is given in terms of $\log_{10}(B(A/B))$ but converted to linear scale for easy comparison throughout this thesis. | 66 |
| 3332 6.1 | The amount of data collected in each detector used within this analysis. The data collected at the near and far detector, for both neutrino beam (FHC) and antineutrino beam (RHC), is measured as the number of protons on target (POT). | 92 |
| 3336 6.2 | The fully contained subGeV samples, defined as events with visible energy $E_{vis} < 1.33\text{GeV}$, used within this oscillation analysis. | 95 |

| | | |
|----------------|---|-----|
| 3338 6.3 | The fully contained multiGeV samples used within this oscillation analysis. Both the sample name and description are given. | 97 |
| 3340 6.4 | The purity of each atmospheric sample used within this analysis, broken down by charged current (CC) and neutral current (NC) interactions and which neutrino flavour interacted within the detector. Asimov A oscillation parameter sets are assumed (given in Table 2.2). Electron neutrino and antineutrino events are separated to illustrate the ability of the separation likelihood cuts used within the multiGeV and multiring sample selections. | 98 |
| 3347 6.5 | The reconstructed cosine zenith and lepton momentum binning as- signed to the atmospheric samples. The “cos(θ_Z) Bins” column il- lustrates the number of bins uniformly distributed over the $-1.0 \leq$ $\cos(\theta_Z) \leq 1.0$ region for fully and partially contained samples and $-1.0 \leq \cos(\theta_Z) \leq 0.0$ region for up- μ samples. DB: Does this belong in the appendix? | 99 |
| 3353 6.6 | The neutrino energy binning for the different neutrino flavours. “Right” sign indicates neutrinos in the FHC beam and antineutrinos in the RHC beam. “Wrong” sign indicates antineutrinos in the FHC beam and neutrinos in the RHC beam. The binning of the detector response is identical for the FHC and RHC modes as well as at ND280 and SK. . . | 111 |
| 3358 6.7 | List of cut variables that are included within the shift/smear fit docu- mented in [199]. | 121 |
| 3360 6.8 | Reconstructed event topology categories on which the SK detector systematics [199] are based. | 122 |
| 3362 6.9 | Sources of systematic errors specified within the grouped into the “cali- bration” systematics model. | 125 |
| 3364 6.10 | Visible energy binning for which the correlated SK detector systematics are based | 126 |
| 3366 7.1 | Description of the four layers of the Earth invoked within the constant density approximation of the PREM model [211]. | 134 |

| | | |
|------|--|-----|
| 3368 | 7.2 The quadratic polynomial fits to the PREM model for four assumed | |
| 3369 | layers of the PREM model. The fit to calculate the coefficients is given | |
| 3370 | in [212], where $x = R/R_{Earth}$ | 154 |